

Spectromicroscopic investigation of local redox processes in resistive switching transition metal oxides

Thomas Heisig

Information

Band / Volume 79

ISBN 978-3-95806-609-0

Forschungszentrum Jülich GmbH
Peter Grünberg Institut (PGI)
Elektronische Materialien (PGI-7)

Spectromicroscopic investigation of local redox processes in resistive switching transition metal oxides

Thomas Heisig

Schriften des Forschungszentrums Jülich
Reihe Information / Information

Band / Volume 79

ISSN 1866-1777

ISBN 978-3-95806-609-0

Bibliografische Information der Deutschen Nationalbibliothek.
Die Deutsche Nationalbibliothek verzeichnet diese Publikation in der
Deutschen Nationalbibliografie; detaillierte Bibliografische Daten
sind im Internet über <http://dnb.d-nb.de> abrufbar.

Herausgeber
und Vertrieb: Forschungszentrum Jülich GmbH
 Zentralbibliothek, Verlag
 52425 Jülich
 Tel.: +49 2461 61-5368
 Fax: +49 2461 61-6103
 zb-publikation@fz-juelich.de
 www.fz-juelich.de/zb

Umschlaggestaltung: Grafische Medien, Forschungszentrum Jülich GmbH

Druck: Grafische Medien, Forschungszentrum Jülich GmbH

Copyright: Forschungszentrum Jülich 2022

Schriften des Forschungszentrums Jülich
Reihe Information / Information, Band / Volume 79

D 82 (Diss. RWTH Aachen University, 2021)

ISSN 1866-1777
ISBN 978-3-95806-609-0

Vollständig frei verfügbar über das Publikationsportal des Forschungszentrums Jülich (JuSER)
unter www.fz-juelich.de/zb/openaccess.



This is an Open Access publication distributed under the terms of the [Creative Commons Attribution License 4.0](https://creativecommons.org/licenses/by/4.0/),
which permits unrestricted use, distribution, and reproduction in any medium, provided the original work is properly cited.

Abstract

The ongoing digitization of the world has led to a growing demand for energy- and cost-efficient storage and processing of data. As the existing memory and computing technologies run into fundamental physical limitations, novel devices and computing concepts are required to meet the demand. One of the most promising technologies for future non-volatile memory- and computing-applications are redox-based resistive switching devices. Such a device is composed of a metal-insulator-metal stack that allows the reversible and non-volatile switching of the electrical resistance through application of voltage signals. The resistance change is suspected to be caused by the formation and migration of ionic defects within a small filamentary region of the device. However, despite extensive research efforts the details of the microscopic redox processes that drive resistive switching are still under debate. The aim of this thesis is the elucidation of the switching mechanism in two classic resistive switching oxides, namely SrTiO_3 and Ta_2O_5 , by employing spectromicroscopic techniques.

First, the influence of the SrTiO_3 thin film properties on the switching characteristics is investigated. It is demonstrated that the film thickness and the crystallographic defect structure are decisive factors that determine the polarity of the resistance hysteresis. By combining spectromicroscopy and atomistic simulations, the role of extended defects as fast cation diffusion path is identified. Cation migration takes place along extended defects during device operation, which results in spatially confined phase separations. *In operando* transmission electron microscopy of defect rich SrTiO_3 films provides evidence for a localized valence change from Ti^{4+} to Ti^{3+} caused by the electroforming process. In the high resistance state a homogeneous oxygen distribution is observed, whereas in the low resistance state nanometer sized oxygen-deficient regions are visible, which form at island boundaries.

To characterize conductive filaments in Ta_2O_5 using photoelectron spectroscopy, a novel device layout is employed that combines a crossbar structure and graphene electrodes. Photoemission electron microscopy of functional Ta_2O_5 memristive devices reveals the presence of oxygen-deficient nanoscale filaments. The filament composition is quantified using core level spectroscopy and an oxygen vacancy concentration of 16% is measured in the low resistive state. The results further clarify the long debated question whether the filament is composed of a suboxide or metallic phase by demonstrating that no metallic tantalum component is present in the filament.

Kurzfassung

In unserer zunehmend digitalisierten Welt herrscht eine wachsende Nachfrage nach kostengünstiger Datenspeicherung und -verarbeitung. Angesichts der Tatsache, dass bestehende Speichertechnologien an ihre physikalischen Grenzen stoßen, werden neue Komponenten und Konzepte benötigt um die Nachfrage zu decken. Eine der vielversprechendsten Technologien für nichtflüchtige Speicher- und Logikanwendungen sind redox-basierte resistiv schaltende Bauelemente. Diese Bauteile, bestehend aus einem Metall-Isolator-Metall Stapel, können durch Anlegen einer Spannung reversibel und nicht-flüchtig ihren elektrischen Widerstand ändern. Es wird angenommen, dass die Widerstandsänderung auf die Bildung und Migration von ionischen Defekten zurückzuführen ist. Obwohl das resistive Schalten eingehend untersucht wurde, sind die Details der mikroskopischen Prozesse noch immer nicht vollständig verstanden. Das Ziel dieser Arbeit ist die Aufklärung der Schaltmechanismen in zwei klassischen resistiv schaltenden Oxiden, namentlich SrTiO_3 und Ta_2O_5 , durch Verwendung von spektromikroskopischen Analysemethoden.

Zunächst wird der Einfluss der Schichteigenschaften von SrTiO_3 Dünnschichten auf das resistive Schaltverhalten untersucht. Es wird gezeigt, dass die Schichtdicke und die Defektstruktur entscheidende Faktoren darstellen, welche die Polarität der Widerstandshysterese festlegen. Durch Kombination von Spektromikroskopie und atomaren Simulationen wird gezeigt, dass ausgedehnte Defekte als Kationen-Diffusionspfade fungieren. Die Migration von Kationen findet entlang der ausgedehnten Defekte während des Schaltvorgangs statt und führt zu lokalen Phasenseparationen. Mittels *in operando* Transmissionselektronenmikroskopie von defektreichen SrTiO_3 Filmen wird der Valenzwechsel von Ti^{4+} zu Ti^{3+} nachgewiesen. Während im hochohmigen Zustand eine homogene Sauerstoffkonzentration vorgefunden wird, sind im niederohmigen Zustand nanometergroße Sauerstoff-defizitäre Bereiche sichtbar, welche sich entlang von Inselgrenzen bilden.

Um leitfähige Filamente in Ta_2O_5 mittels Photoelektronenspektroskopie zu charakterisieren, wird eine Bauteilarchitektur verwendet, die eine Kreuzpunktstruktur und Graphenelektroden kombiniert. Photoemissionselektronenmikroskopie von funktionalen Ta_2O_5 memristiv schaltenden Bauelementen zeigt die Präsenz von Sauerstoff-defizitären nanoskaligen Filamenten. Eine Sauerstoffleerstellenkonzentration von 16 % konnte für den niederohmigen Zustand bestimmt werden. Die Ergebnisse zeigen weiterhin, dass das Filament aus einer suboxid Phase besteht und nicht wie oft angenommen aus metallischem Tantal.

Contents

1	Introduction	1
2	Background	5
2.1	Fundamentals of SrTiO ₃	5
2.2	Fundamentals of Ta ₂ O ₅	8
2.3	Electronic transport mechanism	11
2.4	Resistive switching in valence change materials	17
3	Experimental methods	25
3.1	Pulsed laser deposition	25
3.2	Radio frequency magnetron sputter deposition	25
3.3	Device fabrication and electrical characterization	27
3.4	Conductive atomic force microscopy	33
3.5	X-ray absorption spectroscopy	33
3.6	Photoelectron emission spectroscopy	35
3.7	Photoemission electron microscopy	37
4	Growth and characterization of thin oxide films	41
4.1	Structure and morphology of PLD grown SrTiO ₃ thin films	41
4.2	Structure and morphology of Ta and Ta ₂ O ₅ thin films	46
4.3	Engineering the oxygen content in sputtered TaO _x thin films	50
4.4	Spectroscopic signatures of Ta ₂ O ₅ thin films reduced by electrical stress	55
4.5	Summary	57
5	Resistive switching in SrTiO₃ and Ta₂O₅ thin film devices	59
5.1	Resistive switching in SrTiO ₃ thin film devices	59
5.1.1	Eightwise switching in SrTiO ₃	59
5.1.2	Counter-eightwise switching in SrTiO ₃	64
5.1.3	Impact of the thin film thickness and growth temperature on the switching polarity	69
5.1.4	Summary of resistive switching in SrTiO ₃	70

5.2	Counter-eightwise switching in Ta ₂ O ₅ thin film devices	71
5.2.1	General switching characteristics and influence of different top electrode materials	71
5.2.2	Thickness dependence	75
5.2.3	Influence of the atmosphere	76
5.2.4	Temperature dependence	82
5.2.5	Summary of resistive switching in Ta ₂ O ₅	85
6	Spectromicroscopic analysis of switching-induced chemical changes in SrTiO₃	87
6.1	Investigation of eightwise switching in SrTiO ₃	88
6.1.1	<i>In situ</i> delamination of top electrodes	88
6.1.2	PEEM work function analysis	88
6.1.3	Microscopic investigation of switching induced changes in Sr-rich devices	91
6.1.4	Atomistic simulation of cation diffusion along antiphase boundaries . . .	95
6.1.5	Electro-thermal device simulations	97
6.1.6	Summary of eightwise switching in SrTiO ₃	99
6.1.7	Discussion: Origin of the retention stabilization in eightwise switching in Sr-rich SrTiO ₃	99
6.2	Investigation of counter-eightwise switching in SrTiO ₃ by <i>in operando</i> TEM . .	102
6.2.1	Current induced structural and electronic modifications	104
6.2.2	Mapping of the oxygen distribution in different resistive states	106
6.2.3	Summary of counter-eightwise switching in SrTiO ₃	108
6.2.4	Discussion: Origin of the counter-eightwise switching polarity in SrTiO ₃	109
7	Photoemission electron microscopy of Ta₂O₅ devices with graphene electrodes	111
7.1	Spatial resolution of photoemission electron microscopy	111
7.2	Photoelectron spectroscopy through graphene electrodes	114
7.3	Stability of Ta ₂ O ₅ under synchrotron radiation	116
7.4	Spectromicroscopy of functioning Ta ₂ O ₅ graphene devices	118
7.5	Summary	126
7.6	Discussion of the switching mechanism	127
8	Conclusions	133
	Appendix: Fabrication details	137
	List of Figures	153
	Bibliography	157

1 Introduction

In today's information age, data is becoming increasingly important and it profoundly changes the everyday life of people and the way businesses operate. With the ongoing digitization of our society, the demand for cost-efficient data storage is growing and growing. While in 2020 an estimated 50 zettabytes of data was created world wide, it is expected to reach 175 zettabytes by 2025 [1]. Currently, the vast majority of data is stored on hard disk drives (HDD) and Flash memory. While both technologies have seen significant improvements over the last decade, they suffer from high energy consumption, slow access times and a low endurance [2,3]. Especially the slow access time poses a major problem when data needs to be transferred from non-volatile to volatile memories to further process the data. The overall performance of the system is then limited by the low transfer rate of the non-volatile memory. In order to overcome these shortcomings, various emerging memory technologies have been investigated with the goal to complement or replace existing storage concepts.

One of the most promising candidate among the emerging memories is the so-called redox-based resistive switching random access memory (ReRAM) [4–6]. A ReRAM cell is a two-terminal device, which consists of an insulating oxide layer that is sandwiched between two metal electrodes. In these devices, a voltage is applied to switch the device resistance between two or more states. This so-called resistive switching effect allows the non-volatile storage of information in form of the device resistance. Prototypical ReRAM systems have demonstrated an excellent performance combining fast read and write times [7–9], long retention [10], low energy consumption [11] and a high endurance [12], outperforming Flash and HDD. Furthermore, owing to its simple structure, ReRAM offers exceptional scaling- and multi-layer stacking-capabilities [13–15]. Due to these merits, ReRAM is also considered to be a key component for emerging hardware applications in machine learning [16], neuromorphic [17] and in-memory computing [18]. Despite these promising performance metrics, ReRAM suffers from a large intrinsic variability, which hampers its technological exploitation [19]. Several solutions have been proposed to overcome these reliability issues, including material- and process-optimization [20,21]. However, due to the large number of possible material combinations and fabrication techniques, an empirical device optimization is not practical. To transit towards a knowledge based optimization strategy, it is essential to gain a deeper understanding of the microscopic processes that are involved in resistive switching and how they can be controlled.

In transition metal oxide devices, it is generally assumed that resistive switching is driven by formation and migration of oxygen vacancies within the oxide layer [4,22]. This process takes place in a spatially confined region, the so-called conductive filament. Because the formation of oxygen vacancies is associated with a valence change of the transition metal cation, the process is termed valence change mechanism (VCM) [6]. Accordingly, a detailed characterization of conductive filaments is the key to establish a complete picture of the switching mechanism. The study of filaments is, however, inherently difficult due to their small size and the fact that they are covered by electrodes. Furthermore, the composition of a filament may differ only slightly from the surrounding oxide as already small modulations of the oxygen concentration have a strong impact on the device resistance [23–25].

Therefore, analysis methods are required that have a high sensitivity for changes in the chemical and electronic structure and that have a high spatial resolution. These attributes are unified in the field of spectromicroscopy. While spectromicroscopy on the micrometer scale has become a standard method for many analytical tools, only very few techniques are capable of providing spectroscopic information on the nanoscale [26]. Among these techniques, transmission electron microscopy (TEM) and photoemission electron microscopy (PEEM) stand out due to their capability of probing electronic core levels. This allows the determination of oxidation states and gives information about the chemical environment. Accordingly, TEM and PEEM have been successfully employed to study a wide range of resistive switching devices [27–30].

To fully exploit the capabilities of spectroscopic TEM, samples with a high crystallinity are preferred. Under ideal imaging conditions, TEM can probe core levels via electron energy loss spectroscopy (EELS) or energy dispersive X-ray spectroscopy (EDX) with atomic resolution [28,31]. The drawback of this technique is, however, that it requires the preparation of a thin TEM specimen that is cut from a region of interest on the device. Therefore, precise knowledge about the filament location is a prerequisite for the specimen preparation. A further disadvantage of TEM is the possibility of creating additional defects during specimen preparation, e.g. amorphization of the lamella during polishing [32]. Thus, discriminating between preparation and switching induced defects is challenging. To overcome these obstacles, *in operando* TEM can be employed, which enables switching of the specimen within the microscope [33,34]. More importantly, the technique also allows to image a conductive filament in different resistive states, which is crucial for a detailed understanding of the switching process.

Because TEM based EELS often suffers from a low signal-to-noise ratio, it is difficult to obtain spatially resolved information about the oxidation state of the material. This is amplified for heavier elements such as $5d$ transition metal oxides, which feature low intensity loss edges located at high energies [35]. For this reason, many studies on Ta_2O_5 and HfO_2 devices re-

strict their investigation to the determination of the chemical composition [36–39]. Hence, it is highly desirable to utilize complementary spectromicroscopic techniques that provide additional information about the electronic structure of the conductive filament. In principle, this can be achieved by combination of PEEM and X-ray photoelectron spectroscopy (XPS) [29]. However, because XPS is a highly surface sensitive technique, probing conductive filaments through a metallic top electrode is not possible. To overcome this obstacle, two approaches have been successfully demonstrated. The first approach relies on the mechanical removal of the top electrode, which uncovers the filament and makes it accessible for characterization [40]. The downside of this approach is that a device can only be studied in a single resistive state. In the second approach, a graphene top electrode is used to overcome the surface sensitivity of XPS. Due to the nature of graphene, i.e. being only a single atomic layer thick, it is the thinnest electrode material imaginable and to a large extent photoelectron transparent [41]. Accordingly, graphene electrodes enable photoelectron spectroscopy of functional memristive devices [25].

The goal of this thesis is to clarify the switching mechanism in two prominent resistive switching oxides, namely SrTiO_3 and Ta_2O_5 , by using spectromicroscopy. The motivation for selecting SrTiO_3 is based on its well known defect chemistry and spectroscopic signatures. The possibility to grow SrTiO_3 as an epitaxial thin film with adjustable cation stoichiometry and controllable defect structure allows to study the impact of physical film properties on resistive switching characteristics. Although SrTiO_3 is an important model system, it is considered to be technologically irrelevant due to its subpar switching performance and incompatibility with standard semiconductor fabrication processes. In contrast, Ta_2O_5 is a highly attractive material for resistive switching because it unifies excellent switching properties and high integrability into existing semiconductor production lines. Hence, the investigation of Ta_2O_5 follows an application-oriented motive.

Chapter 2 reviews the fundamental properties of SrTiO_3 and Ta_2O_5 with emphasis on the crystal and electronic structure as well as their defect chemistry. The electronic transport mechanism in metal-insulator-metal structures are presented. The chapter concludes with an overview about the existing knowledge of resistive switching in SrTiO_3 and Ta_2O_5 .

In chapter 3 the sample fabrication and analysis techniques are introduced. Chapter 4 presents a thorough characterization of the pristine SrTiO_3 and Ta_2O_5 thin films. The influence of deposition parameters on the film properties will be discussed. Special focus is given to the cation stoichiometry and growth temperature of SrTiO_3 thin films. In addition, a detailed spectroscopic and electrical characterization of TaO_x thin films with a large range of oxygen non-stoichiometry is presented.

The resistive switching characteristics of SrTiO₃- and Ta₂O₅-based devices are discussed in chapter 5. For SrTiO₃ devices, the impact of cation stoichiometry, film thickness and surrounding atmosphere is investigated. Special attention is paid to the polarity of the resistance hysteresis and how it is connected to the thin film properties. Ta₂O₅ devices were analyzed with regard to the top electrode material, film thickness, surrounding atmosphere and temperature.

Chapter 6 is dedicated to the spectromicroscopy of SrTiO₃ devices. The chapter is subdivided into two parts. Part one deals with the investigation of devices with an eightwise switching polarity. Through the combination of PEEM, TEM and atomistic simulations, the mechanistic details of the cation-migration process are uncovered. Extended defects in an otherwise epitaxial SrTiO₃ film serve as fast diffusion paths for Sr²⁺ cations. In the second part of the chapter, counter-eightwise switching devices are studied. Using *in operando* TEM it is demonstrated, that the electroforming process induces a spatially confined reduction of the oxide. Characterization of a device in different resistive states shows a local redistribution of oxygen. Based on these results, a phenomenological model of the switching process is given.

In chapter 7 the spectromicroscopic investigation is extended to Ta₂O₅ devices. By employing graphene electrodes, PEEM of functional Ta₂O₅ devices is enabled. The experimental conditions and limitations are evaluated in depth before the characterization of memristive devices is presented. It is observed that a localized oxygen deficient filament is formed during the electroforming step. Spectroscopic evaluation by XPS gives quantitative information about the composition and electronic structure of the filament. Using XAS, additional information about the near range order in the oxygen deficient filament are derived. Using the insights derived from spectromicroscopy, a review of the most common switching models is given. It is reasoned, that the switching process is caused by a vertical redistribution of oxygen within the conductive filament.

Finally, a summary of the key results obtained within this work is given in chapter 8.

2 Background

In this chapter, the fundamental properties of SrTiO_3 and Ta_2O_5 will be introduced. Special emphasis is given to the crystal structure, defect chemistry and electronic structure of both materials. Afterwards, an overview of the electronic transport mechanism in semiconductors and across metal semiconductor contacts will be given. At the end of this chapter, the resistive switching effect in transition metal oxides is discussed in detail.

2.1 Fundamentals of SrTiO_3

Crystal structure

Strontium titanate is a ternary oxide with a perovskite crystal structure which undergoes a structural phase transition from a tetragonal to cubic phase at 105 K [42]. According to the general crystal structure of ABX_3 perovskites, the larger strontium cation is located at the A-site and the titanium cation occupies the B-site. Figure 2.1 a) and b) schematically depict the unit cell structure of SrTiO_3 . Each titanium cation is coordinated octahedrally by six oxygen anions. Another convenient way to describe the crystal structure of SrTiO_3 is to consider an alternating stack of TiO_2 and SrO atomic planes, which propagate in the $[001]$ direction with a plane distance of $a/2$ between each layer (compare Figure 2.1 a)) [43].

Electronic structure

Intrinsic SrTiO_3 is an insulator with an indirect bandgap of 3.25 eV and a direct bandgap of 3.75 eV [45]. SrTiO_3 has an electron affinity of 3.9-4.1 eV and forms a Schottky contact with most high work function metals [46, 47]. Due to the large difference in electro-negativity between oxygen and metal atoms, the bonding in SrTiO_3 has predominantly an ionic character. Accordingly, the Ti 3d, Ti 4s and Sr 5s valence electrons are transferred to the O 2p orbital, giving rise to the nominal oxidation states Ti^{4+} , Sr^{2+} and O^{2-} . However, to a lesser extent also covalent contributions are present in the oxygen-metal bond, especially for the Ti-O bond [48]. A detailed description of the band structure is given in ref. [49]. Electronic

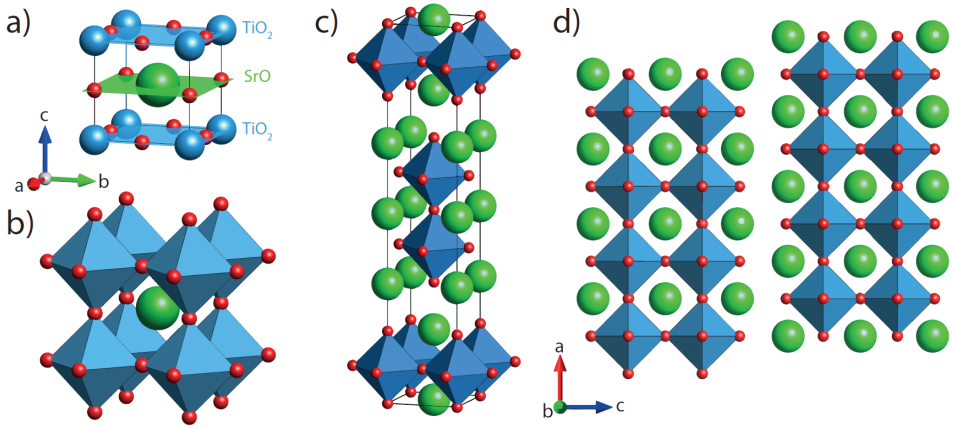


Figure 2.1: Crystal structure of cubic SrTiO₃ in a) the atomic representation and b) showing the octahedral coordination symmetry of O²⁻ around Ti⁴⁺. c) Unit cell of Sr₃Ti₂O₇. d) Crystal structure of a Ruddlesden-Popper type anti phase boundary. Structural data taken from [44].

transport in bulk SrTiO₃ is typically described by so-called Poole-Frenkel emission or by band conduction [50, 51]. In SrTiO₃ metal-insulator-metal structures, the current can also be limited by the transport across a Schottky barrier through tunnelling or thermionic emission [52, 53].

Defect chemistry

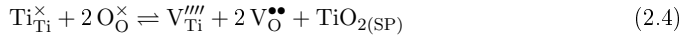
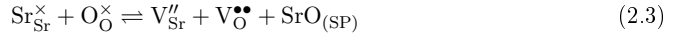
Crystallographic defects are interruptions of the regular periodic pattern in a crystalline solid. Depending on their dimensionality, defects can be categorized into point defects and extended defects. To describe crystallographic defects, the Kröger-Vink notation

$$M_S^C \quad (2.1)$$

is used [54]. In this notation, M represents the species which can be an atom, an ion, a vacancy, an electron, an electron-hole or an interstitial. S denotes the crystallographic site which the species occupies and C denotes the nominal charge with respect to the perfect lattice. A negative charge is illustrated by the prime symbol ($'$), a positive charge by a dot (\bullet) and a neutral charge by a cross (\times). Hence, the regular lattice species in SrTiO₃ are written as Sr_{Sr}[×], Ti_{Ti}[×] and O_O[×]. A substitutional dopants like Fe³⁺, sitting on a titanium lattice site, is written as Fe_{Ti}[']. Vacant sites are indicated by V_O^{••} or V_M^{''} for an O²⁻ anion and a M²⁺ cation vacancy respectively. Here it is noted that the nominal charge of the vacancy is determined by the oxidation state of the vacant ion. In peroxides, oxygen vacancies have only a single positive charge.

Point defects

The intrinsic point defects in SrTiO₃ are almost exclusively vacancy defects (also called Schottky defects), since the formation of interstitial defects (Frenkel defects) is energetically unfavorable due to the close packing of the perovskite structure [55, 56]. Equations 2.2-2.4 show all possible vacancy defects that can occur in SrTiO₃. Equation 2.2 describes the generation of oxygen vacancies accompanied by the formation of molecular oxygen. The equilibration of oxygen with the surrounding atmosphere is observed at comparatively low temperatures of $T > 700$ K [57, 58]. Importantly, every oxygen vacancy is compensated by two electrons in the conduction band. In SrTiO₃, $V_{\text{O}}^{\bullet\bullet}$ act as shallow donors with the donor level being located less than 0.1 eV below the conduction band. Accordingly, oxygen vacancies will be partially ionized at room temperature. The formation of cation vacancies is expressed by equations 2.3 and 2.4. However, the generation of cation vacancies is only observed at high temperatures of $T > 1300$ K [59], which is still considerably lower than the melting temperature of 2350 K [60]. Due to the high defect formation energy of $V_{\text{Ti}}^{\bullet\bullet\bullet\bullet}$ the formation of $V_{\text{Sr}}^{\bullet\bullet}$ is the dominant defect mechanism for the cation sublattice [61, 62]. From the equations it can be seen that the cation vacancy generation goes along with the formation of a secondary phase (SP), which is formed either on the crystal surface or in the bulk as point or extended defect [63]. Besides the intrinsic defects, SrTiO₃ crystals contain small amounts of impurities (extrinsic point defects), which typically have an acceptor-type character [64].



In the context of resistive switching, the creation of oxygen vacancies (equation 2.3) can be considered to be the most important point defect reaction as oxygen vacancies are the most mobile species and act as donor dopant. Both of these properties are essential for resistive switching as will be discussed in more detail in section 2.4.

Extended defects

Extended defects can be categorized according to their dimensionality as follows:

- 1D: Dislocations, linear clusters
- 2D: Stacking faults, grain boundaries, shear planes, antiphase boundaries
- 3D: Voids, inclusions, surface layer

Extended defects in SrTiO₃ are particularly interesting in the context of resistive switching, as their properties can significantly differ from the single crystal in terms of ionic transport [65–67], electronic structure [65, 68] and conductivity [68]. In this sense, extended defects embedded in an otherwise single crystalline matrix can facilitate or inhibit the formation of conductive filaments.

One particularly interesting defect is the so-called Ruddlesden-Popper type anti-phase boundary (RP APB), which forms during the Sr-rich growth of epitaxial SrTiO₃ thin films [69, 70]. The defect name originates from the family of Ruddlesden-Popper compounds that can be described by the sum formula Sr_{*n*+1}Ti_{*n*}O_{3*n*+1} [71]. Figure 2.1 c) shows the unit cell of the Sr₃Ti₂O₇ Ruddlesden-Popper phase. The unit cell contains two extra SrO atomic layers, which are shifted along the *a*/2[111] direction separated by two units of SrTiO₃ perovskite layers [72]. For thin films grown with a small Sr-excess, the additional SrO layers will not order to form a single phase compound, but rather occur as randomly distributed antiphase boundaries in the thin film. Figure 2.1 d) shows a RP APB separating two perovskite domains along the (b) direction. The impact of RP APB on the resistive switching properties of SrTiO₃ devices will be discussed in detail in chapter 6.

2.2 Fundamentals of Ta₂O₅

Crystal structure

Tantalum pentoxide (Ta₂O₅) is a binary transition metal oxide and is the only thermodynamically stable oxide in the tantalum-oxygen system. Ta₂O₅ has two stable low temperature phases: orthorhombic β-Ta₂O₅ [74, 75] and hexagonal δ-Ta₂O₅ [74, 76, 77]. At a temperature of 1320 °C β-Ta₂O₅ undergoes a reversible phase transition into the high temperature modification α-Ta₂O₅ which has a tetragonal crystal structure [78, 79]. The crystal structure of the low temperature modification phase is shown in figure 2.2. Due to the polymorphism between low and high temperature modifications it is difficult to grow pure Ta₂O₅ single crystals using conventional high-temperature techniques [80]. Ta₂O₅ thin films are usually deposited as

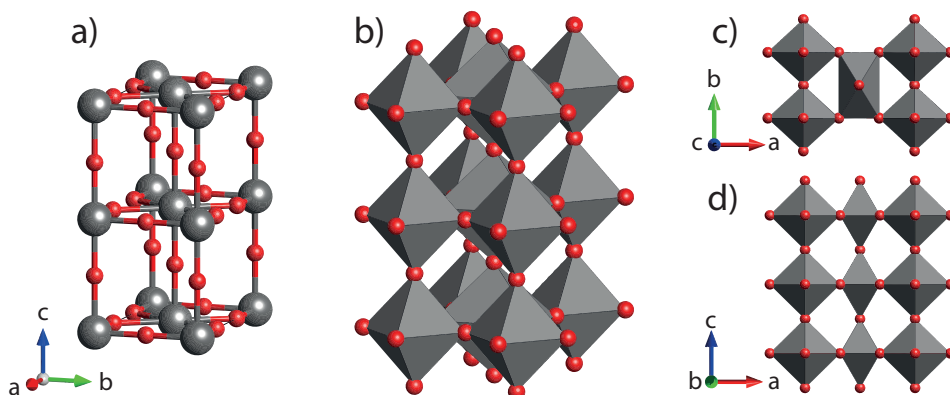


Figure 2.2: Crystal structure of orthorhombic $\beta\text{-Ta}_2\text{O}_5$. a) Atomic representation showing the Ta-O bonds. b) Depiction of the octahedral coordination symmetry of oxygen around Ta. c) Unit cell along the c-axis and d) along the b-axis. Structural data taken from ref. [73].

amorphous solid due to its high crystallization temperature. However, also single and polycrystalline films have been fabricated by sputter deposition and chemical vapor deposition [81,82].

Besides the thermodynamically stable tantalum pentoxide many metastable crystalline phases have been reported in literature, such as Ta_2O [83], TaO [84], Ta_2O_3 [85] and TaO_2 [84]. In these phases, the Ta cation can adopt oxidation states ranging from Ta^{1+} to Ta^{4+} . While none of these metastable phases has been isolated in its pure form, they can be kinetically stabilized under thin film conditions or through impurities. Apart from the crystalline phases, Ta-O compounds can also be grown as amorphous TaO_x thin films with a continuously adjustable oxygen content [86,87]. These amorphous films are kinetically stable up to the crystallization temperature of $\approx 700^\circ\text{C}$ [88], where the films undergo an irreversible phase separation into the thermodynamically stable compounds Ta and Ta_2O_5 . While amorphous compounds are distinguished by their lack of far-range order, they typically show characteristic short-range ordering. For Ta_2O_5 , the local ionic arrangement of Ta^{5+} surrounded by O^{2-} can be described by an octahedral coordination sphere (TaO_6) [89,90]. For sub-stoichiometric TaO_x compounds, the octahedral coordination partially transforms into a square pyramidal coordination (TaO_{5p}). Further, the polyhedra conjunction changes from corner- to edge- and lastly plane-sharing with decreasing oxygen content [90].

Electronic structure

Intrinsic Ta_2O_5 is an insulator with a large bandgap of approximately 4.4 eV [91,92]. Ta_2O_5 has an electron affinity of 3.2 eV and forms a Schottky barrier with high work function metals [91].

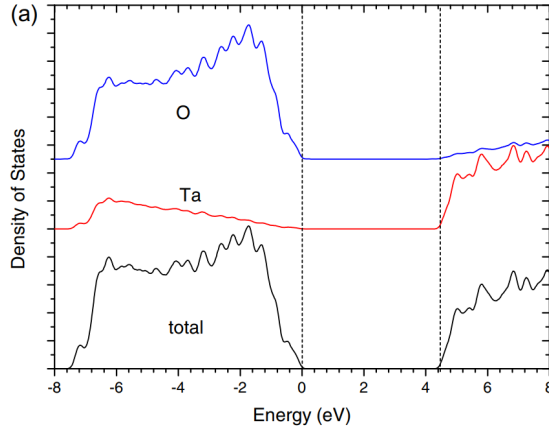
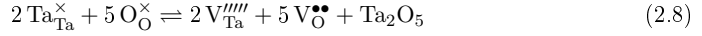


Figure 2.3: Partial density of states for amorphous Ta_2O_5 with a bandgap of 4.4 eV. The valence band is mainly composed of O 2p states and the conduction band of empty Ta 5d states. Reproduced from ref. [99]

In a strictly ionic picture, the valence electrons of the Ta 5d and Ta 6s orbitals have been fully transferred to the O 2p orbitals. Accordingly, the oxidation state of the ions are Ta^{5+} and O^{2-} . The large difference in electronegativity between Ta (1.5) and O (3.44) on the Pauling scale indicates a predominantly ionic bonding character, however, a small covalent contribution exists (compare figure 2.3). A critical parameter to understand the electronic conduction in intrinsic Ta_2O_5 is the oxygen vacancy defect energy level. A range of reports found experimentally and theoretically that oxygen vacancies act as deep donors with trap states in the range of 0.7-0.85 eV below the conduction band [93–97]. The electronic transport in amorphous TaO_x was described by a so-called variable range and nearest neighbor hopping [86,87], whereas Poole-Frenkel conduction was observed in Ta_2O_5 thin films [98].

Defect chemistry

The defect chemistry of intrinsic $\beta\text{-Ta}_2\text{O}_5$ has been consistently described in literature by the point defect reactions 2.5-2.8 [100,101]. Equation 2.5 describes the formation of oxygen vacancies and the associated release of molecular oxygen. In contrast to the closed packed crystal structure of SrTiO_3 , $\beta\text{-Ta}_2\text{O}_5$ tolerates the accommodation of oxygen and tantalum at interstitial sites [101,102]. Equations 2.6 and 2.7 express the formation of Frenkel defects for oxygen and tantalum respectively. Lastly, the Schottky defect formation by removal of a complete unit cell is considered in equation 2.8. Besides the intrinsic defects, Ta_2O_5 contains small amounts of aliovalent impurities [103].



While the defect chemistry of Ta_2O_5 is still an active research area, recent studies suggest that oxygen interstitials play a major role for the generation and diffusion of oxygen vacancies. It was found that the diffusion of oxygen is orders of magnitude faster compared to the cation diffusion [101]. Based on these results, one might surmise that the drift and diffusion processes that lead to resistive switching in Ta_2O_5 devices occur predominantly by the redistribution of oxygen anions. However, under certain conditions also tantalum migration might occur, especially at high temperatures and under high electric fields [102].

2.3 Electronic transport mechanism

The electronic transport in resistive switching metal-insulator-metal (MIM) structures is comprised of multiple current transport mechanism. Determination of the dominant conduction mechanism in memristive devices is often complicated, as the conduction depends on the used materials and variables such as the resistive state, temperature- and voltage ranges. For the purpose of this thesis, it is sufficient to consider the special case of an MIM cell that is composed of an Ohmic bottom interface and a Schottky contact at the top interface. In such cells, the electronic transport across the Schottky barrier as well as the insulator bulk conduction has to be considered. Throughout this thesis, the terms semiconductor and insulator will be used interchangeably, as resistive switching oxides can be treated as wide band-gap semiconductors.

Electronic transport across a Schottky barrier

If a high work function metal is brought into contact with a semiconductor a potential energy barrier for electrons, known as Schottky barrier, is formed. Figure 2.4 illustrates the band alignment leading to the formation of a Schottky junction. Upon contact between metal and semiconductor, electrons flow from the semiconductor to the metal until the Fermi energy is equal throughout the system. The current flow results in the formation of a space charge region (also called depletion region) bending the conduction- and valence-band. Similar to a $p - n$ junction, the Schottky junction shows current rectification. Under forward bias (positive bias

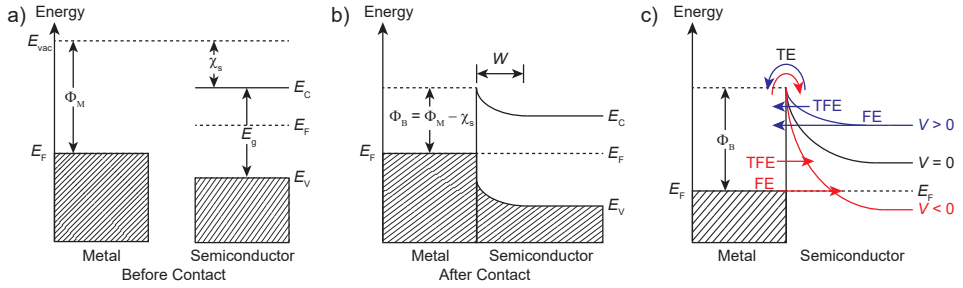


Figure 2.4: Energy level diagram of a high work function metal and a n -type semiconductor before a) and after b) they are brought in contact. With E_F the Fermi energy, E_{vac} the vacuum level, Φ_M the metal work function, χ_s the semiconductor electron affinity, E_C and E_V the conduction and valence band energy and W the depletion region thickness. c) Band diagram of a Schottky junction illustrating the three components of current across the barrier for no bias (black), forward bias (blue) and reverse bias (red). With TE thermionic emission, TFE thermionic field emission and FE field emission. For clarity only the conduction band is shown.

applied to the metal) electrons can flow easily from the semiconductor to the metal, whereas under reverse bias the current transport is suppressed. In a first approximation, the Schottky barrier height can be estimated by the Schottky-Mott rule as the difference between metal work function and semiconductor electron affinity

$$\Phi_B = \Phi_M - \chi_s \quad (2.9)$$

with Φ_B the Schottky barrier height, Φ_m the metal work function and χ_s the semiconductor electron affinity.

The Schottky-Mott rule is only valid for ideal metal-semiconductor junctions and does not consider the presence of surface states that lead to an effect called Fermi level pinning. In practice, the Fermi level pinning can have a significant impact on the junction properties, where a high density of surface states results in a pinning of the Fermi level to the surface state energy and thus making it independent of other material properties, such as the doping concentration. Therefore, it is crucial to precisely control the interface quality between both materials during device fabrication [104]. Typical values for the work functions of noble metals, such as Pt and Au, are in the range of 5-6 eV, whereas the electron affinity of SrTiO_3 and Ta_2O_5 is 3.9-4.1 and 3.3 eV respectively. For Pt/ SrTiO_3 and Pt/ Ta_2O_5 the theoretical Schottky barrier heights according to the Schottky-Mott rule are 1.8-2.0 and 2.6 eV. However, experimentally much smaller barriers are observed with 0.89 eV for Pt/ SrTiO_3 and 1.15-1.42 eV for Pt/ Ta_2O_5 , indicating a strong Fermi level pinning [46, 92].

Figure 2.4 c) depicts schematically the three conduction mechanism that describe the current

transport across a Schottky barrier for zero, forward and reverse bias. The figure illustrates the rectifying properties of the junction. Upon forward biasing, the energy of the conduction band is lifted and the barrier height decreases. This leads to an increased thermionic- and thermionic field emission. In the extreme case where the conduction band is lifted to energies exceeding the Schottky barrier height, electrons can flow freely from the semiconductor into the metal. In contrast, a reverse bias shifts the conduction band to lower energies. This allows for easier tunnelling of electrons from the metal into the conduction band of the semiconductor, due to a decreased tunnelling distance. For the reverse bias, the main current components are tunnelling currents via field emission and thermionic field emission. However, the tunnelling current is typically much smaller compared to the thermionic emission in forward direction, which gives rise to the rectifying properties of the Schottky junction.

Thermionic emission describes a process where electrons with sufficiently high thermal energy overcome the Schottky barrier directly. The resulting current density J_{TE} is given by

$$J_{\text{TE}} = A^* T^2 \exp \left[\frac{-q \left(\phi_B - \sqrt{qE/4\pi\epsilon_r\epsilon_0} \right)}{k_B T} \right] \quad (2.10)$$

$$A^* = \frac{4\pi q m^* k_B^2}{h^3} \quad (2.11)$$

with T the temperature, q the elemental charge, E the electric field, ϵ_r the optical dielectric constant, ϵ_0 the vacuum permittivity, $k_B T$ the Boltzmann constant. A^* is the effective Richardson constant with m^* the effective electron mass and h the Planck constant [105].

Importantly, J_{TE} depends exponentially on the temperature which makes it the dominant transport mechanism at high temperatures and under forward bias.

At low temperatures it is unlikely that electrons have enough thermal energy to overcome the Schottky barrier through thermionic emission. In this temperature regime the current transport occurs predominantly by field emission. In field emission, electrons near the Fermi level tunnel through the barrier. In contrast to a direct tunnelling process, in field emission an applied electric field deforms the Schottky barrier and increases the tunnel probability. This effect takes place predominantly under reverse bias. At an intermediate temperature regime, the current transport occurs by thermionic field emission, which represents a combination of field emission and thermionic emission. In thermionic field emission thermally excited electrons tunnel through a thinner part of the Schottky barrier.

In the context of resistive switching, the resistance changes are studied at a constant temperature and voltage regime. Therefore, an additional parameter needs to be considered that reversibly modulates the Schottky barrier and gives rise to the multiple resistance states of a device. This parameter is the doping concentration of the semiconductor. Considering that the thickness of the depletion region (i.e. the Schottky barrier thickness) is given by

$$W = \sqrt{\frac{2\epsilon_i V_{bi}}{qN_D}} \quad (2.12)$$

with ϵ the semiconductor permittivity, V_{bi} the built-in potential and N_D the doping concentration [106],

it is apparent that increasing doping concentration decreases the Schottky barrier thickness. This in turn increases the tunnelling currents. Therefore, the resistance change in metal oxide based ReRAM cells might be explained by a modulation of the doping concentration at the Schottky interface. A prominent candidate for the dopant species are oxygen vacancies as they are easily formed in oxides and typically have high mobilities. This enables a comparatively easy redistribution of oxygen vacancies under an applied electric field [107].

Electronic transport in bulk semiconductors

If the semiconductor film is very thin, e.g. in the low nanometer range, electrons can tunnel directly from metal to metal electrodes. In this case, the electronic transport inside the semiconductor can be neglected. However, the devices investigated within this thesis have semiconductor thicknesses from 5 to 80 nm. Therefore, it is necessary to consider a modulation of the bulk conduction as the origin of the switching phenomenon. The most prominent bulk conduction mechanism discussed for ReRAM devices are Poole-Frenkel emission, Hopping conduction and Ohmic conduction. In bulk conduction, one of the most important parameter is the material dependent trap energy level ϕ_T . In the following, a short overview over the different conduction mechanism will be given.

Poole-Frenkel emission conduction

Poole-Frenkel emission describes the transport phenomenologically as thermionic field emission of electrons from isolated trap states into the conduction band of the semiconductor.

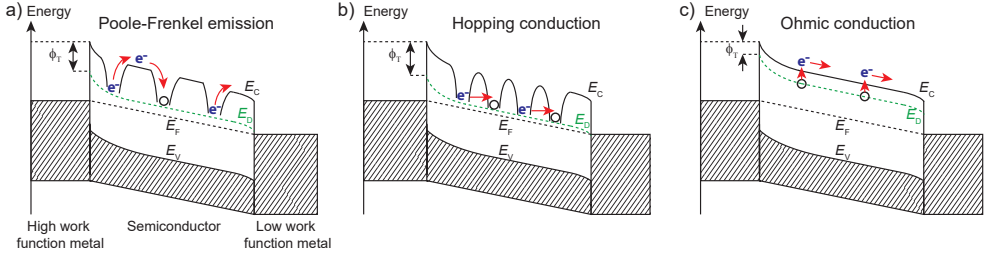


Figure 2.5: Schematic band diagram of metal-insulator-metal structures under forward bias, showing different bulk conduction mechanisms with a) Poole-Frenkel emission, b) Hopping conduction and c) Ohmic conduction. Trap states are shown as black circles, ϕ_T is the trap energy level and E_D is the energy level of the defect band.

The mechanism is depicted in figure 2.5 a). Accordingly, Poole-Frenkel emission is often observed at high temperatures and under high electric fields. After being released from the trap state the electron can move freely through the semiconductor until it relaxes into another trap state or reaches the electrode. The Poole-Frenkel emission current density J_{PF} is given by

$$J_{PF} = q\mu EN_C \exp \left[\frac{-q \left(\phi_T - \sqrt{qE/\pi\epsilon_i\epsilon_0} \right)}{k_B T} \right] \quad (2.13)$$

with μ the electron mobility, N_C the effective density of states in the conduction band, ϕ_T the trap energy level and ϵ_i and ϵ_0 the semiconductor and vacuum permittivity [105].

Hopping conduction

Hopping conduction is based on the tunneling process of electrons between neighboring trap sites. Hence, in hopping conduction the carrier energy can be smaller than the energy potential barrier between two trapping sites. The process is schematically depicted in figure 2.5 b). As Hopping is a tunnel process, it occurs predominantly in semiconductors with high trap densities and small tunnelling distances. Hopping transport is mostly observed in solids with a high degree of defects or disorder, such as amorphous oxides. If the electron localization is very strong electrons will tunnel from one trap to the nearest trap site in space. In this case the transport is called nearest-neighbor hopping. Alternatively, electrons might tunnel into trap sites farther away in space but closer in their energy level. This process is called variable-range hopping or Mott Hopping.

The Hopping current density J_{hop} is given by

$$J_{\text{hop}} = q2N(E_{\text{F}})k_{\text{B}}Tl\nu_{\text{ph}} \exp\left[-2\alpha l - \frac{W}{k_{\text{B}}T}\right] \sinh\left[\frac{q l F}{k_{\text{B}}T}\right] \quad (2.14)$$

with $2N(E_{\text{F}})k_{\text{B}}T$ the number of electrons per unit volume within a range $k_{\text{B}}T$ from the Fermi energy, l the hopping distance, ν_{ph} the vibrational phonon frequency, α the decay length of the localized electron wave function in reciprocal space, W the average site-to-site energy difference and F the applied electric field [108].

Nearest-neighbor hopping is expected if the localization radius of the electron wave function is much smaller than the average hopping distance to a nearest neighbor ($\alpha l \gg 1$). If αl is larger or close to unity, variable-range hopping occurs. According to Mott's law, the temperature-dependent conductivity for variable-range hopping is expected to follow

$$\sigma = \sigma_0 \exp\left[-\left(\frac{T_0}{T}\right)^{1/(d+1)}\right] \quad (2.15)$$

with d the dimensionality in space of the system. In case of a current transport through a switching filament, d can be equal to 1, 2 or 3, depending on the lateral size of the filament and the semiconductor thickness.

Ohmic conduction

Ohmic conduction is observed if mobile charge carriers are present, i.e. electrons in the conduction band or holes in the valence band which can migrate freely under an applied electric field (compare figure 2.5 c). As the transport of current occurs via the conduction- or valence-band, it is sometimes referred to as band-like transport. This conduction mechanism is characterized by a linear current-voltage relationship. The Ohmic current density J_{ohm} is given by

$$J_{\text{ohm}} = \sigma E = q\mu EN_{\text{C}} \exp\left[\frac{-(E_{\text{C}} - E_{\text{F}})}{k_{\text{B}}T}\right] \quad (2.16)$$

with σ the electrical conductivity, μ the charge carrier mobility, N_{C} the effective density of states in the conduction band and $E_{\text{C}} - E_{\text{F}}$ the energy difference between the bottom of the conduction band and the Fermi energy [105].

For intrinsic dielectrics with a large bandgap, the contribution of Ohmic current is negligible as the amount of free charge carriers is small. However, extrinsic dopants or oxygen vacancies can have significant impact on the charge carrier density if the dopant energy level is shallow, i.e. close to the conduction- or close to the valence-band for electrons and holes respectively. Here, the term shallow means that the thermal energy $k_B T$ is large enough to ionize a substantial amount of defects, leading to a high carrier density. Ohmic conduction is particularly interesting in the context of resistive switching, as often a linear current-voltage relationship is observed in the low resistance state of memristive devices.

2.4 Resistive switching in valence change materials

The resistive switching phenomenon describes the reversible change of the electrical resistance in a metal-insulator-metal structure upon electrical biasing. Switching occurs between two or more resistive states, the so-called low and high resistance state (LRS and HRS respectively). If the resistance can be tuned continuously between LRS and HRS, the switching is referred to as analog switching.

Since its discovery in the mid 1960s, resistive switching was observed in a vast amount of materials ranging from oxides, organic molecules, phase change and two-dimensional materials. Likewise, the underlying mechanism that give rise to resistive switching are manifold. This thesis focuses on the investigation of transition metal oxide devices that are believed to operate based on the valence change mechanism (VCM) [4, 6]. This mechanism describes resistive switching through an internal redistribution of mobile dopants under an external electric field. In general, a so-called electroforming step is necessary to bring the initially insulating MIM structure into a switchable state by applying a comparatively high bias to the system. It is suspected that during the electroforming step oxygen anions drift along the electric field direction, are removed from the oxide lattice and leave behind a oxygen vacancies. For each removed oxygen anion, two electrons remain in the oxide causing a valence change of the metal cation. Therefore, oxygen vacancies can be considered as n -type dopant. Depending on the exact device structure the removed oxygen might be accommodated in an oxidizable electrode, leave the system as molecular oxygen or is stored as atomic oxygen inside an inert electrode. Typically, the electroforming process is confined to a small region within the device area, giving rise to its name filamentary switching. Once an oxygen vacancy rich filament has been formed, the application of a smaller electric field enables the redistribution of oxygen anions through ionic drift processes. Hence, switching in VCM type devices can be seen as formation (SET) and rupture (RESET) of an oxygen vacancy rich filament. Per definition, filamentary switching shows no scaling between the LRS and the device area.

VCM-type cells can be classified into unipolar and bipolar resistive switching modes. If the SET and RESET operations are performed with a single voltage polarity, the switching is classified as unipolar. If two opposite polarities are required it is termed bipolar switching. Bipolar switching can be further subdivided into the so-called counter-eightwise and eightwise switching polarities, depending on the voltage polarity that is needed to perform the SET and RESET operation. The terms refer to the cycling direction in which the resistance hysteresis traverses. If it is resembling the drawing direction of the handwritten number eight, it is defined as eightwise switching. In the opposite case is termed counter-eightwise switching. In order to unambiguously apply this terminology to various device layouts, the voltage polarity is always referenced to the Schottky-type interface. If a metal-insulator-metal structure has Schottky barriers at both interfaces or no Schottky barrier at all, no switching polarity can be assigned.

Both material systems investigated in this thesis show bipolar resistive switching and have well defined asymmetric device structures with one Ohmic and one Schottky interface. In the following, the existing knowledge and the suspected mechanism for eightwise switching in SrTiO_3 and counter-eightwise switching in Ta_2O_5 will be introduced.

Eightwise resistive switching in SrTiO_3

SrTiO_3 is arguably one of the most intensively studied resistive switching materials. Due to its well understood defect chemistry, its availability in form of single crystalline substrates and the possibility to grow epitaxial thin films free from extended defects, it is a perfect model material to investigate and simulate resistive switching. Depending on the electrode choice, growth method and electrical treatment, resistive switching in SrTiO_3 can exhibit eightwise, counter-eightwise or coexisting switching polarities. To give an overview of the extensive literature about resistive switching in SrTiO_3 , table 2.1 compares the switching characteristics of various device structures and fabrication methods. From the table it can be seen, that the switching polarity is closely related to the crystallinity of the SrTiO_3 film. For epitaxial devices, a predominantly eightwise switching is observed, whereas polycrystalline and amorphous thin films show counter-eightwise polarities. The implications of this observation will be discussed in more detail in chapters 5 and 6.

In the following, the proposed eightwise switching mechanism for single crystalline SrTiO_3 devices will be introduced. Counter-eightwise switching in SrTiO_3 is believed to follow the same mechanism as switching in Ta_2O_5 , which will be discussed in section 2.4.

Table 2.1: Selection of published work on SrTiO₃ based memristive devices. SrTiO₃ thin films were deposited by molecular beam epitaxy (MBE), pulsed laser deposition (PLD), reactive sputter deposition or atomic layer deposition (ALD).

Reference	Deposition	Device stack	Crystallinity	Polarity
Mikheev 2015 [109]	MBE	Nb:SrTiO ₃ /SrTiO ₃ /Pt	single crystal	8w
Bäumer 2015 [110]	PLD	Nb:SrTiO ₃ /SrTiO ₃ /Pt	single crystal	8w
Bourim 2014 [111]	Verneuil	Nb:SrTiO ₃ /Pt	single crystal	8w
Shibuya 2010 [112]	PLD	Nb:SrTiO ₃ /Sr ₂ TiO ₄ /Au	single crystal	8w or c8w ¹
Münstermann 2010 [113]	PLD	Nb:SrTiO ₃ /Fe:SrTiO ₃ /Pt	single crystal	8w & c8w ²
Fleck 2014 [114]	Sputter	Ti/SrTiO ₃ /Pt	amorphous	c8w
Nili 2015 [115]	Sputter	Ti/SrTiO ₃ /Pt	amorphous	c8w
Jiang 2020 [116]	Sputter	Ag/Fe:SrTiO ₃ /Pt	amorphous & polycrystalline	c8w
Aslam 2014 [117]	ALD	TiN/SrTiO ₃ /Pt	polycrystalline	c8w
Choi 2014 [118]	ALD	Pt/SrTiO ₃ /Pt	polycrystalline	–

¹ Thin films grown at low temperature exhibited c8w and at high temperatures 8w polarities.

² The polarity could be defined by the magnitude of the applied voltage.

The VCM switching model for eightwise switching in epitaxial Nb:SrTiO₃/SrTiO₃/Pt thin film devices was introduced by Bäumer *et al.* and is depicted in figure 2.6 [119]. **Ⓐ**: In the LRS, an oxygen vacancy rich filament connects the Nb:SrTiO₃ bottom- with the Pt top electrode. Importantly, the oxygen vacancy concentration at the SrTiO₃/Pt Schottky interface is high. The increased donor concentration at the interface reduces the Schottky barrier height and width and current can flow easily through the Schottky junction. The device is in the LRS. **Ⓑ**: Upon applying a negative bias to the Pt electrode, positively charged V_O^{••} drift towards the negatively charged electrode where they recombine with molecular oxygen according to the following RESET reaction



The electrons that are consumed by this reaction stem from the conduction band and the concentration of free charge carrier decreases. The oxygen that is required for this reaction originates from the surrounding atmosphere. Besides molecular oxygen also oxygen containing species, e.g. H₂O and hydroxyls, can serve as potential oxygen source [120]. **Ⓒ**: After most V_O^{••} are filled, the Schottky barrier height and thickness increases, which limits the current flow significantly. The device is now in the HRS.

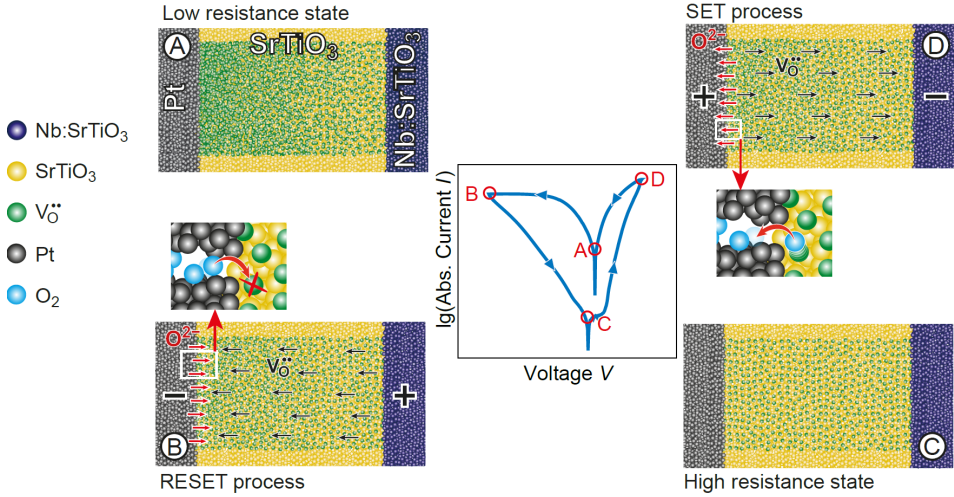


Figure 2.6: Schematic illustration of eightwise switching mechanism in SrTiO_3 .¹ (A) The device is in the LRS with a high oxygen vacancy concentration at the SrTiO_3/Pt . (B) RESET of the device. Inset: O_2 molecules are incorporated into the SrTiO_3 film filling oxygen vacancies. (C) HRS of the device with fewer oxygen vacancies at the interface. (D) SET process at positive voltages. Inset: O^{2-} anions are removed from the lattice leaving oxygen vacancies behind. Modified from ref. [119].

(D): Reversing the polarity by applying a positive voltage to the Pt electrode attracts negatively charged O^{2-} anions. At the interface, the oxygen anions are oxidized to molecular oxygen and leave the oxide as described in the SET reaction



Going beyond this graphical model, the eightwise switching I - V characteristics can be accurately simulated using a numerical model of electron diffusion combined with a Schottky-contact barrier model [25, 121]. Experimental evidence for the creation of oxygen vacancy rich filaments during resistive switching in SrTiO_3 could be obtained from photoemission electron spectromicroscopy and transmission electron microscopy [28, 110]. An unique feature of the switching model is the exchange of oxygen with the surrounding atmosphere (compare equations 2.17 and 2.18). Using oxygen isotope labeling experiments combined with secondary ion mass spectrometry, it was verified that the switching process in SrTiO_3 relies on the exchange of oxygen between the oxide film and the atmosphere [120].

¹Here it is noted that the current is shown in a logarithmic representation. Therefore, the I - V curve does not resemble the handwritten number "8". A switching curve in a linear representation with the characteristic "8" shape is shown in figure 5.1 c).

In addition to the here presented switching model, alternative models have been proposed to explain eightwise switching in SrTiO₃, such as trapping and de-trapping of electrons within interface defect states [109,122], local inversion of the doping character [113], or the presence of a potential barrier at the Nb:SrTiO₃/SrTiO₃ interface [123]. While these models are capable to explain some of the experimental evidence, only the model proposed by Bäumer *et al.* can conclusively describe all observations [119].

A common feature of all models is their description of the switching process as intentional manipulation of point defects. Although the point defect model successfully describes the essence of the switching process, i.e. the resistance change between HRS and LRS, it is not suited to explain other device characteristics such as device-to-device variability, retention failure and ageing effects. Improving these device characteristics, especially the uniformity, is still a major roadblock that needs to be overcome for a technological implementation [2, 22]. Such device properties are often associated with the microscopic film structure of the switching oxide [67]. Accordingly, in chapter 5 and 6 the influence of extended defects and the underlying mechanism will be investigated in detail.

Counter-eightwise resistive switching in Ta₂O₅

Counter-eightwise switching is the predominant switching polarity in most transition metal oxides, such as Ta₂O₅ [7], HfO₂ [124], ZnO [125], MnO₂ [126], TiO₂ [127] and ZrO₂ [128]. Especially, Ta₂O₅ and HfO₂ are of highest technological interest as they are CMOS-compatible and show excellent switching properties for logic and memory applications.

A switching model for the counter-eightwise polarity was proposed by Menzel *et al.* and is shown in figure 2.7 [129]. During the electroforming step, a filament composed of V_O^{••} is generated across the oxide film. **(A)**: The electroformed device in the HRS. The filament is mostly intact but the V_O^{••} concentration is depleted at the Ta₂O₅/Pt interface. This depletion region is called "disc" and the bulk filament is termed "plug". In the HRS, the disc region is large and it limits the current flow through the device. **(B)**: By applying a negative bias to the Pt electrode, positively charged V_O^{••} from the plug drift towards the Schottky interface. Consequently, the disc region is reduced and the device is SET. **(C)**: The V_O^{••} concentration is high throughout the oxide and current can flow easily between both electrodes. The device is in the LRS. **(D)**: A positive voltage at the Pt electrode repels V_O^{••} and the disc region increases. The device is RESETs to the HRS. Importantly, the counter-eightwise model is based on a purely internal redistribution of oxygen vacancies and is therefore clearly distinguishable from the eightwise model.

Counter-eightwise switching can be accurately simulated by a numerical drift-diffusion model of electronic and ionic transport combined with a Schottky contact barrier [24]. Neverthe-

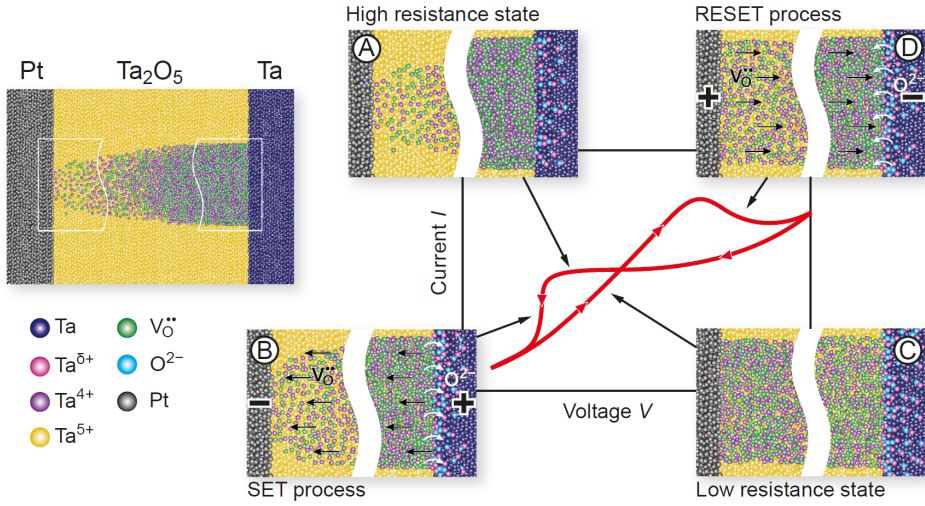


Figure 2.7: Schematic illustration of the counter eightwise switching mechanism. **(A)** The electroformed device is in the HRS which features a low oxygen vacancy concentration at the $\text{Ta}_2\text{O}_5/\text{Pt}$ interface. **(B)** SET process of the device. **(C)** LRS of the device with a high concentration of oxygen vacancies at the interface. **(D)** RESET process at positive voltages. Modified from ref. [129].

less, direct experimental evidence for the creation of oxygen vacancy rich filaments is scarce. Especially, mapping filaments in different resistive states has turned out to be an exceptionally challenging task due to their small size in the order of 10 to 100 nm [36, 130, 131]. This restricts the spectroscopic characterisation of filaments to techniques with high spatial resolution, such as transmission electron microscopy. For larger filament structures in the micrometer region, photoemission electron microscopy provided evidence for oxygen deficient filaments [132]. However, it is not clear if the results are transferable to nanometer sized filaments that are formed at lower electric fields.

With detailed information about the chemical composition of nanometer sized filaments being inaccessible so far, many studies have focused on alternative techniques to obtain information about conductive filaments. A common approach is the temperature dependent characterization of the current transport in memristive devices [133, 134]. As discussed in section 2.3, different conduction mechanisms have distinct temperature dependencies. Therefore, it is possible to gain information about the physical properties of conductive filaments by electrical transport measurements. Unfortunately, the interpretation of the results is often ambiguous. The conduction in Ta_2O_5 resistive switching devices was extensively studied and is described by a variety of different conduction mechanisms, including: Phonon-assisted tunnelling between traps [94], variable range and nearest neighbour hopping [86, 133], Efros-Shklovskii variable range hopping [134], percolation through metallic Ta clusters [135] and Poole-Frenkel emission

[136, 137].

Besides the electronic conduction mechanism, there is also no consensus about the underlying switching mechanism. Although the here presented switching model of an internal redistribution of oxygen vacancies is widely accepted in the scientific community [4, 22], new models were recently proposed that are based on the thermophoresis effect. In this model, resistive switching is described through a lateral diffusion of oxygen or tantalum [38, 39, 138, 139]. Accordingly, detailed information about the composition and electronic structure of switching filaments is indispensable to clarify the physical origins of the resistive switching effect in Ta_2O_5 . Therefore, it is attempted in chapter 6 to experimentally shed light on the nature of switching filaments.

3 Experimental methods

In this thesis, memristive devices based on SrTiO₃ and Ta₂O₅ thin films were fabricated and characterized. SrTiO₃ films were deposited via pulsed laser deposition and Ta₂O₅ films were grown by reactive sputter deposition or plasma oxidation. In this chapter the deposition processes, device fabrication and the most important spectroscopic techniques will be introduced.

3.1 Pulsed laser deposition

Pulsed laser deposition (PLD) is a deposition technique for the growth of complex oxide thin films through a laser induced ablation of material from a target. A detailed description of the PLD process is given in refs. [140,141]. In this work, single crystalline SrTiO₃ thin films with various degrees of defect densities were fabricated. All SrTiO₃ films were grown on 0.5 wt%-Nb:SrTiO₃ single crystal substrates (*Crystec GmbH*, Germany). As target served a nominally pure SrTiO₃ single crystal. The target was ablated using a KrF excimer laser ($\lambda = 248$ nm) with a repetition rate of 5 Hz and a spot size of 2 mm² at a target-to-substrate distance of 44 mm. The laser fluence was varied between 0.67 and 1.01 J/cm². The samples were grown in an oxygen atmosphere of 0.1 mbar at a substrate temperature of 550-800°C. Film growth was monitored using reflection high-energy electron diffraction. The thin film cation stoichiometry was tuned through the choice of the laser fluence. This effect is discussed in detail in refs. [142] and [143]. By growing at low temperatures of 550°C, extended defects were introduced into the thin film, as will be discussed in more detail in chapter 4.

3.2 Radio frequency magnetron sputter deposition

Sputter deposition is a physical vapor deposition technique that is used to deposit thin films by sputtering material from a target. In magnetron sputtering, a magnetron discharge ignites and sustains a plasma by applying a high voltage between target and substrate. The plasma ions are accelerated by the electric field towards the target. Upon bombardment of the target, material is removed from the surface via sputtering processes and deposits on the substrate

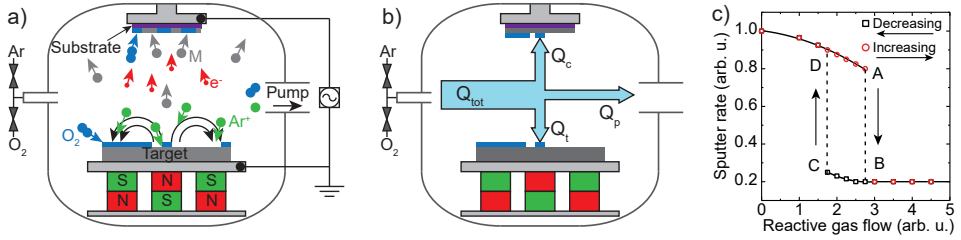


Figure 3.1: a) Schematic of a radio frequency reactive sputtering system. b) Flow and reactive gas consumption in the system, with Q_c consumption of the collecting area, Q_t consumption of the target area and Q_p the fraction of reactive gas that is pumped out of the system. c) Typical experimental curve of the sputter rate as a function of reactive gas flow (modified from ref. [144]).

and the process chamber. In addition, electrons are emitted during the ion bombardment, which further ionize gas atoms that help to sustain the plasma. Besides metals also metal alloys and complex oxide can be used as sputter target. This offers the possibility to deposit a wide range of complex materials. By introducing a reactive gas during the sputtering process, it is possible to deposit a compound material. Depending on the used reactive gas it is possible to form oxides, nitrides, carbides and others. Due to the chemical reaction that takes place during the deposition, it is commonly referred to as *reactive sputtering*. If the formed compound is electrically insulating, it is beneficial to operate in a so-called radio frequency (RF) mode. In contrast to the direct current (DC) operation mode, the polarity of the applied electric field is alternated at a radio frequency of 13.56 MHz. This allows the neutralization of accumulated positive charges on the substrate. Using a RF sputtering process it is possible to deposit high quality insulating thin films such as Al₂O₃, SiO₂ and Ta₂O₅. In this work, an ultra high vacuum (UHV) sputter tool from *SURFACE systems + technology GmbH*, Germany was used. The base pressure of the process chamber is 1·10⁻⁸ mbar. As process gases argon, oxygen and a mixture of 1% O₂ in argon was used. A principle scheme of the sputter tool is shown in figure 3.1 a).

Due to the large number of adjustable process parameters, it is difficult to control and optimize reactive sputter processes. One of the main obstacles for the deposition of thin films with defined oxygen stoichiometries, is the deposition rate dependency on the reactive gas flow [144]. To understand this behavior, it is necessary to consider the reactive gas consumption during the deposition. Figure 3.1 b) depicts the three possible consumption pathways Q_c , Q_t and Q_p for the total flow Q_{tot} of reactive gas in the system. Q_c describes the consumption at the collecting area, namely the substrate and chamber walls. Q_t specifies the consumption at the target surface and Q_p is the fraction of reactive gas that is pumped out of the system. The consumption of the reactive gas Q_c and Q_t is a result of a chemical reaction between the sputtered material and the reactive gas to form a stable solid. Thus, the sputtered material is effectively acting as a sublimation pump. The situation is further complicated by the fact

that the formed compound material has generally a much lower sputter yield compared to the pure target. This gives rise to a hysteric behavior between sputter rate and reactive gas flow as shown in figure 3.1 c). Sputtering with a reactive gas flow of zero yields a high sputter rate, as the target is in its metallic form. Upon increasing the reactive gas flow to point A, the sputter rate drops as an increasing part of the target surface reacts with the gas and forms a compound with lower sputtering yield. At the point A, a critical gas flow is reached where the complete target surface is covered by the compound material. The sputtering rate drops to point B, which in turn decreases the reactive gas consumption of Q_c , as less material is deposited on the collecting area. Accordingly, the partial pressure of the reactive gas abruptly increases at the transition from A to B. Therefore, sputtering under high reactive gas flows occurs from a fully reacted target surface. Deposition under these conditions is sometimes referred to as sputtering from a "poisoned" target. Reducing the reactive gas flow up to point C partially removes the surface compound on the target as the reactive gas concentration is too low to fully saturate the newly forming metallic target surface. Again, an avalanche like transition from point C to point D is observed that indicates the transition from a poisoned to a metallic target mode.

In the poisoned target mode, the deposition yields in general stoichiometric thin films. Sputtering in the metallic target mode, however, allows the growth of sub-stoichiometric films. In addition to the reactive gas flow, further parameters can be optimized, such as the target to substrate distance, sputter power, pump speed and total process pressure. A detailed study of the sputter power and process pressure for the deposition of TaO_x thin films will be presented in chapter 4.

3.3 Device fabrication and electrical characterization

Depending on the desired device properties, samples have to fulfill various requirements. It is often necessary to be able to contact devices via microprobes, through wire or manual bonding. Furthermore, the device fabrication on single crystalline substrates or the usage of graphene electrodes requires individually adjusted fabrication schemes. Therefore, a variety of different device stacks and sample geometries have been employed and developed in this thesis. In the following section, the fabrication of different samples is presented and their advantages and disadvantages are discussed. All fabrication details and deposition parameter are listed in the appendix.

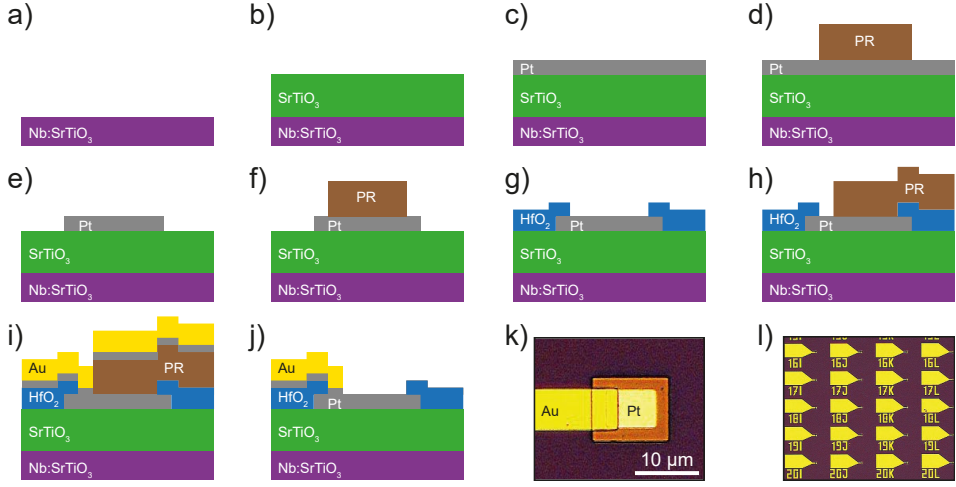


Figure 3.2: Sample fabrication of SrTiO₃ devices contacted by metal leads. a) Nb:SrTiO₃ single crystalline substrate serving as bottom electrode. b) Deposition of a SrTiO₃ thin film via PLD. c) Electron beam evaporation of the Pt top electrode. d) Lithography to define the top electrode area followed by e) ion beam etching and lift-off of the photoresist (PR). f) Partial covering of the electrode area by photoresist and g) deposition of an HfO₂ insulating layer with subsequent lift-off process. h) Final lithography step to define the metal contacts. i) Electron beam deposition of the Pt/Au contact leads and j) lift off of the remaining photoresist. k) Optical microscope image of a single device and l) device arrangement on the sample.

Noble metal top electrodes for electrical characterization and delamination

For metal-insulator-metal structures with noble metal top electrodes, a 30 or 80 nm Pt or Au layer was electron-beam evaporated onto as-prepared oxide thin films. The top electrodes were structured into square pads with areas ranging from 100×100 down to $5 \times 5 \mu\text{m}^2$ through optical lithography and dry etching in an Ion Beam Etching tool (*Ionfab 300plus*, *Oxford Instruments*). This sample architecture can be used for electrical characterization via microprobes and for top electrode delamination experiments. Direct contact of the microprobes with the top electrode restricts their use to electrical measurement set-ups with soft probe needles. Furthermore, significant contact resistance might be observed between top electrode and the probe tip, which can hinder a quantitative analysis of the device characteristics.

SrTiO₃ devices with metal contact leads for *in operando* electron microscopy

SrTiO₃ devices with metal contact leads were fabricated to allow the electrical addressing of devices in transmission electron microscopes. The fabrication scheme is shown in figure 3.2. Because the samples are fabricated on a continuous bottom electrode, that can not be

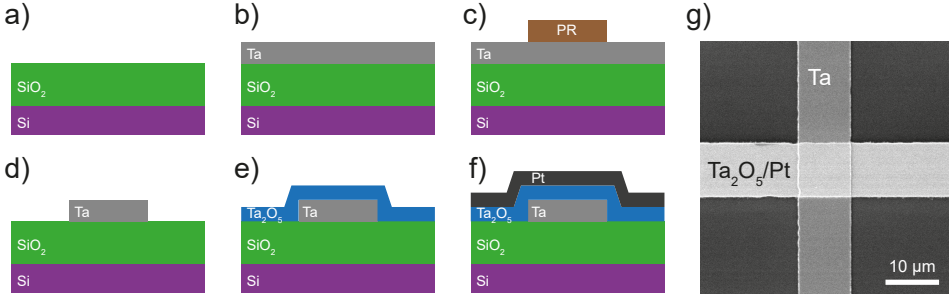


Figure 3.3: Sample fabrication of Ta_2O_5 crossbar devices. a) Si/ SiO_2 substrate. b) Sputter deposition of the Ta bottom electrode. c) Lithography to structure the bottom electrode and d) ion beam etching and lift-off of the photoresist. e) Reactive sputter deposition of the Ta_2O_5 switching layer. f) Electron beam evaporation of the Pt top electrode. g) Electron microscopy image of a finished crossbar device after a final lithography and etching step.

easily structured, a crossbar device structure can not be used. Hence, an insulating layer is added between the contact leads and the switching layer. The final result is a sample that features individually addressable devices with small device areas and large contact pads on a continuous bottom electrode. This device design allows for electrical contact via wire or manual bonding by hand using silver paste and aluminium wire. This sample architecture can be used for a wide variety of electrical and microscopic characterization. The metal leads minimize the contact resistances and allow for an accurate and reproducible electrical characterization. Further, contacting with hard piezo-controlled probe needles is possible, which enables operation in enclosed systems. The drawback of this device structure is the overlap between contact lead and top electrode. For surface sensitive techniques, e.g. photoelectron spectroscopy, this overlap region is intransparent. Coincidentally, switching often takes place in this overlap region, impeding the characterization of the switching induced changes.

Ta_2O_5 crossbar devices for atmosphere dependent electrical characterization

To investigate the atmosphere dependence of Ta_2O_5 based devices, crossbar samples were fabricated according to Figure 3.3. The sample stacks were designed in a way so that the $\text{Ta}_2\text{O}_5/\text{Pt}$ interface is in contact with the ambient atmosphere. The benefit of this stack sequence is to maximize the influence of the atmosphere on the active Schottky interface. Further, Pt electrodes can be fabricated as thin layer (down to 3-6 nm) while Ta electrodes need to exceed 10 nm to achieve a sufficient conductivity. Accordingly, the thin electrode further facilitates exchange of oxygen species with the atmosphere. With the Schottky interface at the top part of the stack, characterization of the interface using surface sensitive techniques is possible. The viability of this approach was successfully tested with electron beam-induced

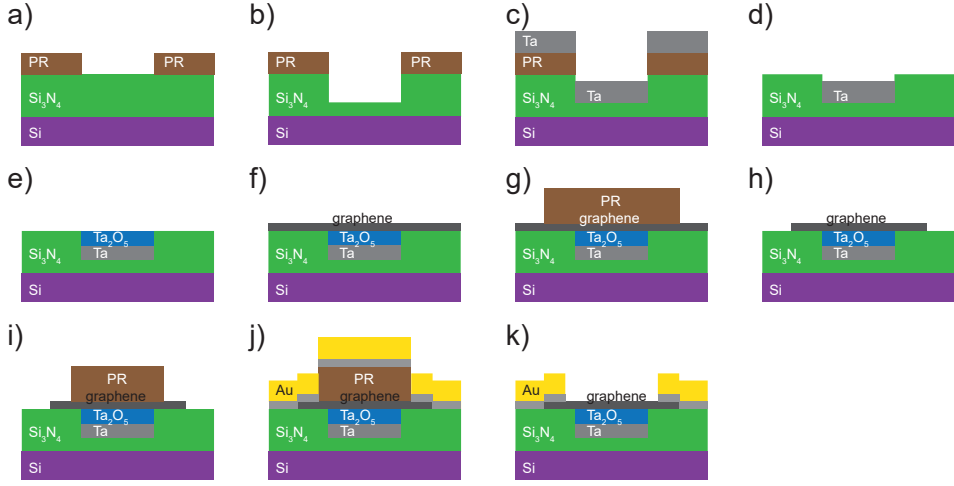


Figure 3.4: Sample fabrication of graphene crossbar devices. a) Si_3N_4 substrates after lithography to define the bottom electrode. b) RIBE etching of trenches. c) Filling the trenches with Ta by sputter deposition and d) lift-off of the photoresist. e) Partial oxidation of the Ta layer by an oxygen plasma treatment. f) Graphene deposition onto the flat substrate. g) The desired top electrode area is protected by photoresist. h) Structuring of the graphene electrode using oxygen plasma and subsequent photoresist lift-off. i) The majority of the graphene electrode is covered by photoresist only leaving the graphene edges exposed. j) Metallic leads are evaporated to contact the graphene electrode. k) Final device structure after photoresist lift-off

current imaging¹.

Ta_2O_5 graphene crossbar devices for *in operando* spectroscopy

Graphene crossbar devices were designed to achieve photoelectron transparent top electrodes. A crossbar structure was chosen to allow the imaging of the complete device area with spectromicroscopic techniques. The fabrication process is schematically shown in figure 3.4. To fabricate flat crossbar structures, 40 nm deep trenches were etched into Si_3N_4 substrates via reactive ion beam etching (RIBE) using CF_4 as process gas. Si_3N_4 was chosen as substrate material because it is sufficiently insulating to prevent shortcuts. However, it is not as insulating as SiO_2 , which reduces charging effects in spectroscopy experiments. Furthermore, Si_3N_4 is an oxygen free insulator, which enables the measurement of the O *K*-edge absorption spectrum of the device without interference of the substrate. Afterwards, the trenches were filled by an approximately 38 nm thick metallic Ta bottom electrode via sputter deposition. Note that the trenches have not been filled completely to account for the film expansion during

¹More details on this topic can be found in the Masters thesis of Kalle Goß, Peter Grünberg Institute, Forschungszentrum Jülich GmbH, Jülich, Germany.

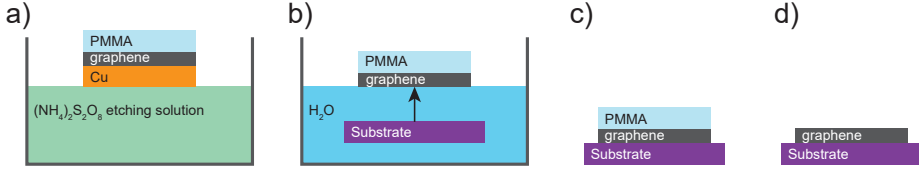


Figure 3.5: Wet graphene transfer process onto arbitrary flat substrates a) Copper etching in an aqueous $(\text{NH}_4)_2\text{S}_2\text{O}_8$ etching solution. b) The graphene/PMMA stack is picked up with a flat substrate. c) Transferred graphene/PMMA stack after removal from water and drying. d) Finished graphene transfer after dissolving the PMMA layer in organic solvents.

the oxidation process in the next step. The resistive switching oxide layer was produced by partially oxidizing the metallic Ta bottom electrode in an oxygen plasma. The resulting oxide thicknesses varied from 4-9 nm depending on the used process power (compare figure 4.5). Plasma oxidation was chosen above sputtered Ta_2O_5 films as it increases the hydrophilicity of the substrate, which is beneficial for the adhesion and stability of the transferred graphene. However, also devices with sputtered Ta_2O_5 were fabricated and showed similar switching properties. Monolayer graphene was deposited directly after the plasma treatment and patterned via photolithography and oxygen plasma etching. The transfer process is discussed in detail below. In a final step, the graphene electrodes were contacted via metallic leads. Different combination of metals have been tested to achieve good adhesion to the substrate while minimizing the contact resistance to the graphene top electrode. 5 nm Ti followed by 70 nm Au gave good contact but had poor adhesion to the substrate resulting in partial delamination of the leads. The optimal material combination was found to be 10 nm Pt followed by 70 nm Au possessing excellent adhesion and little contact resistance.

PMMA supported graphene transfer

Transfer ready monolayers of graphene on copper were purchased from *Graphenea, San Sebastian, Spain*. A poly(methyl methacrylate) (PMMA) layer was spincoated onto the graphene layer to support and protect the graphene against mechanical stress during the transfer process. The copper substrate was etched in a 0.1 mol L^{-1} $(\text{NH}_4)_2\text{S}_2\text{O}_8$ etching solution for 3-20 h (see figure 3.5). After completion of the etching process, the etching solution is replaced with purified water. Afterwards, the plasma treated substrate is submerged into the water and lifted to pick up the graphene/PMMA stack. After removing most of the access water at the substrate/graphene interface using a N_2 spray gun, the sample is annealed at 50, 100 and 150 °C for 30 min respectively to further dry and improve the graphene/substrate adhesion. In a final step, the PMMA layer is dissolved in an organic solvent, rinsed in isopropyl alcohol and N_2 blow-dried. Several solvents have been studied to obtain the cleanest graphene surface, free of PMMA residues. However, complete removal of PMMA was impossible using only solvents.

Table 3.1: Typical switching parameters for different materials and device stacks. For some samples the switching parameters may differ.

Switching Parameter	SrTiO ₃	Ta ₂ O ₅ /(Pt, Au)	Ta ₂ O ₅ /Graphene
Forming voltage (V)	+5	-2 to -4	-4 to -7
SET current compliance	5 to 50 mA	10 μ A to 5 mA	1 μ A to 2 mA
SET voltage (V)	+4	-2 to -3	-2 to -5
RESET voltage (V)	-4	+2 to +3	+3 to +5

Best results were obtained using concentrated acetic acid (98 %) at elevated temperatures of 80 °C for 3 h. Further increasing the process time did not improve the surface quality and even led to delamination of graphene in some cases. The remaining PMMA particles are likely composed of highly cross-linked polymer particles that are insoluble due to their high atomic mass. Annealing treatments at several hundred °C in inert atmospheres (Ar/H₂) can effectively remove left over PMMA. However, it is not possible to use heat treatments on this type of devices, as the Ta₂O₅ layer is reduced during the process and the device loses its switching properties. Overall the PMMA contamination on the graphene layers had only minor effects on the spectromicroscopic characterization.

Electrical characterization

Noble metal top electrodes were directly contacted with tungsten whisker probes, while the continuous bottom electrode was contacted by aluminium wire bonding. For graphene samples and samples with evaporated leads, the devices were contacted via tungsten whisker probes for *ex situ* experiments and via aluminium wire bonding for *in situ* experiments. For SrTiO₃ based devices, the Nb:SrTiO₃ substrate served as electrically grounded bottom electrode and for Ta₂O₅ devices, a 30 nm thick metallic Ta film was used as bottom electrode. *I-V* sweeps and pulse measurements were performed with a *Keithley 2611(A-B) Source Meter*. All *I-V* sweeps were performed by ramping the voltage from 0 V to the forming, SET or RESET voltage or until the current compliance is reached. Table 3.1 displays typical switching parameters used in this work. The step size was 20 mV and the holding time before measurement was 5 ms. The current compliance for forming and SET is specified for each device under consideration. For both materials, SrTiO₃ and Ta₂O₅, no current compliance was needed during the RESET. The device resistance was obtained from the slope of a linear fit of read-out sweeps between +0.2 and -0.2 V, or in case of pulse measurements, at a read-out voltage of 0.2 V.

Temperature-dependent conduction measurements from 80 to 350 K were performed using a *CRX-VF Cryogenic Probe Station, Lake Shore Cryotronics Inc.*. The probe station was equipped with a turbo molecular pump, allowing to reach pressures of 7×10^{-6} mbar.

Atmosphere-dependent switching experiments were conducted in a home-built *Mark-II* probe station. Turbo molecular pumping and gas inlets enabled switching in vacuum, N₂, Ar/H₂ and O₂ atmospheres between 5×10^{-6} mbar and 1 bar.

Sheet resistances were measured in a standard Van-der-Pauw configuration by contacting the four corners of a square 1×1 cm² sample via ultra-sonic Al wire bonding using a *Hall Effect Measurement System Model 8404*, Lake Shore Cryotronics Inc.

3.4 Conductive atomic force microscopy

The combined AFM/C-AFM measurements were performed using a *VT-SPM system*, *Scienta Omicron GmbH, Tautausstein, Germany* operating at room temperature under UHV conditions. The detection of the local surface conductance was achieved using silicon cantilevers with a boron doped polycrystalline diamond coating. The cantilever tips had a nominal radius of less than 150 nm and a spring constant of 25 N m⁻¹ (AppNano, DD-ACTA-10).

3.5 X-ray absorption spectroscopy

X-ray absorption describes the interaction of a solid with high energetic electromagnetic irradiation. If an X-ray photon is absorbed by a solid, an electron can be promoted from an occupied into an unoccupied excited state. This transition can only occur if the photon energy is larger than the energy gap between the initial and final state. This gives rise to the so-called absorption edges, where a strong increase in absorption is observed if the photon energy becomes sufficiently large to overcome the energy gap. As both, the initial and final state are dependent on the local electronic structure of the atoms in the solid, X-ray absorption spectroscopy (XAS) can be used to measure the energy depended absorption and investigate the electronic structure of a given sample. In contrast to diffraction based techniques, such as X-ray diffraction, XAS is sensitive to the near range order and thus can also be employed on amorphous solids. In an XAS experiment, the absorption is measured as a function of photon energy. Therefore, a photon source with continuously tunable energy is required. Such photon sources, that also have a high brilliancy and intensity, are available at soft X-ray beamlines at most modern synchrotron. Classically, the absorption was measured by shining the X-ray beam through a thin (few tens of micrometers) specimen and measure the decrease in intensity of the beam after it passed through the sample. However, there are several limitations to this approach. First, the sample needs to be fabricated on thin substrates or membranes, making them prone to mechanical stress and altering their electrical behavior due to a missing heat

sink. Second, the measured absorption is averaged over the whole specimen thickness making it difficult to study changes that occur only in a thin part of the specimen. To overcome these limitations, many modern XAS beamlines can operate in a so-called total electron yield mode. Here, the electron current leaving the sample is measured. This mode takes advantage of the effect that the photon absorption is often accompanied by photoelectron emission processes via the Auger effect. After excitation of an electron into an unoccupied state, it leaves behind an electron core hole. This core hole can be filled by electrons in higher energy shells and the energy difference is transferred to a second electron, increasing its kinetic energy. The excited electron moves through the solid, interacting with additional electrons via elastic and inelastic scattering processes. The latter process generates low energy secondary electrons, which in turn might further scatter inelastically. This cascading process leads to the generation of a large number of low energy electrons. If their energy is sufficient to overcome the work function of the solid, they can leave the sample and be detected. The emitted electrons can be detected directly using an electron detector or by measuring the sample current. As the intensity of emitted electrons is proportional to the concentration of electron holes, it is also proportional to the absorption of X-ray irradiation. Using this approach, only the top most surface is studied (in the range of a few nanometers) due to the small escape depth of electrons.

Following the IUPAC notation, absorption edges are labeled after the orbital from which a core electron is extracted. With increasing principal quantum number n , the absorption edges are labeled progressively starting from the letter K ($n = 1, 2, 3, \dots$ correspond to K, L, M, \dots edges). A lowercase number after the letter indicates from which degenerated orbital within one principal quantum number the electron was excited (e.g. L_1, L_2, L_3 edges correspond to $2s, 2p_{1/2}$ and $2p_{3/2}$ orbitals). Due to a lack of absorption edges in an accessible energy range for tantalum, only the oxygen absorption was studied within this thesis. For this, electrons from the $O\ 1s$ orbital were excited. Accordingly, the oxygen absorption edge is labeled $O\ K_1$ edge (the lowercase number in case of the K shell is often neglected as only a single energy level exists).

A closely related technique is the so-called electron energy loss spectroscopy (EELS), which is often employed in transmission electron microscopes. EELS allows to study absorption edges by measuring the energy loss of primary electrons that are transmitted through a specimen. Accordingly, EELS provides the same information as XAS but at a much higher spatial resolution.

3.6 Photoelectron emission spectroscopy

Photoelectron emission spectroscopy (PES) is a surface sensitive characterization technique that is based on the photoelectric effect. In PES, electrons are excited by photons and escape the solid. Considering the band structure of solids, electrons exhibit binding energies ranging from a few electron volts (eV), e.g. valence band electrons, to several tens of keV for core level electrons. Depending on the used photon source, PES is divided into ultra violet (UPS) and X-ray photoelectron spectroscopy (XPS). UPS is typically used to study the valence band and XPS to study the core level structure. The kinetic energy of excited electrons E_{kin} can be calculated according to

$$E_{kin} = \frac{1}{2} m_e \cdot v^2 = h\nu - E_{bin} - \Phi \quad (3.1)$$

with m_e the electron mass, v the velocity, e the elemental charge and $h\nu$ the photon energy. E_{bin} is the binding energy of the excited electron and Φ is the work function of the solid.

As the photon energy is typically known, it is possible to calculate the binding energy of photoelectrons that leave the solid by measuring their kinetic energy. Because the binding energy is an element specific property, it is possible to identify the elemental composition of a sample. Furthermore, the exact binding energy of the core level electron depends on the chemical environment of the atomic species. By measuring the so-called chemical shift of a core level, it is possible to analyze the bonding character and the oxidation state of species in a sample.

The photoemission process can be described by the so-called three-step model of photoemission. Figure 3.6 depicts schematically the photoemission process as described by the three-step model. Upon irradiation of a solid with electromagnetic irradiation, photons refract at the solid surface and propagate through the solid. The photon intensity decreases very slowly within the solid due to the weak interaction between photons and electrons. Nevertheless, a small fraction of photons is absorbed in a surface near region and excite electrons. This photo-excitation process is step one in the three-step model. Step two describes the propagation of an excited electron through the solid. During the propagation, electrons might undergo elastic and inelastic scattering processes with other electrons or crystal defects. If an electron scatters inelastically, parts of its kinetic energy is transferred to a secondary electron. Because it is unknown how much energy a primary electron has lost through inelastic scattering during its propagation to the surface, it is not possible to determine its initial binding energy. The generated secondary electrons and the inelastically scattered primary electrons produce a featureless background signal in a photoemission spectrum. In the last step of the model,

the electron has arrives at the surface and leaves the solid if its kinetic energy exceeds the work function Φ of the sample. After the electron is emitted from the surface, it propagates through the vacuum and is detected by an electron detector.

Only primary electrons that leave the sample without energy loss provide information about the electronic structure of the solid. Therefore, the *inelastic mean free path* (IMFP) λ_{in} of electrons is the most important quantity that determines the information depth of a photoemission experiment. The intensity drop due to inelastic scattering along a distance l can be described by an exponential damping according to

$$I(l) = I_0 \exp\left(-\frac{l}{\lambda_{in}}\right). \quad (3.2)$$

with $I(l)$ the intensity of primary electrons after they have traveled the distance l and I_0 the initial intensity of the primary electrons.

The IMFP of an excited electron is a strong function of its kinetic energy. While the exact quantity of the IMFP is material dependent, the same correlation between IMFP and kinetic energy is observed for all materials. Generally, electrons with higher kinetic energies travel faster through the solid and have a lower chance to scatter before they reach the surface. This gives the possibility to increase the information depth of a PES experiment by using higher energy photons. If hard X-ray radiation is used, the technique is referred to as hard X-ray photoelectron emission spectroscopy (HAXPES). Depending on the used kinetic energy of the electron, the IMFP can range from only a few Ångstroms to several tens of nanometers.

Core level in XPS are labeled using the nl_j nomenclature where n is the principal quantum number, l is the angular momentum in letter notation ($l = 0, 1, 2, \dots$ corresponds to s, p, d, ...) and j is the total angular momentum quantum number that is defined as $j = |l \pm s|$ (where s is the spin angular momentum and can be $\pm 1/2$). Core level with an angular momentum of $l = 0$ give rise to a single peak, whereas core level with $l > 0$ appear as a doublet. This effect is known as spin-orbit splitting or $j-j$ coupling and arises from the interaction between spin and angular momentum of an unpaired electron, which can be either parallel or anti-parallel. The relative peak ratio of the two doublet components is determined by the number of possibilities that exist for parallel or anti-parallel pairing. The degeneracy d can be calculated according to $d = 2j + 1$. For the Ta 4f core level with $n = 4$ and $l = 3$, the total angular momentum calculates to $j = 3 \pm 1/2 = 7/2$ and $5/2$, with $7/2$ being the anti-parallel (low binding energy) and $5/2$ the parallel (high binding energy) component. Calculating the degeneracy for both values yields $d = 8$ and 6 . Thus the area ratio between the Ta 4f_{7/2} and the Ta 4f_{5/2} peak is $8/6$. To account for the spin orbit splitting, peak models for core level spectra are constrained with respect to their theoretical doublet peak area.

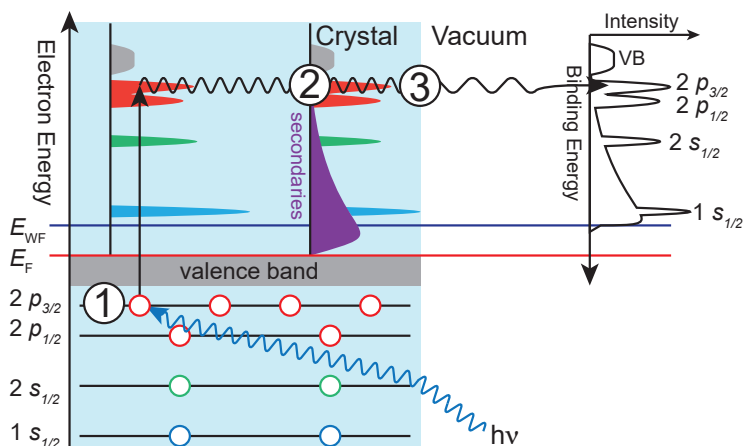


Figure 3.6: Three-step model of photoemission. After an electromagnetic wave is refracted at the surface of the crystal it penetrates through the solid and eventually excites a photoelectron (1). The photoelectron travels through the solid (2) and undergoes elastic and inelastic scattering processes with other electrons. The inelastic scattering produces secondary electrons. After reaching the surface, the electron wave diffracts at the surface (3) and the photoelectron emits into the vacuum. Note, that only electrons with sufficient kinetic energy ($E_{\text{kin}} \geq E_{\text{WF}}$) can escape the solid.

The PES measurements presented in this thesis were performed either with a *Versa Probe 5000* from *Physical Electronics Inc., USA* or the *NanoESCA* from *Scienta Omicron GmbH, Taunusstein, Germany* in the spectroscopy mode. Both instruments are equipped with a monochromatic $\text{AlK}\alpha$ X-ray source. All spectra were evaluated using CasaXPS Version 2.3.16. Prior to quantitative analysis, a Shirley background was subtracted. For insulating samples charge compensation was achieved using an electron flood gun on the *Versa Probe 5000*. Charging in the *NanoESCA* was accounted for by referencing the spectra using a well known core level peak ($\text{Au}^0 4f_{7/2}$ at a binding energy of 84.0 eV or $\text{Ta}^{5+} 4f_{7/2}$ with a binding energy of 26.7 eV) and applying a rigid shift to the spectra.

3.7 Photoemission electron microscopy

In photoemission electron microscopy (PEEM), photoelectrons are imaged using a set of electromagnetic lenses. This enables the magnification and imaging of a sample surface. Similar to PES, electrons are excited by electromagnetic irradiation and depending on the used wavelength, PEEM is categorized into UV-PEEM, X-PEEM or HAXPEEM (for ultraviolet, X-ray and hard X-ray irradiation respectively). In contrast to classical XAS and PES techniques, where the lateral resolution is limited by the size of the photon beam (typically several tens

to hundreds of μm), PEEM gives the possibility to perform XAS and PES in a spatially resolved manner. This allows for probing the electronic structure of solids on the nanometer scale. In addition to XAS and XPS, the electronic structure can also be analyzed through so-called work function scans, which are used to measure the local work function of a sample.

For the PEEM studies presented in this thesis, two different instruments were used. The *NanoESCA* from *Scienta Omicron GmbH, Taunusstein, Germany* (described in detail in ref. [145] and [26]) and the *SPELEEM III* from *Elmitec GmbH, Germany* (described in detail in ref. [146] and [147]). While the exact beam path and the microscope geometry differ between the microscopes, they share the same fundamental building blocks. The basic operation principle of a PEEM is shown in figure 3.7 using a schematic of the *NanoESCA* microscope. As the sample is part of the beam path it has to be oriented precisely parallel to the lens system in order to avoid comatic aberrations. Upon irradiation of the sample, photoelectrons are emitted from the sample surface and are accelerated towards the objective lens by a high electric field. Typical operating voltages of 12 kV (20 kV for the *SPELEEM*) are used to accelerate and bundle the emitted photoelectrons. These high electric fields are necessary to achieve the highest spatial resolution of the microscope and to increase the signal intensity by collecting photoelectrons from a wider range of emission angles. After the photoelectrons have been accelerated into the imaging column, they pass through a set of projection lenses, which further magnify the image. Detection of the photoelectrons is achieved using a 2D detection unit composed of a micro-channel plate, a scintillator screen and a charge-coupled device camera. To obtain energy-filtered images, the instrument is operated in the imaging ESCA mode. Here, the photoelectrons are separated according to their kinetic energy by a hemispherical energy analyzer. To eliminate the spherical aberrations that are caused by the first hemisphere, a second hemisphere is attached and the beam path is completed by an exit lens system. If no spatial information is required, the microscope can be operated in the spectroscopy mode, where electrons pass only through one hemisphere and are collected by a 1D channeltron detector. This mode provides the same functionalities as a standard photoelectron spectrometer, without the possibility to acquire angle resolved spectra.

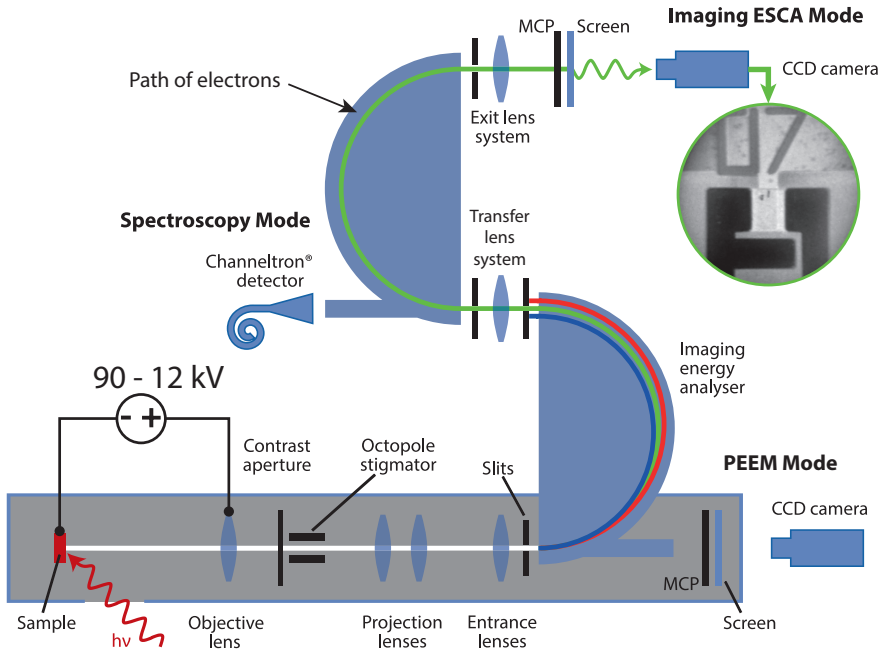


Figure 3.7: Schematic layout of the *NanoESCA* photoemission electron microscope. A sample is irradiated by photons and emits photoelectrons, which are accelerated towards the objective lens. The electrons travel through the image column and are directly detected in the PEEM mode. Energy resolved imaging is achieved by passing the electrons through both hemispherical energy analyzers. For acquiring non-spatially resolved spectra, photoelectrons pass only through the first hemisphere and are afterwards detected by a channeltron detector. Modified from ref. [148].

4 Growth and characterization of thin oxide films

Before switching-induced changes are analyzed in memristive devices, it is essential to gain thorough knowledge about the elemental composition, the micro- and the electronic structure of the pristine thin films. In this thesis the resistive switching effect of SrTiO_3 and Ta_2O_5 is studied. First, the properties of SrTiO_3 thin films grown by pulsed laser deposition will be presented in section 4.1. The characterization focuses on the effect of cation non-stoichiometry and the thin film defect structure.

Afterwards, the fabrication of Ta and Ta_2O_5 thin films by reactive sputter deposition is discussed in section 4.2. An alternative approach for fabrication of Ta_2O_5 thin films for resistive switching by plasma oxidation will be demonstrated. The surface morphology and structure of the prepared films is analyzed. Afterwards, the influence of growth conditions on the oxygen stoichiometry of TaO_x is presented. Special emphasis is given to the spectroscopic characterization by XPS. The impact of the oxygen deficiency on the electrical resistance is discussed. Lastly, the effect of electro-reduction on the spectroscopic signature is presented.

4.1 Structure and morphology of PLD grown SrTiO_3 thin films

Growing SrTiO_3 by PLD gives the possibility to precisely control the cation stoichiometry and defect structure by tuning the deposition parameters [112,142]. This renders SrTiO_3 to an ideal model system that allows to investigating the relationship between thin film- and resistive switching-properties. Accordingly, thin films with various cation non-stoichiometries and defect densities were fabricated and characterized.

Influence of the cation non-stoichiometry

The cation stoichiometry of complex oxides grown by PLD can be adjusted through different approaches, e.g. ablating from non-stoichiometric targets or by variation of the growth

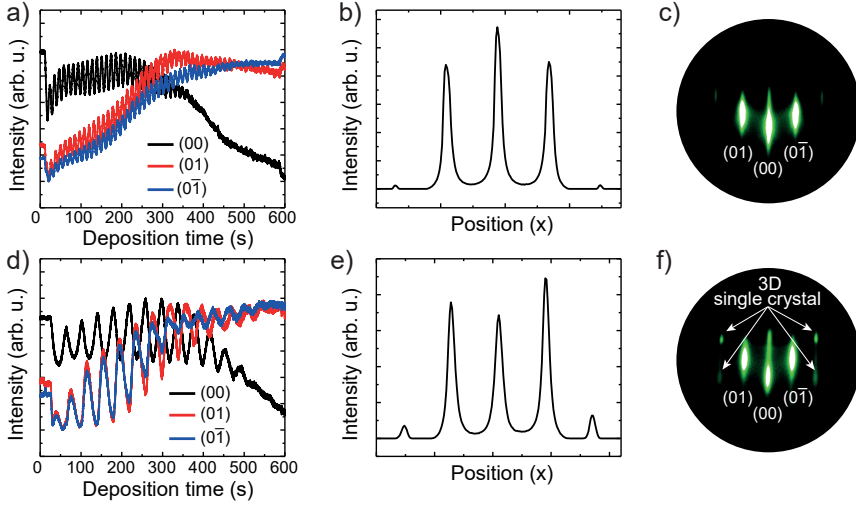


Figure 4.1: Impact of the laser fluence on the growth of SrTiO₃. a) RHEED intensity as a function of time for a deposition with a laser fluence of 1.01 J cm^{-2} . b) Line profile extracted from the RHEED pattern in c) after deposition. d) RHEED intensity, e) line profile and f) RHEED pattern for a deposition with a laser fluence of 0.66 J cm^{-2} .

conditions. For the growth parameters used in this work, a reliable way to change the cation stoichiometry is the adjustment of the laser fluence [149–152]. In the case of SrTiO₃, the variation of the cation stoichiometry with the laser fluence results from a combination of preferential scattering of low atomic mass species, e.g. Ti in SrTiO₃, and incongruent ablation from a stoichiometric target [142]. The interplay of both processes results in the growth of Sr-rich thin films at low laser fluences. Accordingly, Ti-rich films can be deposited at high fluences. As will be discussed in chapter 5, the cation stoichiometry has a pronounced influence on the resistive switching properties of SrTiO₃ memristive devices. Especially, the excess of Sr in the thin film was found to improve the switching properties of such devices [110].

In the following, the growth and morphology of a stoichiometric and a Sr-rich thin film will be compared. For this, 20 nm films with varying laser fluences were grown at a substrate temperature of 800°C. The growth mode and rate was monitored by reflection high-energy electron diffraction (RHEED). Figure 4.1 a) and d) show the RHEED intensity as a function of the deposition time for a film grown at a laser fluence of 1.01 and 0.66 J cm^{-2} . The oscillating RHEED intensity is indicative for a two-dimensional layer by layer growth [153]. Each oscillation corresponds to the growth of a single unit cell (u.c.) layer. As expected, the growth rate at a high fluence is significantly higher (11.6 s/u.c.) compared to the low fluence (48.3 s/u.c.). Based on the deposition time, the stoichiometry can be determined as described

in ref. [141]. For the film grown at a high laser fluence of a cation ratio of $\text{Sr}/(\text{Sr}+\text{Ti}) \approx 0.5$ is determined, whereas the low fluence film has a cation ratio of 0.53. A detailed description of the deposition parameters is given chapter 3 and all film stoichiometries in this thesis are listed in the appendix in table A1.

Besides the determination of the growth rate, RHEED gives also valuable information about the growth mode and the thin film properties. Figure 4.1 b) and e) show line profiles extracted from the RHEED pattern in c) and f) respectively. By comparing the intensity from the specular spot (00) to those of the 1st order diffraction spots (01) and (0 $\bar{1}$), a qualitative estimation for the composition of the termination layer can be obtained. If the uppermost atomic layer is formed by SrO, a high intensity of the 1st order diffraction spots is expected due to the higher atom form factor of Sr compared to Ti [154, 155]. Likewise, TiO₂ termination leads to a high intensity of the specular spot. As expected, the stoichiometric film features a RHEED pattern with a higher specular spot intensity. Comparing the RHEED line profiles with the literature indicates, that the stoichiometric film exhibits predominantly a TiO₂ termination, whereas the Sr-rich thin film is SrO terminated [141]. As mentioned in chapter 2, small amounts of Sr excess can be incorporated into the bulk film through the formation of Ruddlesden-Popper type anti phase boundaries. However, if the Sr excess is large, a SrO secondary phase grows at the film surface in the form of single crystalline islands [143]. This process goes along with the appearance of additional diffraction spots in the RHEED pattern. Such spots emerge if the electron beam transmits through the islands and produces a transmission diffraction pattern [156]. Looking at the post deposition RHEED pattern in figure 4.1 c) and f), additional diffraction spots can be seen in both cases but the intensity is lower for the stoichiometric sample. This confirms, that the Sr-rich growth leads to the formation of single crystalline islands at the surface.

The morphology and microstructure of the two thin films has been studied using atomic force microscopy (AFM) and TEM. The results are shown in figure 4.2. The stoichiometric thin film shows a well defined surface morphology with a distinct step-terrace structure. The terrace structure is adapted from the surface morphology of the substrate and confirms a atomically flat surface. In contrast, the Sr-rich thin film exhibits a high density of islands that are randomly distributed across the surface. To investigate the microstructure of the film, a lamella was cut from the Sr-rich sample and the film was investigated by TEM. Figure 4.2 c) shows a cross-sectional view of the thin film. A single crystalline film quality can be observed. Occasionally, extended defects are visible that are identified as Ruddlesden-Popper type antiphase boundaries (see section 2.1 for more information).

¹The TEM characterization within this chapter was performed by Dr. Hongchu Du, Ernst Ruska-Center, Forschungszentrum Jülich, Jülich, Germany.

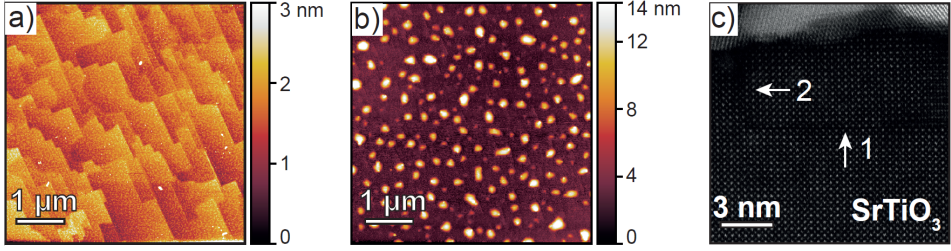


Figure 4.2: Surface morphology of a) a stoichiometric and b) a Sr-rich 20 nm SrTiO_3 thin film grown by PLD. c) High-angle annular dark-field TEM image of the Sr-rich thin film. Arrows indicate Ruddlesden-Popper type antiphase boundaries running parallel (1) and perpendicular (2) to the surface¹.

Influence of the substrate temperature

Depending on the growth conditions SrTiO_3 can grow in different modes, namely island, layer-by-layer or step-flow growth. One key parameter that determines the growth mode is the substrate temperature. Typically, for low deposition temperatures island growth is observed, whereas high temperatures lead to a step-flow growth. At intermediate temperatures, a layer-by-layer growth dominates. In the case of SrTiO_3 , a transition from island to layer-by-layer growth occurs at approximately 550°C and to a step-flow mode at temperatures above 800°C [157]. The reason for the occurrence of different growth modes can be attributed to the temperature dependent mobility of adatoms on the substrate surface [158, 159]. At low substrate temperatures, the adatom mobility is low and clustering of the arriving species causes the formation of islands.

In order to investigate the impact of the substrate temperature on the thin film structure, thin films were prepared at low temperatures and characterized by electron microscopy. To further increase the defect density, the films were grown at low laser fluences to additionally introduce a Sr-excess. In the following, the structural properties of such films are discussed and in chapter 5 their resistive switching properties will be analyzed.

Figure 4.3 a) shows a scanning electron microscopy (SEM) image of a 100 nm $\text{Sr}_{1.17}\text{Ti}_1\text{O}_{3.17}$ thin film deposited at 550°C . To prevent charging of the surface during the measurement, a homogeneous layer of 30 nm Pt was evaporated onto the sample prior to SEM analysis. From the image it can be seen that the surface exhibits characteristic square-shaped morphological features with varying sizes. To investigate the thin film in a cross-sectional view, a lamella was prepared by focused ion beam etching and characterized by TEM. Figure 4.3 b) displays a high-angle annular dark-field (HAADF) overview image of the thin film cross-section. Interestingly, it can be observed that the first few nanometers of the film exhibit an epitaxial crystal structure. After approximately 20 nm, triangular shaped extended defects emerge, which are

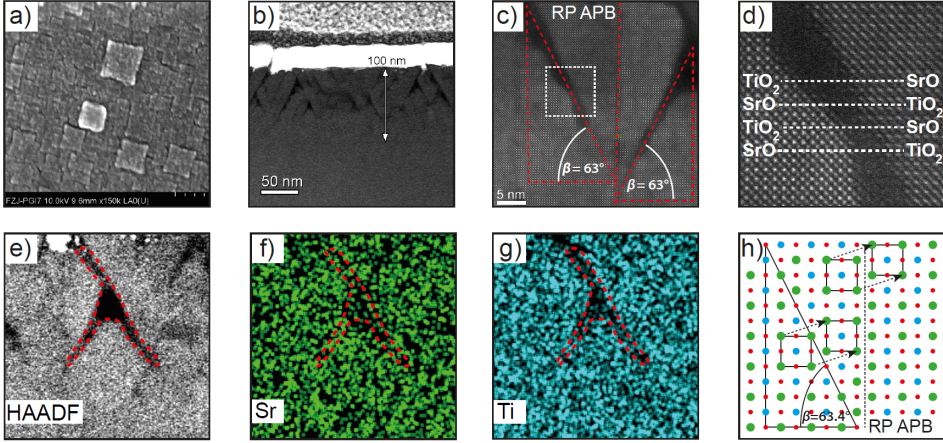


Figure 4.3: Electron microscopy of a 100 nm Sr_{1.17}Ti₁O_{3.17} thin film. a) SEM image of the film surface. The oxide surface was covered with a 30 nm Pt film prior to the experiment to minimize charging. b) Cross sectional high-angle annular dark field (HAADF) image. c) Magnification of a film section with defects and d) close up of the image section marked by a white box in (c). e) HAADF of a large defect structure and elemental maps acquired by EDX for f) Sr L α , g) Ti K α . h) Schematic representation of the defect structure.

visible as regions with dark contrast. As the brightness of a HAADF image is proportional to its mass density, it can be concluded that the dark regions are less dense compared to the surrounding. To clarify the origin and nature of the defects, a high resolution HAADF image was acquired at the bottom of a defect (compare Figure 4.3 c)). The image exhibits atomic resolution and clearly resolves the mostly single crystalline film structure. In this film section, two different extended defects can be distinguished. First, a Ruddlesden-Popper type antiphase boundary (RP APB) is present in the center of the image marked by the red dashed line. The RP APB starts from a $a/2[111]$ screw dislocation and propagates along the $[010]$ crystal plane towards the film surface. Second, two adjacent defects can be recognized. They start from the central RP APB defect and run along the $[021]$ and $[0\bar{2}1]$ crystal planes as evidenced by the agreement between theoretical angle $\beta = \arctan(2/1) \approx 63.4^\circ$ and measured angle of 63° . 4.3 d) shows a digitally magnified section of the white box marked in c)). Due to their higher atomic mass and radius, SrO columns appear brighter in the HAADF image compared to TiO₂ columns. Taking a closer look at the stacking order of the SrO and TiO₂ columns on the two sides of the defect, it becomes apparent that the lattices are shifted by $a/2$ against each other. This means that TiO₂ columns on one side of the defect are opposed by SrO columns on the other side. To further investigate the composition of the defects, energy-dispersive X-ray spectroscopy (EDX) was performed and the results are presented in figure 4.3 e-g). To maximize the signal-to-noise ratio a particularly big defect was investigated. Panel e) shows an overview HAADF image of the analyzed region. Looking at the Sr and Ti elemental

maps in panel f) and g), a dark contrast within the red dashed region can be observed. This confirms that less material is present in this region. Comparing the intensities of the Sr and Ti maps indicates a slight Sr-excess. However, a precise determination of the defect composition is not possible due to a low signal-to-noise ratio.

Based on the structural analysis, it is surmised that the growth mode changed from a layer-by-layer growth for the first 20 nm to a island growth mode at later stages. Deliberately growing the thin film at low laser fluences resulted in a Sr-rich thin film and induced the formation of RP APB in the upper 80 nm of the film. This is in good agreement with literature results and can be explained as follows [143]. In the first growth stage, the film and the film surface is progressively enriched with SrO. After the surface is saturated with SrO, the formation of RP APB is induced through the stacking of SrO atomic planes. This explains, why the first 20 nm of the film exhibit an epitaxial structure and are defect free. Due to the comparably low substrate temperature, the adatom mobility is low and the island growth leads to the formation of a large number of extended defects. Island growth appears to occur along the $[021]$ and $[0\bar{2}1]$ crystal plane, giving rise to the characteristic triangular shaped defects. From the surface morphology it can be seen that the islands grow in a square structure, which is not surprising as SrTiO_3 has a cubic crystal structure with a fourfold rotational symmetry. Considering that the islands grow in the vertical and lateral direction, it is expected that a so-called self shadowing effect occurs [160]. As a consequence, voids with less material are forming underneath the islands, visible here as dark regions. However, as the adatom mobility is not zero and the PLD process is not completely directional, the regions are partially filled. Figure 4.3 h) shows a possible atomic model representation of the defect structure. Starting from a vertical RP APB, a second antiphase boundary can form along the $[021]$ crystal plane. Both defects are similar and only differ in their propagation direction.

4.2 Structure and morphology of Ta and Ta_2O_5 thin films

Due to its industrial relevance as high-k dielectric, Ta_2O_5 thin films have been fabricated by a manifold of deposition methods. In the context of resistive switching, especially the deposition by reactive sputtering is widely employed due to its ease of operation and because it enables a precise control over the film properties. However, sputtering is a complex process that requires optimization to fabricate well defined and reproducible films. In the following section, the fabrication and thin film properties of Ta and Ta_2O_5 films will be investigated.

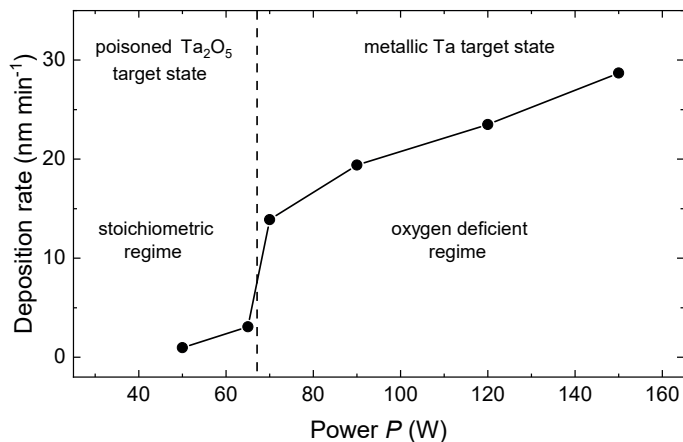


Figure 4.4: Deposition rate of TaO_x thin films as a function of the sputter power. The dashed line indicates the transition between the poisoned (Ta₂O₅) and metallic target state.

Sputter deposition of Ta and Ta₂O₅ thin films

All tantalum films presented in this thesis were prepared by RF magnetron sputtering from a metallic Ta target. Ta films were sputtered in pure argon (N6 purity) and oxides were prepared in an Argon/Oxygen (N5 purity) gas mixture. The depositions were performed at room temperature onto insulating Si/100 nm Si₃N₄ or Si/430 nm SiO₂ substrates. Detailed information about the deposition process and parameters can be found in the appendix in table A2.

First, the influence of the process power on the deposition rate was investigated. For this, thin films were deposited with various process powers and the film thickness was subsequently measured by X-ray reflection (XRR). Figure 4.4 shows the deposition rate of TaO_x as a function of the sputter power. For high sputter powers, a linear correlation between deposition rate and power is observed, which is in good agreement with previous reports [161,162]. At lower powers, a sudden drop of the deposition rate can be observed at approximately 65 W. This drastic change in the deposition rate indicates that the target state changes from a metallic to an oxidized state. The so-called poisoning of the target occurs when the reaction between target and reactive gas is faster than the ablation rate of the target (see 3.2 for more details). The poisoned target has a decreased ablation rate compared to the metallic state and as a consequence the deposition rate drops [144]. In section 4.3 it will be demonstrated that sputtering from a metallic target at low oxygen partial pressures results in the forma-

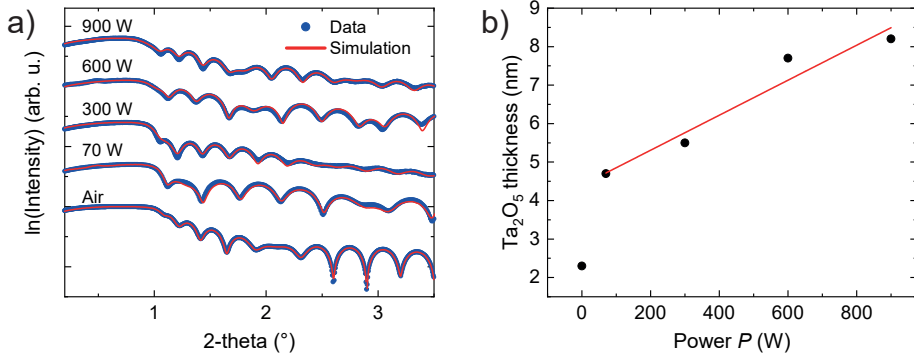


Figure 4.5: Power series of plasma oxidized Ta films. a) X-ray reflectivity measurements of native oxide and Ta₂O₅ films prepared by plasma oxidation. b) Oxide thickness as a function of the process power.

tion of oxygen deficient TaO_x films. Sputtering from a poisoned target always yields fully stoichiometric Ta₂O₅.

Plasma oxidation of metallic Ta films

In general, stoichiometric oxides are used for the fabrication of resistive switching devices. This allows the utilization of strongly oxidizing methods for the fabrication of Ta₂O₅ thin films. One of such methods is the O₂ plasma oxidation of metallic Ta thin films. To investigate the suitability of this approach, a series of metallic Ta films were treated for 15 min with an O₂ plasma using various process powers. Figure 4.5 a) shows XRR data and fits of the resulting bi-layer Ta/Ta₂O₅ stack. The Ta₂O₅ thickness was extracted from the fit and is shown in figure 4.5 b) as a function of the process power. For untreated Ta films, a native oxide is observed with a thickness of approximately 2.3 nm. The native oxide formation is self-limiting due to the sluggish oxygen diffusion in Ta₂O₅ at room temperature. However, the exact thickness of native oxide films may vary between samples depending on their storage time and conditions. A plasma treatment with 70 W results in the formation of a 4.7 nm thick Ta₂O₅ layer. Increasing the process power reveals a linear correlation between oxide thickness and process power. For the highest process power, a Ta₂O₅ thickness of 8.2 nm was measured. This trend can be explained by the increasing kinetic energy of oxygen ions with at high process powers and thus having a greater penetration depth. Importantly, the oxide thicknesses that can be fabricated using this process (5-9 nm) are ideally suited for the application in resistive switching devices.

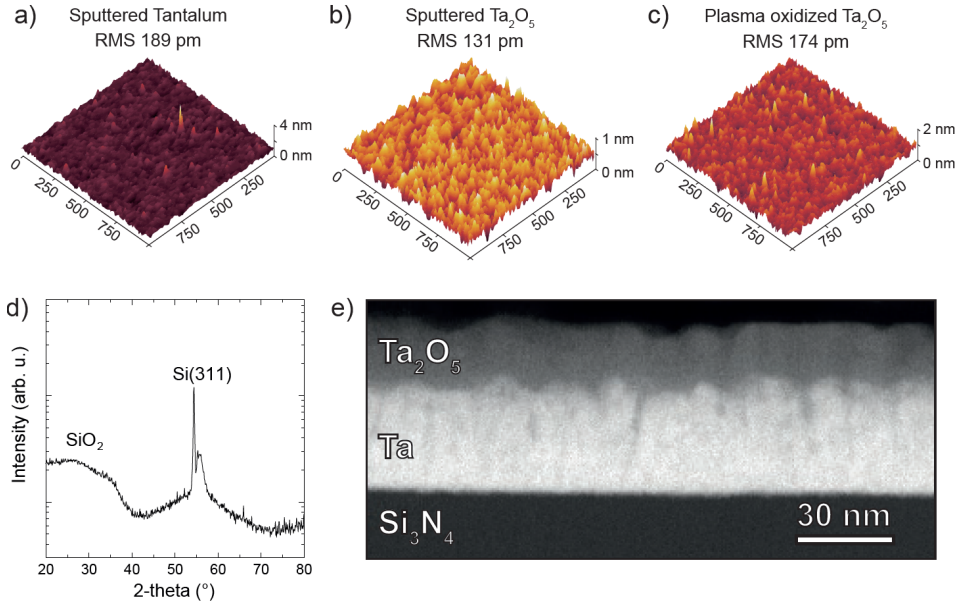


Figure 4.6: Thin film properties of Ta and Ta₂O₅ layers. AFM image for a) 30 nm sputtered Ta b) 15 nm sputtered Ta₂O₅ and c) 8 nm of Ta₂O₅ fabricated by plasma oxidation of a 30 nm sputtered Ta film using a process power of 900 W. d) Grazing incidence XRD of a 100 nm Ta₂O₅ thin film. e) TEM image of a Ta/Ta₂O₅ stack fabricated by plasma oxidation.

Surface morphology and crystal structure

For the fabrication of resistive switching MIM-structures, one requirement is to have precise control over the thin film and interface properties in order to achieve reproducible switching characteristics. Therefore, the deposition processes have been optimized to give smooth thin films with defined thicknesses and interface qualities. Figure 4.6 a-c) shows AFM morphology images of as-prepared thin films. All films are exceptionally smooth with root mean squared roughness values below 200 pm, indicating homogeneous growth without pinholes or formation of large crystallites. Further, it can be seen that the oxygen plasma treatment induces no surface roughening. To investigate the crystal structure of the Ta₂O₅ oxide films, grazing incidence XRD was performed on 100 nm sputtered Ta₂O₅ thin films (compare figure 4.6 d)). No diffraction peaks other than the Si(311) peak from the substrate could be identified. This proves that the sputter process gives amorphous Ta₂O₅ films. This is expected for a room temperature sputter deposition [163]. Figure 4.6 d) shows a TEM image of a Ta/Ta₂O₅ bilayer in a cross-sectional view. For both films, no crystallographic features are visible, verifying that also the metallic tantalum and the plasma oxidized Ta₂O₅ films have an amorphous structure.

4.3 Engineering the oxygen content in sputtered TaO_x thin films

During reactive sputtering, various parameter can have a impact on the thin film properties. In this section, the influence of the deposition parameters on the oxygen stoichiometry is discussed in detail. For this, TaO_x films with various reactive gas flows and deposition rates were fabricated and analyzed by XPS.

As evidenced in figure 4.5, metallic tantalum forms a 2-3 nm thick natural Ta₂O₅ layer if it is exposed to an ambient atmosphere. Because XPS is a highly surface sensitive technique, it is necessary to prevent the natural oxide formation. Therefore, all samples have been transferred under UHV conditions from the deposition chamber directly into the XPS machine. The base pressure during the transfer was always below 3·10⁻⁸ mbar and the influence of the residual gas in the UHV environment was determined to be negligible over periods of several days, i.e. no measurable change in stoichiometry occurred during this period.

It is also possible to analyze the stoichiometry of TaO_x films that have a natural oxide layer using bulk sensitive methods. A typical example for such a technique is Rutherford backscattering spectrometry, which has been successfully used to measure the oxygen content in TaO_x over a wide stoichiometry range [86, 134]. However, in this work only XPS was employed as it also provides detailed information about the electronic and chemical structure of a sample.

Ta 4f core level and valence band spectroscopy

In order to evaluate the oxygen content of a deposited TaO_x thin film by XPS, different approaches can be used. A common way to analyze the elemental composition of a given sample is to measure a core level spectrum for each element in the sample and reference the peak integral to a sample standard with known composition. In the case of tantalum oxide it was shown that comparing the integral of the O 1s and the Ta 4f core level gives reliable results for small oxygen vacancy concentrations [164]. The drawback of this methods is that two core level spectra have to be acquired with high precision to obtain accurate peak areas. Further, the O 1s core level is known to be influenced by oxygen containing adsorbents, such as CO, CO₂ and H₂O, which are readily present in UHV systems. Therefore, the stoichiometry was determined through fitting of the Ta 4f core level spectrum.

Figure 4.7 shows typical Ta 4f spectra acquired from thin films with various oxygen contents. To obtain accurate results, a single peak model was constructed that was used to fit all samples. For this, a peak doublet was fitted to a pure Ta₂O₅ reference sample and the peak shape, position, full width at half maximum (FWHM) and spin-orbit splitting was determined.

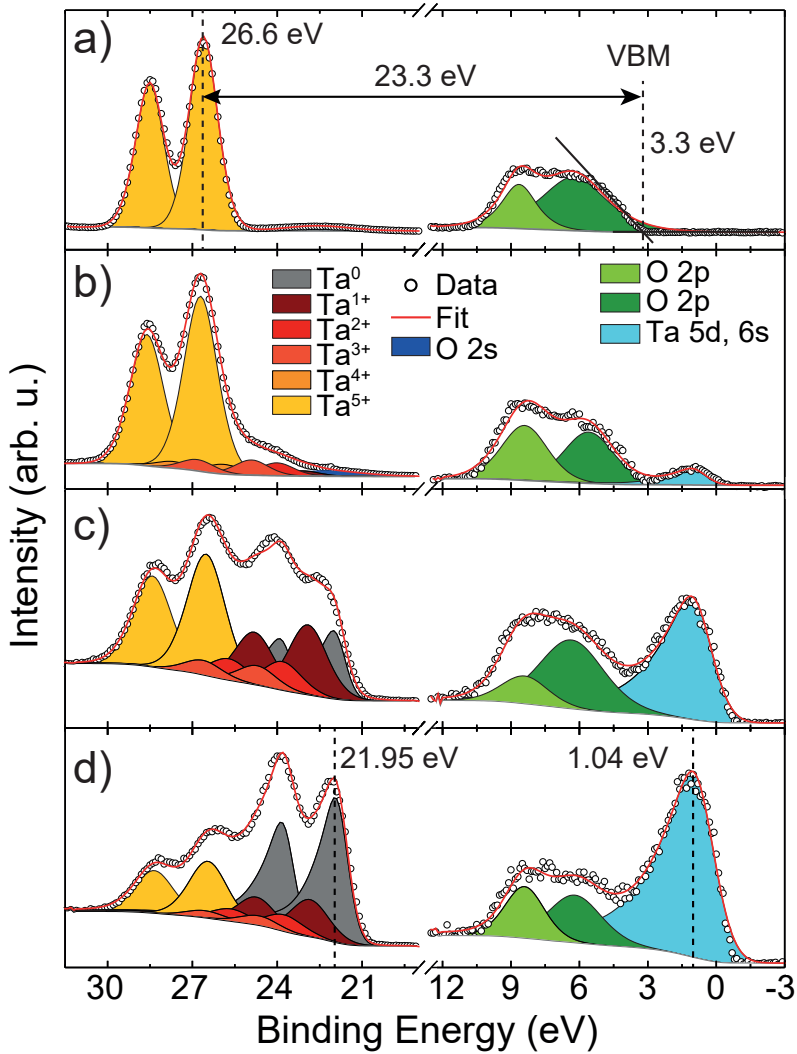


Figure 4.7: Ta 4f core level and valence band spectra of sputtered tantalum oxide films with various oxygen contents. a) Pure Ta_2O_5 , b) TaO_x with a O/Ta ratio of 2.15, c) 1.30 and d) 0.98. The y-axis of the valence band is rescaled by a factor of 10 for better visibility.

Based on these values, Ta⁴⁺, Ta³⁺, Ta²⁺ and Ta¹⁺ doublets were introduced to the peak model to describe the reduced components. The metallic Ta⁰ component was uniquely fitted with a peak shape measured from a metallic reference sample. The Ta⁰ component exhibits an asymmetric line shape that is characteristic for metals. To prevent an over-parametrisation of the peak model, all components were constrained in their peak shape, position and FWHM. Only the peak area of each component was allowed to vary.

Based on the contribution of each component to the total peak area, it is possible to determine the O/Ta ratio according to

$$\sum_{n=1}^5 \frac{[\text{Ta}^{+n}] \cdot \frac{n}{2}}{100} = \frac{[\text{Ta}^{+1}] \cdot \frac{1}{2} + [\text{Ta}^{+2}] \cdot \frac{2}{2} + [\text{Ta}^{+3}] \cdot \frac{3}{2} + [\text{Ta}^{+4}] \cdot \frac{4}{2} + [\text{Ta}^{+5}] \cdot \frac{5}{2}}{100} \quad (4.1)$$

with [Ta⁺ⁿ] the peak area fraction of a tantalum component in % and *n* the formal oxidation state.

The Ta 4f core level clearly shows, that reducing the oxygen content leads to the formation of various components ranging from Ta⁵⁺ to Ta⁰. As expected, the contribution of components with lower oxidation states increases in expense of higher oxidation states if the oxygen content is decreased. This leads to a gradual shift of the core level from 26.60 eV (Ta⁵⁺) to 21.95 eV (Ta⁰). This so-called chemical shift is a direct measure of the electron density of the Ta cation. For high oxidation states, the Ta cation is charged positively and the negatively charged core level electrons feel a strong Coulomb attraction. Similarly, if Ta is only slightly positively charged or neutral, the Coulomb attraction is weaker. In the case of Ta, the chemical shift is pronounced and has a value of 4.65 eV between Ta⁵⁺ and Ta⁰.

For fully stoichiometric Ta₂O₅, the valence band is almost entirely composed of O 2p states (shown in green in figure 4.7) and the valence band maximum is located at 3.3 eV. Considering that Ta₂O₅ has a band gap of 4.4 eV, the Fermi-level is located 1.1 eV below the conduction band minimum. Hence, Ta₂O₅ can be assumed to be a *n*-type semiconductor. Reducing the oxygen content results in appearance of an additional peak that is located at a binding energy of 1.04 eV. This component can be assigned to a defect band that is formed by Ta 5d and 6s orbitals [165]. As expected, decreasing the oxygen content in a sample results in an increased contribution from Ta states in the valence band.

Controlling the stoichiometry of TaO_x thin films

As demonstrated in the previous section, it is possible to deposit and characterize TaO_x thin films with various degrees of oxygen deficiency. However, the important question remains

how the stoichiometry can be controlled through the deposition conditions. Here, two approaches are demonstrated. In the first approach, the deposition rate is changed through the sputter power and in the second approach, the oxygen partial pressure in the chamber is varied.

Thin films were prepared using sputter powers from 50 to 250 W (compare table 4.1) and analyzed by XPS. In figure 4.8 a) the corresponding Ta 4f core level spectra are shown. Upon increasing the sputter power, a clear shift towards lower oxygen contents is visible (compare figure 4.8 b)). To understand this behavior, it is necessary to consider that the reaction rate between Ta and oxygen is finite and mainly determined by the oxygen partial pressure. During the sputter series, the $p(\text{O}_2)$ is kept constant, while the sputter rate is increased. As a result, the amount of oxygen that can react with the growing film decreases. This allows the deposition of a wide range of TaO_x stoichiometries from $1.5 > x > 0$. Below sputter powers of 65 W a target poisoning occurs, which leads to fully stoichiometric films. Therefore, the stoichiometry regime $2.5 > x > 1.5$ is inaccessible by only changing the sputter power (see section 3.2 for more details).

In a second deposition series, the deposition rate was kept constant and the oxygen partial pressure was varied between $0.9 \cdot 10^{-4}$ and $5.3 \cdot 10^{-4}$ mbar (compare table 4.1). Following the same argumentation as before, an increasing oxygen partial pressure increases the oxide formation rate. As expected, the oxygen content of the thin film is a function of the $p(\text{O}_2)$ (compare figure 4.8 c) and d)). Again, a poisoning of the target is observed at a $p(\text{O}_2)$ of $5.3 \cdot 10^{-4}$ mbar. This inhibits the fabrication of stoichiometries in the range of $2.5 > x > 1.65$.

Besides the oxygen content, fitting of the Ta 4f core level gives also valuable information about the distribution of the individual oxidation states. Figure 4.8 f) shows the peak area

Table 4.1: Sputter parameter for the TaO_x thin film deposition and calculated O/Ta ratio for films deposited at a target to substrate distance of 50 mm and a gas composition of 1% O₂ in Ar.

Power variation			Pressure variation		
Power (W)	Pressure (mbar)	O/Ta ratio	Power (W)	Pressure (mbar)	O/Ta ratio
50	$5 \cdot 10^{-2}$	2.5	65	$9 \cdot 10^{-3}$	0
67	$5 \cdot 10^{-2}$	1.46	65	$2 \cdot 10^{-2}$	0
70	$5 \cdot 10^{-2}$	1.28	65	$4 \cdot 10^{-2}$	1.17
90	$5 \cdot 10^{-2}$	0.98	65	$4.5 \cdot 10^{-2}$	1.31
120	$5 \cdot 10^{-2}$	0.79	65	$5 \cdot 10^{-2}$	1.45
150	$5 \cdot 10^{-2}$	0.64	65	$5.2 \cdot 10^{-2}$	1.65
250	$5 \cdot 10^{-2}$	0.43	65	$5.3 \cdot 10^{-2}$	2.5

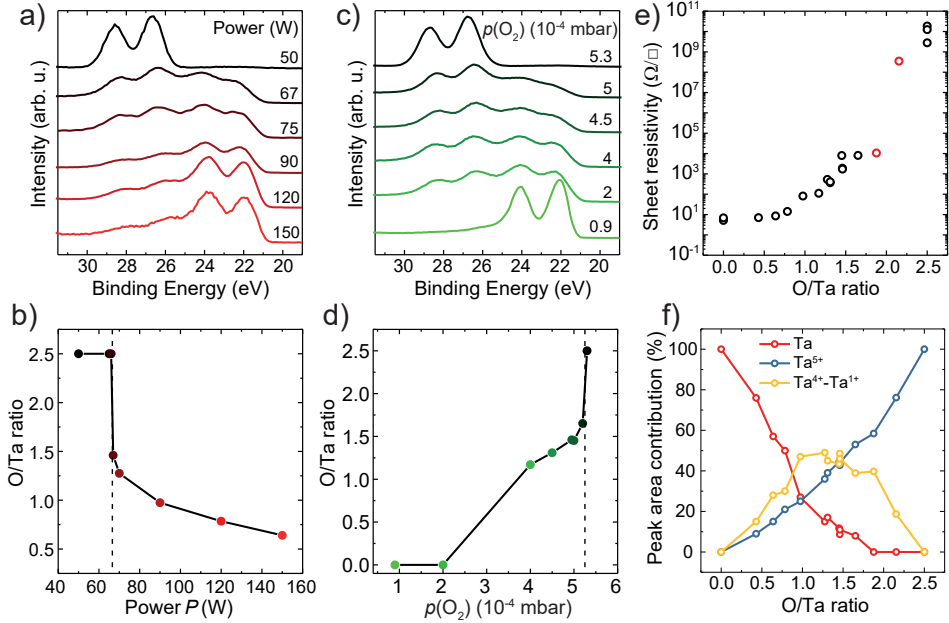


Figure 4.8: Power and pressure series of sputtered TaO_x thin films. a) Ta 4f core level spectra of films sputtered with a power of 50 (black), 67, 70, 90, 120 and 150 W (red). b) O/Ta ratio as a function of deposition power. The dashed line indicates a transition between the poisoned and the metallic target state c) Ta 4f core level spectra for films sputtered with a $p(\text{O}_2)$ of $5.3 \cdot 10^{-4}$ (black), $5 \cdot 10^{-4}$, $4.5 \cdot 10^{-4}$, $4 \cdot 10^{-4}$, $2 \cdot 10^{-4}$ and $9 \cdot 10^{-5}$ mbar (green). d) O/Ta ratio as a function of $p(\text{O}_2)$. e) Sheet resistivity as a function of the O/Ta ratio. The red data points represent films that were grown using a high pump rate sputter process (compare table A2). f) Peak area contributions of Ta^0 , Ta^{5+} and suboxide components as a function of the O/Ta ratio.

contributions for Ta⁰, Ta⁵⁺ and the suboxide components. The suboxides (Ta⁴⁺-Ta¹⁺) are summed up to a single component for better visibility. In the O/Ta range from 2.5 to 1.5 the main component is Ta⁵⁺ and from 0.8 to 0 it is Ta⁰. In the intermediate region from 1.5 to 0.8 the suboxides show a maximum contribution. However, Ta⁵⁺ and Ta⁰ are overall the most common oxidation states. This behavior reflects the tendency of tantalum to form the thermodynamically stable oxidation states (Ta⁰ and Ta⁺⁵), whereas the suboxides never exceed a contribution of 50% of the total peak area. Looking at the trend of the individual components, it is evident that Ta⁵⁺ changes linearly over the whole stoichiometry range. Similarly, the Ta⁰ component also follows an inverse linear trend but it drops to zero at an O/Ta ratio of 1.9. Importantly, this means that Ta⁰ is not expected to occur in a stoichiometry range between 1.9 to 2.5. The reason for this behavior is not obvious but a possible explanation is that the formation of metallic clusters becomes unlikely in an increasingly oxygen rich matrix. The suboxides show a parabolic distribution.

To understand the resistive switching phenomenon in Ta₂O₅-based memristive devices it is important to evaluate the effect of oxygen vacancies on the electronic conduction. Therefore, the sheet resistivity was determined for all TaO_x thin films and plotted as a function of the O/Ta ratio (see figure 4.8 e)). Starting from metallic tantalum with a resistivity of 8 Ω/□, the resistivity steadily increases by several orders of magnitude until an O/Ta ratio of 1.9 is reached. At this point, a sudden jump in resistivity from 10 k to 350 MΩ/□ occurs. The fully stoichiometric thin films have resistivities in the order of 10 GΩ/□. Connecting the conclusions drawn from the XPS analysis and the sheet resistivity, it becomes clear that oxygen vacancies increase the conductivity of TaO_x films over the whole stoichiometry regime but have the highest impact at a O/Ta ratio of approximately 2.0.

4.4 Spectroscopic signatures of Ta₂O₅ thin films reduced by electrical stress

In section 4.2 it was demonstrated, that it is possible to fabricate TaO_x thin films with various degrees of oxygen content. The range of non-stoichiometry is, however, limited by a poisoning of the metallic Ta target. As a consequence, stoichiometries between TaO_{1.7} and TaO_{2.2} cannot be easily deposited in a standard sputter process without *in situ* monitoring and real time process control. Nevertheless, this range of non-stoichiometry is especially relevant for the suspected valence changes processes that occur during resistive switching. As shown in figure 4.8 e), a slight increase in the oxygen content from $x=1.9$ to 2.2 changes the resistivity by over four orders of magnitude. Interestingly, TaO_x regions in this stoichiometry range could be reproducibly observed in fully oxidized samples after degradation by a high electric field. In the following, the degradation process and the spectroscopic signatures will

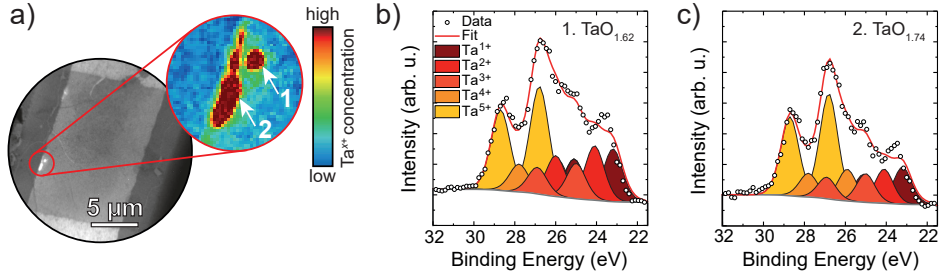


Figure 4.9: X-PEEM analysis of a Ta/Ta₂O₅/Graphene device after high voltage arcing. a) X-PEEM photoelectron image of a device after an arcing event taken at Ta 4f core level binding energies. Inset: Magnification of an area with high amounts of reduced tantalum. The X-PEEM image was acquired by averaging over binding energies from 22–26 eV, corresponding to reduced tantalum states. b) Fitted Ta 4f core level spectrum integrated over the region of interest labeled with "1" in (a) and c) spectrum from region "2".

be evaluated to examine the effect of low oxygen vacancy concentrations on the electronic structure.

In situ electro-reduction of Ta₂O₅

Electro-reduction of oxides is a common phenomenon that occurs if the electrical field strength exceeds the dielectric strength of an insulator or semiconductor [166–168]. In contrast to a soft breakdown performed during electroformation of ReRAM devices, a "hard breakdown" can take place if no protective measures, such as a current or voltage limiter, is used during the forming process. Typically, this hard breakdown leads to the creation of a conductive path through the insulator and as a result the electric field across the insulator drops. This breakdown can be understood as an extreme case of the switching process in memristive devices. During investigation of Ta/Ta₂O₅/graphene devices, occasionally dielectric breakdowns were caused by high voltage arcing inside a photoemission electron microscope. While a fast-acting fuse was in place to limit the amount of current that during the arcing event, damage of the devices was evidenced by changes in morphology and melting of metal contacts. However, the electrical degradation of the Ta₂O₅ films can be used to study the effect of high currents and electric fields on the chemical and electronic structure and to investigate failure mechanism of devices. Figure 4.9 a) shows an exemplary device after a dielectric breakdown. From the PEEM image, the appearance of a small bright region along an edge of the crosspoint can be observed. The inset shows that two separate regions have formed, labeled with "1" and "2". Extracting and fitting of the Ta 4f core level from these regions confirms that the oxide film is strongly reduced in this area. For region 1, a stoichiometry of TaO_{1.62} and for region 2, a stoichiometry of TaO_{1.74} was determined. Interestingly, the contribution of individual

components differs from TaO_x films with a similar stoichiometry fabricated by reactive sputtering. Most importantly, no Ta^0 component is present in the electro-reduced case whereas comparable sputtered films have a Ta^0 fraction of approximately 10%. This demonstrates that the O/Ta ratio alone is not sufficient to describe the chemical and electronic structure of reduced TaO_x compounds.

Transferring these observation to the context of resistive switching, two important conclusions can be drawn:

1. Assuming that the dielectric breakdown can be considered as an extreme case of the electroformation process, the extracted O/Ta ratio of ≈ 1.6 serves as an estimate for the lower boundary of the filament stoichiometry.
2. Metallic tantalum is not necessarily involved in the switching process, as electro-reduction does not result in the formation of a Ta^0 component.

The spectromicroscopic investigation of Ta/ Ta_2O_5 /graphene devices will be continued in chapter 7, where devices are investigated that were operated with appropriate switching voltages and currents.

4.5 Summary

In this chapter, the growth of different metal oxide thin films was presented. In section 4.1 it was demonstrated that the cation stoichiometry of PLD grown SrTiO_3 thin films can be adjusted by tuning the laser fluence. Low laser fluences result in Sr-rich thin films, while higher fluences give stoichiometric films. It was found that the accommodation of excess Sr occurs predominantly through the formation of SrO island on the film surface. To a lesser extent, the Sr-rich growth also induced the formation of extended defects in form of Ruddlesden-Popper type anti phase boundaries. By deliberately reducing the deposition temperature, SrTiO_3 films with high densities of extended defects could be fabricated. TEM characterization indicates that the extended defects are closely related to Ruddlesden-Popper type anti phase boundaries. The characteristic triangular microstructure of the films can be explained by an island growth along preferential crystallographic planes inducing a self shadowing effect during deposition. Defect regions contain overall less material compared to the surrounding regions and show a slight Sr-excess.

In section 4.2, the preparation of Ta and Ta_2O_5 films by reactive sputter deposition and oxygen plasma oxidation was introduced. All films show a smooth surface with a low roughness. XRD and TEM analysis confirmed that all thin films were amorphous. XRR measurements

of plasma oxidized Ta films revealed a linear relationship between the process power and the thin film thickness.

The influence of the sputter power and the oxygen partial pressure was studied for deposition of TaO_x thin films. The film stoichiometry was investigated by *in situ* XPS. It was demonstrated that both parameters can be used to continuously tune the thin film composition in a wide stoichiometry range. Fitting of the Ta 4f core level gave insights into the electronic structure of the thin films. By plotting the individual tantalum components against the O/Ta ratio, it was observed that Ta^{5+} and Ta^0 linearly change with the oxygen content. The sub oxide distribution, however, exhibits a semicircle shape. By measuring the sheet resistivity for all sub-stoichiometric films, an exponential dependency of the resistivity against the oxygen content could be identified for O/Ta ratios up to a value of 1.9. Further increasing the oxygen content resulted in an abrupt increase in resistance of several orders of magnitude.

Lastly, the effect of electro-reduction on Ta_2O_5 memristive devices was investigated. X-PEEM characterization revealed the formation of oxygen vacancy rich $\text{Ta}_2\text{O}_{5-x}$ regions, formed after a high voltage arcing. Extracting and fitting of the Ta 4f core level provide an information basis for the structure of conductive filaments. No evidence for a metallic Ta^0 component was found.

5 Resistive switching in SrTiO₃ and Ta₂O₅ thin film devices

In this chapter, the resistive switching properties of SrTiO₃ and Ta₂O₅ based devices will be studied in detail. To gain deeper insights into the physical origins of the switching process, electrical characterization is performed in different atmospheres and at different temperatures. The results presented in this chapter have been published in parts in:

T. Heisig, J. Kler, H. Du, C. Baeumer, F. V. Hensling, M. Glöck, M. Moors, A. Locatelli, T. O. Menteş, F. Genuzio, J. Mayer, R. A. De Souza and R. Dittmann, "Antiphase Boundaries Constitute Fast Cation Diffusion Paths in SrTiO₃ Memristive Devices," *Advanced Functional Materials* **2020**, 30, 48, p. 2004118.

5.1 Resistive switching in SrTiO₃ thin film devices

As mentioned in section 2.4, depending on the fabrication method and film thickness, SrTiO₃ can possess an eightwise or counter-eightwise switching polarity. In this section, both polarities will be discussed. Afterwards, the impact of the SrTiO₃ thin film properties on the switching polarity will be elucidated.

5.1.1 Eightwise switching in SrTiO₃

In this section, Nb:SrTiO₃/20 nm SrTiO₃/Pt metal-insulator-metal (MIM) devices are investigated. An equivalent circuit diagram of such a device is depicted in Figure 5.1 a). As all eightwise switching curves presented in this thesis have qualitatively similar switching characteristics, the general features and the terminology will be introduced on the basis of the prototypical I - V curve shown in figure 5.1 b)-d).

In the untreated (or pristine) state, the MIM cell exhibits a high resistance in the gigaohm region ($\geq 10^9 \Omega$). Upon biasing the device in the forward direction of the Schottky diode, i.e. applying a positive voltage to the high work function Pt electrode, current starts to flow (compare "1" in figure 5.1 b)). If the positive bias is further increased, a sudden increase in

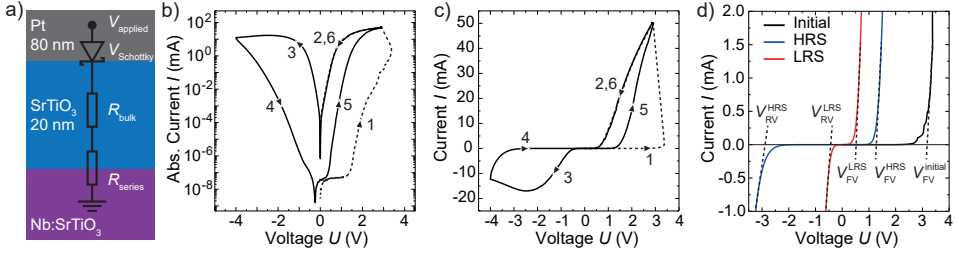


Figure 5.1: a) Equivalent circuit diagram of the Nb:SrTiO₃/20 nm SrTiO₃/Pt device. b) Logarithmic and c) linear representation of a typical I - V curve showing the electroforming (dashed line) and the subsequent switching cycle. d) Magnified part of the I - V curve in c) showing the low current region. Dashed lines indicate the forward- and reverse voltage.

current is observed. This is seen as a kink in the I - V curve in 5.1 c) at 3.4 V. This so-called electroforming process reduces the device resistance to the kilohm range ($\leq 10^5 \Omega$). In order to prevent damage from high currents, the device is protected by a current compliance that limits the maximum current. In this case a current compliance of 50 mA was used. The device is now in the low resistance state (LRS). Generally, the resistance change is non-volatile and the device remains in a conductive state if the voltage is removed. However, for some devices the LRS is unstable and the resistance will gradually increase over time. The time that passes until the LRS state becomes indistinguishable from the initial or high resistance state (HRS) is called the retention time. Retention times in SrTiO₃ can vary from a few minutes up to several weeks or month.

From the LRS state the device can be reset to the HRS by applying a negative bias (see "3" in figure 5.1 b) and c)). For a typical reset a voltage between -3 and -4 V is required. Exceeding -4 V quickly results in a permanent device failure, which is often evidenced by damaged top electrodes. In contrast to the LRS, the HRS is always stable under ambient conditions. From the HRS the device can be set into the LRS state again by applying a positive bias. Besides the here shown quasi-static I - V sweeps, devices can also be operated using short voltage pulses. However, to study the switching mechanism it is beneficial to measure full I - V curves as they provide additional information about the voltage dependent current transport mechanisms.

Figure 5.1 d) shows the low current regime of the LRS, HRS and the virgin device state. From the plot it becomes evident, that all states have a non-linear current voltage relationship, which is expected for a device with a Schottky junction. To characterize the junction, two important parameters are considered. The forward- (V_{FV}) and reverse voltage (V_{RV}). These parameters indicate the minimal voltage that is required to observe an increasing current flow. In the virgin state, the device has a very high forward voltage exceeding 3 V. Once the device is formed, the forward voltage decreases to 1.3 and 0.5 V for the HRS and LRS respectively.

This indicates, that the largest change of the Schottky barrier occurs during the electroforming process. Nevertheless, the modulation of the Schottky barrier between LRS and HRS has a great impact on device resistance. Looking at the negative voltage branch, a significant change of the reverse voltage between LRS and HRS is visible. The HRS exhibits a typical Schottky diode behavior where $V_{RV} \gg V_{FV}$. In contrast, the LRS is almost symmetrical with $V_{FV} \approx V_{RV}$, which is indicative for a high doping concentration.

Role of the cation stoichiometry

The influence of the cation stoichiometry in epitaxial SrTiO₃ devices is discussed at length in refs. [110, 152, 169]. Here, the most important differences between Sr-rich and stoichiometric SrTiO₃ will be briefly summarized. The conclusions drawn from the influence of the cation stoichiometry will serve as basis for the discussion of the spectromicroscopic data in chapter 6.

Figure 5.2 shows a comparison of the switching characteristics between a Sr-rich and a stoichiometric sample. The thin film stoichiometry was estimated based on the deposition rate as described in ref. [141]. The Sr-rich sample has a cation ratio of $\text{Sr}/(\text{Sr}+\text{Ti}) \approx 0.53$ and the stoichiometric sample a ratio of $\text{Sr}/(\text{Sr}+\text{Ti}) \approx 0.5$. Comparing the I - V curves in figure 5.2 a) and d) illustrates the main differences between both samples. Sr-rich devices show a distinct forming step (dashed lines) at high positive voltages, whereas the forming step in the stoichiometric sample is indistinguishable from the subsequent set process. The kink in the I - V curve of the Sr-rich sample at approximately +3 V is caused by a rapid decrease of the device resistance in combination with an active current compliance. Due to the rapid decrease of the device resistance, the source measuring unit reduces the applied voltage to stay within the selected current limit. This gives rise to the observed kink shape. Here it is important to note that the used Keithley 2611 source measuring unit has a response time in the μs region. This means that for a short amount of time (several microseconds) an undefined current passes through the sample. This so-called overshoot current is only limited by the series resistance of the circuit.

It can be seen that the devices on the stoichiometric sample that have been operated with lower currents show no complete set. This is especially evident in the negative voltage branch. For the 10 and 20 mA devices, the current is decreased by several orders of magnitude compared to the 30 and 50 mA devices. It is not surprising that the current compliance has a large impact on the I - V curves, as it is one of the most important switching parameters. The reason for this is that the current limit controls the Joule heating induced temperature increase during switching. Because Joule heating depends quadratically on the current, a small increase of the current limit can lead to a significantly higher temperatures.

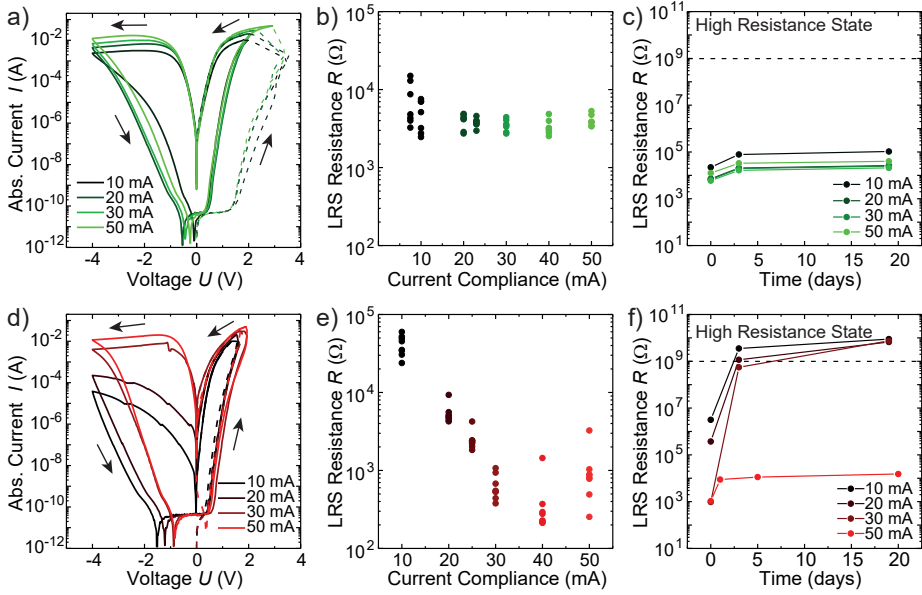


Figure 5.2: Representative switching curves of Nb:SrTiO₃/20nm SrTiO₃/Pt devices. Samples with a Sr-rich (green) and a stoichiometric (red) SrTiO₃ layer are compared. a) I - V curves of the Sr-rich sample. Each curve represents an individual device switched with the specified current compliances. The dashed lines indicate the electroforming process. b) LRS resistances as a function of the current compliance. At least 5 devices per current compliance were measured. c) Retention measurement of the LRS. d) I - V curves, e) LRS resistance and f) retention of the stoichiometric sample. Modified from ref. [170].

To investigate how the current compliance effects the switching, multiple devices on each sample were switched with current limits from 5 to 50 mA. The influence of the current compliance on the LRS is illustrated in figure 5.2 b) and e). Interestingly, the LRS is almost constant for the Sr-rich sample with a resistance of approximately $3 \times 10^3 \Omega$. Only devices switched with currents below 10 mA exhibit a slight higher resistance and a larger data spread. In contrast, the stoichiometric sample shows a significantly higher LRS for currents below 25 mA. This indicates that the set process is not completed at low currents. This is in accordance with the conclusions derived from the I - V curves. For higher currents the LRS resistance decreases until it reaches a minimum of $3 \times 10^2 \Omega$ at 40 mA. Further increasing the current to 50 mA leads to a slight increase of the resistance.

For their use as non-volatile memory the so called retention time is a key parameter that determines how stable a programmed resistive state is. Compellingly, the stability of a resistive state is often closely connected to the underlying processes that drive resistive switching. Accordingly, it is sometimes possible to deduce conclusions about the switching mechanism

from the retention behavior of a device [110,171]. Therefore, the stability of the LRS state was investigated over a time span of several days. Figure 5.2 c) and f) shows the evolution of the LRS resistance over time. For the Sr-rich sample, an initial increase of the resistance of approximately one order of magnitude is observed after a time span of three days. After this, the LRS state is stable for at least 17 days. Importantly, no difference in the stability is observed for different current compliances. In contrast, the LRS state of the stoichiometric sample is unstable for current compliances below 50 mA. Already after 3 days the LRS state for 10 and 20 mA reached the HRS resistance and the 30 mA is only slightly below the threshold. A further increase of the resistance after 17 days is observed, where all devices switched with low currents converged to a single resistance state. The device that was switched with 50 mA shows a stable retention after a small increase of resistance after 1 day. With this, the device resembles the retention behavior of a Sr-rich device.

To recapitulate, the main differences in the switching behavior of Sr-rich and stoichiometric thin films can be summarized by the following observations:

1. Sr-rich thin films have a higher initial resistance, forward voltage and show a distinct forming step.
2. Stoichiometric thin films require higher currents to achieve a complete set to the LRS.
3. Sr-rich thin films have a superior LRS stability that is independent of the current limit.

In the following, the physical origins of the different switching behavior will be discussed. To understand the high initial resistance and forward voltage in Sr-rich samples, it is mandatory to know how the thin film properties effect the Schottky barrier. As described in section 2.1, the surface of SrTiO₃ can be terminated either by a TiO₂, a SrO layer or by a mixture of both. For a Sr-rich growth, the surface is expected to be completely SrO terminated [143], whereas a stoichiometric growth gives a mixed terminated surface [141]. It is known that the Schottky barrier height is very sensitive to surface and interface states, which are formed by the atomic layers that are the closest to the surface. Hence, it can be predicted that a different Schottky barrier is formed for SrO and mixed terminated surfaces due to the different electronic structure of the surface [172]. Further, it was reported that SrO terminated thin films are chemically reactive whereas a TiO₂ termination is considered to be mostly inert [141]. Exposing SrO terminated SrTiO₃ film to an ambient atmosphere leads to the formation of SrCO₃ [173]. Depending on the exact nature of the interface states, the SrO termination can either increase or decrease the Schottky barrier height. This effect was studied in detail in ref. [169]. As expected from the measured *I-V* characteristics, the Schottky barrier height for Sr-rich films is higher ($\Phi_B \approx 1.00$ eV) compared to the Schottky barrier of stoichiometric films (0.91 eV). Therefore, it can be assumed that the differences in the initial state correspond to a modified Schottky barrier due to different interface properties.

The observed scaling of the LRS in stoichiometric films is likely related to the missing electroforming step. Considering that the forming in Sr-rich devices takes place at high electric fields, a high overshoot current flows until the current compliance becomes active. As the overshoot current is independent of the current compliance, the filament is formed equally in all cases. This implies that the forming procedure is the predominant step that defines the LRS resistance in the Sr-rich case. Contrary, if no distinct forming process occurs the LRS depends on the current compliance. To test this hypothesis, switching of Sr-rich devices could be repeated with a passive series resistance that limits the overshoot current. In this case, also a scaling of the LRS resistance would be expected for Sr-rich devices.

A similar argument can be made to explain the observed retention characteristics of both samples. As the forming process in the Sr-rich case produces similar filaments independent of the current compliance, the retention characteristics are also similar. For the stoichiometric sample, however, it can be argued that a stable retention is only observed if the filament is formed with a sufficiently high current. This is only the case for the device switched with 50 mA. The question remains why high currents and a pronounced electroforming is beneficial to achieve a stable LRS. This question will be discussed in more detail in chapter 6.

5.1.2 Counter-eightwise switching in SrTiO₃

In this section, the resistive switching properties of 80 nm Sr-rich SrTiO₃ devices are analyzed. As mentioned in section 2.4, SrTiO₃ devices can exhibit a counter-eightwise switching polarity if the oxide is deposited as amorphous or polycrystalline thin film [114, 115, 117]. To emulate this effect for PLD grown thin films, extended defects were intentionally introduced by performing depositions at low substrate temperatures as described in chapter 4.1.

As expected for devices with thicker oxide films, the initial resistance increases and the forming step requires higher voltages and longer forming times. The electroforming time can vary from milliseconds to several minutes. For this reason, electroforming is performed by applying a constant positive voltage to the Pt electrode until a specified current limit is reached. Figure 5.3 a) shows a direct current forming procedure. In this particular case, the device was biased with a constant voltage of 5 V until a current of 1 mA is reached. During the biasing time, the conductivity steadily increases until a rapid increase of current can be observed after approximately 60 s. Within the next 5 s the current compliance is reached and the device is considered to be formed. While individual devices show a large variation in the forming time, the general $I-t$ trend is similar in all cases. After electroforming, the device switches in a counter-eightwise polarity (figure 5.3 b) and c)). Starting in the LRS, the device can be reset

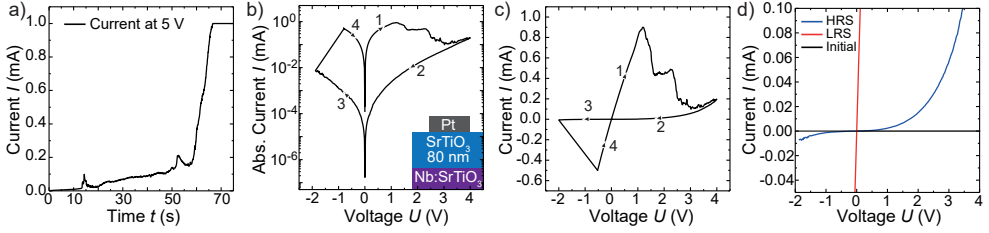


Figure 5.3: Counter-eightwise switching characteristics of a Nb:SrTiO₃/80 nm SrTiO₃/Pt device. a) I - t curve of a direct current electroforming procedure using a bias of 5 V. b) Logarithmic and c) linear representation of a typical counter-eightwise I - V curve. d) Low current region of the I - V curve in c).

by applying a voltage sweep from 0 to 4 V. Because the reset process is self-limiting, no current compliance is needed. In general, the reset occurs gradually and the HRS state depends on the reset voltage. For this sample a complete reset was achieved at 4 V. Performing the reset with smaller voltages yields intermediate resistance states. Typical HRS resistances are in the order of $\geq 10^6 \Omega$. Biasing the device in the reverse Schottky diode direction (negative voltages applied to the Pt electrode) a set is observed at approximately -2 V. As the set is a self-accelerating process, a current limit is required to prevent permanent damage of the device. For this device, a current compliance of 1 mA was used. Characteristic for the counter-eightwise polarity is the apparently instantaneous set as evidenced by the jump of the I - V curve to lower voltages (compare figure 5.3 b) and c) number 3 to 4). The resistance of the LRS is generally in the kilo-ohm region ($\approx 10^3 \Omega$).

Taking a closer look at the low current region shown in 5.3 d), reveals important differences to the eightwise polarity. First, the initial state is insulating over a large voltage range of ± 6 V (here only an excerpt from -2 to 4 V is shown). This is expected as, in a first approximation, the electric field is inversely proportional to the distance between bottom and top electrode. However, the situation is complicated because the electric field is not homogeneous across the insulator but a large voltage drop occurs at the Schottky barrier. The second key difference is the linear (or ohmic) I - V relationship of the LRS state. This indicates that the Schottky barrier is doped degenerately and is not the dominant current limiter of the device, as this would give rise to a non-linear I - V characteristic. Considering that the LRS resistance is in the order of a few kilo-ohms, it is likely that the main resistance is caused by the conduction through the bulk (or plug) part of the filament.

Influence of the atmosphere on counter-eightwise switching SrTiO₃

As the operation principle of transition metal oxide memristive devices relies on the formation and redistribution of oxygen vacancies, it is conceivable that the surrounding atmosphere and

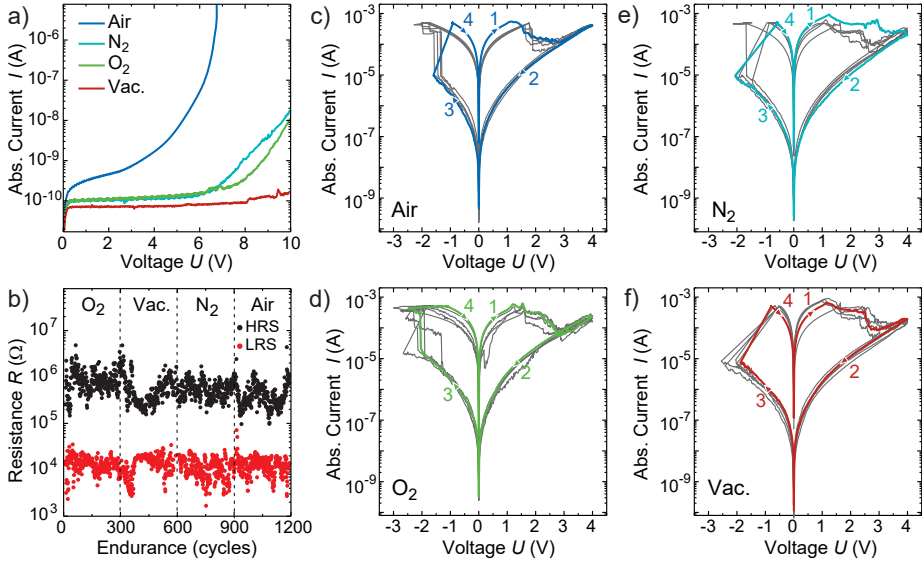


Figure 5.4: Switching characteristics of a Nb:SrTiO₃/80nm SrTiO₃/Pt device in various atmospheres. a) I - V sweep of a pristine device biased in different atmospheres. b) Switching of the device in different atmospheres using short voltage pulses. I - V curves the device in c) air, d) O₂, e) N₂ and f) vacuum. The first I - V curve is colored and subsequent cycles are shown in gray.

in particular the oxygen partial pressure, has an impact on the device properties [120, 171]. Besides the oxygen partial pressure also the humidity is to have an effect on the electronic and ionic properties of oxides in general [174] and SrTiO₃ [175, 176] in particular. Accordingly, it was investigated how the surrounding atmosphere affects the switching characteristics.

In a first step the sample was placed in a vacuum chamber equipped with micro probes for electrical characterization. After storing the sample for 24 h at a pressure of $\approx 10^{-6}$ mbar, I - V sweeps from 0 to 10 V were employed. Similarly, I - V sweeps were performed in N₂, O₂ and air atmosphere. For this, the evacuated chamber was flooded with the specified gas and electrical characterization was performed under constant gas flow. Between each atmosphere change, the chamber was completely evacuated. Figure 5.4 a) shows the I - V sweeps of the same device in different atmospheres. Importantly, the device remained in a pristine state and a small current limit of 10 μA was employed to ensure that no electroforming occurred between the individual measurements. Interestingly, one can observe a clear influence of the atmosphere on the I - V characteristics. Under vacuum conditions, the device has extremely insulating properties. Even under a high bias of 10 V, the current barely exceeds 10^{-10} A. Under N₂ and O₂ atmospheres, however, the current rises at approximately 7 V up to a maximum current of $\approx 10^{-8}$ A at 10 V. Comparing both gases, N₂ and O₂, only minor differences are noticeable.

The most striking change is visible for the measurement in air. Over the entire voltage range a comparably high current is observed. This observation was verified by repeating the measurement on five nominally identical devices. To exclude that a partial electroforming is causing the current differences between atmospheres, the order in which the atmospheres were studied was varied. For all devices, the general trend $I_{\text{Air}} \gg I_{\text{N}_2} \approx I_{\text{O}_2} > I_{\text{Vac.}}$ was found.

To understand this strong effect of the surrounding atmosphere, it is necessary to identify the component that causes the increasing current in air. By volume air contains 78.09% N₂, 20.95% O₂, 0.93% Ar, $\approx 1\%$ H₂O (on average at sea level) and small amounts of other trace gases [177]. From these main components N₂ and O₂ can be excluded as origin for the high conductivity in air, as the devices remain insulating in the corresponding pure atmospheres. Further, Ar is considered to be chemically inert. Therefore, it is unlikely that Ar has a big impact on the conductivity. H₂O on the other hand is highly reactive towards oxides. It is known that humidity can affect the electronic properties of memristive devices, which renders it the most probable candidate that influences the conductivity [120, 178–180]. The slight current increase in N₂ and O₂ atmospheres compared to vacuum can be explained by trace amounts of H₂O impurities in the gas supply, which are typically in the low parts-per-million range. The underlying mechanism that leads to a sensitivity towards moisture is still an active research area and depends on the details of used materials, their microstructure and the fabrication process [181]. For oxygen vacancy rich oxides, it is known that water is incorporated into the oxide matrix through dissociation of H₂O. This process can be expressed according to



where $\text{OH}_{\text{O}}^{\bullet}$ represents a hydroxide ion (OH^-) on a regular oxygen anion lattice site.

The incorporated protons can migrate through the bulk oxide via proton hopping (similar to the Grotthuss mechanism) or through a vehicle-type mechanism. This increase the ionic conductivity of the SrTiO₃ layer [182]. Besides the incorporation of H₂O, also the modulation of the Schottky barrier is discussed as possible origin of the moisture sensitivity of SrTiO₃ ReRAM devices [178]. Both mechanism, an increased ionic conduction or a Schottky barrier modulation, could be responsible for the observed sensitivity to moisture of the initial state.

Going beyond the characterization of the initial state, also the switching properties were studied in different atmospheres. For this, devices were electroformed in air and subsequently switched 300 times in each atmosphere (compare figure 5.4 b)) using voltage pulses. A general trend is observable where the HRS resistance decreases with increasing number of cycles.

Table 5.1: Switching parameters in different atmospheres extracted from the I - V curves in figure 5.4 c-f). The values are averaged over 10 switching cycles for each sample.

	Air	N_2	O_2	Vacuum
$R_{\text{HRS}} (\Omega)$	$4.8 \cdot 10^5$	$1.8 \cdot 10^6$	$1.1 \cdot 10^6$	$3.4 \cdot 10^6$
$R_{\text{LRS}} (\Omega)$	$4.5 \cdot 10^3$	$1.8 \cdot 10^3$	$2.4 \cdot 10^3$	$1.1 \cdot 10^3$
$R_{\text{HRS}}/R_{\text{LRS}}$	$1.1 \cdot 10^2$	$1.0 \cdot 10^3$	$4.6 \cdot 10^2$	$3.0 \cdot 10^3$
$V_{\text{SET}} (\text{V})$	-1.4	-1.8	-2.3	-2.2
$V_{\text{RESET}} (\text{V})^1$	1.6	1.2	1.4	1.2

¹ V_{RESET} is defined as the smallest voltage at which the current starts to decrease.

However, it is not clear if this effect is caused by the atmosphere or if it is an aging effect of the device. Due to the large cycle-to-cycle variance of the device, it is difficult to determine if the atmosphere has an effect just from the resistance values. Therefore, devices were switched using I - V sweeps. This allows the quantification of additional switching parameters, such as set and reset voltage. Representative I - V curves from a single device are shown in figure 5.4 c-f) and the switching parameters are given in table 5.1. Again, the devices could be switched repeatedly in all atmospheres. Interestingly, V_{SET} differs significantly between dry atmospheres and air. While the set in air occurs already at a voltage of -1.4 V, under vacuum conditions -2.2 V are required. This large difference in the set voltage can be understood by the fact that the HRS state is less insulating in air and thus the critical set current is reached at lower voltages. Further, the memory window ($R_{\text{HRS}}/R_{\text{LRS}}$) is the smallest in air and is over one magnitude larger in vacuum, again due to the comparatively conductive HRS state in air.

From the obtained results of the atmosphere dependent measurements, it can be concluded that the SrTiO_3 based memristive devices interact with the surrounding atmosphere. In particular, the initial state of the devices is highly sensitive to H_2O containing atmospheres, decreasing the resistance by several orders of magnitude. Further, the atmosphere has an impact on the switching properties, where operation in dry atmospheres and under vacuum conditions requires higher set voltages. Finally, the presence of humidity reduces the memory window by approximately one order of magnitude. A more detailed discussion of the origin of the atmospheric influence on counter-clockwise switching memristive devices will be given in section 5.2.3.

5.1.3 Impact of the thin film thickness and growth temperature on the switching polarity

Previous studies could show, that the switching polarity in Sr₂TiO₄ memristive devices is determined by the defect density and the thin film thickness [67]. To investigate if a similar correlation is also observed in SrTiO₃ devices, samples grown at various temperatures and film thicknesses. Afterwards they have been electrically characterized. For this, a large number of devices were switched on each sample. To test if a sample shows eightwise or counter-eightwise switching, the electroforming step was performed either by an I - V sweep or by using a DC bias as described in sections 5.1.1 and 5.1.2.

Figure 5.5 a) shows the switching polarity of Nb:SrTiO₃/SrTiO₃/Pt devices as a function of growth temperature and film thickness. From the graph a clear correlation between the switching polarity and the growth temperature can be seen. Samples grown at 800 °C exhibit an epitaxial crystal quality and almost exclusively show eightwise switching. An exception is the 80 nm thin film sample, that also features counter-eightwise switching. Reducing the growth temperature leads to a transition towards a counter-eightwise polarity. For temperatures below 700 °C, only counter eightwise switching was observed. Under these growth conditions, SrTiO₃ films have a high density of antiphase and island-boundaries (compare section 4.1). Interestingly, in the transition region at $T = 700$ °C, the sample exhibits both switching polarities in a single device (coexisting polarities). Two exemplary I - V curves of a device with coexisting polarities are shown in figure 5.5 b). Initially, the device started with an eightwise polarity, but upon cycling of the device, the polarity changed to counter-eightwise switching. Characteristic for such a device is the shared resistive state between both polarities, i.e. the LRS of the eightwise cycle corresponds to the HRS of the counter-eightwise cycle. Similar observations of coexisting polarities have been observed in TiO₂ memristive devices [127]. Since the occurrence of coexisting polarities indicates the presence of two competing switching mechanism, it represents an intricate special case. Thus, for the purpose of this thesis, the investigation of devices with coexisting polarities will be neglected.

To understand what causes the transition between eightwise and counter-eightwise switching, it is important to consider how the film properties influence the electrical and ionic properties of the memristive devices. As discussed in chapter 2.4, eightwise switching in SrTiO₃ can be explained by a modulation of the Schottky barrier height and thickness through oxygen vacancies. Upon increasing the film thickness of the SrTiO₃, the bulk resistance of the oxide layer increases while the Schottky barrier is unaffected. If the oxide layer reaches a critical thickness, it can be assumed that the modulation of the Schottky barrier alone is not sufficient to establish a conductive LRS state and an oxygen vacancy rich filament is formed between bottom- and top electrode (the so-called "plug"). In contrast to other classical counter-eightwise switching systems that employ oxidizable electrodes, no oxygen vacancies

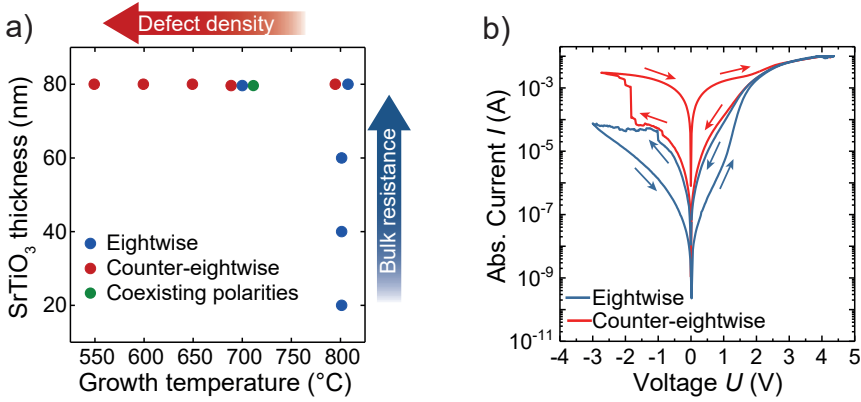


Figure 5.5: Impact of the thin film thickness and growth temperature on the switching polarity. a) Switching polarity of samples composed of SrTiO_3 films grown at various temperatures and with different thicknesses. All thin films were grown with a cation ratio of $\text{Sr}/(\text{Sr} + \text{Ti}) \approx 0.53$. b) I - V characteristics of an 80 nm SrTiO_3 device grown at 700°C that showed coexisting switching polarities.

can be generated at Nb: SrTiO_3 the bottom electrode. For this reason, a DC electroforming step with a high positive bias is required that generates a large amount of oxygen vacancies. Afterwards, switching is facilitated by the redistributed of oxygen vacancies throughout the SrTiO_3 layer. Reducing the growth temperature on the other hand, leads to a high concentration of extended defects. It has been suspected that such defects facilitate diffusion processes, i.e. oxygen migration, and could therefore favor an internal redistribution of oxygen vacancies within the SrTiO_3 layer, leading to counter-eightwise switching [68, 112, 183]. However, by measuring and simulating oxygen isotope diffusion profiles, no evidence was found for fast grain-boundary diffusion in dislocation-rich single crystalline SrTiO_3 [66, 184, 185]. Thus, the impact of extended defects on the ionic mobility and electronic properties is still an active research area and most likely depends on the details of the defect structure and the electric field. The effect of extended defects for resistive switching will be discussed in more detail in section 6.2.

5.1.4 Summary of resistive switching in SrTiO_3

In summary, the resistive switching properties of Nb: SrTiO_3 / SrTiO_3 /Pt memristive devices were investigated. Depending on the SrTiO_3 thin film properties, eightwise, counter-eightwise and coexisting switching polarities could be observed.

For epitaxial thin films below 80 nm, only eightwise switching was obtained. Eightwise switching is characterized by non-linear I - V characteristics in both resistive states, indicating a

Schottky barrier limited current transport. Comparing devices fabricated from stoichiometric and Sr-rich SrTiO₃ layers revealed that Sr-rich devices require an electroforming step at higher positive voltages. A general trend was observed where the Sr-rich devices exhibit a superior LRS retention even for small switching currents. Because of this, the comparison between stoichiometric and Sr-rich devices can be used to study underlying mechanism that give rise to a stable retention or retention failure using spectromicroscopy, as presented in chapter 6.

Counter-eightwise switching was observed in 80 nm thick SrTiO₃ films and was especially common in samples grown at lower temperatures with a high defect density. In contrast to the eightwise polarity, the LRS state in counter-eightwise switching SrTiO₃ exhibits an ohmic I - V characteristic. This indicates that the LRS resistance is dominated by bulk conduction and not by the Schottky barrier. Atmosphere dependent measurements revealed a clear correlation between the pristine device resistance and the surrounding atmosphere. For dry atmospheres, the resistance was several orders of magnitude higher. This suggests that the conductivity in the pristine device is caused by ionic conduction of protonic defects. Switching in all atmospheres proved to be possible for at least a few hundred switching cycles. This demonstrates that switching is possible under UHV conditions, which is essential to study the switching mechanism via *in operando* spectromicroscopy in a TEM (see chapter 6).

5.2 Counter-eightwise switching in Ta₂O₅ thin film devices

In this section, the resistive switching characteristics of Ta₂O₅ based devices are analyzed. The switching behavior of cells with different top electrodes will be investigated. Further, the impact of the oxide film thickness and preparation method of the Ta₂O₅ film will be discussed.

5.2.1 General switching characteristics and influence of different top electrode materials

Figure 5.6 shows the I - V characteristics of a Ta/Ta₂O₅ stack with a-c) Pt and d-f) single layer graphene as top electrode. Single layer graphene electrodes were employed to enable the characterization of the switching layer by surface sensitive spectroscopy, which will be presented in chapter 7. Both electrode materials have a high work function of 5.5-5.9 eV for Pt [186] and 4.5 eV for graphene [187]. Hence, the formation of a Schottky junction with Ta₂O₅ is expected in both cases.

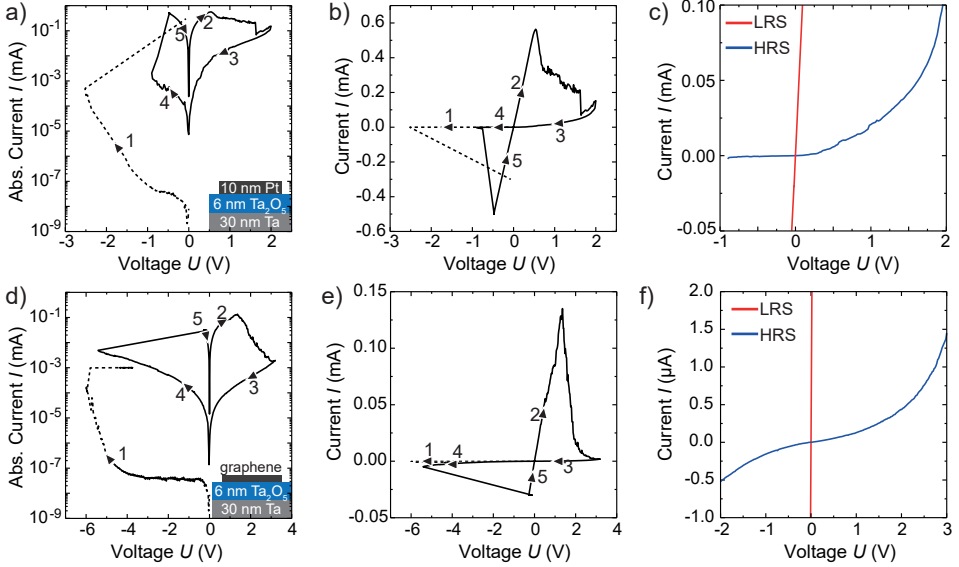


Figure 5.6: Counter-eightwise switching curves of 30 nm Ta/6 nm Ta_2O_5 devices with different top electrodes. a) Logarithmic and b) linear representation of an exemplary counter-eightwise I - V curve of a device with Pt electrode. The dashed lines indicate the forming step. c) Low current region of the I - V curve in b). d) Logarithmic and e) linear switching curve of a device with graphene top electrode. f) Low current region of the I - V curve in e).

All investigated devices show a typical counter-eightwise switching behavior. Initially, the devices are highly insulating and they can be electroformed by applying a negative voltage to the top electrode (compare dashed lines in figure 5.6 a) and d)). Graphene devices are formed with the smallest possible current limit to minimize the electrical stress that is applied to the graphene electrode. After the forming step the cells are in the LRS and can be reset to the HRS by applying a positive voltage. Upon biasing with a negative voltage, the devices set into the LRS state again. Typical switching parameters are given in table 5.2. Similarly to the counter-eightwise switching in SrTiO_3 , both device stacks show a completely ohmic LRS state, while the HRS exhibits a non linear current-voltage relationship (see figure 5.6 c) and f)). Comparing both device stacks, however, three key differences can be identified. First, devices with graphene electrodes require higher forming, set and reset voltages. Second, the HRS and LRS of graphene devices are shifted towards higher resistances. Lastly, the memory window is almost one order of magnitude higher for graphene devices.

To understand the origin of the quantitative differences between Pt and graphene devices, it has to be considered that graphene electrodes introduce an additional series resistance to the MIM stack. Typical values for the resistance of graphene top electrodes are in the order of 1-4 k Ω (compare figure A4 in the appendix). Considering that the LRS resistance of a Ta_2O_5

Table 5.2: Switching parameters for 30 nm Ta/8 nm Ta₂O₅ devices with different top electrodes.

	Pt	Graphene
$R_{\text{HRS}} (\Omega)$	$2.1 \cdot 10^5$	$9.8 \cdot 10^6$
$R_{\text{LRS}} (\Omega)$	$9.1 \cdot 10^2$	$9.3 \cdot 10^3$
$R_{\text{HRS}}/R_{\text{LRS}}$	$2.3 \cdot 10^2$	$1 \cdot 10^3$
$V_{\text{set}} (\text{V})$	-0.8	-5.4
$V_{\text{reset}} (\text{V})$	0.5	1.4

device is typically a few kilo-ohms, it becomes evident that the graphene series resistance has a significant contribution to the overall LRS resistance. In contrast, Pt electrodes have only a negligible resistance below 100 Ω . This means, that the LRS resistance in Pt devices is governed almost solely by the conductive filament. Therefore, in the case of a graphene device, the applied voltage drops partly over the series resistance, whereas in the case of Pt devices no voltage drop across the top electrode occurs. Accordingly, the electric field is smaller in graphene devices and higher reset voltages are required. The question remains why the graphene device exhibits a higher HRS state. The series resistance of graphene is in the HRS much lower compared to the device resistance and can therefore be excluded as a possible cause for the increased HRS. However, the origin of this so-called deep reset might be explained by the oxygen blocking properties of the graphene layer. Recent studies have found that in counter-eightwise switching Ta₂O₅ devices to a small extent also an oxygen exchange with Pt electrodes can occur. This concomitant process leads to a resistance hysteresis of opposite polarity [188]. It was proposed that the HRS in Ta/Ta₂O₅/Pt devices is limited by the exchange of oxygen with the Pt electrode. However, this process can be suppressed by introducing an oxygen blocking layer and a complete reset can be achieved that yields a higher HRS [189]. Graphene is known to exhibit such oxygen blocking properties [190]. Therefore, the increased HRS state of graphene devices is attributed to the suppression of oxygen vacancy generation at the graphene Ta₂O₅ interface.

Due to its chemical nature, i.e. being composed out of a single layer of carbon, graphene is very sensitive to thermal stress and prone to oxidize, especially if molecular oxygen is present. Thermal treatments in air showed that single layer graphene is stable up to $\approx 470^\circ\text{C}$ [191]. Above this temperature, the graphene quality quickly starts to degrade. While this temperature appears to be relatively high, it is known that during resistive switching temperatures of 720°C can easily be reached for a short duration [27, 192]. Therefore, it is mandatory to study the stability of graphene electrodes over a large number of cycles to evaluate how the thermal and electrical stress affects the graphene. For this, devices were cycled in pulse operation for several thousand cycles and characterized by Raman spectroscopy. Figure 5.7 a)

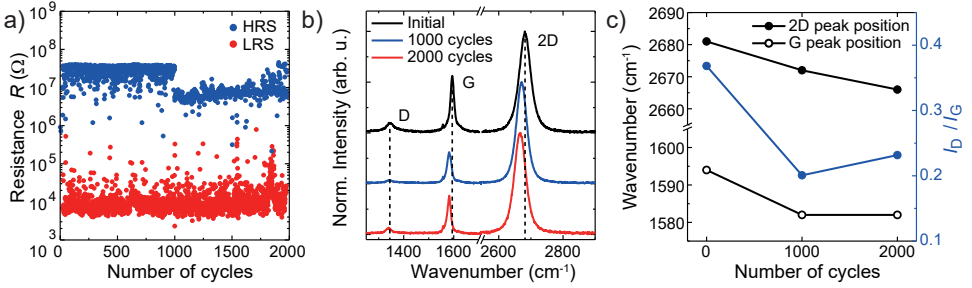


Figure 5.7: Long term switching stability of graphene electrodes. a) Endurance measurement of a Ta/8nm Ta_2O_5 /graphene cell. The set voltage was -7 V using 30 μA current compliance and the reset voltage was 3.2 V. b) Raman spectra of the graphene top electrode before (black), after 1000 cycles (blue) and after 2000 cycles (red). c) Peak area ratio I_D/I_G (blue) and peak position of the 2D and G band (black) as a function of the number of switching cycles.

shows a typical endurance measurement over 2000 cycles.¹ All investigated devices could be cycled at least 5000 and up to 20000 times before a breakdown occurred. In order to minimize the electrical stress during cycling, the switching voltage and current was chosen as small as possible while still allowing reliable switching. Figure 5.7 b) shows the Raman spectra of a device before, after 1000 and after 2000 switching cycles. The laser spot had the same size as the device crosspoint area of $10 \times 10 \mu\text{m}$. Thus, the measured spectra represent an average of the whole device area. To verify the reproducibility of the observed changes, a total of 5 devices were studied. For all devices similar trends were observed, which will be discussed for an exemplary device in the following.

Useful information about the structural and electronic properties of graphene can be extracted from the defect D, G and 2D band [193]. The intensity of the D band is indicative for the defect or disorder density of the graphene layer. High temperature thermal annealing in air or Ar^+ ion bombardment are known to increase the defect density and proportionally the intensity of the D peak [191, 194]. The defect concentration can be estimated by calculating the peak area ratio I_D/I_G , which is given in figure 5.7 c). Interestingly, I_D/I_G decreases after the first 1000 cycles, which indicates that fewer defects are present after switching. Further increasing the number of cycles to 2000, leads to an increase in the I_D/I_G ratio, however, it remains below the initial defect concentration. Intuitively this is surprising, as the electrical biasing of the device should induce new defects rather than reducing the amount of defects. This behavior might be explained by the self-healing properties of graphene layers. It was reported that the D band decreases during annealing in an inert Ar atmosphere. This effect was attributed to the recombination of mobile carbon adatoms with vacancies in the graphene layer [195]. It

¹The jump in the HRS resistance after 1000 cycles occurred after the sample was removed from the measurement setup for Raman characterization. The reason for this is unclear but could be related to contact problems between the probe tip and the sample, which would limit the applied voltage for the reset.

can be surmised that the same process can take place in air during switching with the heat that is produced by Joule heating. However, in opposition to the healing process, the creation of new defects can occur through a reaction of graphene with O₂. Therefore, it is assumed that the self-healing process is dominant in the early stages of the endurance test until the defect formation prevails in later stages. Considering that the reaction between graphene and oxygen results in the formation of volatile components (CO and CO₂) it is reasonable that a gradual decrease of carbon content leads to a degradation of the graphene layer and ultimately to a device failure, which is observed in graphene devices typically between 5000 and 20000 cycles.

Besides the D band, information about the doping concentration and structural properties can be extracted from the position and intensity of the G and 2D Raman band [196, 197]. Figure 5.7 c) shows the wavenumbers of the G and 2D band for the different stages of the endurance test. From the graph it is visible, that the wavenumbers of the 2D and G bands are shifting to lower wavenumbers. The shift of both bands indicates a change of the doping concentration induced by adsorbed gas molecules, such as CO, NO₂, H₂O or O₂ [198]. Shifting to lower wavenumbers, i.e. red shifting, suggests either desorption of acceptor dopants (H₂O, N₂O), adsorption of electron donating species (CO, O₂) or both. This processes could be facilitated by Joule heating as the adsorbents are stable at room temperature and elevated temperatures are required to trigger the desorption of molecules.

5.2.2 Thickness dependence

Understanding the relationship between film properties and electrical characteristics of a device is crucial to explain the working principles behind resistive switching. In this sense, it is especially important to investigate the influence of the insulator thickness, as it is known to have a great impact on the device functionality as well as on the underlying mechanism [148, 199]. Therefore, the influence of the Ta₂O₅ thickness will be studied in the following.

Figure 5.8 shows representative $I-V$ curves of a typical Ta/Ta₂O₅/Pt stack with increasing Ta₂O₅ thickness. Table 5.3 summarizes the switching parameters. While the general shape of the curves is similar, distinct differences can be noticed in the forming and switching behavior. Most importantly, with increasing film thickness the forming voltage increases from -1.42 V to -3.14 V from 4 nm to 8 nm Ta₂O₅. This is not surprising as the initial device resistance also increases with the film thickness while the electric field strength decreases. Interestingly, the LRS resistance does not follow a clear trend and the lowest resistance is observed for the 6 nm device with $5.1 \cdot 10^2 \Omega$. In contrast, the HRS resistance clearly scales with the insulator thickness. Unexpectedly, the HRS resistance decreases with increasing film thickness from

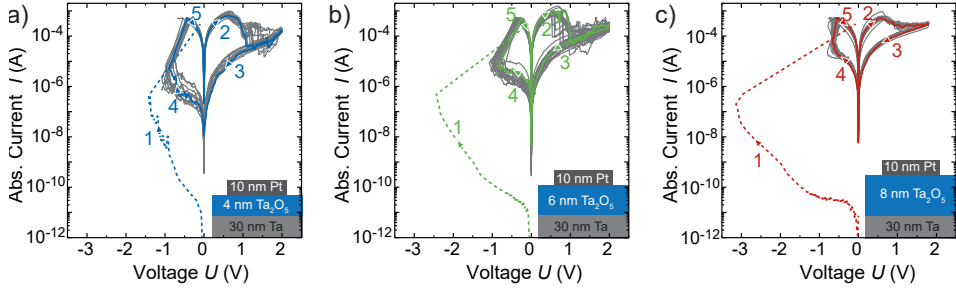


Figure 5.8: Thickness dependence of the Ta_2O_5 switching layer. Representative forming and I - V characteristics of a) 4, b) 6 and c) 8 nm Ta_2O_5 samples fabricated by O_2 plasma oxidation of the Ta films. For each device 25 I - V curves are shown in grey and the first sweep is shown in colour. The current limit was set to $300 \mu\text{A}$.

$2.6 \cdot 10^5$ to $1.9 \cdot 10^4 \Omega$ for 4 nm to 8 nm respectively. Consequently, the memory window is the largest for the 4 nm device with $3.0 \cdot 10^2$ being one order of magnitude higher than the memory window of the 8 nm device. Lastly, the set voltage also shows scaling with the film thickness. The highest absolute voltage is required for the 4 nm film with -0.90 V , whereas the 8 nm film sets at -0.66 V .

At a first glance it seems counter-intuitive that the HRS state scales inversely with the film thickness, as a thicker film should also provide a higher resistance. While this is true for the initial device state, it is not necessarily the case for formed devices. Because both states, LRS and HRS, are considerably more conductive as the initial state it can be assumed that the resistance of both states is governed entirely by the conductive filament. Therefore, the HRS resistance is a measure of how effectively the filament can be reset. This process is seemingly more effective for thinner films that have been formed with low voltages. One may surmise that the increasing forming voltage has an impact on the composition and size of the created filaments, making them increasingly difficult to reset. This explanation is in accordance to the HRS I - V asymmetry. For the 4 nm Ta_2O_5 film, the HRS shows a rectifying behavior, i.e. more current passes in the positive voltage polarity. This is expected for a Schottky barrier limited transport. In contrast, the 8 nm film shows an almost ohmic behavior resembling the LRS state.

5.2.3 Influence of the atmosphere

It was demonstrated in section 5.1.2 that the switching atmosphere, especially the humidity, can have a substantial influence on the electrical characteristics of resistive switching devices. Therefore, a similar study was repeated for Ta_2O_5 based devices to clarify if the atmospheric influence is a general feature of counter-eightwise switching.

Table 5.3: Switching parameters for 30 nm Ta/Ta₂O₅/Pt devices with different Ta₂O₅ thicknesses. The values are averaged over 25 switching cycles for each sample.

	4 nm Ta ₂ O ₅	6 nm Ta ₂ O ₅	8 nm Ta ₂ O ₅
$R_{\text{Pristine}} (\Omega)^1$	$1.8 \cdot 10^8$	$2.6 \cdot 10^9$	$1.9 \cdot 10^{10}$
$R_{\text{HRS}} (\Omega)$	$2.6 \cdot 10^5$	$4.8 \cdot 10^4$	$1.9 \cdot 10^4$
$R_{\text{LRS}} (\Omega)$	$8.7 \cdot 10^2$	$5.1 \cdot 10^2$	$1.1 \cdot 10^3$
$R_{\text{HRS}}/R_{\text{LRS}}$	$3.0 \cdot 10^2$	$9.3 \cdot 10^1$	$1.8 \cdot 10^1$
$V_{\text{Form.}} (\text{V})$	-1.42	-2.44	-3.14
$V_{\text{set}} (\text{V})$	-0.90	-0.82	-0.66
$V_{\text{reset}} (\text{V})$	0.62	0.57	0.58

¹ The resistance of the pristine state was determined by a linear fit of the forming I - V curve from 0 to -1 V.

For this, devices were formed and switched in air to verify that they exhibit an ordinary switching behavior. Afterwards, the sample was placed in a vacuum probe station and heated to 90°C for 12 h. This was done to minimize the residual water content in the chamber and in the sample. For the experiment a crossbar device architecture was used with a 15 nm thick sputtered Ta₂O₅ layer fabricated as described in chapter 3.3. The actual Ta₂O₅ thickness might be smaller across the edge step due to a non ideal coverage during the sputter deposition. Figure 5.9 a) shows the atmosphere dependent switching characteristics of a device. Starting in air, well defined and reproducible counter-eightwise switching is observed. The device was kept in the HRS before the chamber was evacuated. After 12 h of storing the sample at 90°C under vacuum, the device was allowed to cool down to room temperature before the electrical characterization was continued. Comparing the I - V curve measured in vacuum with those measured in air, several distinct differences can be seen. First, the HRS in vacuum is considerably more insulating. In air, the current rises to $1 \cdot 10^{-7}$ A at -1 V, whereas in vacuum a current of only $5 \cdot 10^{-10}$ A can be measured. This current decrease by almost three orders of magnitude significantly impacts the set voltage by increasing V_{set} from -1.7 to -6.8 V. Interestingly, trying to reset the device to the HRS was impossible in vacuum for all tested devices. Applying a positive voltage to the top electrode leads to a linear increase in current. However, no reset occurs even for high voltages up to 6 V. Further increasing the positive bias led in some cases to a permanent device breakdown. For this reason, the reset voltage was limited to 4-6 V. To test if the atmosphere permanently effects the device or if the changes are reversible, the devices were exposed to air and subsequently to vacuum again. Panel 3. shows switching in air after the vacuum treatment. It is evidenced that the switching characteristics of the device has been completely restored and no permanent change is apparent. Testing the device for a last time in vacuum atmosphere shows again the highly insulating HRS as well as the missing reset. Figure 5.9 b) displays the switching yield obtained from 16 individual

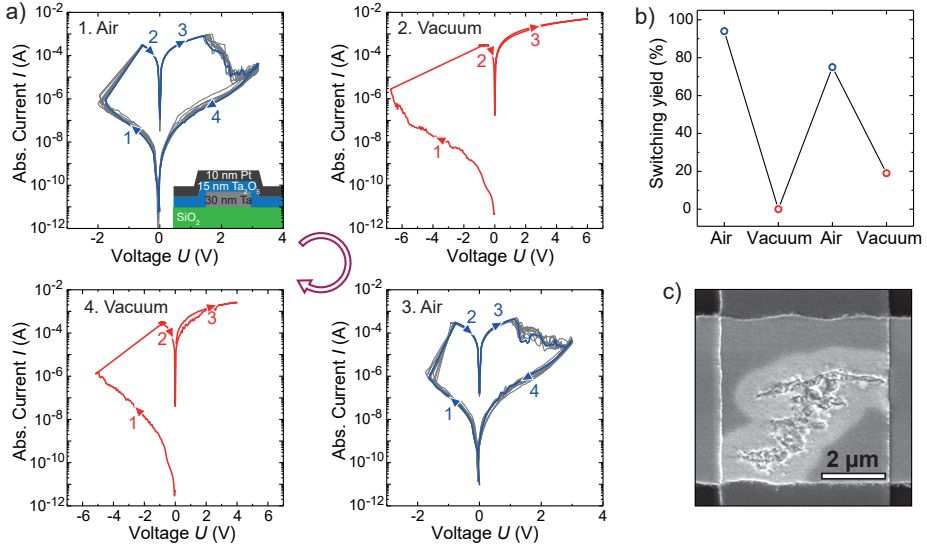


Figure 5.9: Influence of the atmosphere on the switching characteristics of Ta/ Ta_2O_5 /Pt devices. a) Representative switching curves of a single device in 1. Air, 2. Vacuum, 3. Air and 4. Vacuum. b) Switching yield of all tested devices in vacuum and air atmosphere. A total of 16 devices were measured. c) Scanning electron microscope image of a typical device failure occurred during an attempted reset process in vacuum.

devices as a function of the atmosphere. From this plot, it is apparent that the vacuum atmosphere almost always inhibits resistive switching. Further, the vacuum treatment has a negative influence on the device stability, as some devices did not recover in air and failed to switch again. In all cases the same failure mechanism was observed. The devices could not be reset and remained stuck in the LRS. In figure 5.9 c) a typical device breakdown is shown, which occurred in vacuum under high positive bias. Upon increasing the positive voltage, a high current of several milliamperes caused damage to the Pt electrode. Typically, the defects extend over several micrometers and show indicators for melting of the top electrode. The defects are surrounded by recrystallized Pt, which is visible as bright contrast. These defects are indicative for very high temperatures.

From these results, it can be concluded that Ta_2O_5 memristive devices interact strongly with the surrounding atmosphere. In particular, in absence of air, devices become much more insulating and the reset is inhibited. These observations are in good agreement with the results obtained for counter-clockwise switching SrTiO_3 . Interestingly, similar effects were found by Goux [171] and Lübber *et al.* [200]. The interpretation of the results, however, varies from each other. While Goux argued that switching in O_2 -poor environments results in the degradation of the device due to a loss of oxygen in the surrounding of the filament, Lübber found that

H_2O is crucial for resistive switching by acting as a redox active species. Unfortunately, both models cannot explain all experimental results obtained from the here presented experiment. In order to be conclusive, a model should reflect the effect of the atmosphere on the initial and HRS state, i.e. the higher conductivity in air, and the inhibition of the reset. For this, a combination of both models is proposed.

First, the increased conductivity is explained by the reaction of H₂O with intrinsic oxygen vacancies according to



If oxygen vacancies are filled by H₂O, the conductivity of the Ta₂O₅ film increases due to the ionic conductivity from the incorporated protons. However, to explain the observed atmospheric dependence, the reaction has to be reversible at moderately low temperatures of 90 °C in a vacuum environment. Further, the incorporation of protons should have a significant effect on the conductivity of Ta₂O₅ thin films. Lastly, the amount of intrinsic oxygen vacancies must be high enough to allow the accommodation of a substantial amount of protons.

Starting with the question whether the reaction 5.2 is reversible at low temperatures, a literature survey shows that the water content in hydrated amorphous Ta₂O₅ powders rapidly decreases after heat treatments above 50 °C [201]. While a direct comparison is difficult as the experiment was performed under ambient conditions, it shows that the removal of H₂O from Ta₂O₅ can occur well below the here used 90 °C. Additionally, the annealing in vacuum further shifts the thermodynamic equilibrium towards the release of H₂O. The effect of water content on the conductivity of Ta₂O₅ thin films was reported several times in literature and could be directly linked to a Grotthus-type proton conduction [201, 202]. The total conductivity can increase by several orders of magnitude with increasing proton content. Therefore, it seems reasonable that in ambient conditions, the HRS is determined by the ionic conductivity. The question remains if sputtered, nominally fully oxidized, Ta₂O₅ thin films contain H₂O under ambient conditions. The effect of incorporation of protons during reactive sputtering of Ta₂O₅ was investigated by Abe *et al.* using secondary ion mass spectrometry [203]. Analysing films sputtered in dry Ar/O₂ atmosphere revealed, that even for nominally dry atmospheres Hydrogen to Tantalum ratios of approximately 0.02 (or 2%) are observed. Even though a direct comparison is difficult, as the Hydrogen content will be influenced by the residual gas composition of the sputter chamber, the gas purity and the deposition parameters, it illustrates that proton impurities should not be neglected.

Now it will be discussed why the reset process is inhibited under vacuum conditions. Classically, the counter-clockwise switching mechanism considers only the internal redistribution of oxygen vacancies. Therefore the atmosphere should not affect the reset process. However, this simple picture neglects electrode reactions and oxygen exchange processes through permeable electrodes. First, the set in vacuum and air is compared. Figure 5.10 a) shows a side by side comparison of both processes. The set in vacuum requires almost four times more voltage than in air, leading to much higher electric fields through the Ta₂O₅ layer. Although the

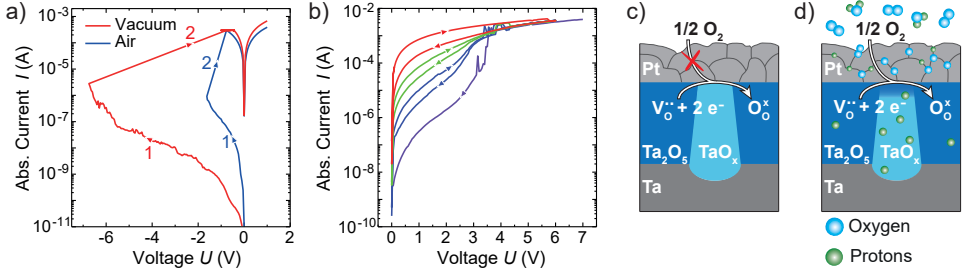
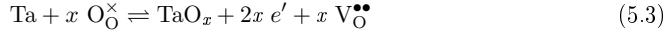


Figure 5.10: Influence of the atmosphere on the switching characteristics of Ta/ Ta_2O_5 /Pt devices. a) Side by side comparison of the set under vacuum (red) and in air (blue). b) Device response to successive reset sweeps in air after a vacuum set. Schematic illustration of the device state in c) vacuum and in d) air.

current limit was set to $300 \mu A$ in both cases, the transient current under vacuum conditions is expected to reach much higher values due to discharge of capacitances in combination with a slow acting current compliance [171]. Therefore, the set process in vacuum can be assumed to be much more vigorous. This effect is evidenced by a decreased LRS resistance by a factor of 2 after a set in vacuum, indicating that more oxygen vacancies have been created. The generation of excess oxygen vacancies can either be associated with further oxidation of the Ta bottom electrode, or through the release of molecular oxygen. The processes can be described by the following equations



Taking into account that the electric field direction during the set leads to a drift of oxygen anions towards the bottom electrode, equation 5.3 appears more likely. Equation 5.4 on the other hand is only expected to take place if local temperatures are high enough to partially decompose the oxide. Coming back to the initial question why the reset process is inhibited, one may surmise that the local oxygen vacancy concentration is so high that no reset is possible. This effect is known as a hard or permanent dielectric breakdown and can also occur under ambient conditions if no current compliance is used [22].

The question remains why exposing the sample to air recovers the switching ability of the cells. To explain this effect, the recovery process of a device after exposure to air will be discussed. Figure 5.10 b) shows subsequent reset sweeps of a device that was first set in vacuum and then exposed to air. From the I - V curves it is evident, that the recovery process is gradual and requires several sweeps until a stable HRS is established. This gradual process

indicates that oxygen as well as an electric field is necessary for the recovery. Considering that air contains various sources of oxygen it is conceivable that equation 5.4 is now taking place in the reverse direction, i.e. oxygen species from the atmosphere oxidize the filament. The reaction consumes electrons to reduce molecular or atomic oxygen to oxygen anions. It appears counter intuitive that the reaction occurs when a positive bias is applied to the Pt electrode, i.e. when the interface is depleted of electrons. Accordingly, it is presumed that the effect of an applied voltage is mainly a thermal effect, accelerating the diffusion of oxygen species through the electrode. The reaction itself, filling of oxygen vacancies, does not require an applied voltage and takes place spontaneously at room temperature [204]. However, this is only possible if the Pt electrode is permeable for gas molecules. Interestingly, studies could show that for polycrystalline Pt films, oxygen diffusion through grain-boundaries can take place at moderate temperatures and through film thicknesses of at least 100 nm [205, 206]. Likewise, the evacuation of oxygen from the oxide lattice through Pt electrodes into the atmosphere during the electroforming process in memristive devices was reported [207, 208]. Figure 5.10 c) and d) schematically illustrate the LRS of a device in vacuum and in air respectively. In a vacuum after annealing, most of the protonic defects have been removed as well as any adsorbed oxygen species in the electrode or interface regions. By exposing the device to air, oxygen vacancies are partly filled by water molecules and molecular oxygen (equations 5.2 and 5.4).

5.2.4 Temperature dependence

As discussed in section 2.3, the electronic transport in noble metal-insulator-metal structures can be governed by a transport across a Schottky barrier, by bulk conduction through the insulator or by a combination of both. Due to the similar I - V dependence of many transport mechanism, it is difficult to differentiate which process is dominant based only on I - V curves. Further insights might be gained by measuring the temperature dependent electronic transport in memristive devices as the individual mechanism have distinct temperature dependencies. One of the main obstacles is the differentiation between bulk and Schottky dominated transport mechanism. Therefore, the temperature-dependent resistance change of a oxygen deficient TaO_x film was compared to a Ta_2O_5 memristive device. Using this approach, the thin film sample serves as a Schottky barrier free reference to investigate the bulk transport. For the device investigation, $\text{Ta}/\text{Ta}_2\text{O}_5/\text{graphene}$ devices were used to compare the results to devices investigated in chapter 7.

Figure 5.11 shows the temperature dependent resistance change of a TaO_x thin film and a Ta_2O_5 memristive device in the LRS. Both samples show a decrease of resistance with increasing temperature, i.e. they have a negative temperature coefficient of resistance. This behavior is typical for semiconductors and indicates that the current transport is a thermally

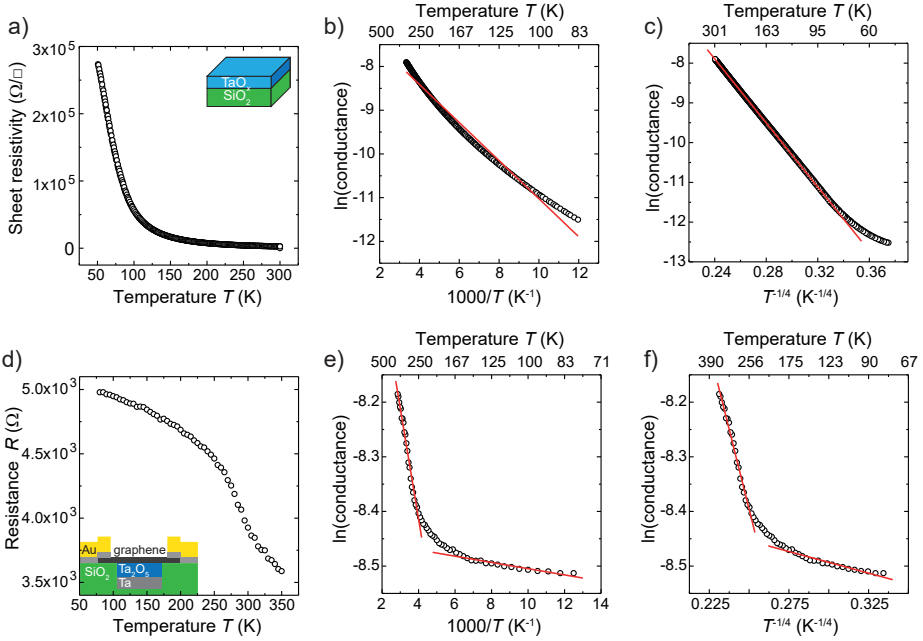


Figure 5.11: Low temperature conductivity of a TaO_x thin film and a Ta_2O_5 /graphene device. a) Sheet resistivity of a TaO_x thin film with $x = 1.9$ as a function of the temperature. b) Arrhenius plot of $\ln(\text{conductance})$ vs T^{-1} . c) Mott 3D variable range hopping plot showing $\ln(\text{conductance})$ vs $T^{-1/4}$. d), e) and f) same plots as in a), b) and c) for a 30 nm Ta /8 nm Ta_2O_5 /graphene device in the LRS state.

activated. First, the TaO_x thin film sample will be discussed. A thin film with a stoichiometry of TaO_x with $x = 1.9$ was investigated, as it is close to an expected filament stoichiometry (compare section 4.4). Figure 5.11 b) shows a typical Arrhenius plot of the logarithmic conductance against the reciprocal of the temperature. If the conduction mechanism follows the simple relationship for thermally activated charge carriers

$$R \propto \exp\left(\frac{E_a}{2 k_B T}\right) \quad (5.5)$$

a linear relationship between $\ln(\text{conductance})$ and $1/T$ is expected. However, from the plot it is evident that no linear behavior exists. This indicates, that the low temperature conduction in TaO_x is not a simple thermal activation of electrons above the mobility edge. As discussed in section 2.3, for highly disordered systems hopping conduction can occur. According to Mott's law (equation 2.15) hopping conduction can be differentiated from other conduction mechanism by its characteristic temperature dependence. For three-dimensional

or two-dimensional variable range hopping a temperature dependence of $T^{-1/4}$ or $T^{-1/3}$ is predicted [108]. In the special case of a strong on-site electron-electron Coulomb repulsion so called Efros-Shklovskii variable range hopping can be observed with a temperature dependence of $T^{-1/2}$ [209]. The here investigated thin film has a thickness of approximately 300 nm, which is substantially thicker than the expected hopping length of a few nanometers. Therefore, three-dimensional or Efros-Shklovskii hopping is expected. Figure 5.11 c) shows the logarithmic conductance against $T^{-1/4}$. For temperatures above 80 K a linear correlation is visible. Below this temperature the curve deviates from the linear dependency, indicating a change of the conduction mechanism at very low temperatures. Here it is noted that the data showed an almost equally good linearity for $T^{-1/3}$, while $T^{-1/2}$ deviated significantly from the linear trend. Accordingly, the conductivity in TaO_x thin films with a stoichiometry of $x = 1.9$ can be well described by the three-dimensional variable range hopping mechanism in a temperature regime of $80\text{ K} < T < 300\text{ K}$

In the following the temperature dependent resistance change of the Ta/Ta₂O₅/graphene device in the LRS state is discussed. Here two important differences to the thin film case are evident. First, the graphene electrode introduces an additional series resistance to the circuit, which is in the range of 1-2 kΩ. Considering that the resistance of the LRS is in the order of a few kΩ, it is apparent that the resistance of the graphene electrode has a significant contribution to the total resistance. Second, it is expected that a Schottky barrier forms at the Ta₂O₅/graphene interface and thus an additional contribution from the interface barrier to the total resistance is possible. Figure 5.11 d) shows the LRS device resistance as a function of the temperature. It can be seen that the temperature dependence is much weaker compared to the thin film case with the resistance decreasing by less than 40% from 80 K to 350 K. Similar observations have been made before for Ta₂O₅/Pt devices [133, 134]. This indicates that the electronic transport occurs via a temperature insensitive conduction mechanism, such as trap assisted tunnelling. Figure 5.11 e) shows the corresponding Arrhenius plot. It is obvious that at least two different regions can be distinguished, one at low temperatures $T < 150\text{ K}$, which is fairly temperature insensitive and one at $T > 150\text{ K}$ with a stronger temperature dependence. Graves *et al.* attributed the occurrence of two conduction regions to a "hot" current contribution from a Schottky emission process at high temperatures and a "cold" current due to variable range hopping at low temperatures [133]. From figure 5.11 e) it can be seen that no linear correlation between $\ln(\text{conductance})$ and $T^{-1/4}$ exists. This further indicates the existence of two conduction mechanism.

In summary, the temperature dependence of TaO_x thin films and Ta₂O₅ devices vary from each other. While the conduction in the thin film is accurately described by the variable range hopping model, the memristive devices exhibits at least two different conduction regimes. Determining the dominating transport mechanism in graphene based devices

is further complicated by the series resistance of graphene, which also varies with temperature [210].

5.2.5 Summary of resistive switching in Ta₂O₅

In this section, the resistive switching characteristics of Ta/Ta₂O₅ devices with Pt and graphene top electrodes have been studied. For both device structures qualitatively similar counter-eightwise switching was observed. Quantitative comparison of the switching parameter revealed, that graphene devices exhibit a higher memory window but require significantly higher switching voltages. The higher switching voltages have been attributed to an additional series resistance introduced by the graphene electrode and the suppression of oxygen exchange processes with the Schottky electrode. Using Raman spectroscopy it was demonstrated, that graphene electrodes are stable for at least 2000 thousand switching cycles. Thus, graphene electrodes show suitable switching characteristics and a sufficiently high endurance to be used for *in operando* X-PEEM spectromicroscopy as presented in chapter 7.

The influence of the Ta₂O₅ thickness was investigated and a correlation between the film thickness and the forming voltage was observed. For thin films, a small forming voltage was sufficient, whereas thick films required higher voltages. The memory window scaled inversely with the oxide thickness and the thinnest oxide film exhibits the highest memory window.

Importantly, switching in different atmospheres revealed that the reset process in Ta₂O₅ is inhibited under vacuum conditions. This experimental observation is inconsistent with many counter-eightwise switching models presented in literature. To explain this atmosphere dependence an extended switching model was proposed that includes the interaction between oxygen species from the surrounding atmosphere and the oxide thin film.

Moreover, temperature dependent conductivity measurements indicate that the conduction in TaO_x thin films occurs by variable range hopping. For the LRS in Ta/Ta₂O₅/graphene devices, no conclusive interpretation of the conductivity data was possible. This illustrates the need for physicochemical information about the composition and size of switching filaments in order to be able to accurately describe the current transport. Such a filament characterization will be attempted in chapter 7.

6 Spectromicroscopic analysis of switching-induced chemical changes in SrTiO₃

As presented in chapter 2, resistive switching in valence change materials is typically explained by a redistribution of oxygen vacancies under an applied electric field. However, this simple mechanistic picture of the switching process is not suited to describe more complex device characteristics, such as failure mechanism, aging effects or device-to-device variability. The underlying mechanism that give rise to these device characteristics are not well understood and have been connected to phase separations, microstructural defects or a change of the filament position. Therefore spectromicroscopy may be employed to further clarify the details of switching and failure processes in SrTiO₃ memristive devices.

In the first section of this chapter, eightwise switching in SrTiO₃ is investigated. As discussed in chapter 5, the cation stoichiometry of the SrTiO₃ switching layer has a big impact on the LRS stability. While stoichiometric films have a poor LRS retention, Sr-rich films show a strongly improved LRS stability. Therefore, a comparison between both systems represents a compelling approach to study the retention failure and stabilization mechanism.

In the second section, the counter-eightwise polarity is studied using *in operando* TEM. In contrast to the eightwise polarity, very little is known about the counter-eightwise switching in SrTiO₃. Although it can be suspected that the mechanism is similar to that of other counter-eightwise switching oxides, direct experimental evidence is missing so far. In order to clarify the origin of the counter-eightwise polarity in SrTiO₃, spectromicroscopy is used to map the switching induced chemical and structural changes. The results presented in this chapter have been published in parts in:

T. Heisig, J. Kler, H. Du, C. Baeumer, F. V. Hensling, M. Glöß, M. Moors, A. Locatelli, T. O. Menteş, F. Genuzio, J. Mayer, R. A. De Souza and R. Dittmann, "Antiphase Boundaries Constitute Fast Cation Diffusion Paths in SrTiO₃ Memristive Devices," *Advanced Functional Materials* **2020**, 30, 48, p. 2004118.

6.1 Investigation of eightwise switching in SrTiO₃

In this section, spectromicroscopy is used to investigate the local micro- and electronic-structure of eightwise switching SrTiO₃ devices after operation. For this purpose two samples were analyzed, one with a stoichiometric and one with a Sr-rich SrTiO₃ layer. The cation ratios of the two samples were Sr/(Sr+Ti) \approx 0.5 and 0.53 respectively. Additionally, the influence of the current compliance was studied, as it is a crucial parameter for achieving stable device operation. While low currents lead to an incomplete SET process, which results in bad retention times and low memory windows, high currents can cause irreversible device breakdowns. This renders the current compliance to an ideal parameter that can be used to study the switching process and possible failure mechanism.

6.1.1 *In situ* delamination of top electrodes

One of the main difficulties in characterizing resistive switching filaments in MIM devices by photoelectron spectroscopy, is the buried nature of the switching layer. This problem becomes evident if one considers that the information depth of photoelectron spectroscopy is below 5 nm, which is much smaller than the employed top electrode thickness of 30 nm. To overcome this surface sensitivity, different approaches have been developed. One of the most successful approach is based on *in situ* delamination of the top electrodes to expose the switching layer. For the surface sensitive analysis presented in this section, this delamination approach was employed and the top electrodes were mechanically removed under UHV ($p < 10^{-7}$ mbar) conditions. The top electrode removal under UHV conditions is critical, as oxygen deficient filaments easily re-oxidize in ambient atmospheres, which significantly changes their spectroscopic fingerprint. The details of the sample preparation can be found in chapter 3 and details of the top electrode removal are given in ref. [148]. To ensure a complete top electrode removal, all devices have been checked for Pt residues by either acquiring a Pt 4f core level spectrum or through a work function scan.

6.1.2 PEEM work function analysis

The work function of a semiconductor surface contains manifold information about the electronic structure of a sample. In principle, it is possible to correlate the cation oxidation state with the work function in transition metal oxides [211], which would allow a quantification of oxygen vacancy rich filaments. Unfortunately, the work function is extremely sensitive to a number of factors, such as adsorbates, surface morphology and surface termination [212, 213]. This makes a quantitative evaluation of the work function difficult and typically additional information from complimentary measurements are required to unambiguously interpret work

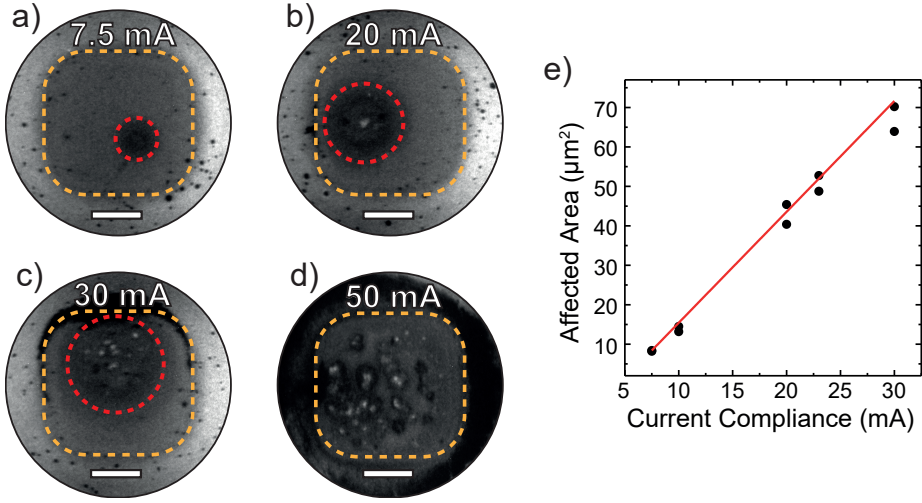


Figure 6.1: PEEM work function analysis of Sr-rich SrTiO₃ devices with a cation ratio of Sr/(Sr+Ti) \approx 0.53. Energy filtered PEEM image of devices switched with a) 7.5, b) 20, c) 30 and d) 50 mA, acquired at an electron energy of 4.1 eV using an UV light source. Scale bar, 5 μ m. The device area is indicated by the orange dashed line and the affected area by a red dashed circle. e) Measured affected area as a function of current compliance. Modified from ref. [170].

function shifts [132]. Therefore, the here presented work function measurements are not used to evaluate changes of the electronic structure. Nevertheless, mapping the local work function of a switched device is a reliable method to localize and measure the size of switching induced changes. Here, UV-PEEM is used to map the work function of delaminated devices.

Sr-rich SrTiO₃ devices

Figure 6.1 shows PEEM work function images of devices composed of a Sr-rich SrTiO₃ layer with removed top electrodes. The devices were switched prior to the top electrode removal using current limits from 7.5 to 50 mA. For all current compliances, at least two devices were investigated. The switching curves for selected devices are shown in figure 5.2. The former electrode area can be easily distinguished from the surrounding SrTiO₃ surface, as the regions have a slightly different work function. The differences in the work function are likely induced by different surface conditions, such as adsorbates. For all switched devices, a circular region with dark contrast was observed inside the device area (red dashed circles in figure 6.1 a-c)). By comparing switched and pristine devices (data not shown), it could be verified that only switched devices showed a distinct contrast inside the device area. This confirms that the observed contrasts stem from switching related effects. In the following, these regions

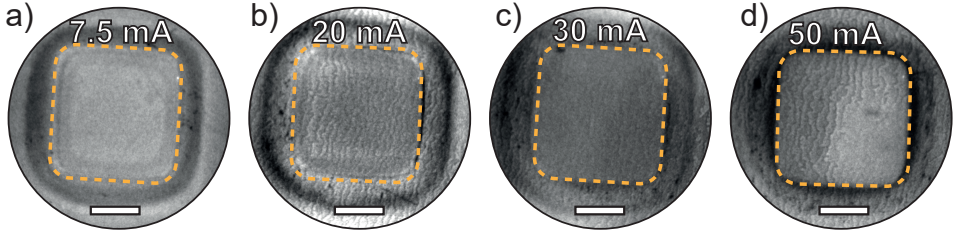


Figure 6.2: PEEM work function analysis of stoichiometric SrTiO₃ devices with a cation ratio of Sr/(Sr+Ti) \approx 0.5. Energy filtered PEEM image of devices switched with a) 7.5, b) 20, c) 30 and d) 50 mA, acquired at an electron energy of 4.1 eV using an UV light source. Scale bar, 5 μ m. The device area is indicated by the orange dashed line.

will be referred to as affected areas. Additionally, features with a bright contrast appeared inside the affected area of the devices that were switched with a high current. Because PEEM work function images are sensitive to the local electronic structure, one may assume that these contrast indicate the presence of oxygen vacancies. However, such contrast can also be induced by other switching related effects, such as the formation of secondary phases or desorption of surface contaminants.

Figure 6.1 e) displays the measured size of the affected area as a function of the current compliance. Interestingly, a linear correlation between the area and the current compliance can be recognized. For a current compliance over 30 mA, the affected area exceeded the device area (compare figure 6.1 d)). Therefore, only affected areas for devices switched with current compliances up to 30 mA are shown. The origin of the correlation between current compliance and affected area size will be discussed later in this section.

Stoichiometric SrTiO₃ thin film devices

In the following, devices fabricated from a stoichiometric SrTiO₃ layer will be discussed. Figure 6.2 again shows PEEM work function images of devices with removed top electrode. In contrast to the Sr-rich sample, no features are observed within the device area. For some devices it was possible to resolve the step-terrace structure of the epitaxial thin film, visible as dark lines. This is possible because PEEM is very sensitive to the surface morphology. Interestingly, the 50 mA device features a flat region without step terraces within the device area. This could be caused by a surface reconstruction to minimize the surface energy [214]. However, such surface reconstructions typically require high temperatures ($T > 800^\circ\text{C}$) and long annealing times of several hours [215]. While these temperatures might be reached during switching with high currents, they only occur for a short time (milliseconds to seconds).

In summary, from the work function analysis of samples with different cation stoichiometries, two important conclusions can be drawn. First, the cation stoichiometry has a pronounced effect on the switching induced work function changes. For Sr-rich devices, large changes in the local work function occurred within an affected region. For the stoichiometric sample, no changes in the work function could be observed. This indicates, that the observed changes in the Sr-rich sample are not related to oxygen vacancies, as these changes should also occur in the stoichiometric sample. Second, the size of the affected area in the Sr-rich sample scales with the used current compliance. In the following sections, the origin of the work function changes in Sr-rich devices will be examined in more detail.

6.1.3 Microscopic investigation of switching induced changes in Sr-rich devices

To further characterize the switching-induced changes, the topography and the local conductivity of the affected region was investigated. For this, a delaminated sample was transferred from the PEEM into a conductive atomic force microscope (C-AFM) under UHV conditions. The expected filament position was extracted from the work function scans in figure 6.1. To maximize the chance of locating the conductive filament, the device switched with a high current compliance of 50 mA shown in figure 6.1 d) was investigated. Figure 6.3 compares the topography of a) the pristine thin film and b) a filamentary region after top electrode removal.¹ By comparing the topography of the pristine and switched film, it can be seen that the filament region is significantly rougher and shows large islands on the surface. Small islands are also visible on the as prepared film, however, they do not exceed a height of 4 nm and have diameters typically below 150 nm. The origin of these growth induced islands is discussed in more detail in section 4.1 and ref. [143]. In contrast, the islands that stem from of the electrical treatment are higher (approximately 13 nm) and have a characteristic ring-shape morphology. These islands can be correlated to the bright features in figure 6.1 d). This could indicate, that switching induces the segregation of a secondary phase at the SrTiO₃/Pt interface.

Figure 6.3 c) displays the current map that was acquired simultaneously with the topography scan in b). In the current map, three distinct regions can be identified. First, a region with very low conductivity, visible as dark features, is observed. By correlating the topography and current map, it can be seen that the region with low conductivity coincides with the islands in the topography map. The second region is characterized as a homogeneously conductive area. The third region exhibits a medium conductivity similar to that of pristine SrTiO₃. Based on these results, it can be assumed that the area with high conductivity represents the oxygen vacancy rich filament, whereas the region with medium conductivity

¹Conductive AFM measurements were performed by Maria Glöß, Peter Grünberg Institut, Forschungszentrum Jülich GmbH, Jülich, Germany

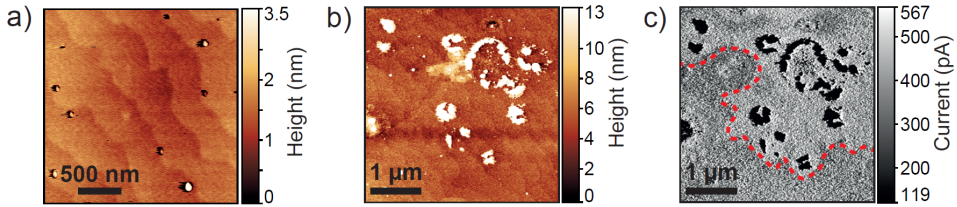


Figure 6.3: Surface topography of a) the as prepared Sr-rich SrTiO₃ thin film, b) the filament area of the delaminated device and c) the corresponding current map. The red dashed line indicates the transition from the conductive to the region with medium conductivity. For the investigation, a device switched with 50 mA was used. Modified from ref. [170].

is the surrounding film. Further, the islands that appear inside and around the filament could indicate the formation of an insulating secondary phase such as SrO, Sr(OH)₂ or SrCO₃ [216].

While work function and topography scans deliver valuable information about the size and structure of the switching-induced changes, they do not provide information about the chemical composition of the filament area. For this, X-PEEM was employed at the Nanospectroscopy beamline at Elettra synchrotron laboratory (Trieste, Italy) using the endstation described in ref. [147].² X-PEEM was used to map the Ti 3p and Sr 3d core levels across a filament region.

Figure 6.4 a) shows an energy filtered image of a filament obtained at an electron energy of $E_{\text{bin}} = 36.2 \text{ eV}$. The selected binding energy corresponds to the feature in the Ti 3p core level spectrum that can be attributed to a Ti³⁺ component. Therefore, a high concentration of Ti³⁺ appears bright in the image. It is apparent, that a Ti³⁺ rich area of irregular shape is observed, enclosed by the red dotted line. The region is surrounded by a Ti⁴⁺ matrix. Inside the Ti³⁺ rich area small dark spots are visible, revealing that the filament is not homogeneous but is heterogeneously structured at sub-micron lengths. The corresponding Ti 3p XPS spectra of the filament and the surrounding region are presented in Figure 6.4 b). Quantification of the core level spectrum reveals, that the filament consists of up to 30 % Ti³⁺, while the surrounding area is composed almost entirely of Ti⁴⁺. The high fraction of Ti³⁺ can be attributed to a reduction of the SrTiO₃ film and thus indicates the presence of a large amount of oxygen vacancies.

The same region was measured again at a binding energy corresponding to the Sr 3d core level. The energy filtered image obtained at an electron energy of $E_{\text{bin}} = 131.9 \text{ eV}$ is shown in figure 6.4 c) and the corresponding spectra are depicted in d). This binding energy was selected to visualize the differences in the low binding energy region of the peak (compare the

²X-PEEM measurements were performed by Dr. Christoph Baeumer, Peter Grünberg Institut, Forschungszentrum Jülich GmbH, Jülich, Germany

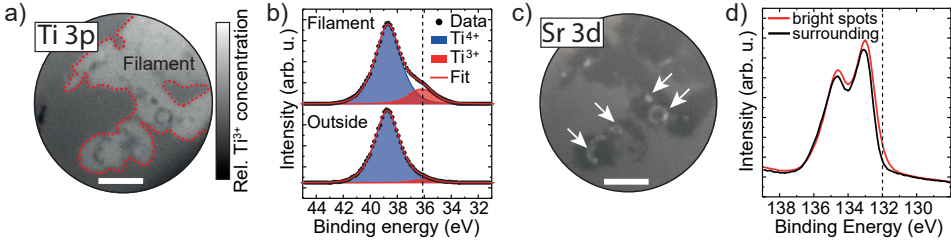


Figure 6.4: Spectromicroscopic filament investigation. a) X-PEEM image of the filament region acquired at a binding energy of 36.2 eV showing the Ti^{3+} concentration based on the Ti 3p core level spectrum (scale bar: 2 μm). The dashed red line indicates the filament boundary. b) Ti 3p XPS spectra extracted from the filament and surrounding area. The dashed line indicates the selected binding energy in (a). c) X-PEEM image based on the Sr 3d core level spectrum at a binding energy of 131.9 eV. d) Sr 3d spectra extracted from the bright spots (marked with white arrows in (c)) and the surrounding area. Modified from ref. [170].

dashed line in d)). The image shows a darker region that coincides with the Ti^{3+} rich region observed in a). Inside the filament, several features can be identified as bright spots (marked by white arrows). Again, these features are also observed in the Ti 3p core level image as dark spots. Extracting the Sr 3d core level spectra from the bright spots reveals, that the peak (red spectrum) is shifted towards lower binding energies compared to the surrounding regions (black spectrum). This suggests that an additional low binding energy component is present. Intuitively, one might assume that this additional component can be assigned to a SrO , $\text{Sr}(\text{OH})_2$ or SrCO_3 secondary phase. However, all of these Sr compounds have higher binding energies compared to SrTiO_3 and are therefore not suitable to explain the spectral difference [217]. Lenser *et al.* observed a similar spectral change, which they attributed to the formation of SrO and Sr''_{Ti} anti-site defects [29]. It is likely, that in the here presented case, a similar phase separation occurred.

Due to the limitation of PEEM and AFM, that is, low or no sensitivity to the buried layers, scanning transmission electron microscopy (STEM) was employed to study a filament in a cross-sectional view.³ For this, a lamella was cut across the filament presented in figure 6.1 d), including parts of the islands that emerged during the electrical treatment. Figure 6.5 a) displays a high-resolution dark-field (DF) TEM image of the SrTiO_3/Pt interface where an island (surface precipitate) is located. For the most part the film exhibits an epitaxial crystal quality, which is only disrupted by a Ruddlesden-Popper type antiphase boundary (RP APB) located directly beneath the island (compare the orange dashed line). The RP APB consists of one vertical [010] and two horizontal [100] planes. Figure 6.5 b) shows a high angle annular dark-field (HAADF) image of the area marked with a white box in a). The HAADF image clearly resolves that the SrTiO_3 lattices on both sides of the APB are displaced relative to each

³STEM investigation was performed by Dr. Hongchu Du, Ernst Ruska-Center, Forschungszentrum Jülich, Jülich, Germany.

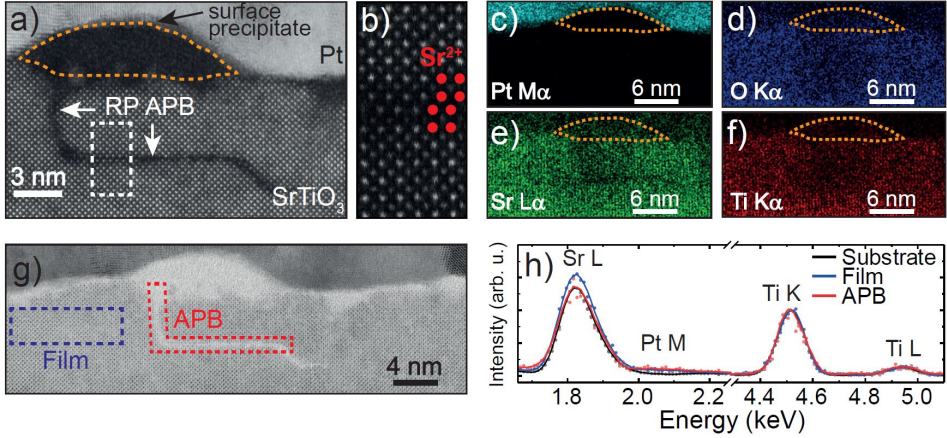


Figure 6.5: Cross sectional TEM analysis of a filament area. a) DF-STEM image of the filament cross-section and b) HAADF image of the white box in (a). c-f) EDX elemental maps acquired using c) Pt $M\alpha$, d) O $K\alpha$, e) Sr $L\alpha$ and f) Ti $K\alpha$ emission peaks. g) Annular bright-field (ABF) image of the same region. h) Smoothed (solid lines) spectra of the Sr $L\alpha$ and Ti $K\alpha$ lines normalized to the Ti $K\alpha$ peak. EDX spectra were summed from regions of interest shown in (g) to enhance the signal-to-noise ratio. Modified from ref. [170].

other by $a/2[111]$, with the intermediate TiO₂ plane missing. This results in two adjacent SrO atomic planes. The z component is along the projection direction and is therefore not visible.

In order to obtain information about the elemental distribution of the filament section, energy dispersive X-ray (EDX) mapping was employed. Figure 6.5 c-f) shows the EDX maps of Pt, O, Sr and Ti respectively. The Pt map indicates no interdiffusion of Pt into the SrTiO₃ layer. Further, it is confirmed that the island is not composed of Pt, as no signal is detected in this region. The oxygen map appears almost homogeneous within the SrTiO₃ layer and the precipitate. However, a small decrease of intensity can be noticed at the RP APB location. Importantly, the Sr $K\alpha$ map shows a distinct Sr depletion in the vicinity of the RP APB. This is unexpected, as the double SrO plane structure of the RP APB should be considerably richer in Sr than the bulk [31]. The Ti map closely resembles the oxygen map.

To quantify the cation ratio around the APB and the thin film stoichiometry, atomic Sr/Ti ratios were determined from EDX spectra extracted from these regions. The SrTiO₃ single crystal substrate served as an internal standard for calibration [28]. Figure 6.5 h) shows the EDX spectra extracted from the regions shown in g) and the substrate. The increased intensity of the Sr $L\alpha$ line reveals a $5 \pm 2\%$ Sr enrichment in the thin film (blue) compared to the substrate (black). This is consistent with the expected stoichiometry based on the PLD growth

rate and laser fluence [218]. The Sr excess is likely incorporated into the thin film as randomly distributed small RP faults [219]. Another possibility for the accommodation of excess Sr is the presence of Ti vacancies [150]. In contrast to the grown thin film, the stoichiometry of the area surrounding the RP APB, shows a cation ratio similar to the substrate. This indicates, that the Sr excess that was incorporated into the film during growth, precipitates out of the thin film in the vicinity of the RP APB. Unfortunately, the a poor signal-to-noise ratio arising from less material and from overlapping Pt M α and Sr L α emission lines hinders a quantification of the precipitate composition.

6.1.4 Atomistic simulation of cation diffusion along antiphase boundaries

In the last section it was demonstrated, that resistive switching of Sr-rich SrTiO₃ devices induces a phase separation in the vicinity of the switching filament. Intriguingly, TEM analysis indicates that the phase separation occurs preferentially at RP APBs. Based on these results it can be assumed that the extended defects act as fast cation-diffusion paths.

To clarify the role of RP APBs, molecular static and molecular dynamic simulations were performed to investigate how extended defects impact the ionic diffusion in SrTiO₃.⁴ The simulations were carried out using the LAMMPS (Large-scale atomic/molecular massively parallel simulator) code [221], employing empirical pair potentials derived by Pedone *et al* [222]. For this, a high-order ($n=10$) RP phase was used as a model system. This selection is motivated because such a RP phase exhibits an APB as well as an extended bulk phase. The unit cell of Sr₁₁Ti₁₀O₃₁ is depicted in figure 6.6 a). First, the relative defect formation energy for a strontium vacancy was calculated for different lattice sites in the simulation cell (compare figure 6.6 b)). The defect formation energy for the APB site is considerably lower ($\Delta E = -0.28$ eV) compared to the defect energy of the perovskite lattice. This means that the energetically most stable position for Sr vacancies is at the APB. Considering that the cation diffusion in SrTiO₃ is exclusively occurring via a vacancy diffusion mechanism, it can be assumed that the strontium diffusion is enhanced by the presence of Sr vacancies. The values for the different perovskite sites are almost equal in energy. This demonstrates that the APB has no long range effect on adjacent lattice sites.

To gain insights into the migration processes of Sr cations, static lattice simulations based on the nudge-elastic band method were performed. Figure 6.6 c) shows selected strontium migration paths within the Sr₁₁Ti₁₀O₃₁ unit cell and figure 6.6 d) depicts the corresponding energy profiles. The migration paths in the perovskite type bulk phase (paths 1 and 2) have a high energy barrier of 4.0 eV. These values are in good agreement with values obtained

⁴The simulations were performed by Joe Kler, Institute of Physical Chemistry, RWTH Aachen University, Aachen, Germany, as a part of his doctoral thesis and reproduced by his kind permission. Detailed information can be found in ref. [170].

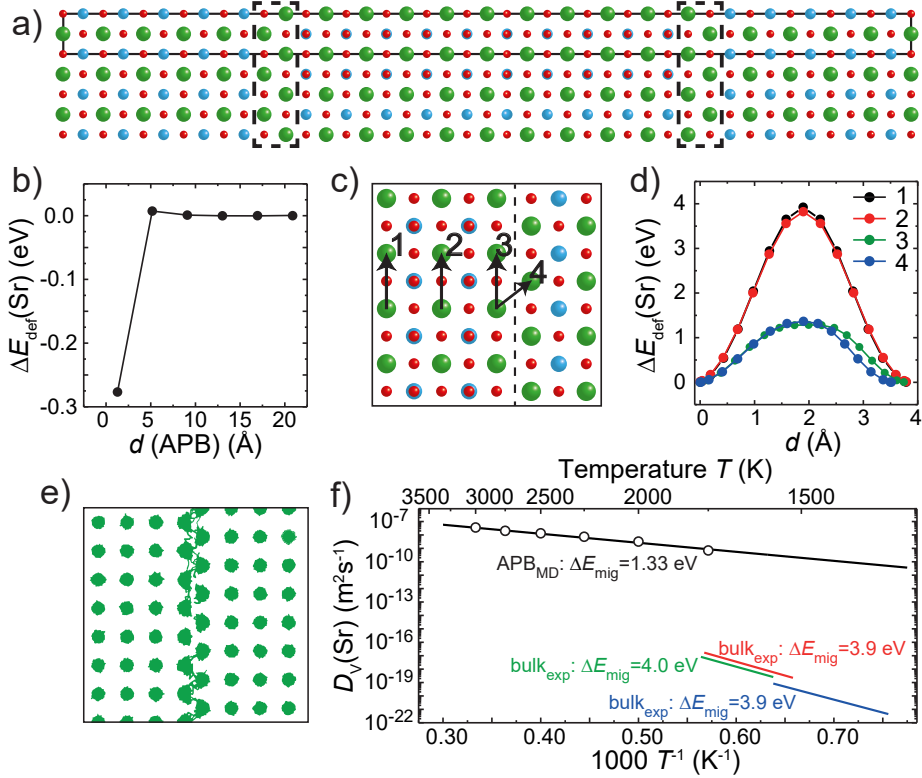


Figure 6.6: Molecular static and dynamic simulations of Sr²⁺ behaviour at RP APB. a) Illustration of the Sr₁₁Ti₁₀O₃₁ unit cell (solid black line) used in the atomistic simulations. Sr²⁺ in green, Ti⁴⁺ in blue, and O²⁻ in red. The RP APBs are marked by dashed black lines. b) Defect formation energy of a Sr vacancy as a function of distance to the APB. c) Magnified part of the unit cell, with the simulated migration path indicated schematically by black arrows. d) Strontium migration energies for the individual migration paths. e) Molecular dynamic trajectories of Sr²⁺ at $T = 2000$ K. f) Diffusion coefficients of strontium along an APB obtained from molecular dynamic simulations (black) and experimental values in bulk SrTiO₃ by Meyer *et al.* (red) [220] and Gömann *et al.* (blue and green) [55] as a function of (reciprocal) temperature. Modified from ref. [170].

experimentally [55, 220] and computationally for SrTiO₃ [66, 223]. Migration in the double SrO plane structure of the RP APB can occur via two possible pathways, along or across the APB (paths 3 and 4). Both paths have a significantly lowered migration barrier of 1.3 eV. This confirms that the Sr diffusion in the APB is greatly increased. Further, the lowered migration barrier enables Sr diffusion at much lower temperatures than the SrTiO₃ cation equilibration temperature of 1300 K [59].

To quantify the effect of APBs on the diffusion of Sr cations, molecular dynamics simulations were carried out. For this, the dynamics of a $12 \times 12 \times 1$ unit cell large supercell containing 14976 ions (Sr₃₁₆₈Ti₂₈₈₀O₈₉₂₈) was simulated. An initial Sr vacancy concentration of 1% was introduced into the supercell and equally distributed between APB and bulk phase. Figure 6.6 e) shows the Sr cations trajectories in a section of the supercell including an APB. It can be noticed that the Sr cations only move in the RP APB and remain immobile in the bulk phase. A closer look at the cation trajectory reveals that the cations move along the same migration paths that were calculated in the nudged-elastic band simulations to have a low migration barrier. The obtained diffusion coefficients for Sr migration in the RP APB structure yield a migration enthalpy of 1.33 eV. This compares remarkably well with the static migration barriers. Since Sr cations did not execute any jumps in the bulk phase, due to the high migration barrier of 4.0 eV, no diffusion coefficient for Sr cations outside the RP APB could be determined. To estimate the impact of RP APBs on the strontium diffusion, the APB diffusion coefficients obtained from molecular dynamics simulations are compared to experimental data for single crystal SrTiO₃ by Meyer [220] and Gömann *et al.* [55] (see figure 6.6 f). It can be noticed that the APB diffusion coefficient is orders of magnitude higher (by a factor of over 10^9 for $T < 1500$ K) than the bulk diffusion coefficient. From these results it can be concluded that the diffusion along RP APBs is considerably faster and can take place at lower temperatures.

6.1.5 Electro-thermal device simulations

In section 6.1.2 it was demonstrated, that the area in which switching induced changes occur scales with the current compliance. In order to understand this behavior, it is necessary to have a closer look on the temperature development during resistive switching.

For this, a SrTiO₃ device was modeled and an electro-thermal simulation was performed to obtain a temperature map of the device during electrical biasing.⁵ Figure 6.7 a) shows the used device geometry. For the simulation, a filament with a radius of 500 nm was assumed, based on the X-PEEM results presented in section 6.1.3. To simplify the simulation, a 10 nm SrTiO₃ film was used instead of a 20 nm film which was investigated experimentally. Further,

⁵The simulations were performed by Sebastian Siegel, Peter Grünberg Institut, Forschungszentrum Jülich GmbH, Jülich, Germany. Detailed information can be found in ref. [170].

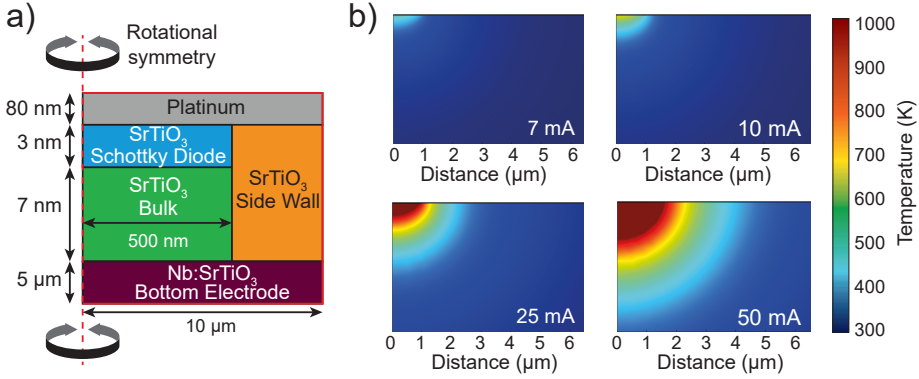


Figure 6.7: Electro-thermal simulation of SrTiO₃ memristive device. a) Schematic depiction of the simulated device structure with a filament radius of 500 nm (green and blue) and a SrTiO₃ thickness of 10 nm. Red lines indicate the simulation boundaries with the boundary conditions $T = T_{amb}$ and $J = 0$. b) Temperature distribution at a bias of $V_{max} = 3$ V and at a current compliance of 7, 10, 25 and 50 mA.

the bottom electrode length is underestimated in the simulation, which might cause small deviations from the actual series resistance of the circuit. Therefore, a one-to-one comparison to the devices studied in the previous sections is not possible. However, it can be assumed that the general trends obtained from the simulation can be transferred to the case of 20 nm SrTiO₃ devices. It is likely that the simulation underestimates the temperature evolution due to a smaller bulk resistance of the SrTiO₃ layer. In figure 6.7 b) the temperature distribution of the simulated device geometry is shown for different current compliances. It can be seen, that the maximum temperature and the radial extension of the temperature increases with increasing current compliance. This is not unexpected as Joule heating is described by the following relationship

$$P \propto I^2 \cdot R \quad (6.1)$$

with P the power converted to thermal energy, I the current and R the device resistance.

For low current compliances, the temperature increase is limited to a very small region and does not exceed the filament diameter significantly. Increasing the current, however, induces local heating of regions next to the filament through heat dissipation. For a current compliance of 25 mA the heated region extends several micrometers into the bulk of the device. Based on these results, it can be assumed that the area scaling of the switching induced changes presented in figure 6.1 can be explained by heating of comparably large areas around the filament due to Joule heating and heat dissipation. The lateral expansion of these areas depends strongly on the current compliance.

Interestingly, the maximum temperature reached in the simulations exceeded 1000 K. In this temperature regime, it is expected that oxygen anions are mobile. In contrast, the temperatures are still too low for cation migration in bulk SrTiO₃. However, in the previous section it was demonstrated that Sr cations exhibit a significantly reduced migration energy along RP APBs. Therefore, it can be assumed that cation migration can take place in RP APBs if devices are switched using high current compliances. This is in accordance with the observed secondary phase formation discussed in section 6.1.3.

6.1.6 Summary of eightwise switching in SrTiO₃

In this section, it was demonstrated that the cation stoichiometry of SrTiO₃ has a profound influence on the microscopic structure of the switching filaments. For stoichiometric thin film devices, no local phase separations were observed in PEEM work function scans. In contrast, Sr-rich devices exhibit a modified work function in an affected area, which scales with the current limit. The investigation of conductive filaments by C-AFM and X-PEEM revealed, that the resistance change in SrTiO₃ devices is caused by the formation of a spatially confined conductive region with a high Ti³⁺ concentration. This observation is in good agreement with the proposed valence change mechanism for eightwise switching in SrTiO₃ [119].

A closer examination of the microscopic filament structure in Sr-rich devices shows, that switching leads to the formation of insulating Sr-rich islands at the SrTiO₃/Pt interface. By TEM it was found that the Sr-rich islands preferentially form above RP APBs. Using atomistic simulations it could be clarified that RP APBs act as fast diffusion paths for strontium cations.

Electro-thermal simulation of a biased device confirmed that Joule heating generates high temperatures in the vicinity of the conductive filament. Simulations using different current limits show that the maximum temperature and the spatial extension of the heated area scale with the current limit. For high currents, local temperatures can exceed 1000 K, which is sufficient to trigger the cation diffusion along RP APB.

6.1.7 Discussion: Origin of the retention stabilization in eightwise switching in Sr-rich SrTiO₃

Based on the insights obtained from experiment and simulation, it is now discussed how the local precipitation of Sr-rich secondary phases impacts the switching and retention behavior of SrTiO₃ memristive devices. For this, switching model of Cooper and Baeumer *et al.* will serve as basis for the discussion of the switching mechanism [34]. The model is extended to

include the role of crystallographic defects and phase separations, which have been observed in Sr-rich devices.

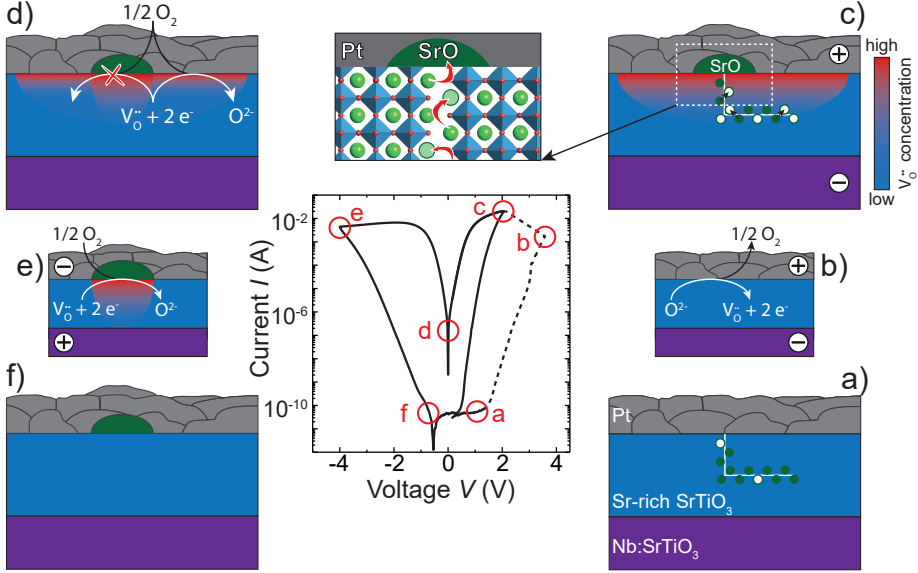


Figure 6.8: Proposed model for retention stabilization of the LRS in eightwise switching Sr-rich SrTiO₃ devices. An exemplary electroforming (dashed line) and switching I - V curve is depicted together with schematics of the device in different states. a) Pristine state: The Sr-rich SrTiO₃ layer (blue) is sandwiched between a Nb:SrTiO₃ bottom electrode (purple) and a Pt top electrode (gray). A Ruddlesden-Popper defect (white line) is shown in the SrTiO₃ layer with Sr²⁺ (green circles) and Sr²⁺ vacancies (white circles with green contour). b) SET: Oxygen anions are released from the lattice and leave behind oxygen vacancies and electrons. c) Precipitation of excess strontium forming a SrO phase. Inset: Sr²⁺ vacancy diffusion. d) LRS: A high concentration of oxygen vacancies is present at the Schottky interface. Regions without SrO start to reoxidize. e) RESET: Oxygen anions are reincorporated into the lattice at the SrO covered regions. f) HRS: All oxygen vacancies are filled.

Figure 6.8 shows the proposed electroforming and switching model. In the pristine device state, the Sr-rich SrTiO₃ layer is fully oxidized and the device is insulating (figure 6.8 a)). As a result of the Sr-rich growth, RP APB (white lines) are randomly distributed throughout the thin film. Due to their reduced formation energy, Sr vacancies accumulate at the APB site.

Upon application of a positive bias to the top electrode, negatively charged oxygen anions drift towards the polycrystalline Pt electrode (figure 6.8 b)). At the interface, the oxygen anions are oxidized to atomic or molecular oxygen and are released from the crystal lattice, leaving behind oxygen vacancies and electrons. It is likely that the released oxygen is stored inside

the Pt electrode or leaves the device in form of molecular oxygen. The electrons, however, are transferred into the conduction band, where they contribute to current transport. With increasing current flow, Joule heating generates high temperatures. This further accelerates the oxygen anion drift. At a certain bias, the electric field and the local temperature is high enough to trigger a self accelerating reaction. This results in the generation of a large amount of oxygen vacancies, i.e. the conductive filament. In the I - V curve this is visible as an abrupt increase in current (compare point (b)). The device is now in an electroformed state.

Without a current compliance the current passing through the electroformed device under high bias would lead to an irreversible dielectric breakdown. With current compliance, however, the voltage is reduced to stay within the current limit (point "c" in the I - V curve). During this stage of the switching cycle, the highest temperatures are reached. As demonstrated by PEEM and electro-thermal simulations, the current compliance can be used to control the maximum temperature and the spatial extent of the heated areas. If the temperatures are high enough, i.e. if a high current limit is used, cation diffusion can take place. Based on the STEM and AFM experiments, it is suspected that the strontium excess precipitates out of the SrTiO₃ bulk and forms a secondary phase at the SrTiO₃/Pt interface. This occurs preferentially at RP APBs due to the reduced Sr²⁺ migration energy within the defect (figure 6.8 c)). The inset schematically depicts the strontium diffusion via Sr vacancies within the SrO double plane structure of the RP APB. As cation diffusion in the SrTiO₃ bulk is orders of magnitude slower compared to the diffusion along the defect, no secondary phases form in stoichiometric SrTiO₃ thin films under similar current limits. Additionally, the driving force to form a secondary phase is higher in the case of Sr-rich SrTiO₃, due to the thermodynamically unfavorable composition.

If the applied voltage is removed, a non-volatile decrease of the resistance is observed. The device is in the LRS (figure 6.8 d)). However, the LRS is not completely stable and the resistance increases over time. This increase is typically assigned to a reoxidation of the conductive filament. While stoichiometric devices tend to completely reoxidize within hours, Sr-rich devices are stable for weeks after an initial resistance increase is observed (compare figure 5.2). This difference in stability of the LRS state can be explained by the oxygen blocking properties of the SrO precipitates. If the device is kept in the LRS state for a longer time, oxygen from within the Pt electrode or oxygen from the surrounding atmosphere can diffuse to the SrTiO_{3-x}/Pt interface and fill oxygen vacancies. This reaction is exergonic and thus does not require the presence of an electric field or any other external driving force. In the stoichiometric case, a complete oxidation of the filament can take place. In the Sr-rich device, however, the precipitates act as diffusion barrier and prevent a reoxidation. Considering that the filament area is much larger than the area covered by precipitates explains why the LRS resistance in Sr-rich devices initially increases and then becomes stable. The

uncovered regions reoxidize and the filament size decreases until only SrO covered regions remain oxygen vacancy rich. Importantly, the question remains how the SrO islands can retain the LRS while at the same time being highly insulating as it was observed in C-AFM. Here it is proposed that the triple phase boundary (SrTiO₃/SrO/Pt) acts as the main current path.

If a negative bias is applied, the situation changes and also regions covered by SrO are oxidized (figure 6.8 e)). The device is reset into the HRS. For the oxidation of SrO covered regions, two possible scenarios are conceivable. First, the applied electric field attracts the remaining oxygen vacancies from underneath the SrO precipitate towards the SrO/Pt interface, where they eventually recombine. Alternatively, the temperature that is generated during the RESET causes the vacancies to diffuse towards the SrTiO₃/Pt interface along a chemical gradient, where they also recombine. If the oxygen vacancies from regions covered by SrO are also filled, the device is in the HRS (figure 6.8 f)). The HRS is resembling the pristine device state, with the exception that the SrO precipitations remain and that the subsequent SET processes require lower voltages.

6.2 Investigation of counter-eightwise switching in SrTiO₃ by *in operando* TEM

With an increasing switching oxide thickness, it becomes more important to utilize spectromicroscopic techniques that allow a cross-sectional mapping of the chemical and electronic structure. Especially, the vertical distribution of oxygen within the switching layer is of importance to understand the memristive behavior in counter-eightwise switching oxides. While depth resolved spectromicroscopy is inaccessible with PEEM, transmission electron microscopy (TEM) is predestined for this purpose. Modern aberration corrected TEM offers unparalleled spatial resolution down to the atomic scale combined with spectroscopic techniques such as energy dispersive X-ray (EDX) and electron energy loss spectroscopy (EELS). By preparing a TEM specimen through focused ion beam milling, it is possible to cut a cross-sectional lamella from a device. This allows a vertically resolved characterization of the switching layer.

A common approach to characterize switching filaments is to cut a lamella from a switched device with known filament location. To locate the filament different approaches can be used such as C-AFM or PEEM [28, 131]. This approach, however, limits the investigation of a filament to one predefined resistive state, as no switching can be performed after the lamella preparation. Therefore, much work has been focused on the development of *in operando* approaches to allow device operation inside the microscope [33, 34]. For this, the prepared lamella is electrically contacted inside the microscope and a voltage can be applied using

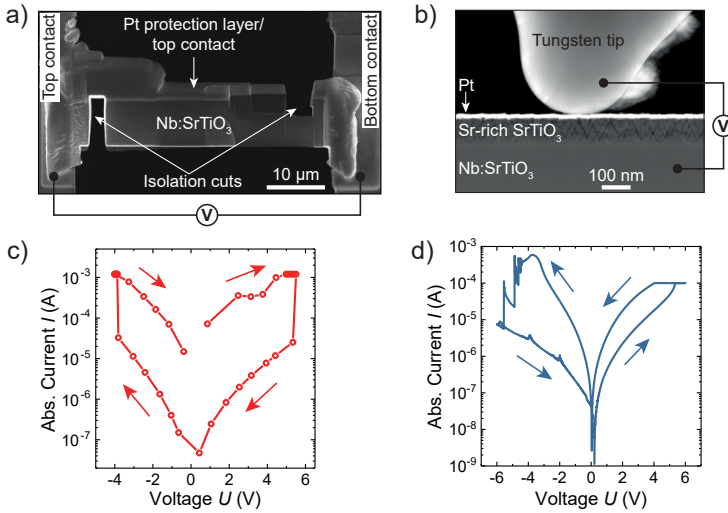


Figure 6.9: *In operando* resistive switching in a TEM. a) Protochip based *in situ* biasing setup. b) Nanofactory holder *in situ* biasing using a piezo controlled tungsten tip. c) Counter-eightwise switching curve measured on the Protochip setup. d) Eightwise switching curve measured using the Nanofactory holder and with the tip placed directly on top of the Pt electrode.

an external power supply. Most importantly, this *in operando* approach offers the possibility to characterize the same filament in different resistive states. Additionally, it is possible to study gradual changes of the device upon increasing currents or number of operation cycles. This could help to understand the origin of variability and aging effects in memristive devices.

In this section, *in operando* TEM characterization of Nb:SrTiO₃/80 nm Sr-rich SrTiO₃/Pt devices was employed to study counter-eightwise switching in SrTiO₃ devices.⁶ The films were grown using the same conditions as described in chapter 4.1. Figure 6.9 a) and b) show the two experimental setups that were used to electrically contact the lamella inside the microscope. The first approach is based on a Protochip TEM holder. Here, the lamella is Pt-welded to a chip. Each side of the chip is electrically addressable. By focused ion beam milling, two insulation cuts are made to separate the bottom and top electrode. This ensures that the voltage is applied across the switching layer and no short circuits are present. The Protochip system offers high spatial resolution and no tungsten tip is needed to address the device. This eliminates contact problems between tip and sample. The downside of this approach is to find the filament in the comparatively large lamella ($\approx 5 \mu\text{m}$). The second approach based on a Nanofactory holder and utilizes a conductive probe tip that can be placed directly onto

⁶All TEM experiments in this chapter were performed by Dr. David Cooper, CEA LETI, Grenoble, France.

the top electrode. Here, the filament position is usually located underneath the probe tip. However, the tip can induce mechanical stress and thus could damage the thin film and give rise to other non-switching related effects.

Figure 6.9 c) and d) show two exemplary *in situ* switching curves measured with the Protochip and Nanofactory setup respectively. Resistive switching was reproducibly accomplished with both setups, however, switching with the Nanofactory holder typically required higher voltages and smaller memory windows were observed. This can be attributed to an additional contact resistance between the probe tip and the top electrode. Interestingly, counter-eightwise (red) and eightwise (blue) switching was observed in both measurement setups. Initially, the lamella showed an eightwise switching polarity. After several switching cycles with successively higher current limits, the polarity changed to counter-eightwise switching. Eightwise switching was not observed in bulk devices and occurred only in the prepared TEM specimen. One possible explanation for this behavior could be the additional phase boundaries (i.e. SrTiO₃/vacuum) of the ≈ 100 nm thin lamella, facilitating oxygen release into the vacuum atmosphere of the microscope. Furthermore, the thermal properties of the lamella are different from bulk devices due to the missing thermal mass. As eightwise switching was already studied in detail using *in operando* TEM [34], the investigation in this section is limited to counter-eightwise switching. Therefore, the terms LRS and HRS used in this section always refer to the resistive states of the counter-eightwise polarity.

6.2.1 Current induced structural and electronic modifications

Before spectroscopy was employed, the effect of high currents on the microscopic structure of the thin films was investigated. For this, a lamella was biased using the Protochip setup. Figure 6.10 shows annular dark-field (ADF) and bright-field (BF) images before (a, b) and after (c, d) electrical treatment. It is apparent, that the current modifies the crystal structure of the thin film. This modification was observed in an approximately 500 nm large region. It is assumed that this is the location where the current passes through the film. The passing current results in the generation of high temperatures due to Joule heating. As a consequence, the thin film homogenizes through grain growth. However, the microstructural modifications cannot be directly associated to the switching mechanism itself, as they can be explained purely by thermal effects. Nevertheless, these modifications can help to locate the filament position.

In order to obtain quantitative physicochemical information about the current induced modifications, EELS was performed on a similar device and the Ti $L_{2,3}$ and the O K -edge were investigated. Similarly to the analogous X-ray technique XAS, EELS can provide information about the coordination symmetry, the oxidation state and local chemical concentrations of

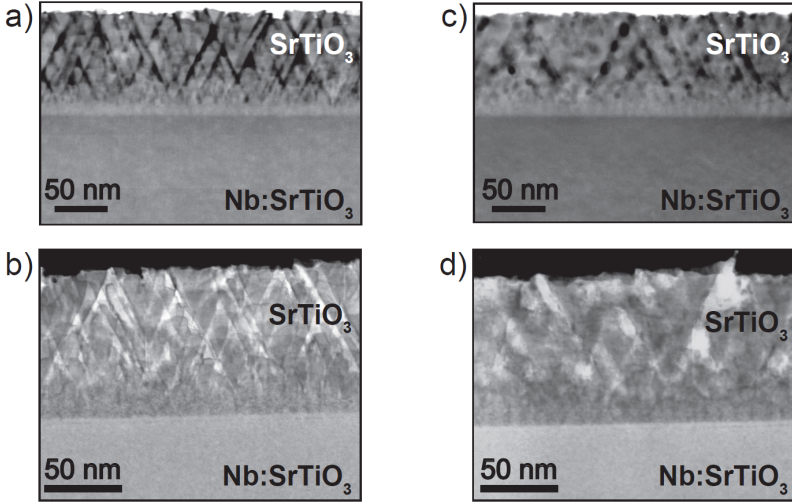


Figure 6.10: Effect of biasing on the grain boundary structure. a) Annular dark-field (ADF) and b) bright-field (BF) images of a pristine SrTiO_3 film. c) ADF and d) BF image of the same film at a different region after electrical treatment. The device was switched 30 times using high currents of up to 1.5 mA.

elements at the nanoscale. Figure 6.11 a) shows a HAADF image of the investigated sample region. The region of interest was selected in such a way, that it contained the area where structural modification were evident. Before switching was performed, a representative EEL spectrum was acquired in the pristine device state, i.e. before electrical treatment. The corresponding Ti $L_{2,3}$ -edge is shown in figure 6.11 b). Comparing the pristine spectrum to literature data taken from single crystalline SrTiO_3 shows, that the grown thin film consists mostly of Ti^{4+} [224]. Additionally, the high density of extended defects in the grown thin film has no apparent influence on the spectral shape. This can be explained by the low energy resolution of the EELS, which outweighs the defect induced peak broadening [148]. After several switching cycles, EEL spectra were acquired in the HRS (blue) and LRS (red) respectively (figure 6.11 b)). Interestingly, the *in situ* biasing has a pronounced effect on the fine structure of the Ti $L_{2,3}$ -edge. Most importantly, a significant broadening of the t_{2g} and e_g peak occurs in both resistive states. The peak broadening is more pronounced in the HRS and also a shift to lower loss energies is observed. This indicates a higher concentration of Ti^{3+} in the HRS compared to the LRS [225].

To confirm this observation, the O K -edge was acquired as well. Figure 6.11 c) shows the corresponding EEL spectra. The O K -edge in SrTiO_3 is mainly composed of three peaks that can be correlated to the hybridization of O 2p orbitals with Ti 3d, Sr 4d and Ti 4sp orbitals. The spectral fine structure of the O K -edge is sensitive to the amount of oxygen non-

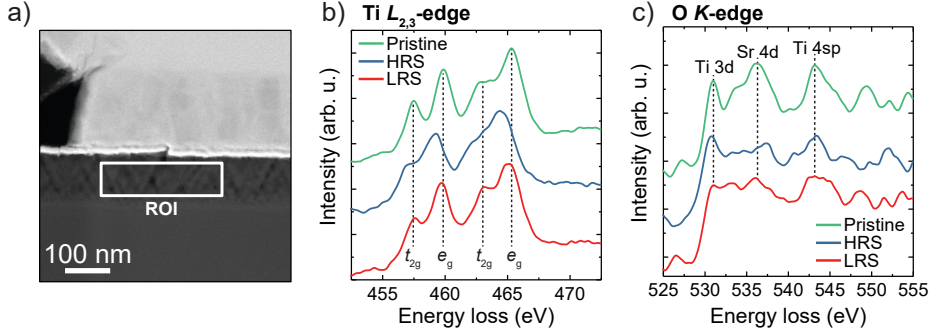


Figure 6.11: Spectroscopy of the switching SrTiO₃ layer. a) High-angle annular dark-field (HAADF) image showing the examined region of interest. b) Ti $L_{2,3}$ -edge and c) O K -edge electron energy loss spectra extracted from the region of interest (ROI) in (a).

stoichiometry [226]. The most pronounced effect of oxygen vacancies on the spectral shape is a decrease of the O 2p–Ti 3d and O 2p–Sr 4d peak combined with an increase of the intensity between the two peaks [119, 226]. A decrease in the O 2p–Sr 4d peak is clearly visible for both resistive states. This confirms the presence of Ti³⁺ that was also observed in the Ti $L_{2,3}$ -edge. However, looking at the O 2p–Ti 3d peak shows a stronger peak intensity decrease in the LRS. This indicates that the LRS has a higher concentration of oxygen vacancies than the HRS. This is in contradiction with the conclusions derived from the Ti $L_{2,3}$ -edge (figure 6.11 b)). Here it is important to consider that also microstructural changes induced by Joule heating, as observed in figure 6.10, can have an impact on the absorption edge. Therefore, a direct correlation between the spectral fine structure and the oxygen vacancy concentration is hindered.

To summarize, the EEL spectra show significant changes between the pristine and switched state. Based on the spectral fine structure it can be concluded that both, HRS and LRS, show signs of Ti³⁺. Comparing both resistive states also reveals spectral differences between HRS and LRS. However, a quantitative interpretation of the fine structure is complicated, as the Ti $L_{2,3}$ -edge indicates a higher degree of reduction in the HRS whereas the O K -edge suggests the LRS is more reduced.

6.2.2 Mapping of the oxygen distribution in different resistive states

In a next step, resistive switching was performed by directly contacting the top electrode with a tungsten probe tip. This approach allows to precisely control the filament position through the probe tip placement. With a known filament position, it is possible to map the oxygen distribution for different resistive states with high spatial resolution. Figure 6.12 a)

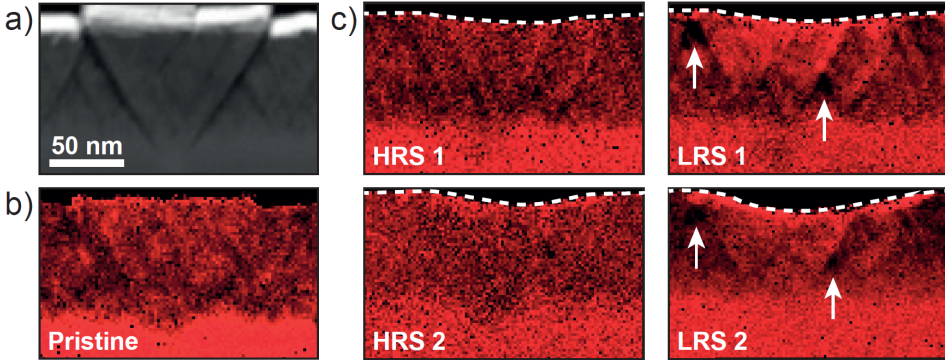


Figure 6.12: EELS mapping of the oxygen distribution in different resistive states. a) HAADF image of the region where the probe tip was placed. b) False color EELS map showing the O/Ti ratio. The map was created by dividing the O K -edge by the Ti $L_{2,3}$ -edge signal. c) False color maps of the same region as in (b), for different resistive states. The white arrows indicate regions with a low oxygen concentration.

shows a HAADF image of a selected sample region where the probe tip was placed for the switching experiments. A region with particularly pronounced island structure was chosen to potentiate any possible effects of the defect structure on the switching mechanism. The corresponding O/Ti ratio map extracted from EELS is shown in figure 6.12 b). In the following discussion, it is assumed that the changes in the O/Ti maps are induced by oxygen migration and titanium is considered to be immobile. While this assumption is only partly justified considering the changes of the thin film microstructure observed in the previous section, it is expected that the diffusion of titanium is much slower compared to the oxygen migration [227].

In the map, a dark region indicates a low oxygen concentration, whereas bright-red regions show high oxygen concentrations. It can be seen that the oxygen distribution in the pristine state is mostly homogeneous across the thin film. Figure 6.12 c) shows a series of O/Ti ratio maps acquired in different resistive states. For this, the device was formed and RESET into the HRS (HRS 1). Subsequently, the device was switched into the LRS (LRS 1). This process was repeated a second time (HRS 2 and LRS 2) and for each device state an O/Ti ratio map was measured. During the electrical treatment it was observed that the probe tip started to deform the specimen surface, which is indicated by the white dashed line. This is likely caused by the high temperatures that arise during the switching process and mechanical stress from the probe tip. A change in the oxygen distribution is apparent between the HRS and LRS state. While the HRS resembles the pristine state, i.e. exhibits a homogeneous oxygen distribution, the LRS clearly shows varying oxygen concentrations. Especially the defect structure of the film can easily be recognized in the LRS. Here it is noted, that the O/Ti maps were acquired over the whole specimen thickness (≈ 100 nm). Accordingly, if the filament

is smaller than the specimen thickness an additional background from the SrTiO₃ matrix is present. This might be the reason why no continuous oxygen depleted filament is visible but rather multiple vacancy rich regions are seen (white arrows in figure 6.12 c)). Nevertheless, the inhomogeneity of the LRS is a clear indicator for oxygen redistribution along antiphase boundaries. Importantly, this process is reversible and the distribution is associated with the resistive state. This excludes measurement artifacts, e.g. purely thermal effects or mechanical strain, as origin for the observed changes.

6.2.3 Summary of counter-eightwise switching in SrTiO₃

In this section, the counter-eightwise switching mechanism in SrTiO₃ memristive devices was investigated by means of *in operando* transmission electron microscopy. For this, lamella were prepared from counter-eightwise switching Nb:SrTiO₃/80 nm SrTiO₃/Pt devices to study the memristive devices in a cross-sectional view. Resistive switching within the microscope was reproducibly achieved using two different experimental biasing setups. Contrary to the switching properties of the bulk device, the lamella exhibited eightwise and counter-eightwise switching polarities. Typically, the lamella started with an eightwise polarity and then transitioned into counter-eightwise switching. It was suspected that the occurrence of eightwise switching is linked to the additional SrTiO₃/vacuum phase boundary and the missing thermal mass of the lamella structure.

The effect of successive switching cycles and high current limits on the film microstructure was investigated by ADF and BF imaging. It was observed that the defect structure of the film is substantially modified by high currents, indicating the generation of high temperatures during biasing. The electronic structure of the film before and after biasing was studied by EELS of the Ti $L_{2,3}$ and the O K -edge. Comparing the pristine film state with the switched film shows large spectral changes. While the pristine state compares well with literature spectra of fully oxidized single crystalline SrTiO₃, the spectra of the switched film show the presence of Ti³⁺ states. Interpretation of the spectral differences between the HRS and LRS, however, is complicated as structural and stoichiometry changes contribute to the spectral shape.

To study the oxygen distribution in both resistive states, O/Ti maps were acquired in the LRS and HRS respectively using quantitative EELS. Interestingly, it was found that the pristine and HRS feature a homogeneous oxygen distribution. In contrast, the LRS exhibits regions with low oxygen concentration particularly along the thin film microstructure. This behavior could be reproduced for multiple switching cycles demonstrating that it is associated to the resistive state and is not induced by artifacts from e.g. heating or strain effects.

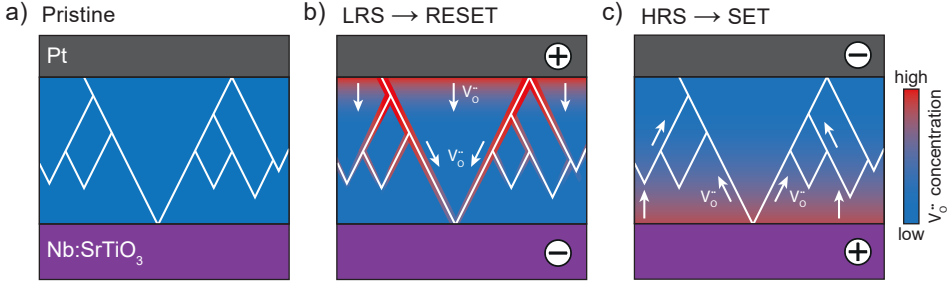


Figure 6.13: Proposed model for counter-eightwise switching in SrTiO_3 . A defect rich SrTiO_3 film (blue) is sandwiched between a Nb:SrTiO_3 bottom- (purple) and a Pt top electrode (grey). The extended defects are indicated by white lines. a) The device is initially in an insulating pristine state. b) After electroforming, the device is in the LRS state and an oxygen vacancy rich filament connects both electrodes. If a positive bias is applied to the top electrode, oxygen vacancies drift towards the bottom electrode. c) In the HRS state, vacancies are homogeneously distributed at the bottom electrode. Applying a negative bias to the top electrode leads to a drift of oxygen vacancies towards the Pt electrode.

6.2.4 Discussion: Origin of the counter-eightwise switching polarity in SrTiO_3

Based on the presented results, the origin of the counter-eightwise polarity in SrTiO_3 is discussed. In the previous chapter 5 it was demonstrated that counter-eightwise switching occurs predominantly in defect rich SrTiO_3 films. Therefore, it can be suspected that defects play an important role in determining the switching polarity. The influence of grain boundaries has already been studied in HfO_2 and SrTiO_3 based memristive devices. It was observed that grain boundaries can act as preferential sites for filament formation [228–232].

Based on the *in operando* TEM results, it is conceivable that in counter-eightwise switching SrTiO_3 devices, extended defects also act as preferential switching locations. One possible explanation for this behavior is the current channeling along defects and cavities that are formed during the growth process of defect rich SrTiO_3 [233,234]. If the defects serve as major current path, the highest temperatures are expected to arise at these positions due to Joule heating. Accordingly, ion migration is enhanced in the surrounding of the defects.

A phenomenological model of the switching process is presented in figure 6.13. Starting from an initially insulating device in the pristine state (figure 6.13 a)), an electroforming step is applied to bring the device in a switchable state. For this, a positive bias is applied to the Pt top electrode (compare chapter 5.1.2). Considering that the electroforming process in eightwise switching also requires a positive bias at the top electrode, it can be assumed that electroforming in both switching polarities involves similar processes. It is suspected

that electroforming in counter-eightwise switching occurs via the generation of oxygen vacancies by releasing lattice oxygen into the atmosphere as molecular oxygen (compare equation 2.18).

Due to the large bulk resistance of the thicker defect-rich SrTiO₃ layer, it is surmised that the electroforming step generates a conductive filament through the complete SrTiO₃ layer. This gives rise to an ohmic LRS (compare 5.3). If the extended defects exhibit an enhanced oxygen diffusion, oxygen vacancies will drift preferentially along the antiphase boundaries and form the filament along the defect structure. Figure 6.13 b) shows the electroformed device in the LRS state. The LRS is characterized by a large oxygen concentration gradient at the antiphase boundaries as observed by TEM (6.12). For the RESET, a positive voltage is applied to the Pt electrode. According to the electric field direction, oxygen vacancies are repelled from the top electrode and drift towards the bottom electrode. In the HRS, the oxygen distribution appeared homogeneously across the device. Thus it is assumed that the vacancies spread over a large region (Figure 6.13 c)). This is a conceivable scenario as the RESET is a self limiting process where the electric field repels oxygen vacancies from the filament. If a negative polarity is applied to the Pt electrode, vacancies are pulled towards the top electrode. If the vacancies reach an extended defect, they preferentially drift along the defect until a continuous filament is formed.

In summary, the origin of the counter-eightwise switching polarity can be explained by two effects: 1. An increased bulk resistance observed in thick SrTiO₃ films leads to the formation of a continuous filament through the switching layer. 2. Extended defects facilitate an internal redistribution of oxygen by acting as drift and diffusion fast paths.

7 Photoemission electron microscopy of Ta₂O₅ devices with graphene electrodes

Due to its excellent CMOS compatibility and exceptional switching properties, Ta₂O₅ is of highest technological relevance for the use in non-volatile memories and neuromorphic computing [17,235]. The details of the switching mechanism in Ta₂O₅ based devices, however, are still under debate. Despite extensive characterization efforts, quantitative information about the structure and composition of conductive filaments is rare.

In this chapter, functioning Ta/Ta₂O₅/graphene devices are investigated with synchrotron based X-PEEM. Using graphene as an ultra-thin top electrode allows a direct spectroscopic characterization of the switching layer [25]. In the first part of this chapter, the spatial resolution of the PEEM instrument is evaluated. Afterwards, it is demonstrated that spectromicroscopy can be performed on Ta₂O₅ films through a graphene layer. In the next section, the effect of the synchrotron beam irradiation on Ta₂O₅ is investigated. It is demonstrated, that the intense synchrotron radiation slightly reduces the Ta₂O₅ layer. The reduction is strongly inhibited by the graphene layer. In the last part, X-PEEM is employed to characterize Ta₂O₅ devices, providing spatially resolved spectroscopic information about the composition and structure of conductive filaments. All PEEM experiments presented in this chapter were carried out at the Nanospectroscopy beamline at the Elettra synchrotron laboratory (Trieste, Italy).

The results presented in this chapter have been prepared for publication:

T. Heisig, K. Lange, A. Gutsche, K. T. Goß, S. Hamsch, A. Locatelli, T. O. Mentş, F. Genuzio, S. Menzel and R. Dittmann, *in preparation*.

7.1 Spatial resolution of photoemission electron microscopy

One of the major obstacles to overcome in the characterization of switching filaments is to resolve their small spatial dimension. Contrary to the micrometer sized filaments that were observed in SrTiO₃ [121], in Ta₂O₅ the filament size is estimated to be in the order of a

few tens of nanometer [38, 131]. It was demonstrated that Ta₂O₅ devices with diameters below 30 nm show stable resistive switching [236], indicating that the filament size can reach very small dimensions. This underlines the importance of using spectromicroscopic techniques with high spatial resolution to image and characterize switching filaments. In this section, the spatial resolution of the *SPELEEM* microscope (Elmitec GmbH, Germany) at the Nanospectroscopy beamline at Elettra synchrotron laboratory (Trieste, Italy) will be discussed [147].

The spatial resolution of modern aberration corrected PEEM instruments is approximately 15-30 nm for imaging using secondary electrons and in the order of 50 nm using core level electrons [147]. However, the actual resolution can be negatively influenced by imperfect alignment of the microscope, sample drift and space charge effects [237]. Also the sample itself can greatly reduce the obtainable resolution. An ideal sample should be flat to prevent electromagnetic field distortions induced by surface morphology. Further, the sample should be conductive to allow charge compensation of the positive surface charge that builds up during photoelectron emission.

To determine the achievable resolution of a non ideal sample, i.e. a sample which is used for resistive switching, a model system composed of a sputtered Ta₂O₅ thin film partly covered by graphene was studied. This selection is motivated because the structure exhibits well-defined and sharp edges with little topography. First, the sample is characterized by AFM to verify that it is suitable to determine the resolution of a PEEM image. Figure 7.1 a) shows an AFM image of a sample section containing a region of Ta₂O₅ and Ta₂O₅/graphene. To measure the sharpness of the graphene edge, a line scan across both regions was taken. From the line scan in figure 7.1 b) it can be seen, that the apparent height of the graphene film is approximately 1.6 nm. The large difference between the theoretical thickness of graphene (0.335 nm) and the measured thickness can be explained by tip-sample interaction of the AFM operated in tapping mode [238]. To determine the resolution of the AFM image, the line profile was fitted using a complementary error function as described in detail in ref. [239]. This approach models a step edge by convolution of a Gauss- and a Heaviside-function. As a measure for the resolution, the full width at half maximum (FWHM) of the Gauss profile is used [147]. For the AFM line scan, a resolution of 23.5 nm was determined. This value reflects the minimum sharpness that is expected for the step edge. Accordingly, the edge can be used to measure the X-PEEM resolution down to 23.5 nm. Figure 7.1 c) shows a secondary electron image X-PEEM of the same sample section. The image was acquired at a photon energy of 200 eV using the same imaging conditions that are employed in the following sections to characterize devices. The image contrast arises from the different work functions of graphene and Ta₂O₅. Figure 7.1 d) shows the extracted line profile from the green box in (c). To obtain an adequate signal-to-noise ratio, a profile with a line width of 7 pixel was extracted. Using the same fitting procedure as before, yields a spatial resolution of 68.8 nm. In a next step, the resolution of a Ta4f

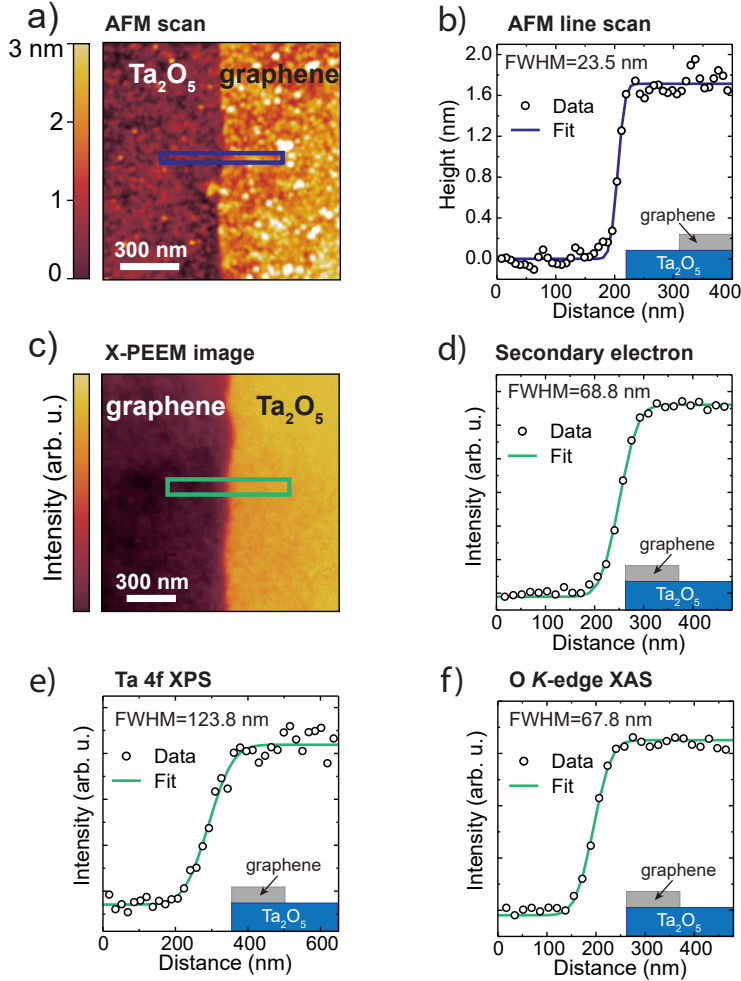


Figure 7.1: Spatial resolution of PEEM. a) AFM image of a sputtered Ta_2O_5 film covered partly by single layer graphene. b) Line scan across the step edge taken along the blue box in (a). c) Secondary electron X-PEEM image of the same region shown in (a) acquired at a photon energy of $h\nu = 200 \text{ eV}$. d) Line scan taken along the green box in (c). e) Line scan extracted from an X-PEEM image of the same region shown in (c) acquired by monitoring the Ta 4f core level electrons ($h\nu = 200 \text{ eV}$). f) Line scan extracted from a secondary electron X-PEEM image obtained at a photon energy of $h\nu = 532 \text{ eV}$ (O *K*-edge XAS).

photoelectron X-PEEM image was determined (image not shown). The line scan is displayed in figure 7.1 e). Here, the attenuation of core level electrons through the graphene layer results in an intensity difference between uncovered and graphene covered Ta₂O₅. A resolution of 123.8 nm was reached. This loss of resolution (compared to the secondary electron image) is due to the low intensity of core level electrons. To obtain acceptable signal-to-noise ratios longer integration times are required. This however, amplifies the noise contribution from sources such as sample or beam drift and from vibrations. Lastly, the resolution of a secondary electron image acquired at a photon energy of 532 eV was determined. This photon energy corresponds to the excitation energy of electrons from the O 1s core level into unoccupied states above the Fermi energy. Accordingly, this value represents the spatial resolution of an O *K*-edge XAS scan (see chapter for 3.5 for more details). The determined FWHM is 67.8 nm, which is very close to the resolution obtained for a secondary electron image at a photon energy of 200 eV (compare figure 7.1 d)).

From these results it can be concluded, that the spatial resolution of secondary electron images is in the order of 70 nm, while the core level photoelectron images reach a resolution down to 125 nm. It is noted that these values represent the best possible resolutions that were reached for this type of sample under standard imaging conditions. While minor improvements of the resolution might be achieved by further optimizing the microscope alignment, disproportionally longer alignment times are required. Thus, the resolution values represent a compromise between the alignment time and achieving an adequate spatial resolution.

7.2 Photoelectron spectroscopy through graphene electrodes

As discussed in chapter 3.6, photoelectron spectroscopy is a surface sensitive technique that is limited by the inelastic mean free path of photoelectrons. To probe the active interface of memristive devices, a thin electrode is required. Considering that the IMFP of electrons in solids is in the order of 1 nm, even the thinnest metal electrodes (approx. 2 nm) strongly attenuate the photoelectron intensity of buried layers [25]. For this reason, graphene represents an ideal electrode material that combines high electrical conductivity with a single atomic layer thickness. In this section, the viability of graphene as photoelectron transparent electrode will be evaluated.

The signal attenuation induced by graphene can be estimated by the Tanuma, Powell and Penn (TPP-2M) formula using bulk values of graphite [240]. For a photon energy of 200 eV and a graphene thickness of 0.335 nm, a transmittance of approximately 60% is expected. However, such calculations are not suited for 2D-materials as they neglect interface effects [241]. Therefore, the transmittance of graphene on Ta₂O₅ was determined experimentally.

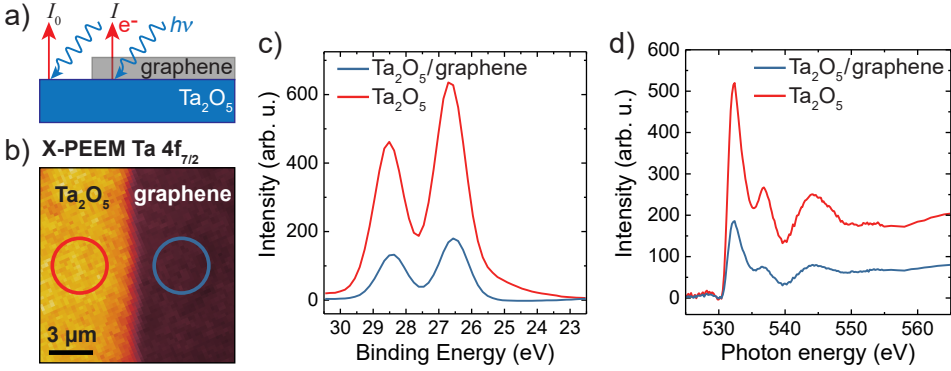


Figure 7.2: Transmittance of graphene electrodes. a) Geometry of the sample with the intensity of photoelectrons emitted from uncovered Ta_2O_5 I_0 and from a graphene covered region I . b) X-PEEM image obtained using Ta $4f_{7/2}$ core level electrons. c) Ta $4f$ XPS spectra extracted from regions marked with circles in (b). The spectra were acquired using a photon energy of 200 eV. d) O K -edge XAS extracted from the regions marked in (b).

Figure 7.2 a) shows the used sample geometry. The transmittance (in percent) is given by

$$T = I/I_0 \cdot 100 \quad (7.1)$$

with the photoelectron intensity I_0 from Ta_2O_5 and I from graphene covered Ta_2O_5 .

This approach is only valid if the emitted photoelectrons are generated in the Ta_2O_5 layer. Therefore, a binding energy was selected that corresponds to the Ta $4f_{7/2}$ core level. Figure 7.2 b) shows an X-PEEM image of a sample section partly covered by graphene. The brightness of the represents the photoelectron intensity. From both sections, a Ta $4f$ XPS spectrum was extracted (compare figure 7.2 c)). From the spectra, it can be seen that the intensity of the graphene covered region (blue) is significantly reduced. Calculating the transmittance gives $T \approx 28\%$. As the IMFP is a function of the photon energy, the transmittance of secondary electrons was measured at photon energies from 520-570 eV, corresponding to the O K -edge. The O K -edge absorption spectrum is shown in figure 7.2 d). The transmittance at a photon energy of 532 eV is 35% and therefore slightly higher than the transmittance at a photon energy of 200 eV. However, the value is still much smaller than the theoretical transmittance of 79%. Table 7.1 summarizes the experimental and theoretical transmittance values.

Table 7.1: Photoelectron transmittance of graphene for different photon energies.

Photon energy (eV)	Measured transmittance (%)	Theoretical transmittance ¹ (%)
200	28	60
532	35	79

¹ Calculated using the TPP-2M equation and the NIST Electron Inelastic-Mean-Free-Path Database [240, 242].

While the experimentally determined values for the transmittance are decreased by a factor of 2 compared to the theoretical prediction, it is still possible to employ graphene as photoelectron transparent electrode. A possible explanation for the lowered transmittance could be the deposition of amorphous carbon contaminants during X-ray irradiation, which is commonly observed due to cracking processes of carbon containing residual gases [243]. Nevertheless, comparing the XPS and XAS spectra from Ta₂O₅ with- and without graphene demonstrates that all spectral features are preserved. Graphene can therefore be considered as suitable electrode material for photoelectron emission spectroscopy experiments of buried switching layers.

7.3 Stability of Ta₂O₅ under synchrotron radiation

Before resistive switching devices are analyzed using synchrotron based PEEM, it is important to evaluate if the highly intense X-ray synchrotron radiation has an effect on the devices. While inorganic materials are less prone to radiation damage compared to organic and soft matter, recent advances in photon sources and focusing optics give the possibility to characterize samples with very intense radiation [244]. Under these extreme conditions also inorganic materials become susceptible to radiation induced damage [245]. Especially, the generation of oxygen vacancies is commonly observed in transition metal oxides if the experiment is performed under UHV conditions [121, 246]. Hence, it is important to carefully study the effects of synchrotron radiation on Ta₂O₅ to differentiate between switching- and radiation-induced changes of the device stoichiometry.

For this, a thin film was exposed to the highest possible photon flux ($\approx 10^{13}$ ph/s) for 20 min while simultaneously acquiring core level spectra. Figure 7.3 a) shows the Ta 4f core level as a function of the irradiation time. Each line represents a single Ta 4f core level spectrum. The 7/2 and 5/2 core level peaks are visible as bright stripes. Upon closer inspection, one notices that the peak positions gradually shift towards higher binding energies. This effect becomes more clear by comparing the spectra at the beginning and after irradiation (see figure 7.3 b)). The irradiation caused a shift of the core level by approximately 0.3eV to higher binding

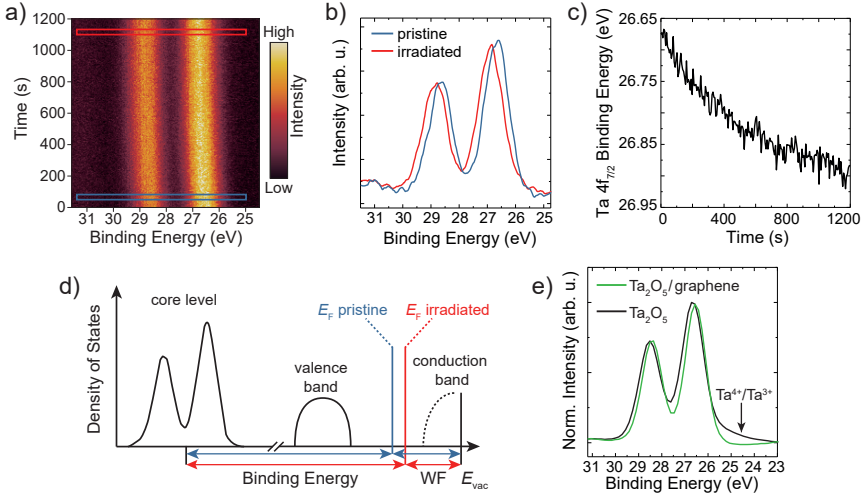


Figure 7.3: Effects of synchrotron radiation on Ta_2O_5 thin films. a) Ta 4f core level as a function of irradiation time. b) Extracted Ta 4f spectra from the blue (pristine) and red (irradiated) box in (a). c) Binding energy of the Ta 4f_{7/2} peak as a function of irradiation time. d) Schematic illustration of the binding energy shift with WF the work function, E_{vac} the vacuum level and E_{F} the Fermi level. e) Ta 4f spectra of uncovered (black) and graphene covered (green) Ta_2O_5 after irradiation.

energies. To correlate the peak shift to the irradiation time, the 7/2 peak was fitted using a Gaussian peak shape for each spectrum and the peak maximum was plotted against the irradiation time (figure 7.3 c)). The plot reveals that the binding energy shifts linearly with the irradiation time for the first 400 s and then slope decreases. This demonstrates that the irradiation induced changes do not completely saturate within the first 20 min and it is likely that the effect continues until a steady state is reached.

At first, the shift towards higher binding energies seems counter intuitive as the creation of oxygen vacancies should lead to the formation of reduced Ta valence states at lower binding energies (compare chapter 4.3). However, it was demonstrated that small oxygen vacancy concentrations do not change the core level peak-shape significantly but induce a shift towards higher binding energies [164]. This can be understood by considering that oxygen vacancies act as n -type dopant and shift the Fermi energy closer to the conduction band. As the binding energy in XPS is a measure of the energy difference between the Fermi level and the respective occupied electronic state, a shift of the Fermi level to the conduction band increases the binding energy of all occupied states [247]. This effect is illustrated in figure 7.3 d). Consequently, the work function should decrease by the same amount, as it is defined as the energy difference between the Fermi level and the vacuum level.

So far, the effect of beam irradiation was studied only on Ta₂O₅ films that are in direct contact to the UHV atmosphere of the PEEM instrument. The question arises if a graphene layer influences the reducing effect of the X-ray beam by protecting the oxide from the UHV environment. A strong impact from photon absorption of graphene, i.e. reducing the effective photon flux that is reaching the Ta₂O₅ film, is not expected as graphene is almost completely transparent for X-ray radiation. Figure 7.3 e) shows the Ta 4f spectra extracted from a region with (green) and without graphene (black). Both regions have been irradiated identically for approximately 4 h. Comparing both spectra reveals that the Ta₂O₅ surface without graphene shows a small contribution of Ta⁴⁺ and Ta³⁺ states at low binding energies. Fitting the core level spectra gives an O/Ta ratio of approximately 2.4 (fitting not shown). In comparison, the graphene covered region shows no sign of reduction. However, evaluation of the peak position indicates that also the graphene covered region exhibits small amounts of oxygen vacancies (comparable to 15 min exposure of an uncovered Ta₂O₅ film). This demonstrates, that the graphene film effectively protects the oxide layer from beam damage. While the reduction is not completely inhibited, the process is slowed down significantly. Based on these results, it is assumed that the beam reduction of graphene covered devices only has a minor influence on the electronic structure compared to the switching induced changes. The justification of this assumption will be given in the next sections.

To summarize, it was demonstrated that irradiation of a Ta₂O₅ thin film with an intense synchrotron X-ray beam under UHV conditions induces the generation of oxygen vacancies. For small oxygen vacancy concentrations, a shift of the Ta 4f core level towards higher binding energies was observed, whereas no signs of suboxides were visible in the spectral shape. It was found that the process occurs gradually over a time span of several minutes to hours. Graphene greatly improves the stability of Ta₂O₅ against beam reduction.

7.4 Spectromicroscopy of functioning Ta₂O₅ graphene devices

In this section, the spectroscopic signatures of switching induced changes will be analyzed in functioning devices. For this, a crossbar device layout with graphene top electrodes was employed (compare figure 7.4 a)). The crossbar design allows the characterization of the entire device area by contacting the graphene outside of the active device area. Figure 7.4 b) and c) show an optical- and electron-microscopy image of an exemplary 10×10 μm² device. While also smaller devices were prepared, the chance for graphene delamination increased with decreasing top electrode thickness. Therefore, the X-PEEM analysis mainly focused on devices with an electrode area of 100 μm² or larger. Considering that the device size is large compared to the filament size, the localization of the switching filament within the device area is a challenging task. For this, devices were first analyzed by work function scans. This allows

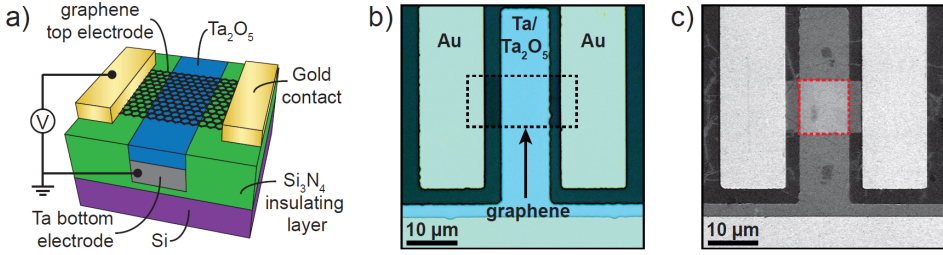


Figure 7.4: Crossbar device layout with graphene top electrodes. a) 3D schematic of the device structure. A Ta_2O_5 channel (blue) is sandwiched between a sputtered Ta bottom electrode (grey) and a graphene top electrode (black honeycomb lattice). The graphene layer is electrically contacted through Pt/Au metal contacts, which are electrically separated from the bottom electrode by an insulating Si_3N_4 layer (green). b) Optical microscope image of a single device. The graphene layer (black dashed line) is visible as slightly darker region. c) SEM image of a similar device imaged using a low acceleration voltage (1 kV). The graphene layer is visible as bright region. The active device area is marked by the red dashed line.

mapping of devices with high spatial resolution and short scan times. The work function scans then serve as a basis for further spectroscopic analysis.

Before introducing the sample into the PEEM chamber, devices were electroformed in air using different current limits. Figure 7.5 a) shows the electroforming step of an investigated device. For this particular device, a deliberately high current compliance of 1 mA was used. This was done to maximize the switching induced changes, i.e. the filament size and oxygen non-stoichiometry, while maintaining the functionality of the device.¹ The I - V curve shows a distinct forming step at a voltage of approximately -4.5 V. This is in good agreement with the observed switching characteristics of graphene devices presented in chapter 5.2. Initially, the pristine device is in an insulating state ($R > 10^8 \Omega$) and drops to a LRS of approximately $5 \times 10^3 \Omega$ after the forming procedure.

In a next step, the device was analyzed by PEEM. Figure 7.5 b) shows a secondary electron PEEM image acquired at an electron energy of 3.2 eV. A field of view was selected which includes the complete device area (solid orange line), to ensure that all possible filament formation sites are within the image. From the image it is clearly visible, that the graphene layer is torn in the middle of the device, leaving a central region of the device uncovered. Such defects in the graphene layer are commonly observed in devices and are caused by the mechanical stress that occurs during the graphene transfer process. A more detailed description of graphene defects is given in the appendix in figure A5. Nevertheless, the electrical characterization confirmed that the device is fully functional. Therefore it can be assumed that the top electrode defect has no effect on the switching properties. Upon closer examination of the

¹Here it is noted that devices were also switched with smaller currents below 100 μA . However, only in devices operated with high currents above 1 mA filaments were observed.

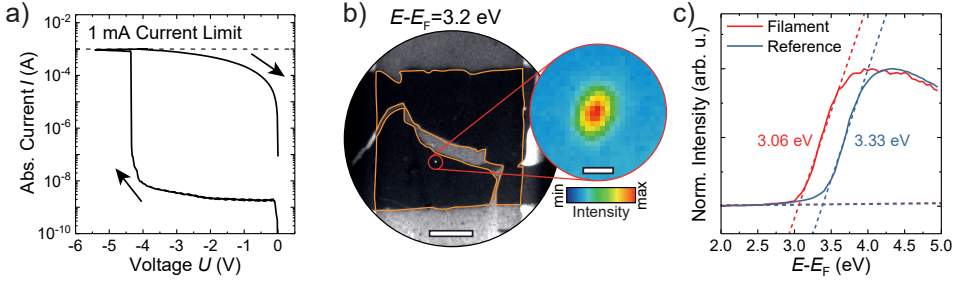


Figure 7.5: Work function analysis of a formed device. a) Electroforming I - V curve of a Ta/8 nm Ta₂O₅/graphene device. b) PEEM image of the electroformed device from (a) at an electron energy of 3.2 eV. The device features a large crack in the graphene layer. The active device area is highlighted by the orange line. Scale bar 3 μ m. Inset: False colour image of a device section featuring a pronounced contrast. Scale bar 100 nm. c) Work function spectra extracted from the feature observed in (b) (red) and the surrounding area (blue).

device area, it can be seen that a single bright feature is located on the device area. The size of the feature can be estimated to be 120 nm or smaller. Precise determination of the feature size is limited by the spatial resolution of the image (approximately 70 nm) and the gradual fading of the feature.

Extracting the work function from the feature and the surrounding region shows that the feature exhibits a decreased work function (see figure 7.5 c)). By fitting the rising edge and the background of the spectra using linear regression, the work function can be determined as the intersection point of both linear fits. Extracting the values of both regions yields 3.06 eV for the feature and 3.33 eV for the reference. This work function shift of -0.27 eV fits well to the previously observed core level shift of Ta₂O₅ reduced by synchrotron radiation (compare section 7.3). The shift towards lower $E-E_F$ values indicates that the Fermi level is located closer to the conduction band, which is expected for an oxygen vacancy rich filament. It can therefore be suspected, that the feature corresponds to the switching filament.

To confirm this hypothesis, the Ta 4f core level of the device was mapped using X-PEEM. Figure 7.6 a) shows an X-PEEM image of the region previously identified as possible filament location. The image was generated by averaging over all images acquired at binding energies from 26-23 eV. As this energy range corresponds to reduced Ta ^{$x+$} ($x = 4, 3, 2, 1$) valence states, a high intensity in the image signifies a high concentration of reduced states. Here it is noted that the high intensity from the region without graphene (solid orange line) is caused by the missing signal attenuation from the graphene layer. Interestingly, the feature previously observed in the work function scan appears at the same location in the core level image.

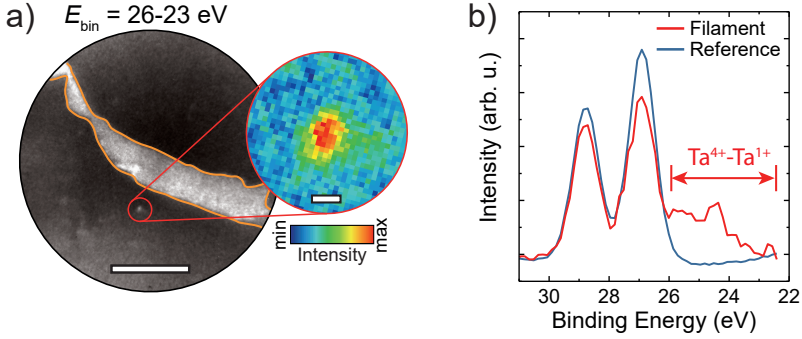


Figure 7.6: XPS signature of a switching filament. a) X-PEEM image of the region localized in figure 7.5, acquired using Ta 4f core level electrons. The image was obtained by averaging multiple images taken at binding energies from 23-26 eV. The solid orange line marks the hole in the graphene electrode (bright region). Scale bar 2 μm . Inset: False colour map of the region of interest. Scale bar 100 nm. b) Ta 4f spectra extracted from the feature (red) and the surrounding region (blue) as reference.

Figure 7.6 b) shows the Ta 4f core level spectra extracted from the feature and the surrounding area as reference. For this, the spectrum of the feature was extracted from a 3×3 pixel sized region (red pixel in the false colour map in figure 7.6 b)). The spectra reveal, that the feature exhibits significant amounts of reduced Ta^{x+} states, whereas the reference spectra shows only Ta^{5+} . Fitting of the core level spectrum yields an O/Ta ratio of 2.1, which corresponds to an oxygen vacancy concentration of $\approx 16\%$. Importantly, no metallic component was found, which is in good agreement with the observations made in chapter 4.4. From the signal intensities of the spectra, it can be concluded that the filament region is still covered by the graphene layer. This is important because a defective graphene layer would cause a partial re-oxidation of the filament between switching in ambient atmosphere and introducing the sample to a vacuum environment.

In a next step, the filament was studied with XAS by measuring the O K -edge of the filament. Figure 7.7 a) shows a secondary electron PEEM image measured at a photon energy of 534 eV. This photon energy was selected as it is located between the t_{2g} and the e_g absorption peaks. This spectral region was found to be sensitive to variations of the oxygen stoichiometry [89]. Again, the filament appears at the same location as before. The O K -edge spectra are shown in figure 7.7 b). To ensure that the graphene has no influence on the spectral shape of the oxygen absorption edge, caused by e.g. polymer residues, a region without graphene was analyzed as well. Comparing the reference spectra (blue) and the region without graphene (green) shows no significant spectral differences. The intensity differences at high photon energies are likely caused by a small beam drift that can occur during the measurement. The reference spectra are in good agreement with data published for Ta_2O_5 [248]. In contrast, the O K -edge

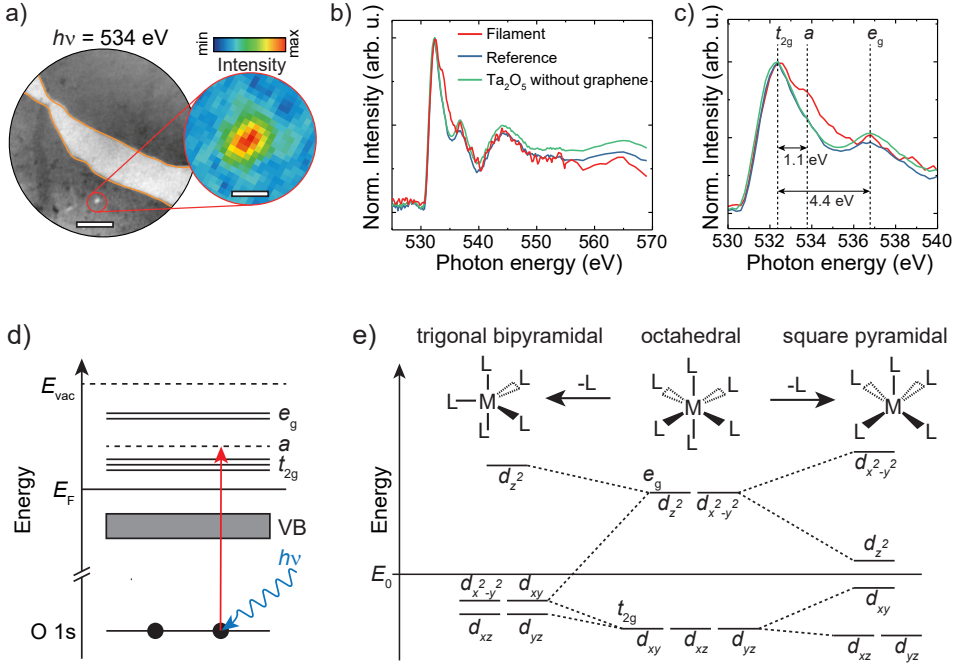


Figure 7.7: O K -edge absorption spectrum of a switching filament. a) PEEM secondary electron image obtained at a photon energy of 534 eV. Scale bar 1, μm . Inset: False colour image of the filament region. Scale bar 100 nm. b) O K -edge spectra of the filament (red), the surrounding region (blue) and from an area without graphene (green). c) Magnification of the spectral region featuring the t_{2g} and e_g peaks. d) Schematic depiction of the X-ray absorption process of O 1s electrons in an octahedral coordination with an additional unoccupied energy level a . e) Energies of the 5d orbitals in an octahedral, trigonal bipyramidal and square pyramidal ligand field. E_0 denotes the average energy of the d-orbitals. The energy diagrams are based on ref. [249] and [250].

spectrum of the filament shows distinct differences in the spectral fine structure. The most striking difference is an additional peak shoulder "a" that appears at a photon energy of approximately 534 eV (compare figure 7.7 c)). The shoulder is located 1.1 eV above the t_{2g} level, which is 1/4 of the energy separation between t_{2g} and e_g level (4.4 eV). Furthermore, the filament spectrum shows an overall higher intensity in the region between the t_{2g} and e_g peak.

To understand these spectral variations, first the O K -edge fine structure of stoichiometric Ta₂O₅ is discussed. The O K -edge stems from the excitation O 1s electrons according to the dipole selection rule into unoccupied O 2p states. In a purely ionic picture, the O²⁻ anion has an electron configuration of O 1s²2s²2p⁶ and therefore no empty O 2p states are available for the excitation. However, covalency in the Ta-O bond reduces the number of filled O 2p states,

giving rise to the O *K*-edge. The fine structure of the absorption edge can be explained by the hybridization of O 2p states with Ta 5d states, which are split into t_{2g} and e_g states by an octahedral ligand field (compare figure 7.7 d)). A third broad peak appears at a photon energy of 544 eV. This peak can be assigned to a hybridization of O 2p with Ta 6sp states [248]. As spectral variations between the filament and the reference occur only in the first part of the spectrum, only peaks originating from the hybridization between O 2p and Ta 5d orbitals will be discussed.

Considering that the filament contains large amount of oxygen vacancies, it is likely that the octahedral coordination geometry changes. The system can compensate for lost ligands either by adapting a lower coordination number or by polymerization of octahedrons from corner-, to edge-, to plane-sharing. However, only polymerization of the octahedrons can not explain the changes of the spectral fine structure. Therefore, it is assumed that the coordination number decreases and a new ligand polyhedra is adopted. Figure 7.7 e) shows the most likely geometries for fivefold coordination and the corresponding orbital energies according to the ligand field theory [249]. The two possible configurations are trigonal bipyramidal (D_{3h} symmetry) and square pyramidal (C_{4v} symmetry). Both configurations would give rise to additional empty states above the t_{2g} level that could explain the occurrence of the peak shoulder *a*. However, it would also induce states above the e_g , which is not observed experimentally. To explain this it is important to consider that the presented configurations are idealized structures. In reality the polyhedra are likely distorted from their ideal angles. Distortion of the coordination polyhedra shifts the orbital energies towards the average energy of the d-orbitals [251]. Therefore, the observed spectral variations in the filament could be explained by transformation of octahedral to distorted fivefold coordination polyhedrons. These observations are in good agreement with literature results that suggest the presence of distorted square pyramidal coordination in reduced TaO_x [89, 90].

Unfortunately, the spectroscopic characterization of the switching filament was limited to the LRS, as no RESET could be achieved after X-PEEM characterization. While in principle the X-PEEM is a non-destructive technique, the device was stuck in the LRS after the spectroscopic investigation. It is assumed, that the prolonged synchrotron X-ray radiation reduced the Ta₂O₅ film over a large area, i.e. the beam footprint of a few μm^2 , which increases the leakage current of the device. As a consequence, no RESET of the filament can be achieved as the electric field drops across the large reduced area and no local heating can occur as the current that passes through the filament is decreased.

In the previous chapter 6 it was demonstrated that switching in SrTiO₃ can induce changes in the device morphology, especially if high currents are applied. Similar observations have also been made for Ta₂O₅ devices [132]. To investigate if a topography change occurs in graphene devices, the filament was studied by AFM. The AFM images are presented in fig-

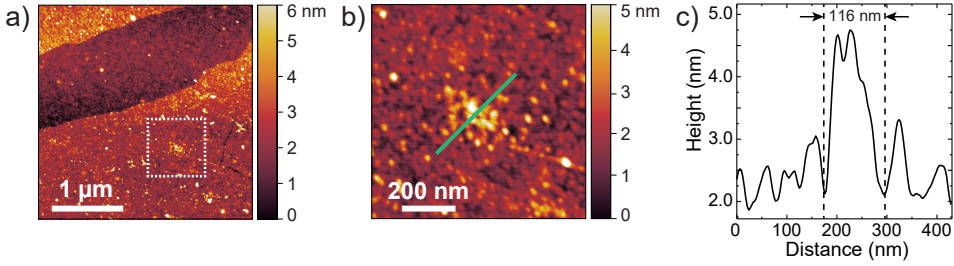


Figure 7.8: AFM-topography of a filament. a) Sample topography of the device in figure 7.5. b) Zoom-in on the filament area marked with a white dashed line in (a). c) Line scan along the green line in (b).

ure 7.8 a) and b). Using the filament position from the X-PEEM images, the filament can be located in the AFM scan. From the topography scans, it can be seen that the filament exhibits an increased height. Smaller topographic features of similar height can be found at other location on the device, however, they presumably originate from the sputter deposition. Figure 7.8 c) shows a line scan across the filament. Measuring the dimension of the filament yields a diameter of approximately 116 nm with a maximum height difference of 2.6 nm. The diameter is in good agreement with the dimensions obtained from the X-PEEM results.

In the following, the possible mechanism are discussed that could explain the observed topography. First, the topography could not be directly related to the switching process itself, but rather to a defect in the film formed during deposition. Such a defect, e.g. a nano pore, could represent a weak point in the oxide film and thus facilitate a dielectric breakdown during electroforming. A second possibility is a volume expansion of the Ta bottom electrode due to partial oxidation and an associated restructuring of the switching matrix. Lastly, it has been proposed, that high temperature gradients during switching induce the migration of cations towards the filament (see chapter 2.4) [38]. Due to the very high activation energy for Ta diffusion, the latter scenario appears to be the most unlikely [101]. An atomic rearrangement on the other hand appears to be the most likely scenario. While a complete crystallization would lead to a phase separation between metallic Ta⁰ and Ta₂O₅, a partial restructuring of the atomic configuration is evidenced by the observed spectral changes in the O *K*-edge. Furthermore, it is known that oxide thin films can undergo significant volume expansion upon introduction of oxygen vacancies [252].

In order to obtain a rough estimation whether the characterized filament can explain the observed resistance change, a simple model is employed to simulate the current flow through the device using the chemical information derived from the X-PEEM measurements. Figure 7.9 a) shows the equivalent circuit diagram of a Ta/Ta₂O₅/graphene device. As discussed in chapter

5.2, the LRS in such devices is governed mainly by two contributions, the series resistance of the graphene electrode (R_{graphene}) and the filament resistance (R_{bulk}).

Under the assumption that the Schottky barrier becomes negligible in the LRS state, the current passing through a cylindrical filament can be calculated according to

$$I = \frac{V}{\rho l_{\text{fil.}}} \left(\frac{\pi d_{\text{fil.}}}{2} \right)^2 \quad (7.2)$$

with V the voltage, ρ the filament resistivity, $l_{\text{fil.}}$ the filament length and $d_{\text{fil.}}$ the filament diameter.

With the Ta₂O₅ film thickness as an approximation for $l_{\text{fil.}} = 8$ nm and the measured diameter from X-PEEM and AFM $d_{\text{fil.}} \approx 120$ nm, the only unknown parameter is the filament resistivity. In chapter 4.3, the sheet resistances of TaO_{*x*} thin films for a wide range of O/Ta ratios were determined. By combining the chemical information derived from the Ta 4f X-PEEM measurement and the sheet resistance values from the reference TaO_{*x*} films, it is possible to estimate the filament resistivity. Fitting of the Ta 4f core level peak yields an O/Ta ratio of 2.1 for the filament (see figure 7.6). Extrapolating the resistivity for this O/Ta ratio from data shown figure 4.8 f) gives a filament resistivity of $\rho \approx 0.33 \Omega \text{ cm}^2$. For easier assessment of the result it can be compared to the resistivity of graphite perpendicular to the basal plane ($\rho \approx 0.3 \Omega \text{ cm}$) [253]. Accordingly, the filament resistivity ranks below that of most intrinsic semiconductors, e.g. Si or Ge, but above the metallic regime.

Using these values as an input for equation 7.2 yields the current for a given voltage. Figure 7.9 shows the measured I - V curve of the device in figure 7.5 and the calculated current values for three filament diameters. To account for the series resistance of the graphene top electrode, a resistance of 2.5 k Ω was subtracted from the measured resistance values. The value was estimated based on resistance measurements of similar graphene electrodes (compare figure A4). The error bars indicate the estimated uncertainty of the series resistance. Comparing the simulated current with the experimental data shows a good agreement between prediction and measured current. For a filament diameter of 120 nm the best fit is obtained, which compares well to the experimental findings.

Here it is emphasized, that this simple model should only serve as a rough estimation to test if the experimentally derived filament size and composition yield reasonable resistance values. The model neglects the influence of the Schottky barrier and assumes an homogeneously conductive filament. However, the linear I - V characteristic of the LRS (compare figure 5.6)

²The resistivity was calculated by multiplying the measured sheet resistivity of 10.6 k Ω/\square of a TaO_{*x*} film ($x \approx 2$) with the film thickness of 310 nm. The thin film thickness was determined by XRR.

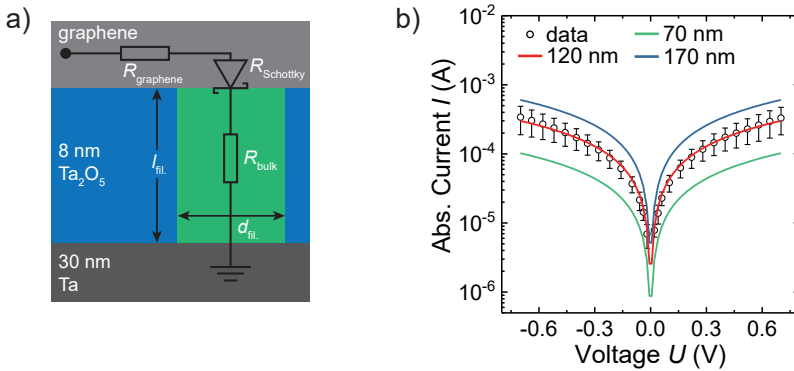


Figure 7.9: Current simulation of a switching filament. a) Equivalent circuit diagram of a Ta/Ta₂O₅/graphene device in the LRS. The green area represents the filament. b) Experimental I - V characteristic (black circles) of the LRS state of the device in figure 7.5. A series resistance of 2.5 k Ω was subtracted from the experimental data to account for the series resistance of graphene. The error bars indicate the uncertainty of the graphene resistance. The solid lines show the simulated I - V curve for a filament diameter of 70 (green), 120 (red) and 170 nm (blue).

indicates that the Schottky barrier is not dominating the current transport in the LRS. Considering that X-PEEM is limited to a probing depth of approximately 2-3 nm, it is unclear if the determined O/Ta ratio is homogeneous along the filament length, or if an oxygen vacancy gradient is present.

7.5 Summary

In summary, this chapter presented an approach to characterize Ta₂O₅ resistive switching devices with spectromicroscopy. Using a state of the art PEEM instrument combined with highly intense synchrotron radiation, a spatial resolution of 70 nm for secondary electron imaging and XAS was achieved. Imaging with core level electrons in an XPS measurement reduced the obtainable resolution to 120 nm. Measuring the photoelectron transparency of a single layer graphene electrode confirmed that graphene is a suitable top electrode material to perform photoelectron emission spectroscopy of buried layers. While the determined graphene transmittance is well below the theoretical value, it was still possible to acquire high resolution XPS and XAS spectra of graphene covered Ta₂O₅ layers. Importantly, no influence of the graphene electrode on the oxygen absorption edge was observed, which indicates that no substantial amounts of PMMA polymer contaminants are present. Studying the effect of synchrotron radiation on Ta₂O₅ revealed that the beam has a reducing effect on the oxide. Over the time span of several minutes, oxygen vacancy generation becomes evident as a continuous shift of the Ta 4f core level towards higher binding energies. This effect is sup-

pressed by graphene, possibly by acting as a protection layer against the UHV environment of the PEEM instrument. Measuring the peak shift, i.e. the reduction process, as a function of time shows that the process is slow and does not impair the quantification of switching filaments.

X-PEEM analysis based on photoelectron threshold spectroscopy revealed that some of the electroformed devices featured a small, confined region with a reduced work function. Mapping the Ta 4f core level of a region with reduced work function confirmed the presence of reduced Ta^{x+} valence states, which are indicative for oxygen vacancies. A filament composition of O/Ta \approx 2.1 could be determined. Importantly, using the determined chemical shifts deduced from TaO_x reference films, verified the absence of a metallic Ta⁰ component. Analysing the O K-edge of the filament demonstrates that the generation of oxygen vacancies leads to a rearrangement of the octahedral coordination symmetry. Comparing the spectral fine structure with literature results suggests that the ligand coordination in the filament consists of distorted octahedral polyhedra with a contribution from either square pyramidal or trigonal bipyramidal coordination.

The morphology of the filament was studied by AFM. The filament diameter was estimated based on a slightly modified topography to be 120 nm, fitting well to the size estimated from the X-PEEM measurement. Additionally, the filament region increased in height by approximately 2 nm. This could be induced by oxidation of the bottom electrode or through lattice expansion due to oxygen vacancies. To verify that the observed filament composition and structure give physically sensible current voltage characteristics, a simple model was used to simulate the experimental read-out *I-V* sweep in the LRS. Using the resistivity value from a reference TaO_x thin film with a comparable oxygen stoichiometry and the filament dimension from PEEM and AFM experiments confirmed, that the experimentally derived parameters describe the LRS *I-V* characteristics reasonably well.

7.6 Discussion of the switching mechanism

As discussed in the beginning of this chapter, the underlying physicochemical processes that give rise to counter-clockwise switching in tantalum oxide are still under controversial debate. With experimental evidence from various spectromicroscopic techniques and electrical transport measurements, different models have been proposed to explain the resistive switching properties of tantalum oxide. In the following, the most commonly invoked models in literature are introduced and evaluated based on the experimental results presented in this chapter.

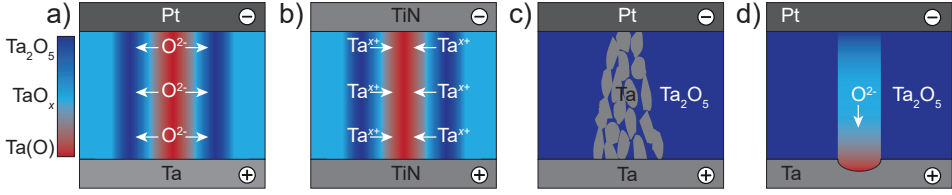


Figure 7.10: Proposed switching mechanisms in tantalum oxide. The suggested processes that lead to a filament formation are illustrated. a) Thermophoresis induced radial oxygen migration based on ref. [138,139]. The false colour bar indicates the amount of oxygen vacancies (red: high concentration, dark blue: low concentration). b) Cation accumulation due to thermophoresis as proposed in ref. [38]. c) Percolation through metallic Ta clusters according to ref. [135]. d) Classic VCM switching model based on electric field and Joule heating induced oxygen drift [254, 255].

Model 1: Thermophoresis induced radial oxygen migration. This model is based on experimental observation from X-ray fluorescence, EELS and X-ray absorption spectroscopy [131, 139], where Ta-rich conductive filaments were observed surrounded by an oxygen rich halo. Figure 7.10 a) schematically depicts the measured oxygen vacancy distribution. Importantly, the investigated devices were fabricated from a slightly reduced Ta_2O_{5-x} layer. Three distinct regions could be identified, an oxygen poor region (red), a surrounding region with increased oxygen concentration (dark blue) and the remaining device area with a medium oxygen concentration (light blue). To describe this oxygen distribution and explain the switching behaviour, a quasi-3D model was used to model the ionic flux during device operation through a combination of Fick diffusion, thermophoresis (also called Soret diffusion) and ionic drift [138]. In this model, oxygen anions diffuse along the temperature gradient from high temperatures towards low temperatures, i.e. away from the conductive filament. This process is known as thermophoresis. Opposing to the thermophoresis, Fick diffusion leads to the diffusion of oxygen anions towards the filament along the concentration gradient. By using the filament radius as state variable, the model is capable to describe the resistance change between LRS and HRS through shrinking and expanding of the filament.

Importantly, in the here presented device, no lateral variation of the oxygen concentration around the filament was observed in the O *K*-edge XAS measurements. The reason for this might be related to the stoichiometry of the switching layer. While thermophoresis of oxygen was observed in TaO_x layers with slight oxygen deficiency, here fully oxidized Ta_2O_5 was used. Furthermore, the authors reported that the lateral diffusion took place over a large number of cycles (10^5) [139]. This might indicate that the thermophoresis of oxygen is not related to switching between LRS and HRS, but rather represents a concomitant process that could explain aging effects, device failure and cycle-to-cycle variability.

Model 2: Thermophoresis induced cation accumulation. This model is very similar to the previously discussed model, however, here it is proposed that thermophoresis drives the

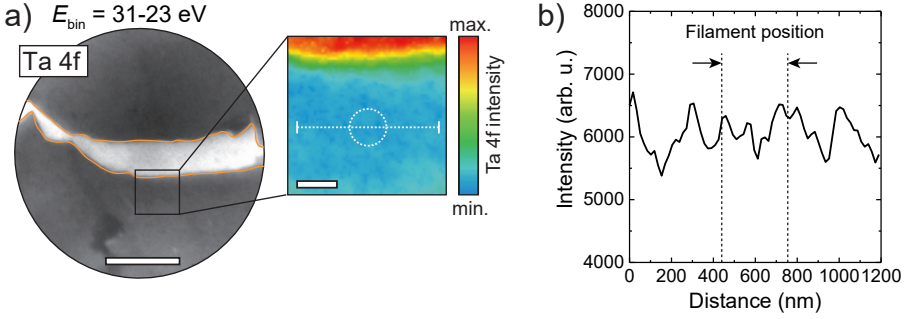


Figure 7.11: Local Ta concentration of the switching filament. a) X-PEEM image of the filament region localized in figure 7.5, acquired using Ta 4f core level electrons. The image was obtained by averaging multiple images taken at binding energies from 23-31 eV. Scale bar $2 \mu\text{m}$. Inset: False color map of the magnified filament region. Scale bar 300 nm . The white dashed circle indicates the filament position. b) Line profile extracted from the white dashed line in (a). The black dashed lines shows the filament position.

accumulation of Ta^{x+} cations towards the filament (compare figure 7.10 b)). The model is based on TEM results, which show an enrichment of Ta in a filamentary region as evidenced by HAADF imaging and EDX mapping [38, 39]. Notably, in this model the thermophoresis causes motion of Ta towards higher temperatures, which is opposite to the direction of oxygen diffusion in model 1. As a matter of fact, the direction of the thermophoresis flux in Ta_2O_5 cannot be predicted, as no model of heat transport exists so far [38]. Furthermore, it is noted that the investigated device architecture is comprised of a symmetrical TiN/ TaO_x /TiN stack with a comparably thick (50 and 120 nm respectively) switching layer. Nevertheless, the devices feature qualitatively similar bipolar resistive switching characteristics.

To test the cation accumulation model, the local Ta concentration inside and around a conductive filament needs to be analyzed. For this, an X-PEEM image of the filament was measured using Ta 4f core level electrons. Single images were acquired over the complete binding energy range of the Ta 4f core level ($23-31 \text{ eV}$) and averaged (compare 7.11 a)). Accordingly, the intensity of the image is a direct measure of the Ta concentration. If a filament is composed of an increased amount of Ta, it should produce a higher signal compared to the surrounding matrix. However, as evident from the false color image, no local intensity fluctuations above the signal-to-noise ratio can be observed. The high intensity in the top part of the image (red region) is caused by the absence of the graphene layer. Considering that Ma *et al.* found a significant Ta enrichment of $\approx 20\%$ [38], it is unlikely that such a high Ta enrichment is not visible in the intensity profile (figure 7.11 b)).

Given that model 2 does not agree with the experimental results it can not explain resistive switching in Ta/ Ta_2O_5 /graphene samples. Furthermore, the diffusion of Ta is orders

of magnitude slower compared to oxygen diffusion [101]. Consequently, the involvement of Ta as mobile species during device operation can be excluded for the here investigated device.

Model 3: Percolation through metallic Ta clusters. Electrical transport measurements and structural analysis by TEM indicate that the conduction mechanism is determined by percolation of electrons through metallic Ta clusters. Accordingly, a switching model was proposed that predicts the presence of a metallic tantalum phase (see figure 7.10 c)) [135]. Based on the conductivity data, a filament size between 5 and 10 nm was estimated. Here it is noted that the metallic filament model is only used to describe the LRS of the device. The mechanism that drives the resistance change between LRS and the HRS remains unclear so far.

A central aspect of this model is the conduction of electrons through a metallic filament, which can be tested by determining the electronic structure of the filament. Surprisingly, it is very difficult to differentiate if a filament is composed of a metal or an sub-oxide phase. The most commonly employed techniques, e.g. TEM based HAADF or EDX, are useful to measure local atomic concentrations but they are not sensitive to the cationic oxidation state. Other spectromicroscopic techniques, such as EELS, could provide information about the electronic structure, however, they are often limited by a low energy resolution and signal-to-noise ratio [36].

Fortunately, X-PEEM is well suited to characterize switching filaments by XPS and XAS. As presented in figure 7.6, it is possible to measure the Ta 4f core level spectrum of a filament with good energy resolution and adequate signal-to-noise ratio. From the XPS results, it was deduced that the filament is composed of a sub-oxide with no metallic contribution. A similar observation was made in devices after a hard electric breakdown. Again, no metallic component was found in the filaments (compare chapter 4.4). Based on these experimental results, it can be concluded that model 3 does not apply for the here investigated devices.

Model 4: Electric field and Joule heating induced drift of oxygen. Figure 7.10 d) depicts the electroforming or SET process in the classic VCM switching model. Upon application of a negative bias to the top electrode, oxygen anions are repelled from the negatively charged electrode and driven towards the oxidizable Ta electrode. Importantly, the drift of oxygen anions is accelerated by high temperatures emerging during biasing due to Joule heating. A reaction between the oxygen anions from the Ta₂O₅ layer with the metallic Ta bottom electrode leads to the formation of a sub-oxide and an oxygen vacancy rich filament. Depending on the electric field direction, oxygen anions are redistributed within the switching layer. If a positive bias is applied to the top electrode, oxygen anions are attracted and form an insulating gap at the Schottky barrier, i.e. the device is RESET into the HRS. A detailed

description of the model is given in figure 2.7. Importantly, the model is based solely on a vertical movement of oxygen.

While the model agrees qualitatively well to the experimental data, it is not possible to verify the mechanism unambiguously without additional spectroscopic information about the filament in the HRS. Nevertheless, it is the only model that can account for all experimental observation, making it the most likely candidate to describe the switching process in Ta_2O_5 .

8 Conclusions

The aim of this thesis was to study the microscopic processes in resistive switching transition metal oxides using spectromicroscopy. In particular, transition electron microscopy and photoemission electron microscopy were employed to characterize conductive filaments in SrTiO_3 and Ta_2O_5 . In the following, the most important results for both material systems will be summarized and concluded.

SrTiO_3 based devices

SrTiO_3 devices with different cation stoichiometries, film thicknesses and defect structures were fabricated and their resistive switching properties characterized. Thin films grown at a high deposition temperature of 800°C exhibit an epitaxial crystal quality with a low defect density. Memristive devices that were fabricated from epitaxial films show an eightwise switching polarity, i.e. the device can be set into the low resistive state by applying a positive voltage to the top electrode. By reducing the deposition temperature and increasing the film thickness, the density of extended defects was increased. Interestingly, memristive devices with defect-rich SrTiO_3 films feature a counter-eightwise switching polarity. This demonstrates that SrTiO_3 is a compelling model system that can be used to study a wide variety of resistive switching effects.

Resistive switching phenomena of eightwise switching SrTiO_3 were investigated by electron microscopy. It was shown that the electroforming process causes localized phase separations in Sr-rich thin films. Based on PEEM and TEM analysis, the secondary phase was identified as a Sr-rich precipitate. Molecular static and molecular dynamic simulations clarified the mechanistic details of the involved cation diffusion processes. Two important insights were obtained. First, the phase separation is thermodynamically driven. Only the Sr excess that was incorporated during growth segregates out of the thin film. Second, the activation energy of Sr migration is greatly reduced along so-called Ruddlesden-Popper type antiphase boundaries. These extended defects readily form during the Sr-rich film growth and serve as fast diffusion path for Sr cations. Accordingly, phase separations occur predominantly at antiphase boundaries. It is expected that the results can be transferred to related A-site rich $\text{A}^{\text{II}}\text{B}^{\text{IV}}\text{O}_3$ and $\text{A}^{\text{III}}\text{B}^{\text{III}}\text{O}_3$ perovskites that form Ruddlesden-Popper defects. These insights might pave the way to improve device properties through defect engineering, either by avoiding or deliberately inducing the growth of extended defects.

The study of SrTiO₃ was extended to counter-eightwise switching devices. By intentionally growing SrTiO₃ at low deposition temperatures and with Sr-excess, films with large densities of antiphase boundaries were obtained. Additionally, an island growth mode resulted in the formation of less dense regions between adjacent islands. To investigate why these films show an opposing switching polarity, *in operando* TEM was employed. It was observed that the electroforming processes causes a local reduction of the SrTiO₃ film. This was evidenced by a characteristic change of the Ti *L* and O *K*-absorption edges that can be linked to a valence change from Ti⁴⁺ to Ti³⁺. Utilizing the fully capabilities of *in operando* TEM, multiple O/Ti maps were recorded of a single specimen in different resistive states. In the pristine and high resistive state a uniform oxygen distribution was observed, whereas the low resistive state featured oxygen rich and depleted regions. Especially the accumulation and depletion of oxygen in the vicinity of extended defects was visible. These results are a direct evidence for an internal redistribution of oxygen within the switching layer and agree well with the proposed valence change mechanism. Further, they highlight the importance of the thin film defect structure as a preferential switching site.

Ta₂O₅ based devices

Prior to the investigation of memristive devices, a reference system for the quantification of oxygen vacancies in Ta₂O₅ was established. It was demonstrated that the oxygen content in TaO_{*x*} thin films can be controlled through careful adjustments of the reactive sputter conditions. *In situ* XPS was employed to probe the electronic structure of TaO_{*x*} over a wide stoichiometry range. It was presented that the Ta4f core level is sensitive to the oxygen stoichiometry and can be used to quantify the oxygen vacancy concentration. A peak model was constructed that accurately describes the core level spectra of all tantalum suboxides. Fitting of the core level gave access to the oxygen content and the oxidation state distribution of the thin films. Furthermore, the impact of oxygen vacancies on the valence band was studied. For oxygen deficient films, an additional peak at the Fermi level was observed. It could be demonstrated that the intensity of this defect band is proportional to the oxygen vacancy concentration. Based on resistivity measurements, a correlation between the electrical conductivity and the oxygen vacancy concentration was established. These findings serve as an important foundation that facilitate the identification and interpretation of switching induced changes in Ta₂O₅ devices. Beyond the case of Ta₂O₅, the employed methods can also be used to characterize other binary transition metal oxides.

The resistive switching characteristics of Ta₂O₅ devices with different oxide thicknesses and top electrodes were analyzed. All devices exhibit a counter-eightwise switching polarity with a linear LRS and a rectifying HRS current-voltage relationship. A trend was observed where thicker Ta₂O₅ films require higher electroforming voltages and have a lower memory window. Comparing Pt and graphene electrodes showed that graphene devices feature higher

electroforming, set and reset voltages. The increased switching voltage was attributed to the additional series resistance of the graphene electrode. The characteristic counter-eightwise switching I - V curves of graphene devices proof that the switching mechanism is similar to noble-metal devices. Importantly, this means that memristive devices with graphene electrodes can serve as a model system to study resistive switching.

The device reliability under external influences was investigated. Measuring the I - V characteristics of devices in ambient and under vacuum conditions revealed that the set process requires significantly higher voltages in a vacuum environment. Further, the vacuum strongly decreased reset yield and caused devices to be stuck in the LRS. The increased set voltage was ascribed to the removal of water impurities from the switching oxide and the consequential decrease of ionic conductivity. To explain the lowered RESET yield, it was suggested that the vacuum set process at high voltages forms a larger and more oxygen deficient filament that can not be RESET without an external oxygen source. The positive effect of oxygen from the atmosphere was demonstrated by recovering that devices that were stuck in the LRS by performing the reset in an oxygen atmosphere. These results imply that the reliability of Ta₂O₅ ReRAM devices could be improved by minimizing the detrimental effects of external influences by engineering oxygen-reservoir or capping layers.

Synchrotron based PEEM on Ta₂O₅ graphene devices was used to determine the composition and electronic structure of the conductive filaments. Photoelectron spectroscopy revealed, that they consist of an oxygen deficient suboxide phase. More precisely, the presence of Ta⁵⁺-Ta¹⁺ oxidation states were observed in the spectroscopic signature of filaments. Importantly, no contribution of a metallic Ta⁰ component could be detected. These insights are in good agreement with the valence change mechanism in which oxygen vacancies act as mobile dopants. The results contradict the proposed model of a metallic filament where the current percolates through metallic grains instead of an oxygen deficient suboxide. The filament was found to have an oxygen to tantalum ratio of ≈ 2.1 , which translates to an oxygen vacancy concentration of 16%. Furthermore, no evidence for the lateral diffusion of tantalum or oxygen was found. This is important because some switching models, that are based on the thermophoresis effect, predict a lateral ion migration during switching. Accordingly, the presented X-PEEM results could clarify that the valence change mechanism is the only model that is consistent with all experimental findings presented in this work.

Overall, the results of this thesis present fundamentally new insights about resistive switching in SrTiO_3 and Ta_2O_5 -based devices. Importantly, the role of extended defects for resistive switching was clarified. This knowledge could be used to facilitate future device design through systematic defect engineering. Spectroscopic information about conductive filaments in Ta_2O_5 resolved the long debated question whether the conductive filament is composed of a metallic or suboxide phase. By mapping the lateral distribution of oxygen and tantalum, it was concluded that the switching process is caused by a vertical redistribution of oxygen vacancies instead of a lateral migration of ions. The obtained quantitative information about the oxygen vacancy concentration in filaments is essential for the physical understanding of the switching process and for device simulations.

Appendix: Fabrication details

PLD deposition parameters for SrTiO₃ thin films

The following table summarizes the deposition parameters for all SrTiO₃ thin films that are presented in this thesis. For all depositions a target to substrate distance of 44 mm, a repetition rate of 5 Hz and a spot size of 2 mm² was used. All thin films were grown on annealed not terminated 0.5 wt-% Nb:SrTiO₃ (*CrysTec GmbH*, Germany) single crystalline substrates.

Table A1: PLD deposition parameter used during this thesis.

Stoichiometry ¹	Purpose	Laser fluence (J/cm ²)	Thickness (nm)	Deposition rate (s/u.c.)	Temperature (°C)
Sr _{0.98} TiO _{2.98}	stoichiometry series	1.01	20	11.6	800
Sr _{1.13} TiO _{3.13}	stoichiometry series	0.67	20	48.3	800
Sr _{1.08} TiO _{3.08}	temperature series	0.67	80	38	550
Sr _{1.08} TiO _{3.08}	temperature series	0.67	80	39	600
Sr _{1.07} TiO _{3.07}	temperature series	0.67	80	36	650
Sr _{1.07} TiO _{3.07}	temperature series	0.67	80	36	700
Sr _{1.12} TiO _{3.12}	temperature series	0.67	80	46	800
Sr _{1.11} TiO _{3.11}	thickness series	0.67	20	44.6	800
Sr _{1.17} TiO _{3.17}	thickness series	0.67	40	57.2	800
Sr _{1.18} TiO _{3.18}	thickness series	0.67	60	63.5	800
Sr _{1.17} TiO _{3.17}	thickness series	0.67	80	58.4	800

¹ The stoichiometry is estimated based on the deposition rate according to refs. [169, 218].

Sputter deposition parameters

The following table summarizes the deposition parameters for all sputtered thin films that are presented in this thesis. For deposition of stoichiometric oxides a target to substrate distance of 1000 mm, for metallic films 10 mm and for sub-stoichiometric films a distance of 50 mm was used. These values correspond to the maximal, minimal and an intermediate (in front of the sputter dome) distances that can be adjusted in the machine respectively. All

depositions, except for the Pt deposition, were performed using a RF sputter process was employed. For low oxygen partial pressure processes, a premix of 1% O₂ in 99% Ar was used.

Table A2: Sputter deposition parameter used during this thesis.

Material	Purpose	RF Power (W)	Pressure (mBar)	Ar/O ₂ flow ratio	Distance (mm)
Ta ₂ O ₅	switching oxide	200	$5 \cdot 10^{-2}$	3/2	100
Ta	bottom electrode	30	$1 \cdot 10^{-2}$	Ar	10
Pt	top electrode	10 (DC)	$1 \cdot 10^{-2}$	Ar	10
HfO ₂	insulating layer	200	$5 \cdot 10^{-2}$	3/2	100
TaO _{2.5}	pressure series	65	$5.3 \cdot 10^{-2}$	99/1	50
TaO _{1.65}	pressure series	65	$5.2 \cdot 10^{-2}$	99/1	50
TaO _{1.45}	pressure series	65	$5.0 \cdot 10^{-2}$	99/1	50
TaO _{1.31}	pressure series	65	$4.5 \cdot 10^{-2}$	99/1	50
TaO _{1.17}	pressure series	65	$4 \cdot 10^{-2}$	99/1	50
TaO ₀	pressure series	65	$2 \cdot 10^{-2}$	99/1	50
TaO ₀	pressure series	65	$9 \cdot 10^{-3}$	99/1	50
TaO _{2.5}	power series	50	$5.0 \cdot 10^{-2}$	99/1	50
TaO _{1.46}	power series	67	$5.0 \cdot 10^{-2}$	99/1	50
TaO _{1.28}	power series	70	$5.0 \cdot 10^{-2}$	99/1	50
TaO _{0.98}	power series	90	$5.0 \cdot 10^{-2}$	99/1	50
TaO _{0.79}	power series	120	$5.0 \cdot 10^{-2}$	99/1	50
TaO _{0.64}	power series	150	$5.0 \cdot 10^{-2}$	99/1	50
TaO _{0.43}	power series	250	$5.0 \cdot 10^{-2}$	99/1	50
TaO _{2.15}	reactive gas series ¹	100	$5.0 \cdot 10^{-3}$	12/1	50
TaO _{1.88}	reactive gas series ¹	100	$5.0 \cdot 10^{-3}$	15/1	50

¹ To achieve a stoichiometry in the range of $1.6 < x < 2.5$, a high pump speed process was used. For this, the films were sputtered with the main shutter open to the turbo molecular pump at very low process pressures.

Fabrication details

In the following, flowcharts, common problems and solutions are listed for each sample type presented in this thesis. It is noted, that individual parameters might have changed during the course of this thesis. Here, the most commonly used processes that gave the best results are described.

Noble metal top electrodes for delamination: SiO₂/Ta/Ta₂O₅/Au

This sample architecture can be used to fabricate single devices with different sizes, which can be contacted directly using a microcontroller and a probe tip. Afterwards, the top electrode can be delaminated as described elsewhere [148] and analyzed with the desired method (e.g. PEEM, SNOM, XPS).

Process Flowchart

1. Clean Si/430 nm SiO₂ substrate using ultrasonication in acetone followed by 2-propanol for 5 min. Blow-dry with N₂.
2. Fabricate 30 nm Ta bottom electrode by sputter deposition, followed by deposition of a 4-20 nm Ta₂O₅ switching layer by reactive sputter deposition.
3. Expose the sample to ambient atmosphere and transfer to the clean room.
4. Deposit 80 nm Au top electrodes via electron beam evaporation (EBE) through a shadow mask at room temperature.
5. After resistive switching of the devices deposit a homogeneous 80 nm Au layer via EBE.
6. Perform delamination as described in detail in ref. [148].

Additional notes

Chances to carry out a successful delamination is determined by the adhesion between oxide and noble metal. The goal is to achieve sufficiently weak adhesion, which still allows to contact the electrodes with soft probe needles without scratching the metal electrode. This is typically accomplished by using gold as electrode material, due to its weak adhesion to oxides. The drawback of using gold is, that the switching and retention properties are considerably worse compared to Pt electrodes. Retention of just a few seconds and irreversible break downs are commonly observed.

To further minimize the adhesion, the evaporation process should be performed at low temperatures. For this, the EBE machine in the cleanroom of the PGI 7 is suitable, as only a low temperature increase during the deposition is observed. It is suspected that the big target to substrate distance is beneficial to prevent passive heating during the evaporation process. Trying to deposit the gold layers in the EBE of the electronic oxide cluster (PGI 7) always resulted in a failed delamination. This is likely caused by a strong temperature increase ($\approx 170^\circ\text{C}$) during deposition.

Noble metal top electrodes for delamination: Nb:SrTiO₃/SrTiO₃/noble metal

Process Flowchart

1. Anneal Nb:SrTiO₃ substrate at 950°C for four hours under ambient atmosphere and verify that the surface has a step terrace structure via AFM.
2. Fabricate SrTiO₃ thin film by PLD.
3. Deposit 80 nm Au or Pt top electrodes via EBE through a shadow mask.
4. After resistive switching of the devices deposit a homogeneous 80 nm Au or Pt layer via EBE.
5. Perform delamination as discussed in detail in ref. [148].

Additional notes

Besides Au, also Pt can be used for delamination. However, the success rate for delamination with Pt is significantly decreased compared to Au. While Au typically yields $\approx 80\%$ delaminated electrodes, with Pt only $\approx 30\%$ are achieved.

Devices with metal contact leads: Nb:SrTiO₃/SrTiO₃/Pt

Metal leads allow to contact devices using manual wire bonding. Additionally, the contact resistance between the probe tip and the metal lead is negligible and thus, the electrical characterization is far more reliable compared to directly placing the probe tip onto the electrode. This sample architecture is preferred if devices need to be operated inside a machine, where no microcontroller can be used to address the device directly or if the probe tip damages the electrodes (e.g. the Mark-II setup).

To fabricate the samples, three lithography steps are necessary. First, the top electrodes are lithographically structured using electron beam evaporation and dry etching. In a next step, the sample is completely covered by an insulating layer except for the electrodes. In a final step, the metal leads are deposited and structured using a lift-off process.

Process Flowchart 1: Structuring of top electrodes

1. Anneal Nb:SrTiO₃ substrate at 950°C for four hours under ambient atmosphere and verify that the surface has a step terrace structure via AFM.
2. Fabricate SrTiO₃ thin film by PLD.
3. Remove mechanically most of the silver paste from the backside of the sample using a scalpel.
4. Deposit a homogeneous top electrode layer, e.g. 10 nm Pt, onto the sample.
5. Dehydrate the sample by heating it to 180°C for 5 min.
6. Coat the sample with AZ5214 photo resist. Softbake the sample at 90°C for 5 min and let the sample cool down to room temperature.
7. Expose the sample to UV light through a photomask for 25 s (optimal exposure time may vary depending on the light intensity).
8. Etch the exposed top electrode layer by ion beam etching (IBE).
9. Remove the remaining photo resist by soaking the sample in dimethyl sulfoxide (DMSO) for 120 min at 80 °C and subsequently wash with acetone and 2-propanol. If the photoresist is not completely dissolved, the resist can be mechanically removed by swabbing with a clean room swabs in 2-propanol. Additionally, the sample can be cleaned with ultrasonication. However, this can lead to contamination of the surface with silver particles from the backside.

Process Flowchart 2: Deposition of an insulating layer

1. Dehydrate the sample by heating it to 180°C for 5 min.
2. Coat the sample with AZ5214 photo resist. Softbake the sample at 90°C for 5 min and let the sample cool down to room temperature.
3. Align the sample in the mask aligner in such a way that the parts top electrode area is concealed. Expose the sample to UV light through a photomask for 25 s (optimal exposure time may vary depending on the light intensity).
4. Develop the exposed photoresist using MIF 326 developer for approximately 50 s.
5. Deposit an approximately 100 nm thick insulating layer, e.g. Ta₂O₅ or HfO₂, via reactive sputtering.

6. Lift-off the remaining photo resist together with the overlaying insulating layer by soaking the sample in dimethyl sulfoxide (DMSO) for 120 min at 80 °C and subsequently wash with acetone and 2-propanol. Depending on adhesion between sample and insulating layer, mechanical cleaning or ultrasonication can be used (compare step 10 in process flowchart 1).

Process Flowchart 3: Forming of the contact leads

1. Dehydrate the sample by heating it to 180 °C for 5 min
2. Coat the sample with AZnLof2020 photo resist. Softbake the sample at 90 °C for 5 min and let the sample cool down to room temperature.
3. Align the sample in the mask aligner in such a way that the parts of inner top electrode area is concealed. Expose the sample to UV light through a photomask for 10 s (optimal exposure time may vary depending on the light intensity).
4. Hard bake the resist at 110 °C for 60 s.
5. Develop the exposed photoresist using MIF 726 developer for approximately 60 s.
6. Deposit 10 nm Pt followed by 100 nm Au by EBE. The Pt film serves as adhesion layer and the additional Au film increases the scratch resistance.
7. Lift-off the remaining photo resist together with the overlaying metal layers by soaking the sample in TechniStrip Ni555 for 120 min at 80 °C and subsequently wash with acetone and 2-propanol.

Additional notes

In some cases photoresist can be difficult to remove if it was exposed to thermal stress or UV light (e.g. during EBE evaporation). To prevent hardening and cross-linking of the resist, it is recommended to avoid temperatures above 100 °C. Thus, the EBE machine from the electronic oxide cluster should not be used with photoresist covered samples.

If the photoresist can not be removed by vigorous swabbing with clean room swabs or by ultrasonication it is typically not possible to remove the remaining photoresist by other methods.

Devices with metal contact leads: Ta/Ta₂O₅/noble metal crossbar device

This sample type can be used to study the effect of different atmospheres on memristive devices. The special feature of this stack arrangement is that the Schottky electrode is in contact with the atmosphere. This is opposite to the conventional stacking order, where the Pt is structured directly onto the substrate and then covered by the switching layer and the ohmic electrode.

Process Flowchart 1: Structuring of bottom electrode

1. Clean Si/430 nm SiO₂ substrate using ultrasonication in acetone followed by 2-propanol for 5 min. Blow-dry with N₂.
2. Fabricate 30 nm Ta bottom electrode by sputter deposition.
3. Expose the sample to ambient atmosphere and transfer to the clean room.
4. Coat the sample with AZ5214 photo resist. Softbake the sample at 90 °C for 5 min and let the sample cool down to room temperature.
5. Expose the sample to UV light through a photomask for 25 s (optimal exposure time may vary depending on the light intensity).
6. Develop the exposed photoresist using MIF 326 developer for approximately 50 s.
7. Etch the exposed parts of the 30 nm Ta bottom electrode by ion beam etching (IBE).
8. Remove the remaining photo resist by soaking the sample in dimethyl sulfoxide (DMSO) for 120 min at 80 °C and subsequently wash with acetone and 2-propanol.

Process Flowchart 2: Structuring of the switching layer and top electrode

1. Deposition a 4-20 nm Ta₂O₅ switching layer by reactive sputter deposition.
2. Expose the sample to ambient atmosphere and transfer to the clean room.
3. Deposit a homogeneous top electrode layer, e.g. 30 nm Pt, onto the sample.
4. Coat the sample with AZ5214 photo resist. Softbake the sample at 90 °C for 5 min and let the sample cool down to room temperature.
5. Expose the sample to UV light through a photomask for 25 s (optimal exposure time may vary depending on the light intensity).

6. Develop the exposed photoresist using MIF 326 developer for approximately 50 s.
7. Etch the exposed parts of the top electrode and Ta₂O₅ switching layer by ion beam etching (IBE).
8. Remove the remaining photo resist by soaking the sample in dimethyl sulfoxide (DMSO) for 120 min at 80 °C and subsequently wash with acetone and 2-propanol.

Additional notes

The Ta bottom electrode forms a thin ($\approx 2\text{-}3\text{ nm}$) native oxide layer if exposed to ambient atmosphere. This native oxide makes contacting the crossbar structure with needles problematic, due to its high resistance. The native oxide layer can be locally removed by placing both probe tips on the Ta bottom electrode and applying a high bias between the probes. This leads to a hard breakdown of the native oxide and the device can be switched as usual until the probe is removed.

Devices with metal contact leads: Ta/Ta₂O₅/graphene crossbar device

Graphene crossbar devices are perfectly suited to perform spectromicroscopy on functional memristors, by imaging through the transparent graphene electrode. This architecture was successfully employed in X-PEEM and scanning near field optical microscopy (SNOM) measurement setups.

The biggest challenge in fabricating graphene crossbar structures is to achieve a flat surface without edges or steps in a margin of just a few nanometers. Therefore, the bottom electrode and the switching oxide are buried into the substrate as described in figure 3.4. This requires precise determination of etching and deposition rates and a detailed process control.

Process Flowchart 1: Planarization and structuring of bottom electrode

1. Clean Si/100 nm Si₃N₄ substrate using ultrasonication in acetone followed by 2-propanol for 5 min. Blow-dry with N₂.
2. Coat the sample with AZ5214 photo resist. Softbake the sample at 90 °C for 5 min and let the sample cool down to room temperature.
3. Expose the sample to UV light through a photomask for 25 s (optimal exposure time may vary depending on the light intensity).

-
4. Develop the exposed photoresist using MIG 326 developer for approximately 50 s.
 5. Etch 40 nm of deep trenches into the exposed parts of the Si₃N₄ switching layer by CF₄ reactive ion beam etching (RIBE).
 6. Fabricate 30 nm Ta bottom electrode by sputtering followed by deposition of 10 nm Ta₂O₅ switching layer by reactive sputter deposition. Thicknesses of the individual layers can be adjusted. It is important that the total thickness of deposited films corresponds to the trench depth.
 7. Lift-off remaining photo resist together with the overlying Ta and Ta₂O₅ layers by soaking the sample in dimethyl sulfoxide (DMSO) for 120 min at 80 °C and subsequently wash with acetone and 2-propanol.

Process Flowchart 2: Deposition and structuring of the graphene electrode

1. Deposit single layer graphene (*Graphenea*, Spain) as described in detail in ref. [256].
2. Coat the sample with AZ5214 photo resist. Softbake the sample at 90 °C for 5 min and let the sample cool down to room temperature.
3. Develop the exposed photoresist using MIF 326 developer for approximately 50 s.
4. Etch the exposed graphene layer using oxygen plasma (clean room PGI 7) with 150 W for 30 s. Oxygen plasma is harmful to the photo resist and prolonged etching or high power processes can cross-link the resist. Etching parameters might therefore be further optimized.
5. Remove the remaining photo resist by soaking the sample in TechniStrip Ni555 for 120 min at 80 °C and subsequently wash with acetone and 2-propanol.

Process Flowchart 3: Forming of the contact leads

1. Dehydrate the sample by heating it to 180 °C for 5 min
2. Coat the sample with AZnLof2020 photo resist. Softbake the sample at 90 °C for 5 min and let the sample cool down to room temperature.
3. Align the sample in the mask aligner in such a way that the parts of inner top electrode area is concealed. Expose the sample to UV light through a photomask for 10 s (optimal exposure time may vary depending on the light intensity).
4. Hard bake the resist at 110 °C for 60 s.

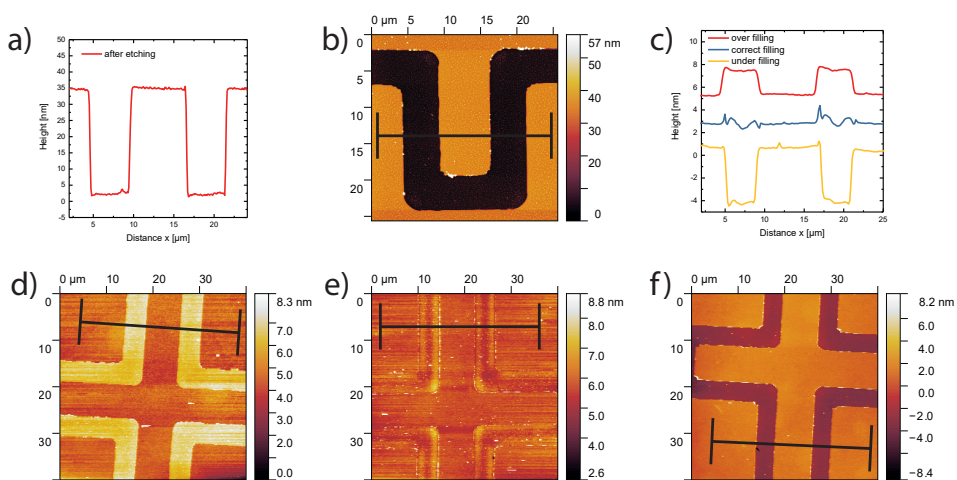


Figure A1: Process control of RIBE etching and subsequent filling of the trenches. a) Line scan of an etched device obtained from the AFM morphology image in b). The etching profile showing almost perfect vertical trenches. The aimed depth was 30 nm and the measured etching depth is with 33 nm slightly higher. These profiles could be obtained very reproducibly with only little deviation between different batches. c) Three typical line scans of samples after filling of the trench showing d) over-, e) correct- and f) under-filling.

5. Develop the exposed photoresist using MIF 726 developer for approximately 60 s.
6. Deposit 10 nm Pt followed by 100 nm Au by EBE. The Pt film serves as adhesion layer and the additional Au film increases the scratch resistance.
7. Lift-off the remaining photo resist together with the overlaying metal layers by soaking the sample in TechniStrip Ni555 for 120 min at 80 °C and subsequently wash with acetone and 2-propanol.

Additional notes: Planarization

Figure A1 shows a exemplary AFM process control of etching and filling of trenches. It was found that Si_3N_4 etching using CF_4 gives highly reproducible results. Importantly, no hardening of the resist was observed after this process step. Figure A1 c) shows typical line scans of trenches after the filling process. Under and over filling are common problems if the deposition rate of the sputter process is not stable. Even for the same process parameters, the deposition rate was found to vary between processes, making a precise filling challenging. Nevertheless, the filling process was accurate enough to achieve a sufficiently planar surface. A margin of ± 5 nm was found to be tolerable for a graphene transfer without tearing.

Another hurdle to overcome is the removal of so-called fence structures that occur along lithographically defined edges. Fence structures were found to form after the filling process and were not related to the etching process. Thus, the origin of the fences can be traced back to the sputtering process and can be explained by one of the following scenarios

- Sputtered material deposits not only in the trench, but also onto the substrate at the edge region, which is not completely covered by photoresist due to the undercut structure of the resist flank. In this case the fence height should be approximately equal or smaller than the deposited film thickness $f \lesssim d$ (compare Figure A3 a)).
- Ions with high kinetic energy that are created in the sputter process bombard the resist flank and cross-link the photoresist, making it insoluble in organic solvents. This effect should apply to the complete photoresist flank and thus the fence height can be much greater than the film thickness $f > d$ (compare Figure A3 b)).

As the fence height typically is in the range of the deposited film thickness, scenario 1 seems more likely. In order to prevent cracking of graphene along the device edges, fences were removed using a series of mechanical polishing procedures. In a first step, the sample was placed in a beaker with 2-propanol and the surface was swabbed using a polyester clean room swab (*Cleansebay's CB-PS714N, Rectangular Swab*) using moderated to high pressure followed by blow-drying with N₂. This process should be performed for at least 5 mins. During this time the swabbing direction should be changed, ensuring a homogeneous polishing. After this, the sample is checked via AFM if the fences have been removed. If the fences remain, a second polishing step is performed by soaking a polyester cleanroom wipe in 2-propanol and placing it on a flat surface. With the sample surface facing the wipe, the sample is repeatedly moved over the wipe along the fiber direction under high pressure. Again, the sample should be turned during this process to obtain a more homogeneous result.

While the mechanical polishing gets rid of most fence structures, it also seems to effect the surface of the deposited film by removing a few nanometers of material. This should be kept in mind as it also will effect the switching characteristics due to the thinner oxide layer.

Additional notes: Contacting graphene electrodes

Contacting graphene electrodes is easiest achieved by metal evaporation. For good contact, a sufficiently large overlap between metal lead and the graphene electrode is recommended (2-3 μm). Figure A4 a) shows the I - V curve of an graphene top electrode measured across the electrode for Ti/Au and Pt/Au metal contacts. From the I - V curve it is visible that both

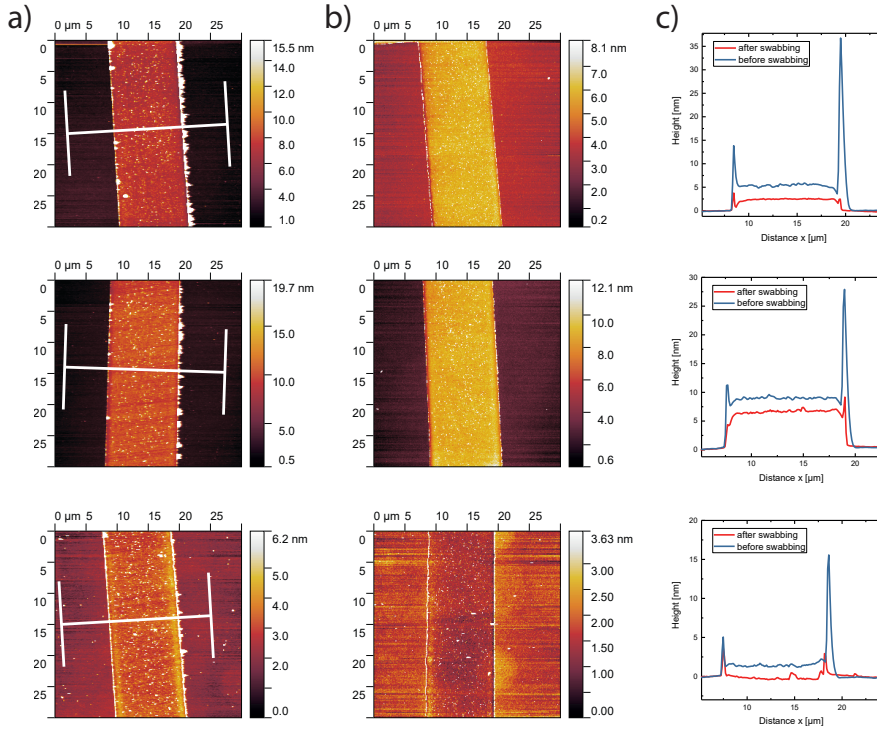


Figure A2: Mechanical removal of fence structures using clean room swaps and tissues. The effect of fence removal is depicted for three exemplary devices. a) AFM morphology scan of a filled trench after the lift-off process and b) after mechanical treatment of the sample. c) Line scans before and after treatment.

metals form an ohmic contact to the graphene. Comparing both metals, Ti and Pt, shows that Pt gives a much more reliable contact and has on average a lower resistance (see figure A4 b)). The reason for the large variability for the Ti/Au contact can be seen in figure A4 c). During the lift-off process to produce the contact leads, the evaporated contacts delaminated from the graphene surface, i.e. Ti has a weak adhesion to graphene and peels off. Therefore, it is advised to use a combination of 10 nm Pt followed by 50 nm of Au to contact graphene electrodes, where Pt provides good contact and adhesion and Au provides mechanical support of the contact.

Additional notes: Graphene electrode defects

Transferring graphene layers using a PMMA assisted wet transfer, induces a corrugation of the graphene layer. This can result in the formation of wrinkles, folds and crumbles [257]. Besides

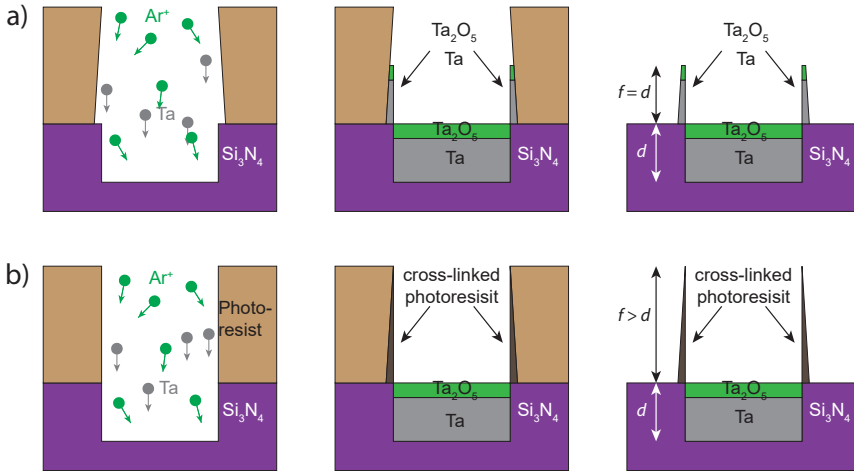


Figure A3: Two possible scenarios for the formation of fences during the trench filling. a) Sputtered material deposits on the undercut of the photoresist. b) Energetic ions cross-link the photoresist polymer, which can not be removed in a lift-off process.

the transfer related defects, also mechanical stress can result in defective graphene. Figure A5 shows typical graphene defects that were observed during device preparation. While wrinkles were observed in almost any sample and device, defects such as folds, holes and crumbles of graphene were less common. Most defects associated with mechanical stress are presumably connected to a weak substrate-graphene adhesion or to fence structures (compare A3). It is likely, that these defects influence the electrical properties of the graphene electrodes, which explains the rather large spread of graphene series resistances observed in figure A4. Nevertheless, the defects have only a minor influence on the device operation.

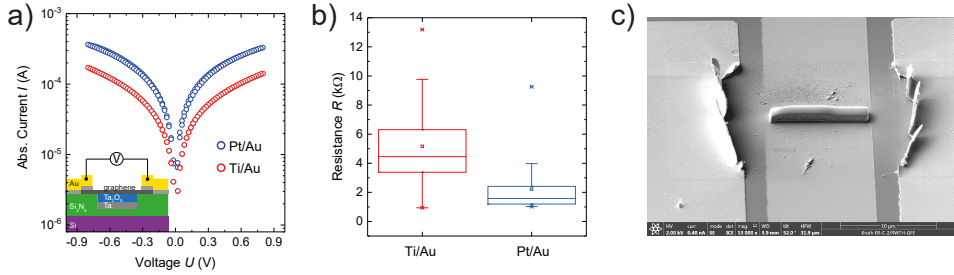


Figure A4: Contacting of graphene electrodes using evaporated metal leads. a) I - V curve of a graphene electrode contacted with leads of Pt/Au (blue) and (Ti/Au). b) Resistance across the graphene electrode for Pt/Au and Ti/Au metal contacts averaged over 20 devices. c) SEM image of a graphene device after evaporation of Ti/Au and the subsequent Lift-off process. The structure in the middle of the device is a Pt layer deposited for TEM lamella preparation.

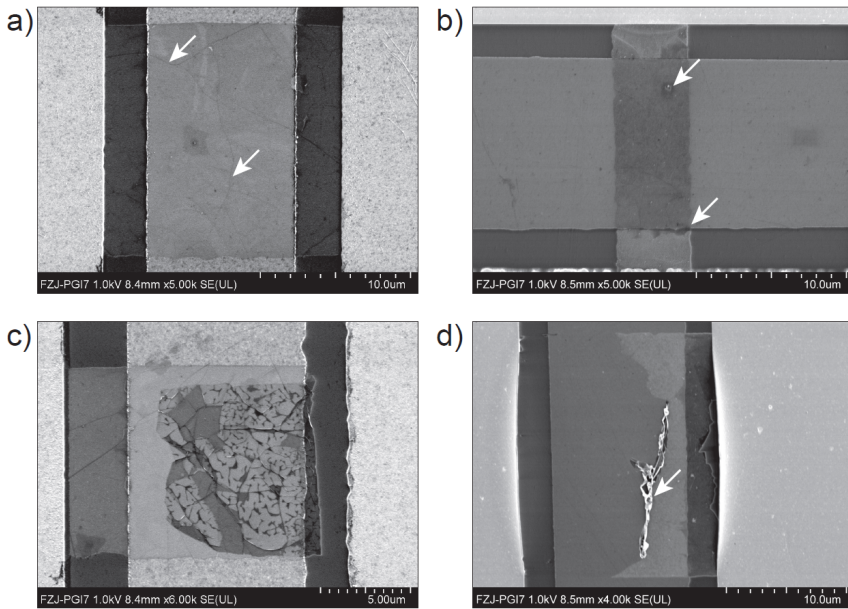


Figure A5: Typical graphene electrode defects investigated by SEM. a) $20 \times 10 \mu\text{m}$ graphene cross-bar device. White arrows point to wrinkles in the graphene layer. b) $5 \times 10 \mu\text{m}$ graphene crossbar device. The top arrow points to a contamination that was present on the Ta₂O₅ layer prior to the graphene deposition. The bottom arrow points to graphene cracks at the crosspoint border, likely caused by fence structures. c) Large part of the graphene electrode folded back onto itself. d) Rolling up (crumpling) of the graphene electrode (white arrow).

List of Abbreviations

- ABF** Annular bright field
- AFM** Atomic force microscopy
- C-AFM** Conductive atomic force microscopy
- DF** Dark field
- EBE** Electron beam evaporation
- EDX** Energy dispersive X-ray spectroscopy
- EELS** Electron energy loss spectroscopy
- FWHM** Full width at half maximum
- HAADF** High-angle annular dark field
- HAXPES** Hard X-ray photoelectron spectroscopy
- HDD** Hard disk drive
- HRS** High resistive state
- IMFP** Inelastic mean free path
- LRS** Low resistive state
- MIM** Metal insulator metal
- PEEM** Photoemission electron microscopy
- PES** Photoelectron emission spectroscopy
- PMMA** Poly(methyl methacrylat)
- ReRAM** Redox-based resistive switching random access memory
- RHEED** Reflection high-energy electron diffraction
- RIBE** Reactive ion beam etching

- ROI** Region of interest
- RP APB** Ruddlesden-Popper type antiphase boundary
- SEM** Scanning electron microscopy
- SP** Secondary phase
- STEM** Scanning transmission electron microscopy
- TEM** Transmission electron microscopy
- u.c.** unit cell
- UHV** Ultra-high vacuum
- UPS** Ultraviolet photoelectron spectroscopy
- XAS** X-ray absorption spectroscopy
- XPS** X-ray photoelectron spectroscopy
- XRR** X-ray reflectivity

List of Figures

2.1	Crystal structure of cubic SrTiO ₃ and Ruddlesden-Popper type anti phase boundaries	6
2.2	Crystal structure of orthorhombic β -Ta ₂ O ₅	9
2.3	Partial density of states for amorphous Ta ₂ O ₅	10
2.4	Energy level diagram of a Schottky junction.	12
2.5	Schematic illustration of different bulk conduction mechanisms.	15
2.6	Schematic illustration of eightwise switching mechanism in SrTiO ₃	20
2.7	Schematic illustration of the counter-eightwise switching mechanism.	22
3.1	Reactive sputter deposition.	26
3.2	Sample fabrication of SrTiO ₃ devices contacted by metal leads.	28
3.3	Sample fabrication of Ta ₂ O ₅ crossbar devices.	29
3.4	Sample fabrication of graphene crossbar devices.	30
3.5	Graphene transfer process.	31
3.6	Three-step model of photoemission.	37
3.7	Schematic layout of the <i>NanoESCA</i> photoemission electron microscope	39
4.1	Impact of the laser fluence on the growth of SrTiO ₃	42
4.2	Morphology of stoichiometric and Sr-rich SrTiO ₃ thin films.	44
4.3	Electron microscopy of a low temperature Sr _{1.17} Ti ₁ O _{3.17} thin film.	45
4.4	Reactive sputter deposition of TaO _x thin films.	47
4.5	X-ray reflectivity measurements of Ta ₂ O ₅ thin films.	48
4.6	Thin film properties of Ta and Ta ₂ O ₅ layers.	49
4.7	Ta 4f core level and valence band spectra of tantalum oxide films with different oxygen contents.	51
4.8	Power and pressure series of sputtered TaO _x thin films.	54
4.9	X-PEEM analysis of a Ta/Ta ₂ O ₅ /graphene device after high voltage arcing.	56
5.1	Eightwise switching characteristics of SrTiO ₃ memristive devices.	60
5.2	Switching characteristics of Sr-rich and stoichiometric SrTiO ₃	62
5.3	Counter-eightwise switching characteristics of Sr-rich SrTiO ₃ memristive devices.	65

5.4	Influence of the atmosphere on the switching characteristics of counter-eightwise switching SrTiO ₃ .	66
5.5	Impact of the thin film thickness and growth temperature on the switching polarity.	70
5.6	Comparison of counter-eightwise switching curves of 30 nm Ta/6 nm Ta ₂ O ₅ devices with different top electrodes.	72
5.7	Long term switching stability of graphene electrodes.	74
5.8	Thickness dependence of the Ta ₂ O ₅ switching layer.	76
5.9	Influence of the atmosphere on the switching characteristics of counter-eightwise switching Ta ₂ O ₅ devices.	78
5.10	Atmosphere dependent set and reset characteristics.	81
5.11	Low temperature conductivity of a TaO _x thin film and a Ta ₂ O ₅ device.	83
6.1	PEEM work function analysis of Sr-rich SrTiO ₃ devices.	89
6.2	PEEM work function analysis of stoichiometric SrTiO ₃ devices.	90
6.3	Topography and current map of a Sr-rich SrTiO ₃ filament.	92
6.4	Spectromicroscopic filament investigation.	93
6.5	Cross sectional TEM analysis of a filament area.	94
6.6	Static and molecular dynamics simulations of Sr ²⁺ behavior at RP APB.	96
6.7	Electro-thermal simulation of SrTiO ₃ memristive device.	98
6.8	Proposed model for retention stabilization in eightwise switching Sr-rich SrTiO ₃ devices.	100
6.9	<i>In operando</i> resistive switching in a TEM.	103
6.10	Effect of biasing on the grain boundary structure.	105
6.11	Spectroscopy of the switching SrTiO ₃ layer.	106
6.12	EELS mapping of the oxygen distribution in different resistive states.	107
6.13	Proposed model for counter-eightwise switching in SrTiO ₃ .	109
7.1	Spatial resolution of PEEM.	113
7.2	Transmittance of graphene electrodes.	115
7.3	Effects of synchrotron radiation on Ta ₂ O ₅ thin films.	117
7.4	Crossbar device layout with graphene top electrodes.	119
7.5	Work function analysis of a formed device.	120
7.6	XPS signature of a switching filament.	121
7.7	O <i>K</i> -edge absorption spectrum of a switching filament.	122
7.8	AFM-topography of a filament.	124
7.9	Current simulation of a switching filament.	126
7.10	Proposed switching mechanisms in tantalum oxide.	128
7.11	Local Ta concentration of the switching filament.	129

A1 Process control of RIBE etching and subsequent filling of the trenches. 146

A2 Mechanical removal of fence structures using clean room swaps and tissues. . . 148

A3 Possible scenarios for the formation of fences during the trench filling. 149

A4 Contacting of graphene electrodes using different metals. 150

A5 Typical graphene electrode defects investigated by SEM. 150

Bibliography

- [1] D. Reinsel, J. Gantz, and J. Rydning, “The digitization of the world from edge to core,” *Framingham: International Data Corporation*, 2018.
- [2] J. J. Yang, D. B. Strukov, and D. R. Stewart, “Memristive devices for computing,” *Nature Nanotechnology*, vol. 8, pp. 13–24, dec 2013.
- [3] Y. Nishi and B. Magyari-Kope, *Advances in non-volatile memory and storage technology*. Woodhead Publishing, 2019.
- [4] R. Waser and M. Aono, “Nanoionics-based resistive switching memories,” *Nanoscience and Technology: A Collection of Reviews from Nature Journals*, vol. 6, no. 11, pp. 158–165, 2007.
- [5] J. J. Yang, M. D. Pickett, X. Li, D. A. A. Ohlberg, D. R. Stewart, and R. S. Williams, “Memristive switching mechanism for metal/oxide/metal nanodevices,” *Nature nanotechnology*, vol. 3, no. 7, pp. 429–433, 2008.
- [6] R. Waser, R. Dittmann, C. Staikov, and K. Szot, “Redox-based resistive switching memories nanoionic mechanisms, prospects, and challenges,” *Advanced Materials*, vol. 21, no. 25-26, pp. 2632–2663, 2009.
- [7] A. C. Torrezan, J. P. Strachan, G. Medeiros-Ribeiro, and R. S. Williams, “Subnanosecond switching of a tantalum oxide memristor,” *Nanotechnology*, vol. 22, p. 485203, dec 2011.
- [8] M. von Witzleben, T. Hennen, A. Kindsmüller, S. Menzel, R. Waser, and U. Böttger, “Study of the SET switching event of VCM-based memories on a picosecond timescale,” *Journal of applied physics*, vol. 127, no. 20, p. 204501, 2020.
- [9] U. Böttger, M. von Witzleben, V. Havel, K. Fleck, V. Rana, R. Waser, and S. Menzel, “Picosecond multilevel resistive switching in tantalum oxide thin films,” *Scientific reports*, vol. 10, no. 1, pp. 1–9, 2020.
- [10] S. Choi, J. Lee, S. Kim, and W. D. Lu, “Retention failure analysis of metal-oxide based resistive memory,” *Applied Physics Letters*, vol. 105, no. 11, p. 113510, 2014.

- [11] G. Sassine, C. Nail, L. Tillie, D. A. Robayo, A. Levisse, C. Cagli, K. E. Hajjam, J.-F. Nodin, E. Vianello, and M. Bernard, "Sub-pJ consumption and short latency time in RRAM arrays for high endurance applications," in *2018 IEEE International Reliability Physics Symposium (IRPS)*, pp. P-MY, IEEE, 2018.
- [12] Y.-B. Kim, S. R. Lee, D. Lee, C. B. Lee, M. Chang, J. H. Hur, M.-J. Lee, G.-S. Park, C. J. Kim, and U.-i. Chung, "Bi-layered RRAM with unlimited endurance and extremely uniform switching," in *2011 Symposium on VLSI Technology-Digest of Technical Papers*, pp. 52-53, IEEE, 2011.
- [13] B. Govoreanu, G. S. Kar, Y. Y. Chen, V. Paraschiv, S. Kubicek, A. Fantini, I. P. Radu, L. Goux, S. Clima, and R. Degraeve, "10x10nm² Hf/HfO_x crossbar resistive RAM with excellent performance, reliability and low-energy operation," in *2011 International Electron Devices Meeting*, pp. 31-36, IEEE, 2011.
- [14] K.-S. Li, C. Ho, M.-T. Lee, M.-C. Chen, C.-L. Hsu, J. M. Lu, C. H. Lin, C. C. Chen, B. W. Wu, and Y. F. Hou, "Utilizing sub-5 nm sidewall electrode technology for atomic-scale resistive memory fabrication," in *2014 Symposium on VLSI Technology (VLSI-Technology): Digest of Technical Papers*, pp. 1-2, IEEE, 2014.
- [15] Y.-C. Chen, H. Li, W. Zhang, and R. E. Pino, "The 3-D stacking bipolar RRAM for high density," *IEEE transactions on nanotechnology*, vol. 11, no. 5, pp. 948-956, 2012.
- [16] S. Mittal, "A survey of ReRAM-based architectures for processing-in-memory and neural networks," *Machine learning and knowledge extraction*, vol. 1, no. 1, pp. 75-114, 2019.
- [17] X. Hong, D. J. Loy, P. A. Dananjaya, F. Tan, C. Ng, and W. Lew, "Oxide-based RRAM materials for neuromorphic computing," *Journal of materials science*, vol. 53, no. 12, pp. 8720-8746, 2018.
- [18] D. Ielmini and H.-S. P. Wong, "In-memory computing with resistive switching devices," *Nature Electronics*, vol. 1, no. 6, pp. 333-343, 2018.
- [19] *International Technology Roadmap for Semiconductors 2.0 - 2015 Edition, Beyond CMOS*. 2015.
- [20] A. Hardtdegen, C. La Torre, F. Cüppers, S. Menzel, R. Waser, and S. Hoffmann-Eifert, "Improved switching stability and the effect of an internal series resistor in HfO₂/TiO_x bilayer ReRAM cells," *IEEE transactions on electron devices*, vol. 65, no. 8, pp. 3229-3236, 2018.
- [21] E. Ambrosi, A. Bricalli, M. Laudato, and D. Ielmini, "Impact of oxide and electrode materials on the switching characteristics of oxide ReRAM devices," *Faraday discussions*, vol. 213, pp. 87-98, 2019.

-
- [22] H. S. Wong, H. Y. Lee, S. Yu, Y. S. Chen, Y. Wu, P. S. Chen, B. Lee, F. T. Chen, and M. J. Tsai, "Metal-oxide RRAM," *Proceedings of the IEEE*, vol. 100, no. 6, pp. 1951–1970, 2012.
- [23] S. Larentis, F. Nardi, S. Balatti, D. C. Gilmer, and D. Ielmini, "Resistive switching by voltage-driven ion migration in bipolar RRAM-Part II: Modeling," *IEEE Transactions on Electron Devices*, vol. 59, no. 9, pp. 2468–2475, 2012.
- [24] A. Marchewka, R. Waser, and S. Menzel, "Physical simulation of dynamic resistive switching in metal oxides using a Schottky contact barrier model," in *International Conference on Simulation of Semiconductor Processes and Devices, SISPAD*, vol. 2015-Octob, pp. 297–300, Institute of Electrical and Electronics Engineers Inc., oct 2015.
- [25] C. Baeumer, C. Schmitz, A. Marchewka, D. N. Mueller, R. Valenta, J. Hackl, N. Raab, S. P. Rogers, M. I. Khan, S. Nemsak, M. Shim, S. Menzel, C. M. Schneider, R. Waser, and R. Dittmann, "Quantifying redox-induced Schottky barrier variations in memristive devices via in operando spectromicroscopy with graphene electrodes," *Nature Communications*, vol. 7, p. 12398, aug 2016.
- [26] M. Escher, N. Weber, M. Merkel, C. Ziethen, P. Bernhard, G. Schönhense, S. Schmidt, F. Forster, F. Reinert, and B. Krömker, "NanoESCA: a novel energy filter for imaging x-ray photoemission spectroscopy," *Journal of Physics: Condensed Matter*, vol. 17, no. 16, p. S1329, 2005.
- [27] Y. Meng Lu, M. Noman, Y. N. Picard, J. A. Bain, P. A. Salvador, and M. Skowronski, "Impact of Joule heating on the microstructure of nanoscale TiO₂ resistive switching devices," *Journal of Applied Physics*, vol. 113, no. 16, p. 163703, 2013.
- [28] H. Du, C. L. Jia, A. Koehl, J. Barthel, R. Dittmann, R. Waser, and J. Mayer, "Nano-sized Conducting Filaments Formed by Atomic-Scale Defects in Redox-Based Resistive Switching Memories," *Chemistry of Materials*, vol. 29, pp. 3164–3173, apr 2017.
- [29] C. Lenser, A. Koehl, I. Slipukhina, H. Du, M. Patt, V. Feyer, C. M. Schneider, M. Lezaic, R. Waser, and R. Dittmann, "Formation and Movement of Cationic Defects during Forming and Resistive Switching in SrTiO₃ Thin Film Devices," *Advanced Functional Materials*, vol. 25, no. 40, pp. 6360–6368, 2015.
- [30] V. R. Nallagatla, T. Heisig, C. Baeumer, V. Feyer, M. Jugovac, G. Zamborlini, C. M. Schneider, R. Waser, M. Kim, C. U. Jung, and R. Dittmann, "Topotactic Phase Transition Driving Memristive Behavior," *Advanced Materials*, vol. 31, p. 1903391, aug 2019.

- [31] F. V. Hensling, H. Du, N. Raab, C. L. Jia, J. Mayer, and R. Dittmann, "Engineering antiphase boundaries in epitaxial SrTiO₃ to achieve forming free memristive devices," *APL Materials*, vol. 7, p. 101127, oct 2019.
- [32] J. Mayer, L. A. Giannuzzi, T. Kamino, and J. Michael, "TEM sample preparation and FIB-induced damage," *MRS bulletin*, vol. 32, no. 5, pp. 400–407, 2007.
- [33] J.-Y. Chen, C.-L. Hsin, C.-W. Huang, C.-H. Chiu, Y.-T. Huang, S.-J. Lin, W.-W. Wu, and L.-J. Chen, "Dynamic evolution of conducting nanofilament in resistive switching memories," *Nano letters*, vol. 13, no. 8, pp. 3671–3677, 2013.
- [34] D. Cooper, C. Baeumer, N. Bernier, A. Marchewka, C. La Torre, R. E. Dunin-Borkowski, S. Menzel, R. Waser, and R. Dittmann, "Anomalous Resistance Hysteresis in Oxide ReRAM: Oxygen Evolution and Reincorporation Revealed by In Situ TEM," *Advanced Materials*, vol. 29, no. 23, p. 1700212, 2017.
- [35] C. C. Ahn, *Transmission electron energy loss spectrometry in materials science and the EELS atlas*. John Wiley & Sons, 2006.
- [36] G. S. Park, Y. B. Kim, S. Y. Park, X. S. Li, S. Heo, M. J. Lee, M. Chang, J. H. Kwon, M. Kim, U. I. Chung, R. Dittmann, R. Waser, and K. Kim, "In situ observation of filamentary conducting channels in an asymmetric Ta₂O_{5-x}/TaO_{2-x} bilayer structure," *Nature Communications*, vol. 4, pp. 1–9, sep 2013.
- [37] S. Privitera, G. Bersuker, B. Butcher, A. Kalantarian, S. Lombardo, C. Bongiorno, R. Geer, D. C. Gilmer, and P. D. Kirsch, "Microscopy study of the conductive filament in HfO₂ resistive switching memory devices," *Microelectronic Engineering*, vol. 109, pp. 75–78, 2013.
- [38] Y. Ma, D. Li, A. A. Herzing, D. A. Cullen, B. T. Sneed, K. L. More, N. T. Nuhfer, J. A. Bain, and M. Skowronski, "Formation of the Conducting Filament in TaO_x-Resistive Switching Devices by Thermal-Gradient-Induced Cation Accumulation," *ACS Applied Materials and Interfaces*, vol. 10, pp. 23187–23197, jul 2018.
- [39] Y. Ma, J. M. Goodwill, D. Li, D. A. Cullen, J. D. Poplawsky, K. L. More, J. A. Bain, and M. Skowronski, "Stable Metallic Enrichment in Conductive Filaments in TaO_x-Based Resistive Switches Arising from Competing Diffusive Fluxes," *Advanced Electronic Materials*, vol. 5, p. 1800954, jul 2019.
- [40] R. Dittmann, R. Muenstermann, I. Krug, D. Park, T. Menke, J. Mayer, A. Besmehn, F. Kronast, C. M. Schneider, and R. Waser, "Scaling Potential of Local Redox Processes in Memristive SrTiO₃ Thin-Film Devices," *Proceedings of the IEEE*, vol. 100, no. 6, pp. 1979–1990, 2012.

-
- [41] J. Kraus, R. Reichelt, S. Günther, L. Gregoratti, M. Amati, M. Kiskinova, A. Yulaev, I. Vlasiouk, and A. Kolmakov, "Photoelectron spectroscopy of wet and gaseous samples through graphene membranes," *Nanoscale*, vol. 6, pp. 14394–14403, dec 2014.
- [42] I. A. Sluchinskaya, A. I. Lebedev, and A. Erko, "Crystal structure, local structure, and defect structure of Pr-doped SrTiO₃," *Journal of Applied Physics*, vol. 112, p. 024103, jul 2012.
- [43] P. A. Cox, *Transition metal oxides: an introduction to their electronic structure and properties*, vol. 30. Oxford university press, 1993.
- [44] K. Lukaszewicz, "Crystal structures of α -(SrO)₂(TiO) and (SrO)₃(TiO₂)₂," *Rocz. Chem.*, vol. 33, pp. 239–242, 1959.
- [45] K. Van Benthem, C. Elsässer, and R. H. French, "Bulk electronic structure of SrTiO₃: Experiment and theory," *Journal of Applied Physics*, vol. 90, pp. 6156–6164, dec 2001.
- [46] J. Robertson and C. W. Chen, "Schottky barrier heights of tantalum oxide, barium strontium titanate, lead titanate, and strontium bismuth tantalate," *Applied Physics Letters*, vol. 74, pp. 1168–1170, feb 1999.
- [47] B. Nagaraj, T. Wu, S. B. Ogale, T. Venkatesan, and R. Ramesh, "Interface characterization of all-perovskite oxide field effect heterostructures," *Journal of Electroceramics*, vol. 8, pp. 233–241, sep 2002.
- [48] Y. A. Abramov, V. G. Tsirelson, V. E. Zavodnik, S. A. Ivanov, and I. D. Brown, "The chemical bond and atomic displacements in SrTiO₃ from X-ray diffraction analysis," *Acta Crystallographica Section B*, vol. 51, no. 6, pp. 942–951, 1995.
- [49] X. G. Guo, X. S. Chen, Y. L. Sun, L. Z. Sun, X. H. Zhou, and W. Lu, "Electronic band structure of Nb doped SrTiO₃ from first principles calculation," *Physics Letters, Section A: General, Atomic and Solid State Physics*, vol. 317, no. 5-6, pp. 501–506, 2003.
- [50] X. Hao, Z. Wang, M. Schmid, U. Diebold, and C. Franchini, "Coexistence of trapped and free excess electrons in SrTiO₃," *Physical Review B - Condensed Matter and Materials Physics*, vol. 91, no. 8, p. 85204, 2015.
- [51] S. A. Mojarad, K. S. Kwa, J. P. Goss, Z. Zhou, N. K. Ponon, D. J. Appleby, R. A. Al-Hamadany, and A. O'Neill, "A comprehensive study on the leakage current mechanisms of Pt/SrTiO₃/Pt capacitor," *Journal of Applied Physics*, vol. 111, p. 014503, jan 2012.

- [52] C. Funck, A. Marchewka, C. Bäumer, P. C. Schmidt, P. Müller, R. Dittmann, M. Martin, R. Waser, and S. Menzel, “A Theoretical and Experimental View on the Temperature Dependence of the Electronic Conduction through a Schottky Barrier in a Resistively Switching SrTiO₃-Based Memory Cell,” *Advanced Electronic Materials*, vol. 4, p. 1800062, jul 2018.
- [53] G. W. Dietz, W. Antpöhler, M. Klee, and R. Waser, “Electrode influence on the charge transport through SrTiO₃ thin films,” *Journal of Applied Physics*, vol. 78, no. 10, pp. 6113–6121, 1995.
- [54] F. A. Kröger and H. J. Vink, “Relations between the Concentrations of Imperfections in Crystalline Solids,” *Solid State Physics - Advances in Research and Applications*, vol. 3, pp. 307–435, jan 1956.
- [55] K. Gömann, G. Borchardt, M. Schulz, A. Gömann, W. Maus-Friedrichs, B. Lesage, O. Kaïtasov, S. Hoffmann-Eifert, and T. Schneller, “Sr diffusion in undoped and La-doped SrTiO₃ single crystals under oxidizing conditions,” *Physical Chemistry Chemical Physics*, vol. 7, pp. 2053–2060, 2005.
- [56] J. Crawford and P. Jacobs, “Point Defect Energies for Strontium Titanate: A Pair-Potentials Study,” *Journal of Solid State Chemistry*, vol. 144, pp. 423–429, may 1999.
- [57] R. Merkle and J. Maier, “How is oxygen incorporated into oxides? A comprehensive kinetic study of a simple solid-state reaction with SrTiO₃ as a model material,” *Angewandte Chemie - International Edition*, vol. 47, no. 21, pp. 3874–3894, 2008.
- [58] T. Bieger, H. Yugami, N. Nicoloso, J. Maier, and R. Waser, “Optical absorption relaxation applied to SrTiO₃ and ZrO₂: An in-situ method to study trapping effects on chemical diffusion,” *Solid State Ionics*, vol. 72, pp. 41–46, sep 1994.
- [59] R. Meyer, A. F. Zurhelle, R. A. De Souza, R. Waser, and F. Gunkel, “Dynamics of the metal-insulator transition of donor-doped SrTiO₃,” *Physical Review B*, vol. 94, p. 115408, sep 2016.
- [60] D. J. Kok, K. Irmscher, M. Naumann, C. Guguschev, Z. Galazka, and R. Uecker, “Temperature-dependent optical absorption of SrTiO₃,” *Physica Status Solidi (A) Applications and Materials Science*, vol. 212, pp. 1880–1887, sep 2015.
- [61] W. Menesklou, H. J. Schreiner, K. H. Härdtl, and E. Ivers-Tiffée, “High temperature oxygen sensors based on doped SrTiO₃,” *Sensors and Actuators, B: Chemical*, vol. 59, pp. 184–189, oct 1999.

-
- [62] M. J. Akhtar, Z. U. N. Akhtar, R. A. Jackson, and C. R. A. Catlow, "Computer Simulation Studies of Strontium Titanate," *Journal of the American Ceramic Society*, vol. 78, pp. 421–428, feb 1995.
- [63] K. Szot and W. Speier, "Surfaces of reduced and oxidized SrTiO₃ from atomic force microscopy," *Physical Review B - Condensed Matter and Materials Physics*, vol. 60, no. 8, pp. 5909–5926, 1999.
- [64] F. Gunkel, *The role of defects at functional interfaces between polar and non-polar perovskite oxides*. Phd thesis, RWTH Aachen University, 2013.
- [65] S. P. Waldow and R. A. De Souza, "Computational Study of Oxygen Diffusion along a[100] Dislocations in the Perovskite Oxide SrTiO₃," *ACS Applied Materials and Interfaces*, vol. 8, pp. 12246–12256, may 2016.
- [66] V. Metlenko, A. H. Ramadan, F. Gunkel, H. Du, H. Schraknepper, S. Hoffmann-Eifert, R. Dittmann, R. Waser, and R. A. De Souza, "Do dislocations act as atomic autobahns for oxygen in the perovskite oxide SrTiO₃?" *Nanoscale*, vol. 6, no. 21, pp. 12864–12876, 2014.
- [67] K. Shibuya, R. Dittmann, S. Mi, and R. Waser, "Impact of defect distribution on resistive switching characteristics of Sr₂TiO₄ thin films," *Advanced Materials*, vol. 22, pp. 411–414, jan 2010.
- [68] K. Szot, W. Speier, G. Bihlmayer, and R. Waser, "Switching the electrical resistance of individual dislocations in single-crystalline SrTiO₃," *Nature Materials*, vol. 5, no. 4, pp. 312–320, 2006.
- [69] Y. Tokuda, S. Kobayashi, T. Ohnishi, T. Mizoguchi, N. Shibata, Y. Ikuhara, and T. Yamamoto, "Growth of Ruddlesden-Popper type faults in Sr-excess SrTiO₃ homoepitaxial thin films by pulsed laser deposition," *Applied Physics Letters*, vol. 99, p. 173109, oct 2011.
- [70] J. H. Haeni, C. D. Theis, D. G. Schlom, W. Tian, X. Q. Pan, H. Chang, I. Takeuchi, and X. D. Xiang, "Epitaxial growth of the first five members of the Sr_{n+1}Ti_nO_{3n+1} Ruddlesden-Popper homologous series," *Applied Physics Letters*, vol. 78, pp. 3292–3294, may 2001.
- [71] S. N. Ruddlesden and P. Popper, "The compound Sr₃Ti₂O₇ and its structure," *Acta Crystallographica*, vol. 11, pp. 54–55, jan 1958.
- [72] M. A. McCoy, R. W. Grimes, and W. E. Lee, "Phase stability and interfacial structures in the SrO-SrTiO₃ system," *Philosophical Magazine A: Physics of Condensed Matter, Structure, Defects and Mechanical Properties*, vol. 75, no. 3, pp. 833–846, 1997.

- [73] L. A. Aleshina and S. V. Loginova, "Rietveld analysis of X-ray diffraction pattern from β -Ta₂O₅ oxide," *Crystallography Reports*, vol. 47, pp. 415–419, may 2002.
- [74] G. S. Oehrlein, F. M. D'Heurle, and A. Reisman, "Some properties of crystallized tantalum pentoxide thin films on silicon," *Journal of Applied Physics*, vol. 55, pp. 3715–3725, may 1984.
- [75] N. C. Stephenson and R. S. Roth, "Structural systematics in the binary system Ta₂O₅-WO₃. V. The structure of the low-temperature form of tantalum oxide L-Ta₂O₅," *Acta Crystallographica Section B Structural Crystallography and Crystal Chemistry*, vol. 27, pp. 1037–1044, may 1971.
- [76] M. Hiratani, S. Kimura, T. Hamada, S. Iijima, and N. Nakanishi, "Hexagonal polymorph of tantalum-pentoxide with enhanced dielectric constant," *Applied Physics Letters*, vol. 81, pp. 2433–2435, sep 2002.
- [77] A. Fukumoto and K. Miwa, "Prediction of hexagonal structure by first-principles calculations," *Physical Review B - Condensed Matter and Materials Physics*, vol. 55, pp. 11155–11160, may 1997.
- [78] S. P. Garg, N. Krishnamurthy, A. Awasthi, and M. Venkatraman, "The O-Ta (Oxygen-Tantalum) Systemf," *Journal of Phase Equilibria*, vol. 17, no. 1, pp. 63–77, 1996.
- [79] R. S. Roth, J. L. Waring, and H. S. Parker, "Effect of oxide additions on the polymorphism of tantalum pentoxide. IV. The system Ta₂O₅-Ta₂WO₈," *Journal of Solid State Chemistry*, vol. 2, no. 3, pp. 445–461, 1970.
- [80] C. Askeljung, B. O. Marinder, and M. Sundberg, "Effect of heat treatment on the structure of L-Ta₂O₅: A study by XRPD and HRTEM methods," *Journal of Solid State Chemistry*, vol. 176, pp. 250–258, nov 2003.
- [81] Y. Nakagawa, I. Morita, M. Takahashi, and S. Kakio, "Optical properties of a piezoelectric Ta₂O₅ single crystal film," *Japanese Journal of Applied Physics, Part 1: Regular Papers and Short Notes and Review Papers*, vol. 46, pp. 4441–4445, jul 2007.
- [82] Y. Le, X. Ma, D. Wang, H. Xiao, and J. Ma, "Synthesis and characterization of single-crystalline δ -Ta₂O₅ epitaxial films on Y-stabilized ZrO₂ (111) substrates," *Ceramics International*, 2020.
- [83] M. P. Usikov and A. G. Khachatryan, "Investigation of Ordering of Interstitial Impurities in Tantalum Using Electron Diffraction Microscope," *Soviet Physics Crystallography (English translation of Kristallografiya)*, vol. 13, no. 6, pp. 910–913, 1969.

-
- [84] N. Schönberg, W. G. Overend, A. Munthe-Kaas, and N. A. Sörensen, "An X-Ray Investigation of the Tantalum-Oxygen System," *Acta Chemica Scandinavica*, vol. 8, pp. 240–245, 1954.
- [85] Bandon D G, Zahavi J, Aladjem A, and Yahalom J, "Phase Transformations in Anodic Oxide Films," *J Vac Sci Technol*, vol. 6, no. 4, pp. 783–787, 1969.
- [86] I. Goldfarb, F. Miao, J. J. Yang, W. Yi, J. P. Strachan, M. X. Zhang, M. D. Pickett, G. Medeiros-Ribeiro, and R. S. Williams, "Electronic structure and transport measurements of amorphous transition-metal oxides: Observation of Fermi glass behavior," *Applied Physics A: Materials Science and Processing*, vol. 107, pp. 1–11, apr 2012.
- [87] I. Goldfarb and R. S. Williams, "Conduction centers in a $\text{Ta}_2\text{O}_5-\delta$ Fermi glass," *Applied Physics A: Materials Science and Processing*, vol. 114, no. 2, pp. 287–289, 2014.
- [88] A. Pignolet, G. M. Rao, and S. B. Krupanidhi, "Rapid thermal processed thin films of reactively sputtered Ta_2O_5 ," *Thin Solid Films*, vol. 258, pp. 230–235, mar 1995.
- [89] S. Kasatkov, E. Filatova, S. Sakhonenkov, A. Konashuk, and A. Makarova, "Relationship between Ta Oxidation State and Its Local Atomic Coordination Symmetry in a Wide Range of Oxygen Nonstoichiometry Extent of TaO_x ," *Journal of Physical Chemistry C*, vol. 123, pp. 6849–6860, mar 2019.
- [90] T. Tsuchiya, H. Imai, S. Miyoshi, P. A. Glans, J. Guo, and S. Yamaguchi, "X-Ray absorption, photoemission spectroscopy, and Raman scattering analysis of amorphous tantalum oxide with a large extent of oxygen nonstoichiometry," *Physical Chemistry Chemical Physics*, vol. 13, no. 38, pp. 17013–17018, 2011.
- [91] J. Robertson, "Band offsets of wide-band-gap oxides and implications for future electronic devices," *Journal of Vacuum Science & Technology B: Microelectronics and Nanometer Structures*, vol. 18, p. 1785, jun 2000.
- [92] V. Y. Zhuo, Y. Jiang, M. H. Li, E. K. Chua, Z. Zhang, J. S. Pan, R. Zhao, L. P. Shi, T. C. Chong, and J. Robertson, "Band alignment between Ta_2O_5 and metals for resistive random access memory electrodes engineering," *Applied Physics Letters*, vol. 102, no. 6, p. 62106, 2013.
- [93] K. V. Egorov, D. S. Kuzmichev, P. S. Chizhov, Y. Y. Lebedinskii, C. S. Hwang, and A. M. Markeev, "In Situ Control of Oxygen Vacancies in TaO_x Thin Films via Plasma-Enhanced Atomic Layer Deposition for Resistive Switching Memory Applications," *ACS Applied Materials and Interfaces*, vol. 9, no. 15, pp. 13286–13292, 2017.

- [94] V. A. Gritsenko, T. V. Perevalov, V. A. Voronkovskii, A. A. Gismatulin, V. N. Kruchinin, V. S. Aliev, V. A. Pustovarov, I. P. Prosvirin, and Y. Roizin, "Charge Transport and the Nature of Traps in Oxygen Deficient Tantalum Oxide," *ACS Applied Materials and Interfaces*, vol. 10, no. 4, pp. 3769–3775, 2018.
- [95] W. S. Lau, L. L. Leong, T. Han, and N. P. Sandier, "Detection of oxygen vacancy defect states in capacitors with ultrathin Ta₂O₅ films by zero-bias thermally stimulated current spectroscopy," *Applied Physics Letters*, vol. 83, no. 14, pp. 2835–2837, 2003.
- [96] T. V. Perevalov, V. A. Gritsenko, A. A. Gismatulin, V. A. Voronkovskii, A. K. Gerasimova, V. S. Aliev, and I. A. Prosvirin, "Electronic structure and charge transport in nonstoichiometric tantalum oxide," *Nanotechnology*, vol. 29, p. 264001, may 2018.
- [97] H. Sawada and K. Kawakami, "Electronic structure of oxygen vacancy in Ta₂O₅," *Journal of Applied Physics*, vol. 86, no. 2, pp. 956–959, 1999.
- [98] P. L. Young, "dc electrical conduction in thin Ta₂O₅ films. I. Bulk-limited conduction," *Journal of applied physics*, vol. 47, no. 1, pp. 235–241, 1976.
- [99] Y. Guo and J. Robertson, "Comparison of oxygen vacancy defects in crystalline and amorphous Ta₂O₅," *Microelectronic Engineering*, vol. 147, pp. 254–259, apr 2015.
- [100] A. E. McHale and H. L. Filler, "Defects and Charge Transport in β -Ta₂O₅: I, Analysis of the Conductivity Observed in Nominally Pure β -Ta₂O₅," *Journal of the American Ceramic Society*, vol. 68, pp. 646–650, dec 1985.
- [101] U. N. Gries, H. Schraknepper, K. Skaja, F. Gunkel, S. Hoffmann-Eifert, R. Waser, and R. A. De Souza, "A SIMS study of cation and anion diffusion in tantalum oxide," *Physical Chemistry Chemical Physics*, vol. 20, pp. 989–996, jan 2018.
- [102] L. Zhu, J. Zhou, Z. Guo, and Z. Sun, "Synergistic Resistive Switching Mechanism of Oxygen Vacancies and Metal Interstitials in Ta₂O₅," *Journal of Physical Chemistry C*, vol. 120, pp. 2456–2463, feb 2016.
- [103] A. E. McHale and H. L. Tuller, "Defects and Charge Transport in β -Ta₂O₅: II, Analysis of the Conductivity of Nb₂O₅-doped β -Ta₂O₅," *Journal of the American Ceramic Society*, vol. 68, pp. 651–656, dec 1985.
- [104] L. J. Brillson and Y. Lu, "ZnO Schottky barriers and Ohmic contacts," *Journal of Applied Physics*, vol. 109, no. 12, 2011.
- [105] F. C. Chiu, "A review on conduction mechanisms in dielectric films," *Advances in Materials Science and Engineering*, vol. 2014, 2014.

-
- [106] B. J. Baliga, "Analysis of junction-barrier-controlled Schottky (JBS) rectifier characteristics," *Solid State Electronics*, vol. 28, pp. 1089–1093, nov 1985.
- [107] S. Menzel, U. Böttger, M. Wimmer, and M. Salinga, "Physics of the Switching Kinetics in Resistive Memories," *Advanced Functional Materials*, vol. 25, no. 40, pp. 6306–6325, 2015.
- [108] N. F. Mott and E. A. Davis, *Electronic processes in non-crystalline materials*. Oxford university press, 2012.
- [109] E. Mikheev, J. Hwang, A. P. Kajdos, A. J. Hauser, and S. Stemmer, "Tailoring resistive switching in Pt/SrTiO₃ junctions by stoichiometry control," 2015.
- [110] C. Baeumer, C. Schmitz, A. H. Ramadan, H. Du, K. Skaja, V. Feyer, P. Muller, B. Arndt, C. L. Jia, J. Mayer, R. A. De Souza, C. Michael Schneider, R. Waser, and R. Dittmann, "Spectromicroscopic insights for rational design of redox-based memristive devices," *Nature Communications*, vol. 6, p. 8610, 2015.
- [111] E. M. Bourim, Y. Kim, and D.-W. Kim, "Interface State Effects on Resistive Switching Behaviors of Pt/Nb-Doped SrTiO₃ Single-Crystal Schottky Junctions," *ECS Journal of Solid State Science and Technology*, vol. 3, pp. N95–N101, jun 2014.
- [112] K. Shibuya, R. Dittmann, S. Mi, and R. Waser, "Impact of defect distribution on resistive switching characteristics of Sr₂TiO₄ thin films," *Advanced Materials*, vol. 22, pp. 411–414, jan 2010.
- [113] R. Muenstermann, T. Menke, R. Dittmann, and R. Waser, "Coexistence of filamentary and homogeneous resistive switching in Fe-doped SrTiO₃ thin-film memristive devices," *Advanced Materials*, vol. 22, pp. 4819–4822, nov 2010.
- [114] K. Fleck, U. Bottger, R. Waser, and S. Menzel, "Interrelation of sweep and pulse analysis of the SET process in SrTiO₃ resistive switching memories," *IEEE Electron Device Letters*, vol. 35, no. 9, pp. 924–926, 2014.
- [115] H. Nili, S. Walia, A. E. Kandjani, R. Ramanathan, P. Gutruf, T. Ahmed, S. Balendhran, V. Bansal, D. B. Strukov, O. Kavehei, M. Bhaskaran, and S. Sriram, "Donor-induced performance tuning of amorphous SrTiO₃ memristive nanodevices: Multistate resistive switching and mechanical tunability," *Advanced Functional Materials*, vol. 25, pp. 3172–3182, jun 2015.
- [116] X. Jiang, M. Wei, C. H. Chan, Y. Wang, R. Lai, J. Wang, J. Dai, and X. Qiu, "Effect of deposition temperature on ultra-low voltage resistive switching behavior of Fe-doped SrTiO₃ films," *Applied Physics Letters*, vol. 116, no. 10, p. 102101, 2020.

- [117] N. Aslam, V. Longo, C. Rodenbücher, F. Roozeboom, W. M. Kessels, K. Szot, R. Waser, and S. Hoffmann-Eifert, "Impact of composition and crystallization behavior of atomic layer deposited strontium titanate films on the resistive switching of Pt/STO/TiN devices," *Journal of Applied Physics*, vol. 116, p. 064503, aug 2014.
- [118] H. Jong Choi, S. Won Park, G. Deok Han, J. Na, G. T. Kim, and J. Hyung Shim, "Resistive switching characteristics of polycrystalline SrTiO₃ films," *Applied Physics Letters*, vol. 104, p. 242105, jun 2014.
- [119] C. Baeumer, *Spectroscopic characterization of local valence change processes in resistively switching complex oxides*. Phd thesis, RWTH Aachen, 2016.
- [120] T. Heisig, C. Baeumer, U. N. Gries, M. P. Mueller, C. La Torre, M. Luebben, N. Raab, H. Du, S. Menzel, D. N. Mueller, C. L. Jia, J. Mayer, R. Waser, I. Valov, R. A. De Souza, and R. Dittmann, "Oxygen Exchange Processes between Oxide Memristive Devices and Water Molecules," *Advanced Materials*, vol. 30, p. 1800957, jul 2018.
- [121] C. Baeumer, C. Funck, A. Locatelli, T. O. MenteÅŸ, F. Genuzio, T. Heisig, F. Hensling, N. Raab, C. M. Schneider, S. Menzel, R. Waser, and R. Dittmann, "In-Gap States and Band-Like Transport in Memristive Devices," *Nano Letters*, vol. 19, pp. 54–60, jan 2019.
- [122] E. Mikheev, B. D. Hoskins, D. B. Strukov, and S. Stemmer, "Resistive switching and its suppression in Pt/Nb:SrTiO₃ junctions," *Nature Communications*, vol. 5, pp. 1–9, jun 2014.
- [123] A. Marchewka, D. Cooper, C. Lenser, S. Menzel, H. Du, R. Dittmann, R. E. Dunin-Borkowski, and R. Waser, "Determination of the electrostatic potential distribution in Pt/Fe:SrTiO₃/Nb:SrTiO₃ thin-film structures by electron holography," *Scientific Reports*, vol. 4, pp. 1–6, nov 2014.
- [124] H. Y. Lee, Y. S. Chen, P. S. Chen, T. Y. Wu, F. Chen, C. C. Wang, P. J. Tzeng, M. J. Tsai, and C. Lien, "Low-power and nanosecond switching in robust hafnium oxide resistive memory with a thin Ti cap," *IEEE Electron Device Letters*, vol. 31, pp. 44–46, jan 2010.
- [125] S. Lee, H. Kim, J. Park, and K. Yong, "Coexistence of unipolar and bipolar resistive switching characteristics in ZnO thin films," *J. Appl. Phys.*, vol. 108, p. 76101, 2010.
- [126] M. K. Yang, J. W. Park, T. K. Ko, and J. K. Lee, "Bipolar resistive switching behavior in Ti/MnO₂/Pt structure for nonvolatile memory devices," *Applied Physics Letters*, vol. 95, p. 042105, jul 2009.

-
- [127] H. Zhang, S. Yoo, S. Menzel, C. Funck, F. Cüppers, D. J. Wouters, C. S. Hwang, R. Waser, and S. Hoffmann-Eifert, "Understanding the Coexistence of Two Bipolar Resistive Switching Modes with Opposite Polarity in Pt/TiO₂/Ti/Pt Nanosized ReRAM Devices," *ACS Applied Materials and Interfaces*, vol. 10, pp. 29766–29778, sep 2018.
- [128] S. Y. Wang, C. H. Tsai, D. Y. Lee, C. Y. Lin, C. C. Lin, and T. Y. Tseng, "Improved resistive switching properties of Ti/ZrO₂/Pt memory devices for RRAM application," *Microelectronic Engineering*, vol. 88, pp. 1628–1632, jul 2011.
- [129] S. Menzel, "Simulation and Modelling of the Switching Dynamics in Electrochemical Metallization and Valence Change Memory Cells," in *NVM Psi-k Workshop: New Horizons for Memory Storage: Advancing Non-volatile Memory with Atomistic Simulations*, 2016.
- [130] F. Miao, W. Yi, I. Goldfarb, J. J. Yang, M. X. Zhang, M. D. Pickett, J. P. Strachan, G. Medeiros-Ribeiro, and R. S. Williams, "Continuous electrical tuning of the chemical composition of TaO_x-based memristors," *ACS Nano*, vol. 6, pp. 2312–2318, mar 2012.
- [131] F. Miao, J. P. Strachan, J. J. Yang, M. X. Zhang, I. Goldfarb, A. C. Torrezan, P. Eschbach, R. D. Kelley, G. Medeiros-Ribeiro, and R. S. Williams, "Anatomy of a nanoscale conduction channel reveals the mechanism of a high-performance memristor," *Advanced Materials*, vol. 23, pp. 5633–5640, dec 2011.
- [132] K. Skaja, C. Bäumer, O. Peters, S. Menzel, M. Moors, H. Du, M. Bornhöfft, C. Schmitz, V. Feyer, C. L. Jia, C. M. Schneider, J. Mayer, R. Waser, and R. Dittmann, "Avalanche-Discharge-Induced Electrical Forming in Tantalum Oxide-Based Metal-Insulator-Metal Structures," *Advanced Functional Materials*, vol. 25, pp. 7154–7162, dec 2015.
- [133] C. E. Graves, N. Dávila, E. J. Merced-Grafals, S. T. Lam, J. P. Strachan, and R. S. Williams, "Temperature and field-dependent transport measurements in continuously tunable tantalum oxide memristors expose the dominant state variable," *Applied Physics Letters*, vol. 110, p. 123501, mar 2017.
- [134] C. M. Rosario, B. Thöner, A. Schönhals, S. Menzel, M. Wuttig, R. Waser, N. A. Sobolev, and D. J. Wouters, "Correlation between the transport mechanisms in conductive filaments inside Ta₂O₅-based resistive switching devices and in substoichiometric TaO_x thin films," *Applied Physics Letters*, vol. 112, p. 213504, may 2018.
- [135] C. M. Rosario, B. Thöner, A. Schönhals, S. Menzel, A. Meledin, N. P. Barradas, E. Alves, J. Mayer, M. Wuttig, R. Waser, N. A. Sobolev, and D. J. Wouters, "Metallic filamentary conduction in valence change-based resistive switching devices: The case of TaO_x thin film with $x \sim 1$," *Nanoscale*, vol. 11, no. 36, pp. 16978–16990, 2019.

- [136] M. Houssa, R. Degraeve, P. W. Mertens, M. M. Heyns, J. S. Jeon, A. Halliyal, and B. Ogle, "Electrical properties of thin SiON/Ta₂O₅ gate dielectric stacks," *Journal of Applied Physics*, vol. 86, pp. 6462–6467, dec 1999.
- [137] N. Novkovski and E. Atanassova, "Origin of the stress-induced leakage currents in Al-Ta₂O₅/SiO₂-Si structures," *Applied Physics Letters*, vol. 86, pp. 1–3, apr 2005.
- [138] P. R. Mickel, A. J. Lohn, B. Joon Choi, J. Joshua Yang, M. X. Zhang, M. J. Marinella, C. D. James, and R. Stanley Williams, "A physical model of switching dynamics in tantalum oxide memristive devices," *Applied Physics Letters*, vol. 102, p. 223502, jun 2013.
- [139] S. Kumar, C. E. Graves, J. P. Strachan, E. M. Grafals, A. L. Kilcoyne, T. Tyliczszak, J. N. Weker, Y. Nishi, and R. S. Williams, "Direct Observation of Localized Radial Oxygen Migration in Functioning Tantalum Oxide Memristors," *Advanced Materials*, vol. 28, pp. 2772–2776, apr 2016.
- [140] D. B. Chrisey and G. K. Hubler, *Pulsed laser deposition of thin films*. Wiley New York, 1994.
- [141] F. V. E. Hensling, *Defect engineering in oxide thin films*. Phd thesis, RWTH Aachen University, 2019.
- [142] S. Wicklein, A. Sambri, S. Amoruso, X. Wang, R. Bruzzese, A. Koehl, and R. Dittmann, "Pulsed laser ablation of complex oxides: The role of congruent ablation and preferential scattering for the film stoichiometry," *Applied Physics Letters*, vol. 101, p. 131601, sep 2012.
- [143] C. Xu, H. Du, A. J. Van Der Torren, J. Aarts, C. L. Jia, and R. Dittmann, "Formation mechanism of Ruddlesden-Popper-type antiphase boundaries during the kinetically limited growth of Sr rich SrTiO₃ thin films," *Scientific Reports*, vol. 6, no. August, p. 38296, 2016.
- [144] S. Berg, T. Nyberg, and T. Kubart, "Modelling of Reactive Sputtering Processes," in *Springer Series in Materials Science*, vol. 109, pp. 131–152, Springer Verlag, 2008.
- [145] O. Renault, N. Barrett, A. Bailly, L. F. Zagonel, D. Mariolle, J. C. Cezar, N. B. Brookes, K. Winkler, B. Krömker, and D. Funnemann, "Energy-filtered XPEEM with NanoESCA using synchrotron and laboratory X-ray sources: Principles and first demonstrated results," *Surface Science*, vol. 601, no. 20 SPEC. ISS., pp. 4727–4732, 2007.
- [146] T. Schmidt, S. Heun, J. Slezak, J. Diaz, K. C. Prince, G. Lilienkamp, and E. Bauer, "Speleem: Combining leem and spectroscopic imaging," *Surface Review and Letters*, vol. 5, no. 6, pp. 1287–1296, 1998.

-
- [147] A. Locatelli, L. Aballe, T. O. Mentes, M. Kiskinova, and E. Bauer, "Photoemission electron microscopy with chemical sensitivity: SPELEEM methods and applications," *Surface and Interface Analysis*, vol. 38, no. 12-13, pp. 1554–1557, 2006.
- [148] A. Köhl, *Micro-spectroscopic investigation of valence change processes in resistive switching SrTiO₃ thin films*. Phd thesis, RWTH Aachen University, 2014.
- [149] E. Breckenfeld, R. Wilson, J. Karthik, A. R. Damodaran, D. G. Cahill, and L. W. Martin, "Effect of growth induced (non)stoichiometry on the structure, dielectric response, and thermal conductivity of SrTiO₃ thin films," *Chemistry of Materials*, vol. 24, pp. 331–337, jan 2012.
- [150] D. J. Keeble, S. Wicklein, L. Jin, C. L. Jia, W. Egger, and R. Dittmann, "Nonstoichiometry accommodation in SrTiO₃ thin films studied by positron annihilation and electron microscopy," *Physical Review B - Condensed Matter and Materials Physics*, vol. 87, no. 19, p. 195409, 2013.
- [151] C. Xu, S. Wicklein, A. Sambri, S. Amoruso, M. Moors, and R. Dittmann, "Impact of the interplay between nonstoichiometry and kinetic energy of the plume species on the growth mode of SrTiO₃ thin films," *Journal of Physics D: Applied Physics*, vol. 47, no. 3, p. 034009, 2014.
- [152] N. Raab, C. Bäumer, and R. Dittmann, "Impact of the cation-stoichiometry on the resistive switching and data retention of SrTiO₃ thin films," *AIP Advances*, vol. 5, p. 047150, apr 2015.
- [153] J. H. Neave, B. A. Joyce, P. J. Dobson, and N. Norton, "Dynamics of film growth of GaAs by MBE from Rheed observations," *Applied Physics A Solids and Surfaces*, vol. 31, pp. 1–8, may 1983.
- [154] P. J. Brown, A. G. Fox, E. N. Maslen, M. A. O'Keefe, and B. T. M. Willis, "Intensity of diffracted intensities," in *International Tables for Crystallography*, pp. 554–595, International Union of Crystallography, oct 2006.
- [155] A. Ichimiya, P. I. Cohen, and P. I. Cohen, *Reflection high-energy electron diffraction*. Cambridge University Press, 2004.
- [156] S. Hasegawa, "Reflection High-Energy Electron Diffraction," in *Characterization of Materials*, Hoboken, NJ, USA: John Wiley & Sons, Inc., oct 2012.
- [157] J. H. Song and Y. H. Jeong, "SrTiO₃ homoepitaxy by the pulsed laser deposition method: Island, layer-by-layer, and step-flow growth," *Solid State Communications*, vol. 125, no. 10, pp. 563–566, 2003.

- [158] J. Choi, C. B. Eom, G. Rijnders, H. Rogalla, and D. H. Blank, "Growth mode transition from layer by layer to step flow during the growth of heteroepitaxial SrRuO₃ on (001) SrTiO₃," *Applied Physics Letters*, vol. 79, no. 10, pp. 1447–1449, 2001.
- [159] G. Koster, G. J. Rijnders, D. H. Blank, and H. Rogalla, "Imposed layer-by-layer growth by pulsed laser interval deposition," *Applied Physics Letters*, vol. 74, no. 24, pp. 3729–3731, 1999.
- [160] T. Karabacak, P. Singh, Y. P. Zhao, G. C. Wang, and T. M. Lu, "Scaling during shadowing growth of isolated nanocolumns," *Physical Review B - Condensed Matter and Materials Physics*, vol. 68, no. 12, 2003.
- [161] A. H. Shukor, H. A. Alhattab, and I. Takano, "Electrical and optical properties of copper oxide thin films prepared by DC magnetron sputtering," *Journal of Vacuum Science & Technology B*, vol. 38, p. 012803, jan 2020.
- [162] P. Misra, V. Ganeshan, and N. Agrawal, "Low temperature deposition of highly transparent and conducting Al-doped ZnO films by RF magnetron sputtering," *Journal of Alloys and Compounds*, vol. 725, pp. 60–68, nov 2017.
- [163] K. Skaja, *Redox processes and ionic transport in resistive switching binary metal oxides*. Phd thesis, RWTH Aachen University, 2016.
- [164] K. Skaja, M. Andrä, V. Rana, R. Waser, R. Dittmann, and C. Baeumer, "Reduction of the forming voltage through tailored oxygen non-stoichiometry in tantalum oxide ReRAM devices," *Scientific Reports*, vol. 8, p. 10861, dec 2018.
- [165] M. V. Ivanov, T. V. Perevalov, V. S. Aliev, V. A. Gritsenko, and V. V. Kaichev, "Electronic structure of δ -Ta₂O₅ with oxygen vacancy: Ab initio calculations and comparison with experiment," *Journal of Applied Physics*, vol. 110, no. 2, p. 24115, 2011.
- [166] G. S. Oehrlein, "Oxidation temperature dependence of the dc electrical conduction characteristics and dielectric strength of thin Ta₂O₅ films on silicon," *Journal of Applied Physics*, vol. 59, pp. 1587–1595, mar 1986.
- [167] Y. Nishioka, H. Shinriki, and K. Mukai, "Influence of SiO₂ at the Ta₂O₅/Si interface on dielectric characteristics of Ta₂O₅ capacitors," *Journal of Applied Physics*, vol. 61, pp. 2335–2338, mar 1987.
- [168] C. Rodenbücher, S. Menzel, D. Wrana, T. Gensch, C. Korte, F. Krok, and K. Szot, "Current channeling along extended defects during electroreduction of SrTiO₃," *Scientific Reports*, vol. 9, no. 1, 2019.

-
- [169] N. Raab, *Fabrication of SrTiO₃ thin films with tailored defect structure for future non-volatile memories*. Phd thesis, RWTH Aachen University, 2017.
- [170] T. Heisig, J. Kler, H. Du, C. Baeumer, F. Hensling, M. Glöß, M. Moors, A. Locatelli, T. O. Menten, F. Genuzio, J. Mayer, R. A. De Souza, and R. Dittmann, “Antiphase Boundaries Constitute Fast Cation Diffusion Paths in SrTiO₃ Memristive Devices,” *Advanced Functional Materials*, vol. 30, p. 2004118, sep 2020.
- [171] L. Goux, P. Czarnecki, Y. Y. Chen, L. Pantisano, X. P. Wang, R. Degraeve, B. Govoreanu, M. Jurczak, D. J. Wouters, and L. Altimime, “Evidences of oxygen-mediated resistive-switching mechanism in TiN/HfO₂/Pt cells,” *Applied Physics Letters*, vol. 97, no. 24, pp. 95–98, 2010.
- [172] M. Minohara, R. Yasuhara, H. Kumigashira, and M. Oshima, “Termination layer dependence of Schottky barrier height for La_{0.6}Sr_{0.4}MnO₃/Nb:SrTiO₃ heterojunctions,” *Physical Review B - Condensed Matter and Materials Physics*, vol. 81, no. 23, 2010.
- [173] A. Staykov, S. Fukumori, K. Yoshizawa, K. Sato, T. Ishihara, and J. Kilner, “Interaction of SrO-terminated SrTiO₃ surface with oxygen, carbon dioxide, and water,” *Journal of Materials Chemistry A*, vol. 6, no. 45, pp. 22662–22672, 2018.
- [174] T. Seiyama, N. Yamazoe, and H. Arai, “Ceramic humidity sensors,” *Sensors and Actuators*, vol. 4, pp. 85–96, jan 1983.
- [175] N. Sata, K. Hiramoto, M. Ishigame, and S. Hosoya, “Site identification of protons in: Mechanism for large protonic conduction,” *Physical Review B - Condensed Matter and Materials Physics*, vol. 54, no. 22, pp. 15795–15799, 1996.
- [176] T. Higuchi, T. Tsukamoto, N. Sata, K. Hiramoto, M. Ishigame, and S. Shin, “Protonic conduction in the single crystal of SrTi_{1-x}Sc_xO₃,” *Japanese Journal of Applied Physics, Part 1: Regular Papers and Short Notes and Review Papers*, vol. 41, no. 4, pp. 2120–2121, 2002.
- [177] A. N. Cox and C. A. Pilachowski, *Allen's Astrophysical Quantities*, vol. 53. Springer, 2000.
- [178] F. Messerschmitt, M. Kubicek, and J. L. Rupp, “How Does Moisture Affect the Physical Property of Memristance for Anionic-Electronic Resistive Switching Memories?,” *Advanced Functional Materials*, vol. 25, no. 32, pp. 5117–5125, 2015.
- [179] I. Valov and T. Tsuruoka, “Effects of moisture and redox reactions in VCM and ECM resistive switching memories,” *Journal of Physics D: Applied Physics*, vol. 51, no. 41, p. 413001, 2018.

- [180] G. Milano, M. Luebben, M. Laurenti, S. Porro, K. Bejtka, S. Bianco, U. Breuer, L. Boarino, I. Valov, and C. Ricciardi, "Ionic Modulation of Electrical Conductivity of ZnO Due to Ambient Moisture," *Advanced Materials Interfaces*, vol. 6, p. 1900803, sep 2019.
- [181] M. Kessel, R. A. De Souza, H. I. Yoo, and M. Martin, "Strongly enhanced incorporation of oxygen into barium titanate based multilayer ceramic capacitors using water vapor," *Applied Physics Letters*, vol. 97, no. 2, pp. 2–4, 2010.
- [182] A. Kruth and J. T. Irvine, "Water incorporation studies on doped barium cerate perovskites," *Solid State Ionics*, vol. 162-163, pp. 83–91, 2003.
- [183] K. Szot, W. Speier, R. Carius, U. Zastrow, and W. Beyer, "Localized metallic conductivity and self-healing during thermal reduction of SrTiO₃," *Physical review letters*, vol. 88, no. 7, p. 75508, 2002.
- [184] R. A. De Souza, V. Metlenko, D. Park, and T. E. Weirich, "Behavior of oxygen vacancies in single-crystal SrTiO₃: Equilibrium distribution and diffusion kinetics," *Physical Review B - Condensed Matter and Materials Physics*, vol. 85, no. 17, pp. 1–11, 2012.
- [185] H. Schraknepper and R. A. De Souza, "Competing descriptions of diffusion profiles with two features: Surface space-charge layer versus fast grain-boundary diffusion," *Journal of Applied Physics*, vol. 119, no. 6, p. 64903, 2016.
- [186] J. Hözl and F. K. Schulte, "Work function of metals," pp. 1–150, Springer, Berlin, Heidelberg, 1979.
- [187] R. Garg, N. Dutta, and N. Choudhury, "Work Function Engineering of Graphene," *Nanomaterials*, vol. 4, pp. 267–300, apr 2014.
- [188] A. Schönhals, C. M. M. Rosario, S. Hoffmann-Eifert, R. Waser, S. Menzel, and D. J. Wouters, "Role of the electrode material on the RESET limitation in oxide ReRAM devices," *Advanced electronic materials*, vol. 4, no. 2, p. 1700243, 2018.
- [189] A. Schönhals, A. Kindsmüller, C. La Torre, H. Zhang, S. Hoffmann-Eifert, S. Menzel, R. Waser, and D. J. Wouters, "Overcoming the RESET Limitation in Tantalum Oxide-Based ReRAM Using an Oxygen-Blocking Layer," in *2017 IEEE International Memory Workshop (IMW)*, pp. 1–4, IEEE, 2017.
- [190] M. Lübben, P. Karakolis, V. Ioannou-Souglерidis, P. Normand, P. Dimitrakis, and I. Valov, "Graphene-modified interface controls transition from VCM to ECM switching modes in Ta/TaO_x based memristive devices," *Advanced materials*, vol. 27, no. 40, pp. 6202–6207, 2015.

-
- [191] H. Y. Nan, Z. H. Ni, J. Wang, Z. Zafar, Z. X. Shi, and Y. Y. Wang, "The thermal stability of graphene in air investigated by Raman spectroscopy," *Journal of Raman Spectroscopy*, vol. 44, pp. 1018–1021, jul 2013.
- [192] M. von Witzleben, K. Fleck, C. Funck, B. Baumkötter, M. Zuric, A. Idt, T. Breuer, R. Waser, U. Böttger, and S. Menzel, "Investigation of the Impact of High Temperatures on the Switching Kinetics of Redox-Based Resistive Switching Cells using a High-Speed Nanoheater," *Advanced Electronic Materials*, vol. 3, p. 1700294, dec 2017.
- [193] L. M. Malard, M. A. Pimenta, G. Dresselhaus, and M. S. Dresselhaus, "Raman spectroscopy in graphene," *Physics Reports*, vol. 473, pp. 51–87, apr 2009.
- [194] M. M. Lucchese, F. Stavale, E. H. Ferreira, C. Vilani, M. V. Moutinho, R. B. Capaz, C. A. Achete, and A. Jorio, "Quantifying ion-induced defects and Raman relaxation length in graphene," *Carbon*, vol. 48, pp. 1592–1597, apr 2010.
- [195] J. Chen, T. Shi, T. Cai, T. Xu, L. Sun, X. Wu, and D. Yu, "Self healing of defected graphene," *Applied Physics Letters*, vol. 102, p. 103107, mar 2013.
- [196] D. Graf, F. Molitor, K. Ensslin, C. Stampfer, A. Jungen, C. Hierold, and L. Wirtz, "Spatially resolved raman spectroscopy of single- and few-layer graphene," *Nano Letters*, vol. 7, pp. 238–242, feb 2007.
- [197] Z. H. Ni, H. M. Wang, Z. Q. Luo, Y. Y. Wang, T. Yu, Y. H. Wu, and Z. X. Shen, "The effect of vacuum annealing on graphene," *Journal of Raman Spectroscopy*, vol. 41, pp. 479–483, may 2010.
- [198] F. Schedin, A. K. Geim, S. V. Morozov, E. W. Hill, P. Blake, M. I. Katsnelson, and K. S. Novoselov, "Detection of individual gas molecules adsorbed on graphene," *Nature Materials*, vol. 6, pp. 652–655, sep 2007.
- [199] W. Kim, *Investigation of switching mechanism in Ta₂O₅-based ReRAM devices*. Phd thesis, RWTH Aachen University, 2017.
- [200] M. Lübben, S. Wiefels, R. Waser, and I. Valov, "Processes and Effects of Oxygen and Moisture in Resistively Switching TaO_x and HfO_x," *Advanced Electronic Materials*, vol. 4, p. 1700458, jan 2018.
- [201] Y. Sone, A. Kishimoto, and T. Kudo, "Proton conductivity of spin-coated Ta₂O₅ nH₂O amorphous thin films from peroxo-polytantalate solution," *Solid State Ionics*, vol. 66, pp. 53–59, oct 1993.

- [202] A. Kishimoto, T. Kudo, and T. Nanba, "Amorphous tantalum and niobium oxide proton conductors derived from respective peroxy polyacids," *Solid State Ionics*, vol. 53-56, pp. 993–997, jul 1992.
- [203] Y. Abe, F. Peng, Y. Takiguchi, M. Kawamura, K. Sasaki, H. Itoh, and T. Suzuki, "Effects of substrate cooling during sputter deposition of hydrogen-containing Ta₂O₅ thin films in H₂O atmosphere on their ion conductivity," *Japanese Journal of Applied Physics*, vol. 47, pp. 7269–7271, sep 2008.
- [204] S. Lecuyer, A. Quemerais, and G. Jezequel, "Composition of natural oxide films on polycrystalline tantalum using XPS electron take-off angle experiments," *Surface and interface analysis*, vol. 18, no. 4, pp. 257–261, 1992.
- [205] R. Schmiidl, V. Demuth, P. Lahnor, H. Godehardt, Y. Bodschwinn, C. Harder, L. Hammer, H. P. Strunk, M. Schulz, and K. Heinz, "Oxygen diffusion through thin Pt films on Si(100)," *Applied Physics A: Materials Science and Processing*, vol. 62, no. 3, pp. 223–230, 1996.
- [206] A. Grill, W. Kane, J. Viggiano, M. Brady, and R. Laibowitz, "Base electrodes for high dielectric constant oxide materials in silicon technology," *Journal of Materials Research*, vol. 7, no. 12, pp. 3260–3265, 1992.
- [207] D. S. Jeong, H. Schroeder, U. Breuer, and R. Waser, "Characteristic electroforming behavior in Pt/TiO₂/Pt resistive switching cells depending on atmosphere," *Journal of Applied Physics*, vol. 104, no. 12, p. 123716, 2008.
- [208] J. P. Strachan, J. Joshua Yang, R. Münstermann, A. Schöll, G. Medeiros-Ribeiro, D. R. Stewart, and R. Stanley Williams, "Structural and chemical characterization of TiO₂ memristive devices by spatially-resolved NEXAFS," *Nanotechnology*, vol. 20, no. 48, 2009.
- [209] A. L. Efros and B. I. Shklovskii, "Coulomb gap and low temperature conductivity of disordered systems," *Journal of Physics C: Solid State Physics*, vol. 8, p. L49, feb 1975.
- [210] C. Yan, J. Wang, and P. S. Lee, "Stretchable graphene thermistor with tunable thermal index," *ACS Nano*, vol. 9, pp. 2130–2137, feb 2015.
- [211] M. T. Greiner, L. Chai, M. G. Helander, W. M. Tang, and Z. H. Lu, "Transition metal oxide work functions: The influence of cation oxidation state and oxygen vacancies," *Advanced Functional Materials*, vol. 22, pp. 4557–4568, nov 2012.
- [212] A. Kahn, "Fermi level, work function and vacuum level," *Materials Horizons*, vol. 3, no. 1, pp. 7–10, 2016.

-
- [213] H. B. Michaelson, "Work functions of the elements," *Journal of Applied Physics*, vol. 21, pp. 536–540, jun 1950.
- [214] M. Lippmaa, M. Kawasaki, A. Ohtomo, T. Sato, M. Iwatsuki, and H. Koinuma, "Observation of SrTiO₃ step edge dynamics by real-time high-temperature STM," *Applied Surface Science*, vol. 130-132, pp. 582–586, jun 1998.
- [215] R. Bachelet, F. Valle, I. C. Infante, F. Sánchez, and J. Fontcuberta, "Step formation, faceting, and bunching in atomically flat SrTiO₃ (110) surfaces," *Applied Physics Letters*, vol. 91, p. 251904, dec 2007.
- [216] W. Jung and H. L. Tuller, "Investigation of surface Sr segregation in model thin film solid oxide fuel cell perovskite electrodes," *Energy and Environmental Science*, vol. 5, no. 1, pp. 5370–5378, 2012.
- [217] R. P. Vasquez, "X-ray photoelectron spectroscopy study of Sr and Ba compounds," *Journal of Electron Spectroscopy and Related Phenomena*, vol. 56, pp. 217–240, jun 1991.
- [218] C. Baeumer, C. Xu, F. Gunkel, N. Raab, R. A. Heinen, A. Koehl, and R. Dittmann, "Surface Termination Conversion during SrTiO₃ Thin Film Growth Revealed by X-ray Photoelectron Spectroscopy," *Scientific Reports*, vol. 5, no. 1, p. 11829, 2015.
- [219] T. Ohnishi, K. Shibuya, T. Yamamoto, and M. Lippmaa, "Defects and transport in complex oxide thin films," *Journal of Applied Physics*, vol. 103, p. 103703, may 2008.
- [220] R. Meyer, R. Waser, J. Helmbold, and G. Borchardt, "Observation of Vacancy Defect Migration in the Cation Sublattice of Complex Oxides by ¹⁸O Tracer Experiments," *Physical Review Letters*, vol. 90, no. 10, p. 4, 2003.
- [221] S. Plimpton, "Fast parallel algorithms for short-range molecular dynamics," *Journal of Computational Physics*, vol. 117, pp. 1–19, mar 1995.
- [222] A. Pedone, G. Malavasi, M. C. Menziani, A. N. Cormack, and U. Segre, "A new self-consistent empirical interatomic potential model for oxides, silicates, and silicas-based glasses," *Journal of Physical Chemistry B*, vol. 110, no. 24, pp. 11780–11795, 2006.
- [223] A. Walsh, C. R. A. Catlow, A. G. Smith, A. A. Sokol, and S. M. Woodley, "Strontium migration assisted by oxygen vacancies in SrTiO₃ from classical and quantum mechanical simulations," *Physical Review B - Condensed Matter and Materials Physics*, vol. 83, p. 220301, jun 2011.

- [224] S. A. Lee, H. Jeong, S. Woo, J.-Y. Hwang, S.-Y. Choi, S.-D. Kim, M. Choi, S. Roh, H. Yu, and J. Hwang, "Phase transitions via selective elemental vacancy engineering in complex oxide thin films," *Scientific reports*, vol. 6, no. 1, pp. 1–10, 2016.
- [225] E. Stoyanov, F. Langenhorst, and G. Steinle-Neumann, "The effect of valence state and site geometry on Ti L_{3,2} and O K electron energy-loss spectra of Ti_xO_y phases," *American Mineralogist*, vol. 92, no. 4, pp. 577–586, 2007.
- [226] D. A. Muller, N. Nakagawa, A. Ohtomo, J. L. Grazul, and H. Y. Hwang, "Atomic-scale imaging of nanoengineered oxygen vacancy profiles in SrTiO₃," *Nature*, vol. 430, no. 7000, pp. 657–661, 2004.
- [227] K. Gömann, G. Borchardt, A. Gunhold, W. Maus-Friedrichs, and H. Baumann, "Ti diffusion in La-doped SrTiO₃ single crystals," in *Physical Chemistry Chemical Physics*, vol. 6, pp. 3639–3644, jul 2004.
- [228] R. Muenstermann, T. Menke, R. Dittmann, S. Mi, C. L. Jia, D. Park, and J. Mayer, "Correlation between growth kinetics and nanoscale resistive switching properties of SrTiO₃ thin films," *Journal of Applied Physics*, vol. 108, p. 124504, dec 2010.
- [229] M. Lanza, G. Bersuker, M. Porti, E. Miranda, M. Nafria, and X. Aymerich, "Resistive switching in hafnium dioxide layers: Local phenomenon at grain boundaries," *Applied Physics Letters*, vol. 101, no. 19, p. 193502, 2012.
- [230] M. Lanza, K. Zhang, M. Porti, M. Nafria, Z. Y. Shen, L. F. Liu, J. F. Kang, D. Gilmer, and G. Bersuker, "Grain boundaries as preferential sites for resistive switching in the HfO₂ resistive random access memory structures," *Applied Physics Letters*, vol. 100, no. 12, p. 123508, 2012.
- [231] S. Petzold, A. Zintler, R. Eilhardt, E. Piro, N. Kaiser, S. U. Sharath, T. Vogel, M. Major, K. P. McKenna, and L. Molina-Luna, "Forming Free Grain Boundary Engineered Hafnium Oxide Resistive Random Access Memory Devices," *Advanced Electronic Materials*, vol. 5, no. 10, p. 1900484, 2019.
- [232] D. H. Kwon, S. Lee, C. S. Kang, Y. S. Choi, S. J. Kang, H. L. Cho, W. Sohn, J. Jo, S. Y. Lee, K. H. Oh, T. W. Noh, R. A. De Souza, M. Martin, and M. Kim, "Unraveling the Origin and Mechanism of Nanofilament Formation in Polycrystalline SrTiO₃ Resistive Switching Memories," *Advanced Materials*, vol. 31, p. 1901322, jul 2019.
- [233] F. Bonoli, P. Godio, G. Borionetti, and R. Falster, "Gate oxide integrity dependence on substrate characteristics and SiO₂ thickness," *Materials Science in Semiconductor Processing*, vol. 4, no. 1-3, pp. 145–148, 2001.

-
- [234] Y. Koga and K. Kurita, “Fabrication of silicon on insulator wafer with silicon carbide insulator layer by surface-activated bonding at room temperature,” *Japanese Journal of Applied Physics*, vol. 59, no. 5, p. 51002, 2020.
- [235] Z. Wang, M. Yin, T. Zhang, Y. Cai, Y. Wang, Y. Yang, and R. Huang, “Engineering incremental resistive switching in TaO_x based memristors for brain-inspired computing,” *Nanoscale*, vol. 8, no. 29, pp. 14015–14022, 2016.
- [236] T. H. Park, S. J. Song, H. J. Kim, S. G. Kim, S. Chung, B. Y. Kim, K. J. Lee, K. M. Kim, B. J. Choi, and C. S. Hwang, “Thickness effect of ultra-thin Ta₂O₅ resistance switching layer in 28 nm-diameter memory cell,” *Scientific Reports*, vol. 5, pp. 1–9, nov 2015.
- [237] A. Locatelli, T. O. Menten, M. Á. Niño, and E. Bauer, “Image blur and energy broadening effects in XPEEM,” *Ultramicroscopy*, vol. 111, pp. 1447–1454, jul 2011.
- [238] P. Nemes-Incze, Z. Osváth, K. Kamarás, and L. P. Biró, “Anomalies in thickness measurements of graphene and few layer graphite crystals by tapping mode atomic force microscopy,” *Carbon*, vol. 46, pp. 1435–1442, sep 2008.
- [239] M. C. Patt, *Bulk and surface sensitive energy-filtered photoemission microscopy using synchrotron radiation for the study of resistive switching memories*. PhD thesis, Jülich, 2016.
- [240] S. Tanuma, C. J. Powell, and D. R. Penn, “Calculations of electron inelastic mean free paths (IMFPS). IV. Evaluation of calculated IMFPS and of the predictive IMFPS formula TPP-2 for electron energies between 50 and 2000 eV,” *Surface and Interface Analysis*, vol. 20, pp. 77–89, jan 1993.
- [241] M. Amjadipour, J. Macleod, J. Lipton-Duffin, A. Tadich, J. J. Boeckl, F. Iacopi, and N. Motta, “Electron effective attenuation length in epitaxial graphene on SiC,” *Nanotechnology*, vol. 30, p. 025704, jan 2019.
- [242] A. Jablonski, “NIST Electron Inelastic-Mean-Free-Path Database,” *National Institute of Standards and Technology, Gaithersburg*, 2010.
- [243] K. Boller, R.-P. Haelbich, H. Hogrefe, W. Jark, and C. Kunz, “Investigation of carbon contamination of mirror surfaces exposed to synchrotron radiation,” *Nuclear instruments and methods in physics research*, vol. 208, no. 1-3, pp. 273–279, 1983.
- [244] L. Mino, E. Borfecchia, J. Segura-Ruiz, C. Giannini, G. Martinez-Criado, and C. Lamberti, “Materials characterization by synchrotron x-ray microprobes and nanoprobe,” *Reviews of Modern Physics*, vol. 90, p. 025007, jun 2018.

- [245] W. Bras and H. Stanley, "Unexpected effects in non crystalline materials exposed to X-ray radiation," *Journal of Non-Crystalline Solids*, vol. 451, pp. 153–160, nov 2016.
- [246] L. Mino, V. Bonino, F. Picollo, M. Fretto, A. Agostino, and M. Truccato, "Tailoring the Local Conductivity of TiO₂ by X-Ray Nanobeam Irradiation," *Advanced Electronic Materials*, vol. 5, p. 1900129, jun 2019.
- [247] A. Nenning, A. K. Opitz, C. Rameshan, R. Rameshan, R. Blume, M. Hävecker, A. Knop-Gericke, G. Rupprechter, B. Klötzer, and J. Fleig, "Ambient pressure XPS study of mixed conducting perovskite type SOFC cathode and anode materials under well defined electrochemical polarization," *Journal of Physical Chemistry C*, vol. 120, no. 3, pp. 1461–1471, 2016.
- [248] L. Soriano, M. Abbate, J. C. Fuggle, M. A. Jiménez, J. M. Sanz, C. Mythen, and H. A. Padmore, "The O 1s x-ray absorption spectra of transition-metal oxides: The TiO₂-ZrO₂-HfO₂ and V₂O₅-Nb₂O₅-Ta₂O₅ series," *Solid State Communications*, vol. 87, pp. 699–703, aug 1993.
- [249] L. Sacconi, "Five coordination in 3d metal complexes," *Pure Appl. Chem*, vol. 17, pp. 95–127, 1968.
- [250] A. L. Companion and M. A. Komarynsky, "Crystal field splitting diagrams," *Journal of Chemical Education*, vol. 41, no. 5, p. 257, 1964.
- [251] T. A. Albright, J. K. Burdett, and M.-H. Whangbo, *Orbital interactions in chemistry*. John Wiley & Sons, 2013.
- [252] G. Mattoni, A. Filippetti, N. Manca, P. Zubko, and A. D. Caviglia, "Charge doping and large lattice expansion in oxygen-deficient heteroepitaxial WO₃," *Physical Review Materials*, vol. 2, no. 5, p. 53402, 2018.
- [253] H. O. Pierson, *Handbook of carbon, graphite, diamonds and fullerenes: processing, properties and applications*. William Andrew, 2012.
- [254] R. Waser, "Redox-based resistive switching memories," *Journal of Nanoscience and Nanotechnology*, vol. 12, no. 10, pp. 7628–7640, 2012.
- [255] A. Siemon, S. Menzel, A. Marchewka, Y. Nishi, R. Waser, and E. Linn, "Simulation of TaO_x-based complementary resistive switches by a physics-based memristive model," in *2014 IEEE international symposium on circuits and systems (ISCAS)*, pp. 1420–1423, IEEE, 2014.

- [256] X. Liang, B. A. Sperling, I. Calizo, G. Cheng, C. A. Hacker, Q. Zhang, Y. Obeng, K. Yan, H. Peng, and Q. Li, "Toward clean and crackless transfer of graphene," *ACS nano*, vol. 5, no. 11, pp. 9144–9153, 2011.
- [257] S. Deng and V. Berry, "Wrinkled, rippled and crumpled graphene: An overview of formation mechanism, electronic properties, and applications," *Materials Today*, vol. 19, pp. 197–212, may 2016.

List of Publications

1. **T. Heisig**, J. Kler, H. Du, C. Baeumer, F. Hensling, M. Glöß, M. Moors, A. Locatelli, T. O. Mentes, F. Genuzio, J. Mayer, R. A. De Souza, R. Dittmann. Antiphase Boundaries Constitute Fast Cation Diffusion Paths in SrTiO₃ Memristive Devices. *Advanced Functional Materials*, 2020.
2. V. R. Nallagatla*, **T. Heisig***, C. Baeumer, V. Feyer, M. Jugovac, G. Zamborlini, C. M. Schneider, R. Waser, M. Kim, C. U. Jung, R. Dittmann. Topotactic Phase Transition Driving Memristive Behavior *Advanced Materials*, 2019.
3. C. Baeumer, C. Funck, A. Locatelli, T. Mentes, F. Genuzio, **T. Heisig**, F. Hensling, N. Raab, C. Schneider, S. Menzel, R. Waser, and R. Dittmann. In-Gap States and Band-Like Transport in Memristive Devices. *Nano Letters*, 2019.
4. C. Baeumer, **T. Heisig**, B. Arndt, K. Skaja, F. Borgatti, F. Offi, F. Motti, G. Panaccione, R. Waser, S. Menzel, and R. Dittmann. Spectroscopic elucidation of ionic motion processes in tunnel-oxide based memristive devices. *Faraday Discussions*, 2018.
5. **T. Heisig**, C. Baeumer, U. Gries, M. Mueller, C. La Torre, M. Luebben, N. Raab, H. Du, S. Menzel, D. Mueller, C.-L. Jia, J. Mayer, R. Waser, I. Valov, R. De Souza, and R. Dittmann. Oxygen Exchange Processes between Oxide Memristive Devices and Water Molecules. *Advanced Materials*, 2018.
6. F. V.E. Hensling, **T. Heisig**, N. Raab, C. Baeumer, and R. Dittmann. Tailoring the switching performance of resistive switching SrTiO₃ devices by SrO interface engineering. *Solid State Ionics*, 2018.

*Authors contributed equally

Conference Talks and Posters

1. **T. Heisig**, J. Kler, H. Du, C. Baeumer, F. Hensling, M. Glöß, M. Moors, A. Locatelli, T. O. Montes, F. Genuzio, J. Mayer, R. A. De Souza, R. Dittmann. Poster: Anionic and cationic stoichiometry variations in the conductive filament of SrTiO₃ memristive devices. *International Conference on Memristive Materials, Devices & Systems (MEM-RISYS)*, 2019.
2. **T. Heisig**, C. Baeumer, U. Gries, M. Mueller, C. La Torre, M. Luebben, N. Raab, H. Du, S. Menzel, D. Mueller, C.-L. Jia, J. Mayer, R. Waser, I. Valov, R. De Souza, and R. Dittmann. Talk: Verification of oxygen exchange processes in SrTiO₃ based memristive devices *Conference on Electronic and Advanced Materials*, 2018
3. **T. Heisig**, C. Baeumer, U. Gries, M. Mueller, C. La Torre, M. Luebben, N. Raab, H. Du, S. Menzel, D. Mueller, C.-L. Jia, J. Mayer, R. Waser, I. Valov, R. De Souza, and R. Dittmann. Talk and Poster: Oxygen exchange processes between oxide memristive devices and water molecules *European Materials Research Society - Spring Meeting*, 2018

Acknowledgments

At the end of this thesis I would like to express my warmest thanks to everyone who was involved in this work through their contribution or by supporting me during my time in Jülich.

First, I would like to thank my PhD mentor Prof. Dr. Regina Dittmann for the supervision of this thesis. I am deeply grateful for her continuing support, encouragement and advice which was essential for the successful realization of this thesis. During my entire time in Jülich she opened me many doors and helped me to develop myself on a scientific and on a personal level.

Furthermore, I would like to thank Prof. Dr. Ulrich Simon for agreeing to act as reviewer of this doctoral thesis.

I am truly thankful to Christoph Bäumer for his guidance throughout my scientific career. His supportive and encouraging nature helped me to advance myself in various aspects of science, ranging from practical lab work and data analysis to writing publications. I would also like to thank him for laying the foundation of this thesis through his years of research in the field of spectromicroscopy and resistive switching.

After arriving in Jülich I had the luck to be placed into the large office, where I enjoyed the company of many fantastic colleagues. Our office was not only a fruitful working space but also a place of strong team spirit where many friendships began. I want to thank my office mates Michael Andrä, Nicolas Raab, Felix Hensling, Jacqueline Börgers, Marc-André Rose, Venkata Raveendra Nallagatla, Doudou Wu, Nuno Casa Branca and Alexandros Sarantopoulos for the great working atmosphere, the helpful discussions and the hours we spent together in the cluster lab repairing instruments and fixing leaks. Thanks go out to René Ebeling who taught me the way of the Forschungszentrum bureaucracy and how to accelerate urgent processes.

I also enjoyed help from many colleagues at the PGI7, the IWEII and from the SFB917. I thank Sebastian Siegel for the electro-thermal simulations and Maria Glöß for conductive AFM measurements. Thanks go to Urska Gabor, for the Raman measurements and to Jacqueline Börgers for low temperature conductivity measurements. I thank Andreas Kindsmüller for helping me with the electrical characterization of tantalum oxide devices.

I thank all present and former colleagues in our institute for the friendly working atmosphere.

This thesis would not have been possible without the support of many colleagues and scientists that were involved in numerous synchrotron beamtimes. My special thanks goes to Christoph Bäumer, Regina Dittmann, Venkata Raveendra Nallagatla, Felix Hensling, Carsten Wiemann, Richard Valenta, Sebastian Hamsch, Alexander Gutsche and Kalle Goß for sharing day and night shifts with me at the synchrotrons. I am most grateful to all beamline scientists that helped me during the beamtimes, namely Dr. Andrea Locatelli, Dr. Tevik Onur Mentesh, Francesca Genuzio, Dr. Vitaly Feyer, Dr. Giovanni Zamborlini, Matteo Jugovac, Dr. Slavomir Nemsak, Dr. Johanna Hackl, Dr. Michael Foerster and Dr. Lucia Aballe. Their willingness to work long hours was essential to the success of many beamtimes and for this I am very thankful.

For the TEM work in this thesis, my gratitude goes to Dr. Hongchu Du, Max Kruth and Dr. David Cooper. I am especially thankful to Prof. Dr. Roger De Souza, Dr. Ute Gries, Dr. Michael Müller and Joe Kler for the close collaboration during my time in Jülich. Their experimental and theoretical expertise on anion and cation transport was key to understand switching related processes on a more fundamental level.

For technical support with the cluster tool I want to thank Georg Pickartz and Jochen Friedrich. I thank Marcel Gerst for help with the electronic setups for device characterization. Moreover, Marcel was always the rescue when an electrical component failed that caused a big chaos in the cluster lab. Special thanks go to René Borowski for sharing his expertise and advice with me and for help with sample fabrication. Especially during beamtime preparations I could always count on René's help. I am grateful to Maria Garcia for continuing help with administrative issues.

Finally, I would like to thank my family and friends for their unflinching support during my studies and the PhD time. The biggest thanks goes to Lena who never stopped to encourage me in times it was needed and for believing in me.

Band / Volume 65

Scalable Control Electronics for a Spin Based Quantum Computer

L. Geck (2021), xiv, 114, xv-xxxiii

ISBN: 978-3-95806-540-6

Band / Volume 66

DNA-capped silver nanoparticles for stochastic nanoparticle impact electrochemistry

L. Nörbel (2021), VI, 142 pp

ISBN: 978-3-95806-541-3

Band / Volume 67

Development, characterization, and application of intraretinal implants

V. Rincón Montes (2021), XII, 173 pp

ISBN: 978-3-95806-553-6

Band / Volume 68

Optogenetic and electrical investigation of network dynamics in patterned neuronal cultures

T. J. J. Hondrich (2021), x, 177 pp

ISBN: 978-3-95806-555-0

Band / Volume 69

Disentangling parallel conduction channels by charge transport measurements on surfaces with a multi-tip scanning tunneling microscope

S. Just (2021), xii, 225 pp

ISBN: 978-3-95806-574-1

Band / Volume 70

Nanoscale four-point charge transport measurements in topological insulator thin films

A. Leis (2021), ix, 153 pp

ISBN: 978-3-95806-580-2

Band / Volume 71

Investigating the Interaction between π -Conjugated Organic Molecules and Metal Surfaces with Photoemission Tomography

X. Yang (2021), xviii, 173 pp

ISBN: 978-3-95806-584-0

Band / Volume 72

Three-Dimensional Polymeric Topographies for Neural Interfaces

F. Milos (2021), 133 pp

ISBN: 978-3-95806-586-4

Band / Volume 73

Development, characterization, and application of compliant intracortical implants

K. Srikantharajah (2021), xiv, 155, xv-xvii pp

ISBN: 978-3-95806-587-1

Band / Volume 74

Modelling, implementation and characterization of a Bias-DAC in CMOS as a building block for scalable cryogenic control electronics for future quantum computers

P. N. Vliex (2021), xiv, 107, xv-xxviii pp

ISBN: 978-3-95806-588-8

Band / Volume 75

Development of Electrochemical Aptasensors for the Highly Sensitive, Selective, and Discriminatory Detection of Malaria Biomarkers

G. Figueroa Miranda (2021), XI, 135 pp

ISBN: 978-3-95806-589-5

Band / Volume 76

Nanostraw- Nanocavity MEAs as a new tool for long-term and high sensitive recording of neuronal signals

P. Shokoohimehr (2021), xi, 136 pp

ISBN: 978-3-95806-593-2

Band / Volume 77

Surface plasmon-enhanced molecular switching for optoelectronic applications

B. Lenyk (2021), x, 129 pp

ISBN: 978-3-95806-595-6

Band / Volume 78

Engineering neuronal networks in vitro: From single cells to population connectivity

I. Tihaa (2021), viii, 242 pp

ISBN: 978-3-95806-597-0

Band / Volume 79

Spectromicroscopic investigation of local redox processes in resistive switching transition metal oxides

T. Heisig (2022), vi, 186 pp

ISBN: 978-3-95806-609-0

Information

Band / Volume 79

ISBN 978-3-95806-609-0

Mitglied der Helmholtz-Gemeinschaft

